A Microflow Cytometer with Simultaneous Dielectrophoretic Actuation for the Optical Assay and Capacitive Cytometry of Individual Fluid Suspended Bioparticles

by

Sean Forrest Romanuik

A Thesis submitted to the Faculty of Graduate Studies of
The University of Manitoba
in partial fulfillment of the requirements for the degree of

Master of Science

Department of Electrical and Computer Engineering
University of Manitoba
Winnipeg, Manitoba
Canada

THE UNIVERSITY OF MANITOBA

FACULTY OF GRADUATE STUDIES
*****
MASTER'S THESIS/PRACTICUM FINAL REPORT

The undersigned certify that they have read the Master's Thesis/Practicum entitled:

**A Microflow Cytometer with Simultaneous Dielectrophoretic
Actuation for the Optical Assay and Capacitive Cytometry of
Individual Fluid Suspended Bioparticles**

submitted by

Sean Romanuik

in partial fulfillment of the requirements for the degree of

Master of Science

The Thesis/Practicum Examining Committee certifies that the thesis/practicum (and oral examination if required) is:

_____
(Approved or Not Approved)

☐ Thesis

Dr. D. Thomson, Advisor, ECE _____   _____

Dr. G. Bridges, ECE _____   _____

Dr. F. Lin, Physics _____   _____

_____   _____

Date: July 9, 2009

(forms\thereptm - 08/95)

Abstract

Fluid suspended biological particles (bioparticles) flowing through a non-uniform electric field E_{ext} are actuated by the induced dielectrophoretic (DEP) force F_{DEP}, known to be dependent upon the bioparticlesø dielectric phenotypes. In this work: a 10-1000 kHz DEP actuation potential ϕ_{DEP} applied to a co-planar microelectrode array (MEA) induces a F_{DEP}, altering passing bioparticle trajectories as monitored using: (1) an optical assay, in which the lateral bioparticle velocities v_{cellx} are estimated from digital video; and (2) a capacitive cytometer, in which a 1.478 GHz capacitance sensor measures the MEA capacitance perturbations ΔC_{MEA} induced by passing bioparticles, which is sensitive to the bioparticlesø elevations h_{cell}. The experimentally observed and simulated v_{cellx} profiles of actuated polystyrene microspheres (PSS) and viable and heat shocked *Saccharomyces cerevisiae* cells verify that the bioparticlesø dielectric phenotypes can be inferred from the resultant trajectories due to the balance between F_{DEP} and the viscous fluid drag force F_{drag}.

Acknowledgements

Table of Contents

List of Figures

List of Tables

List of Copyrighted Material
for Which Permission was Obtained

T.D. Tran, "Development of a zeptofarad (10^{-21} F) resolution capacitance sensor for scanning capacitance microscopy", MSc Thesis, University of Manitoba, 2001.

Reprinted with permission from Thang Duc Tran, August 6 2009.

Used in pages 19 and 20 of this thesis (as Figures 2-6 and 2-7, respectively).

www.spacebiol.ethz.ch/missions/sacestre

Reprinted with permission of from Dr. Isabelle Walther of the Swiss Federal Institute of Technology's Space Biology Group in Zürich, Switzerland, July 28 2009.

Used in page 73 of this thesis (as Figure 7-1).

List of Publications Arising From This Thesis

[Fer07] G.A. Ferrier, A.N. Hladio, D.J. Thomson, G.E. Bridges, M. Hedayatipoor, S. Olson, and M.R. Freeman, õMicrofluidic electromanipulation with capacitive detection for cell diagnositc applicationsö, *Proc. NSTI*, vol. 2, pp. 214-217, 2007.

[Fer08a] G.A. Ferrier, S.F. Romanuik, D.J. Thomson, G.E. Bridges, and M.R. Freeman, õCapacitance signatures for rapid detection of the polarity of the dielectrophoretic force on single yeast cellsö, *Proc. NSTI*, vol. 2, pp. 589-592, 2008.

[Fer08b] G.A. Ferrier, A.N. Hladio, D.J. Thomson, G.E. Bridges, M. Hedayatipoor, S. Olson, and M.R. Freeman, õMicrofluidic electromanipulation with capacitive detection for the mechanical analysis of cellsö, *Biomicrofluidics*, vol. 2, no. 4-044102, pp. 1-13, 2008.

[Fer09a] G.A. Ferrier, S.F. Romanuik, D.J. Thomson, G.E. Bridges, and M.R. Freeman, õA microwave interferometric system for simultaneous actuation and detection of single biological cellsö, *Lab on a Chip*, 2009 (Submitted May 5 2009).

[Fer09b] G.A. Ferrier, S.F. Romanuik, D.J. Thomson, G.E. Bridges, and M.R. Freeman, õRapid classification of biological cells based on dielectrophoretic actuation with simultaneous capacitive detectionö, *Proc. µTAS*, 2009 (Submitted July 1 2009).

[Jar09] M. Nikolic-Jaric, S.F. Romanuik, G.A. Ferrier, G.E. Bridges, M. Butler, K. Sunley, D.J. Thomson, and M.R. Freeman, õMicrowave frequency sensor for detection of biological cells in microfluidic channelsö, *Biomicrofluidics*, vol. 3, no. 3-034103, pp. 1-15, 2009.

[Rom08] S.F. Romanuik, G.A. Ferrier, D.J. Thomson, G.E. Bridges, S. Olson, and M.R. Freeman, õAll-electronic detection and actuation of single biological cells for lab-on-a-chip applicationsö, *Proc. IEEE Sensors*, vol. 1, pp. 634-637, 2008.

[Rom09] S.F. Romanuik, G.A. Ferrier, M.N. Jaric, D.J. Thomson, G.E. Bridges, and M.R. Freeman, õDielectrophoretic actuation and simultaneous detection of individual bioparticlesö, <u>Advances in Biomedical Sensing, Measurements, Instrumentation, and Systems</u>, Eds. A. Lay-Ekuakille and S.C. Mukhopadhyay, Springer ó Verlag, 2009 (Submitted June 3 2009).

Chapter 1
Introduction

1.1   Motivation for Single-Cell Diagnostics

Microbiology traditionally uses bulk sample measurements averaged over many cells to infer how individual cells interact, undergo complicated processes (such as differentiation and gene expression), and react to environmental stimuli [Bre04]. Even amongst colonial populations, individual cells differ in their genetic composition, physiology, biochemistry, and behaviour [Brid00, Dav96, Elo02, Koch96, Sha00]. This heterogeneity has significant consequences with regards to biocide and antibiotic resistance [Bapt99, Sull99, Turn00], industrial fermentation stability and productivity [Pow00, Schu00, Sumn02], food preservative efficacy [Arne00, Stee00, Sumn02], and pathogen virulence [Dav00]. These traditional bulk sample measurements yield ensemble averages over heterogeneous populations, from which it is difficult to probe discrete and intrinsic cell properties such as viability, protein concentration, and mutant allele possession [Wit07, Sims07, Bre04, Dav96, Sha00]. Single-cell diagnostic techniques are characterized by a radically different approach to cellular analysis, in which the properties of a given cell as an individual unto itself are directly probed [Bre04, Dav96, Sha00, Wit07]. By directly studying cells as individuals, single-cell diagnostics afford an investigation of microorganism viability beyond bulk sample resolution [Bar99, Kell98, Roc99], the elucidation of pathogenesis mechanisms [And99, Kuo00, Str01], and the quantification of the invasive forces and motility associated with individual cells [Bech99, Mish98, Schm00]. Single-cell diagnostics also afford studying links between cellular behaviour and biochemistry [Clu00, Keller99, Los99], yielding new insights into chemical signalling pathways and the mechanisms governing coordinated multicellular activities. Single-cell diagnostics also facilitate direct measurements of an individual celløs mechanical properties [Smi00, Yao02]. Furthermore, single-cell diagnostics also facilitate studies of intracellular hydrodynamics, host-pathogen interactions, surface redox activity, and metabolite, protein, and elemental localization [And99, Arc00, Cai02, Past01, Pot01, Ras99]. Within applied science, single-cell diagnostics afford the

quantification of cell population heterogeneity, and the potential to identify, characterize, and physically separate cell subpopulations to preferentially select strains [Kats00, Sten02].

Quantifying the heterogeneity of tumour cell populations facilitates determining the cancerous stage of tumours and investigating the response of tumour cells to customized drug therapies [Han07]. As an example, it is known that certain cancers release tumour cells into blood circulation during their early stages [Rci98]. During the micrometastasis stage of breast cancer, it is common to find 1-10 tumourous cells and an excess of 10^7 red blood cells within a millilitre of blood [Wit07]. Detecting these tumour cells affords diagnosing cancer at this early stage [Bak03, Hus88, Kahn04]. Furthermore, the level of circulating tumour cells can be used as a patient prognosis predictor [Cri04].

In vitro stem cell expansion, necessary for generating a sufficient population for transplantation [Campo04], is accompanied by the differentiation of daughter cell subsets, resulting in a heterogeneous in vitro population [Fla08]. Controlling the composition of stem cell transplants is difficult without the discrimination and isolation of in vitro cell subpopulations afforded by single-cell diagnostics [Fla08].

The above examples clearly demonstrate the advantages of single-cell diagnostics. However, these examples require accurate, high-throughput diagnostic devices which are ultimate goal within the current research and development of single-cell diagnostic tools.

1.2   Conventional & Microscale Flow Cytometry

Flow cytometry has been widely used for high-throughput cell-by-cell analyses of entire populations [Sha95, Mel91, Wat91, Orm00, Yu07, Álv00, Bre04, Huh05, Yi06]. Conventional flow cytometers typically consist of hydrodynamic focusing and fluorescence-activated cell sorting (FACS) stages [Yu07]. FACS commonly involves the staining of samples with fluorescent dyes, preferentially labelling specific features within individual cells, prior to injection [Sha95, Huh05]. By using dyes with different emission spectra that preferentially stain different features, FACS affords distinguishing different cellular features [Yu07]. Once injected, the hydrodynamic focusing stage uses a high-speed, laminar sheath fluid or air flow to tightly focus the sample stream into a detection zone. The FACS stage then optically excites each cell, and detects the subsequently

emitted or scattered photons. The detector output is analyzed to measure such cellular properties as size, shape, viability, cycle phase, deoxyribonucleic acid (DNA) content, and surface markers [Dav96, Viv00, Wins00, Huh05]. Modern cytometers can simultaneously quantify as many as ten distinct features at rates as high as 25 000 cells per second [Steink73, Roe97]. By yielding multiparameter datasets comprised of thousands of individually probed cells, flow cytometry affords indentifying homogeneous subpopulations within overly heterogeneous populations and facilitates investigating the links between single-cell and multicellular culture behaviour [Dav96, Gift95, Joux00, Sha00, Veal00]. The versatility of FACS-based flow cytometers can be furthered by sorting cells via fluorescent characteristics and simultaneous video microscopy [Dav96, Wiet99]. For these reasons, flow cytometry has developed into a powerful analytical tool within cellular and molecular biology [Hard00, Boe01], disease diagnostics [Stein92, Feni98], immunology [Gab95, Gar99], genetics [Wed01], and environmental science [Dub00].

Conventional flow cytometers are expensive, bulky, intricate, and require regular maintenance by skilled technicians [Huh05, Yu07]. Motivated by the demand for single-cell diagnostics, microelectromechanical system (MEMS) technologies have been utilized to develop miniaturized microflow cytometers [Huh05, Yu07]. As microfluidic channel dimensions are comparable with biological cells, microflow cytometers are well suited for single-cell diagnostics [Yu07]. Moreover, MEMS technologies afford low per unit production costs, portability, disposability, minute sample and sheath volume requirements, low power consumption, rapid heat and mass transfer rates, parallel systems for high-throughput analyses, on-chip electronic integration, and simplicity in construction, operation, and maintenance to facilitate on-site measurements [Wit07, Yu07]. Furthermore, MEMS fabrication technologies afford the integration of microflow cytometers with other manipulation and diagnostic modules to produce laboratories-on-a-chip (LoC) and micro-total-analysis-systems (μTAS) capable of implementing complete diagnostic sessions within a single microchip [Huh05, Yi06].

1.3   Electrical Impedance Based Detection within Flow Cytometry

As an alternative to FACS, some flow cytometers detect cells using a Coulter counter scheme in which particles suspended in electrically conducting fluid flow past electrodes defining a detection zone, inducing transient pulses within the monitored inter-electrode resistance [Cou56, Koch99, Yu07]. The Coulter counter principle assumes that the particle has an infinite resistance, which is true even for conducting particles as the interfacial polarization prevents conduction current from flowing through the said particle [Koch99]. Under this assumption, the inter-electrode resistance pulse becomes a measure of the detected particle's cross-sectional area [Koch99]. As such, the inter-electrode resistance is utilized to both count and size detected particles. As a Coulter counter is entirely comprised of electrodes, it is far easier to fabricate and integrate miniaturized micro-Coulter counters than miniaturized FACS systems. However, Coulter counters require a lower density of cells than FACS, to ensure that multiple cells do not simultaneously occupy the detection zone. Rodriguez-Trujillo *et al.* present a micro-Coulter counter which hydrodynamically focuses latex beads flowing past electrodes energized with a 1 MHz sinusoidal potential [Rodr07]. This micro-Coulter counter was able to detect and size 20 μm diameter beads with a throughput of 20 beads per second. Cheung *et al.* present a microflow cytometer that uses dielectrophoretic forces to focus the flow of polystyrene beads into the detection zone of electrodes energized with a 1.7 MHz potential [Che04]. This micro-Coulter counter was able to detect 4.3-6.0 μm diameter beads with a throughput of 100 beads per second. Wood *et al.* present a 100 MHz radio frequency (RF) micro-Coulter counter in which a reflectometer integrated on-chip with a microfluidic system monitors sensing electrode reflectance [Wood07]. This RF micro-Coulter counter was able to detect and size 4-9 μm diameter polystyrene beads with a throughput of approximately 5000 beads per second.

The sensing potential frequency is varied within impedance spectroscopy, to obtain an estimate of probed cell's impedance spectrum. Ayliffe *et al.* presented a microflow cytometer which estimated the impedance spectrum of human polymorphonuclear leukocytes and teleost fish red blood cells over a 100 Hz to 2 MHz bandwidth [Ayl99]. Gawad *et al.* demonstrated a microflow cytometer that utilizes 1.72-

15 MHz impedance spectroscopy to distinguish between normal and ghost human erythrocyte cell subpopulations within a heterogeneous population [Gaw01]. (Ghost cells are cells whose cytoplasmic contents have been removed).

Capacitance cytometry measures the polarization response of dielectric particles flowing through the electric field generated by a set of electrodes [Wit07]. Sohn *et al.* present a capacitive cytometer that probes the polarization within cells, observing a linear relationship between the DNA content of various eukaryotic cells and the transient inter-electrode capacitance perturbations induced as they crossed a 1 kHz electric field [Sohn00]. (As DNA is a highly charged macromolecule, its low-frequency (LF) polarization response can be substantial [Taka63, Bone95, Yang95]). Using their capacitive cytometer, Sohn *et al.* quantified the DNA content of their eukaryotic cells and analyzed the cell-cycle kinetics of a eukaryotic cell population. Sohn *et al.* observed 0.1-2 fF of noise within their capacitive sense signal.

This work presents a microflow cytometer which uses a coplanar microelectrode array (MEA) to simultaneously actuate and detect biological particles (bioparticles) [Rom09, Jar09, Fer09a, Fer09b, Rom08, Fer08a, Fer08b, Fer07]. This microflow cytometer affords two independent methods for simultaneously detecting the response of actuated bioparticles: (1) an optical assay, in which the change in the lateral velocity v_{cellx} of passing bioparticles is estimated from digital video of the MEA detection zone; and (2) a capacitive cytometer, in which a capacitance sensor coupled to the MEA produces a sense signal S proportional to the transient MEA capacitance perturbations ΔC_{MEA} induced by passing bioparticles. The coupled capacitance sensor consists of a 1.478 GHz microwave interferometer. In this work, the optical cell assay and the capacitive cytometer shall be used simultaneously for independent experimental confirmation.

Capacitive sensing with GHz frequencies affords several advantages over the Ö 100 MHz impedance sensing described above. Below 200 MHz, a celløs electrical properties can vary greatly due to ionic currents [Gasc04], electrode polarization [Schwan92], interfacial polarization [Gasc04], the electrical double layer [Peth79], and large potential gradients across cellular membranes and walls [Fost89]. These LF effects can be greatly reduced, or even eliminated, by operating above 1 GHz [Gasc04]. The

reduction of LF effects is shown in the derivation of ΔC_{MEA} as presented in Section 4.1, and is experimental verified by the data presented in Chapters 6, 8, and 9.

1.4   Electrokinetic Actuation

In addition to detecting cells, single-cell diagnostics typically also require a means to excite cells. For example, conventional FACS-based flow cytometers optically excite cells [Sha95, Huh05, Yu07]. Optical methods have also been used to mechanically actuate cells. For example, optical tweezers and fibres have been successfully used to stretch single-cells and even identify their mechanical force constants [Liu07]. These mechanical force constants have proven to be useful parameters within cell diagnostics. For example, Lincoln *et al.* have shown that cancerous breast cells stretch up to five times more than healthy breast cells [Linc04]. However, the same miniaturization and on-chip integration difficulties associated with FACS are also associated with optical actuators.

As an alternative to optical excitation, cells can be actuated using electrokinetic techniques, in which cells are manipulated by electric fields established between electrodes. As electrokinetic actuators usually consist entirely of electrodes, they are far simpler to miniaturize and integrate on-chip than optical actuators. Electrorotation (ROT) and dielectrophoresis (DEP) are the most commonly utilized electrokinetic methods, and have been used to successfully determine if cells are viable, infected, or cancerous [Beck94, Bra08, Gasp98].

During ROT, a rotating electric field induces a frequency-and-material-dependent electric dipole within a dielectric particle, creating a torque as the dipole tries to align itself with or against the field [Arno82, Misc82, Goa98, Hug03]. Goater and Pethig utilized ROT for the real-time assessment of the viability of *Cryptosporidium parvum* oocysts, with a cell rotation processing time on the order of seconds demonstrated [Goa97]. Beyond determining cell viability (defined here in terms of the cytoplasmic membrane's intactness), the ROT spectrum of a cell can be used to estimate the various cellular substructure conductivities and permittivities [Chan97]. In fact, the internal conductivities and permittivities of viable and nonviable baker's yeast (*Saccharomyces cerevisiae*) cells are usually estimated by using ROT in conjunction with cross-sectional

micrographs [Asa76, Asa96, Höl90, Höl97, Hua92]. The rotation of ROT actuated cells are usually detected optically, reintroducing the aforementioned miniaturization and on-chip integration difficulties associated with optical components.

During DEP, an external, non-uniform electric field induces and exerts itself upon an electric dipole within a dielectric particle, producing a net translational force along the gradient of the squared electric field [Pohl78]. As a measure of a biological cell's frequency-and-material-dependent polarization, DEP is sensitive to inherent traits such as surface area and charge, membrane conductivity and structure, nucleic acid content, cell size, and the presence and conductivity of internal membrane-bound vesicles and charged cytoplasmic macromolecules [Peth97]. DEP has been used to successfully distinguish similar cell subpopulations, including human leukocytes [Beck94, Yang99] and T lymphocytes [Peth02], breast cancer cells [Cri02], neurons [Pra04, Hei02], and hematopoietic stem cells from bone marrow and peripheral blood [Tal95, Step96]. Perch-Nielsen *et al.* used DEP as a selective filter, holding cells within a microsystem whilst hemoglobin and heparin were flushed out of the system [Per03]. Flanagan *et al.* measured the DEP response of mouse neural stem/precursor cells and their differentiated glia and neuron derivatives, finding that these cells have distinct dielectric properties [Fla08]. Moreover, Flanagan *et al.* determined that DEP signatures distinguish neural stem/precursor cells from different developmental ages in a fashion that predicts their respective daughter cell differentiation preferences. Their data shows that DEP is sensitive to minor changes in cell phenotype and suggests that the developmental progression of progenitor cell populations can be revealed by the cells' dielectric properties. Flanagan *et al.* further found that DEP can be used to gauge cell population heterogeneity, providing another measure for characterizing stem cell cultures.

Two distinct approaches to the separation of homogeneous subpopulations within an overall heterogeneous population using DEP have been demonstrated: DEP migration (mDEP) and DEP retention (rDEP) [Hua97]. In mDEP, different cell types experience DEP forces with opposing polarities, so that one cell type experiences a positive DEP (pDEP) force and is attracted towards electric field maxima whilst the other cell type experiences a negative DEP (nDEP) force and is repelled from electric field maxima. By exploiting opposing DEP forces, mDEP achieves spatial resolution by focusing different

cell types at different microelectrode regions [Gasc92, Wang93b, Mar94a]. In rDEP, the DEP force competes with fluid flow forces, so that cells experiencing a strong pDEP force are trapped at an electrode edge against the fluid flow drag, whilst other cells are eluted by the fluid flow [Wang93b, Mar94b].

Braschler *et al.* developed an mDEP based device in which electrode chambers in the left side wall of a microfluidic channel induce a DEP force at one frequency, whilst electrode chambers located in the channel's right side wall simultaneously induce an opposing DEP force at a second frequency [Bra08]. The effectiveness of this device is demonstrated by: (1) separating viable and nonviable *Saccharomyces cerevisiae* cells out of a mixed population; and (2) separating healthy and infected red blood cells out of a mixed population [Bra08]. To confirm population separation: (1) a methylene blue stain was used which labels only nonviable *S. cerevisiae* cells; and (2) ethidium bromide, a nucleic acid intercalator, was used to label only infected red blood cells [Bra08].

Huang *et al.* developed an rDEP based device in which DEP forces levitate cells suspended in a microfluidic chamber with a parabolic laminar fluid velocity profile [Hua97]. A given cell within the flow stream obtains an equilibrium height, and a corresponding velocity, based upon the balance of DEP, gravitational, and hydrodynamic lift forces [Hua97]. The effectiveness of the device is demonstrated by separating human leukemia HL-60 cells from peripheral blood mononuclear cells [Hua97]. To confirm population separation, the HL-60 cells were labelled by a Trypan blue dye prior to being mixed with the peripheral blood cells [Hua97].

In this work, suspended bioparticles flow through a microfluidic channel past a coplanar MEA. A 10-1000 kHz electrical potential ϕ_{DEP} applied to the MEA generates an nDEP or pDEP force $\boldsymbol{F_{DEP}}$ which actuates passing bioparticles. This DEP actuation is essentially rDEP, as $\boldsymbol{F_{DEP}}$ competes with the viscous fluid drag force $\boldsymbol{F_{drag}}$ to yield trajectories of time-varying elevation h_{cell} and velocity v_{cell}.

1.5   Thesis Overview

This work presents a microflow cytometer which uses a MEA to simultaneously actuate and detect bioparticles [Rom09, Jar09, Fer09a, Fer09b, Rom08, Fer08a, Fer08b, Fer07]. A pressure differential controls the flow of bioparticles through the microfluidic

channel. A 10-1000 kHz electrical potential ϕ_{DEP} applied to the MEA generates a DEP force $\boldsymbol{F_{DEP}}$ which actuates passing bioparticles. $\boldsymbol{F_{DEP}}$ competes with the viscous fluid drag force $\boldsymbol{F_{drag}}$ to yield trajectories of time-varying elevation h_{cell} and velocity v_{cell}.

The microflow cytometer affords two independent methods for simultaneously detecting the response of actuated bioparticles: (1) an optical assay, in which the change in the lateral velocity v_{cellx} of passing bioparticles is estimated from digital video of the MEA detection zone; and (2) a capacitive cytometer, in which a capacitance sensor coupled to the MEA produces a sense signal S proportional to the transient MEA capacitance perturbations ΔC_{MEA} induced by passing bioparticles. The coupled capacitance sensor consists of a 1.478 GHz microwave interferometer, with narrowband lock-in techniques employed to ensure that ϕ_{DEP} doesn¢t influence S. Conversely, the superimposed 1.478 GHz interrogation potential ϕ_{RF} is sufficiently low to ensure that its contribution to $\boldsymbol{F_{DEP}}$ is negligible. In this work, the optical cell assay and the capacitive cytometer shall be used simultaneously for independent experimental confirmation.

It shall be shown that the ΔC_{MEA} signature induced by a passing bioparticle is proportional to the squared external electric field magnitude to squared ϕ_{RF} magnitude, E_{ext}^2 / ϕ_{RF}^2, along its trajectory. Finite element simulations of E_{ext}^2 / ϕ_{RF}^2 along constant h_{cell} trajectories show that the shape of E_{ext}^2 / ϕ_{RF}^2 is dependent upon h_{cell}. As such, the h_{cell} associated with an experimental S signature can be estimated to within ± 1 μm via comparison with these simulated E_{ext}^2 / ϕ_{RF}^2 plots.

As the capacitance sensor is intended to measure the ΔC_{MEA} induced by passing bioparticles, it is prudent to experimentally verify the relationship between the sensed ΔC_{MEA} and the corresponding sense signal output voltage S. This experimental verification is referred to as calibrating the sensor. The sensor shall be calibrated using unactuated polystyrene microspheres (PSS), of a tightly controlled diameter, real permittivity, and conductivity suspended in deionized water (DI H_2O). The h_{cell} associated with an experimentally observed S signature shall be estimated to within ± 1 μm via comparison with the simulated E_{ext}^2 / ϕ_{RF}^2 plots. As the size and electrical parameters of the PSS are relatively invariant, the ΔC_{MEA} signature of the PSS is accurately computed using the theoretical relationship between ΔC_{MEA} and E_{ext}^2 / ϕ_{RF}^2.

ΔC_{MEA} is then compared to the experimental S signature, thereby estimating the dS/dC_{MEA} proportionality factor (referred to as the sensor's overall sensitivity) which shall be used to convert a given experimental S signature into the corresponding ΔC_{MEA} signature. The capacitive cytometer's resolution $|\delta C_{MEA}|$ is then estimated by converting the background root-mean-squared (RMS) noise within S into the background RMS noise within the sensed ΔC_{MEA}.

Actuated PSS suspended in a diluted methylene blue solution shall then be studied. The initial PSS elevation, h_{cell0}, shall be estimated by comparing S to the simulated E_{ext}^2 / ϕ_{RF}^2 plots. The initial and final lateral PSS velocities, v_{cellx0} and v_{cellxf}, shall be estimated from the optical assay video. A finite element simulation of the PSS trajectory, as subjected to $\boldsymbol{F_{DEP}}$ and $\boldsymbol{F_{drag}}$, shall be compared to the experimentally observed PSS trajectories to verify the experimentally observed DEP spectrum.

The fungus *Saccharomyces cerevisiae* (abbr. *S. cerevisiae*), known as baker's, brewer's, or budding yeast, serves as the representative eukaryotic model within microbiological studies [Phil09, Karp05]. As such, it is prudent to use viable and heat shocked *S. cerevisiae* cells suspended in the diluted methylene blue solution to test the microflow cytometer's ability to simultaneously detect and actuate biological cells. Methylene blue preferentially stains cells whose cytoplasmic membranes have been compromised, affording verification of cellular viability via the optical assay video. The trajectories of actuated *S. cerevisiae* cells are studied in the same manner as the study of the trajectories of actuated PSS as outlined above.

Although the capacitive sensor is implemented using bench scale electronics, it could be miniaturized as a monolithic microwave integrated circuit (MMIC) and integrated on-chip with the microflow cytometer. As such, this work essentially serves as the developmental prototype of a capacitive cytometer with DEP actuation which could be miniaturized and integrated on-chip as a laboratory-on-a-chip (LoC) or micro-total-analysis-system (μTAS). The optical assay aspect of this microflow cytometer is merely to provide an independent confirmation of the viability and experimental DEP response of the actuated bioparticles. If the Clausius-Mossotti factor's real part, Re{$\underline{K}$}, (being the frequency dependent factor within $\boldsymbol{F_{DEP}}$) could be estimated from S alone, then the optical assay would not be required. The elimination of the optical assay components

would facilitate the eventual miniaturization and on-chip integration of this microflow cytometer, as optical components are difficult to miniaturize and integrate on-chip.

1.6   Thesis Organization

This thesis is organized as follows:

- Chapter 2 presents the fabricated microflow cytometer and the apparatus for simultaneous operation as both an optical assay and a capacitive cytometer.
- Chapter 3 derives the time-averaged $\boldsymbol{F_{DEP}}$ experienced by a lossy homogeneous dielectric sphere suspended in a lossy homogeneous dielectric medium and subjected to a non-uniform time-harmonic external electric field.
- Chapter 4 derives an expression for ΔC_{MEA} as induced by a lossy dielectric sphere suspended in a lossy homogeneous dielectric medium and presents the finite element simulations which: (1) predict the trajectory of actuated bioparticles, and (2) predict the ΔC_{MEA} signatures induced by the bioparticles.
- Chapter 5 presents the theoretical DEP spectra of PSS as used in this work.
- Chapter 6 presents the experimental v_{cellx} and ΔC_{MEA} based analysis of a homogeneous PSS population. A calibration of the capacitive cytometer is included.
- Chapter 7 models viable and heat shocked *S. cerevisiae* cells as equivalent lossy homogeneous dielectric spheres, affording the application of the $\boldsymbol{F_{DEP}}$ and ΔC_{MEA} expressions derived in Chapters 3-4. The theoretical DEP spectra of viable and heat shocked *S. cerevisiae* as used in this work is also presented.
- Chapter 8 presents the experimental v_{cellx} and ΔC_{MEA} based analysis of a homogeneous heat shocked *S. cerevisiae* cell population.
- Chapter 9 presents the experimental v_{cellx} and ΔC_{MEA} based analysis of a homogeneous viable *S. cerevisiae* cell subpopulation.
- Chapter 10 concludes this thesis, and discusses future work to be implemented.

Chapter 2

Instrumentation & Experimental Apparatus

2.1   Microflow Cytometer Die Fabricated by Micronit

The masks used to fabricate our microflow cytometer were designed using Cadence's Custom IC Design Tools Virtuoso® Front to Back Design Environment (IC 5.1.41).   Microfluidic device mask designs from several Canadian universities were collected by the Canadian Microelectronics Corporation (CMC), and then submitted to Micronit for batch fabrication using their Sensonit Glass-Based Microfluidic Technology with Metallization process [Mic08].   A micrograph of our microflow cytometer die as fabricated by Micronit is presented as Figure 2-1.
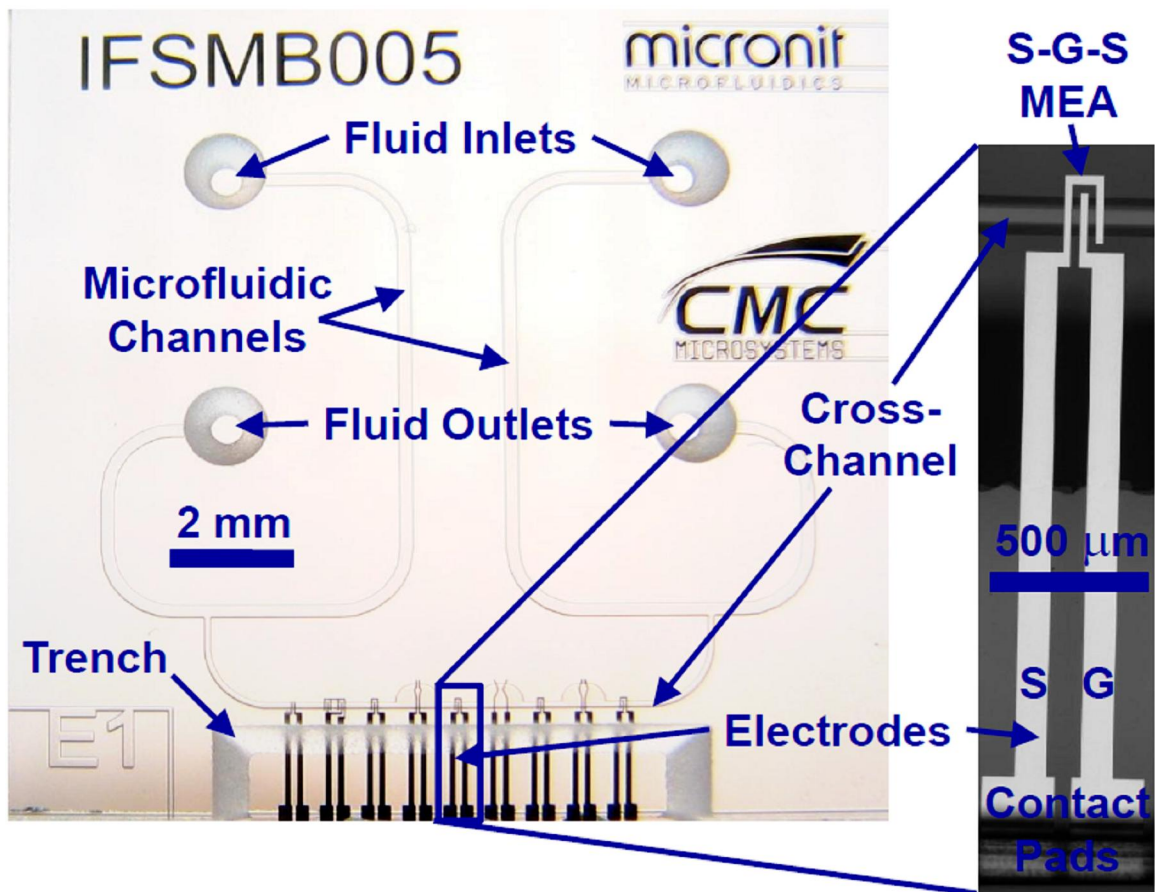
Figure 2-1:   *A micrograph of our microflow cytometer die as fabricated by Micronit.*

The Sensonit fabrication process begins by first etching the 40 μm deep microfluidic channels into the bottom side of a 1.1 mm thick Borofloat glass wafer, using the channel mask for boundary definition. A wet isotropic etch was used to create the channels, resulting in a 40 μm wide undercut of the drawn dimensions. Two 240 μm wide channels were etched, connecting each fluid inlet to a fluid outlet. A 100 μm wide cross-channel was etched between the two 240 μm wide channels, passing over the microelectrode array (MEA) detection zone. This H-channel design was chosen so that the fluid flow within the 100 μm wide cross-channel can be controlled as the fluid flow differential between the two 240 μm wide channels. Cubbies branching off of the microfluidic cross-channel are visible within Figure 2-1. Dielectrophoretic (DEP) forces are to restrain cells in these cubbies whilst various agents are injected into the fluid. These cubbies have not been utilized within this thesis.

The 1.1 mm thick Borofloat glass wafer's top was then powder-blasted to create the fluid ports and the electrode coupling trench, using the powder-blast mask for boundary definition. The trench is 7.992 mm x 1.7 mm at the top and 7.19 mm x 1.3 mm at the bottom. The fluid ports have 1400 μm top and 600 μm bottom diameters.

200 nm deep trenches defining the MEA geometry were then etched into the top side of a 0.7 mm thick Borofloat glass wafer, using the electrode mask for boundary definition. A 20 nm thick tantalum (Ta) adhesion layer and a 180 nm thick platinum (Pt) layer were deposited into these trenches. A micrograph of the principal MEA used for the DEP actuation and capacitive detection of passing cells is inset within Figure 2-1. As it spans the 100 μm wide microfluidic cross-channel, the MEA is an interdigitated Signal-Ground-Signal (S-G-S) pattern formed by 25 μm wide microelectrodes with a 25 μm edge-to-edge spacing. These microelectrodes connect to a pair of 100 μm wide electrodes with a 100 μm edge-to-edge separation which extend out to the die's periphery. These electrodes were made 100 μm wide to reduce the high frequency electrical losses between the die's periphery and the S-G-S pattern. At the die's periphery, each of these wider electrodes form a 228 μm by 300 μm contact pad, with a reduced 50 μm edge-to-edge separation, within the powder blasted trench area to facilitate coupling external

electronics with the MEA. The other electrode geometries visible in Figure 2-1 were not utilized within this thesis.

The two Borofloat glass wafers were then fused together using a direct heat bond. Microfluidic device fabrication was then completed by cutting the fused glass wafers to yield each individual 1.5 cm x 1.5 cm x 1.8 mm die.

2.2   Bonded Microflow Cytometer Assembly

The fabricated microflow cytometer die was bonded on top of a 2.6 cm x 3.1 cm x 1.2 cm Plexiglass block (using Great Planes GPMR6047 30 min Pro Epoxy). Four 1.1 mm diameter holes, aligned with the fluid access ports, were bored into a 1.5 cm x 1.0 cm x 1.1 cm Plexiglass block that was bonded on top of the microflow cytometer die. The microfluidic cross-channel and electrode coupling trench were not obscured by Plexiglass, facilitating the optical monitoring of the microfluidic cross-channel and the coupling of the electrodes to external electronics. Polyethylene tubing with a 300 μm inner and a 1.09 mm outer diameter was then inserted and bonded into the bored holes. Syringe needles (BD 27½ gauge PrecisionGlide) were then partially inserted and bonded into the tubes connected to the uppermost fluid access ports of Figure 2-1. The uppermost ports were chosen as the inlets to allow the injected cells more time to settle before reaching the cross-channel. Prior to inserting and bonding the needles, the closed ends of the needle caps were cut off, and the open-ended caps were placed over the tubing. After inserting and bonding the needles, the needle caps were bonded onto the needle nozzles, to mechanically protect the tubing and the needles. Fluid injection can now be achieved by connecting disposable syringes (BD 3 mL Slip Tip) to the bonded needle nozzles. The complete bonded assembly is presented as Figure 2-2.
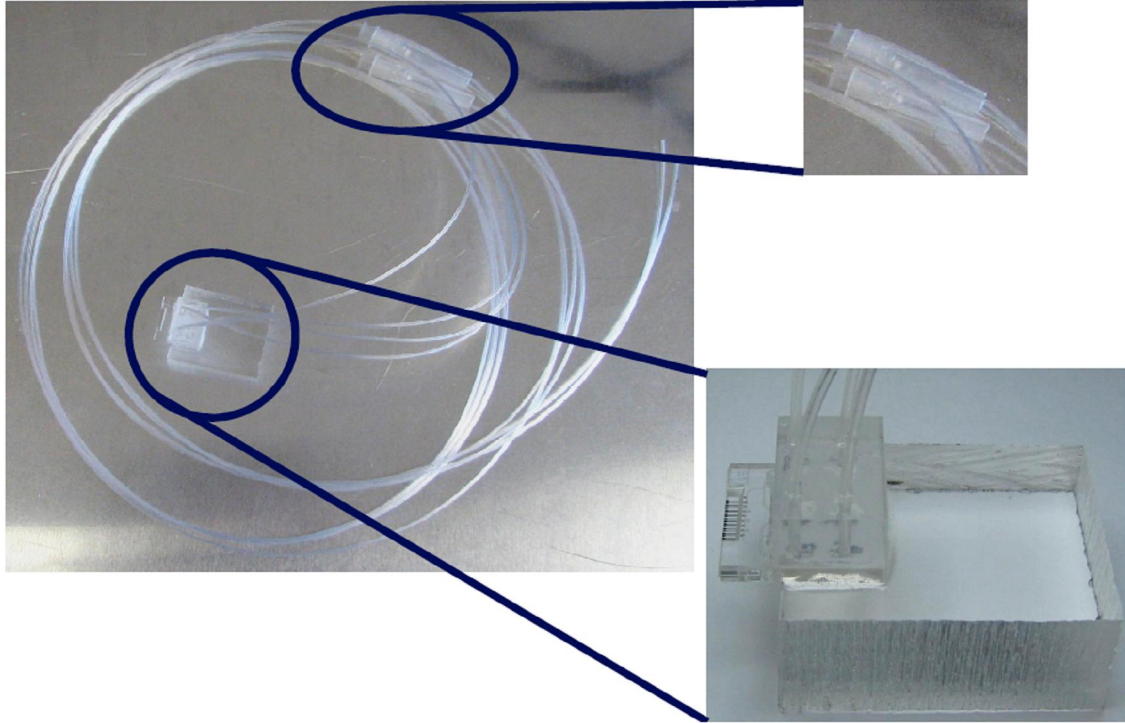
Figure 2-2: *The complete microflow cytometer assembly to facilitate fluid injection, optical cross-channel monitoring, and electrode coupling.*

2.3 Pressure Differential Cross-Channel Flow Rate Control

Recall that the H-channel design of Figure 2-1 was chosen so that the fluid flow within the 100 μm wide cross-channel can be controlled as the fluid flow differential between the two 240 μm wide channels. During operation, the syringes are held in place by metal clamps and the plungers are removed, as shown in Figure 2-3. The microflow cytometer assembly utilizes a gravity driven flow, with the relative elevation of the syringes establishing a fluid pressure differential which in turn establishes a fluid flow differential between the 240 μm wide channels. As such, the fluid flow within the 100 μm wide cross-channel is controlled via the relative elevation of the syringes.
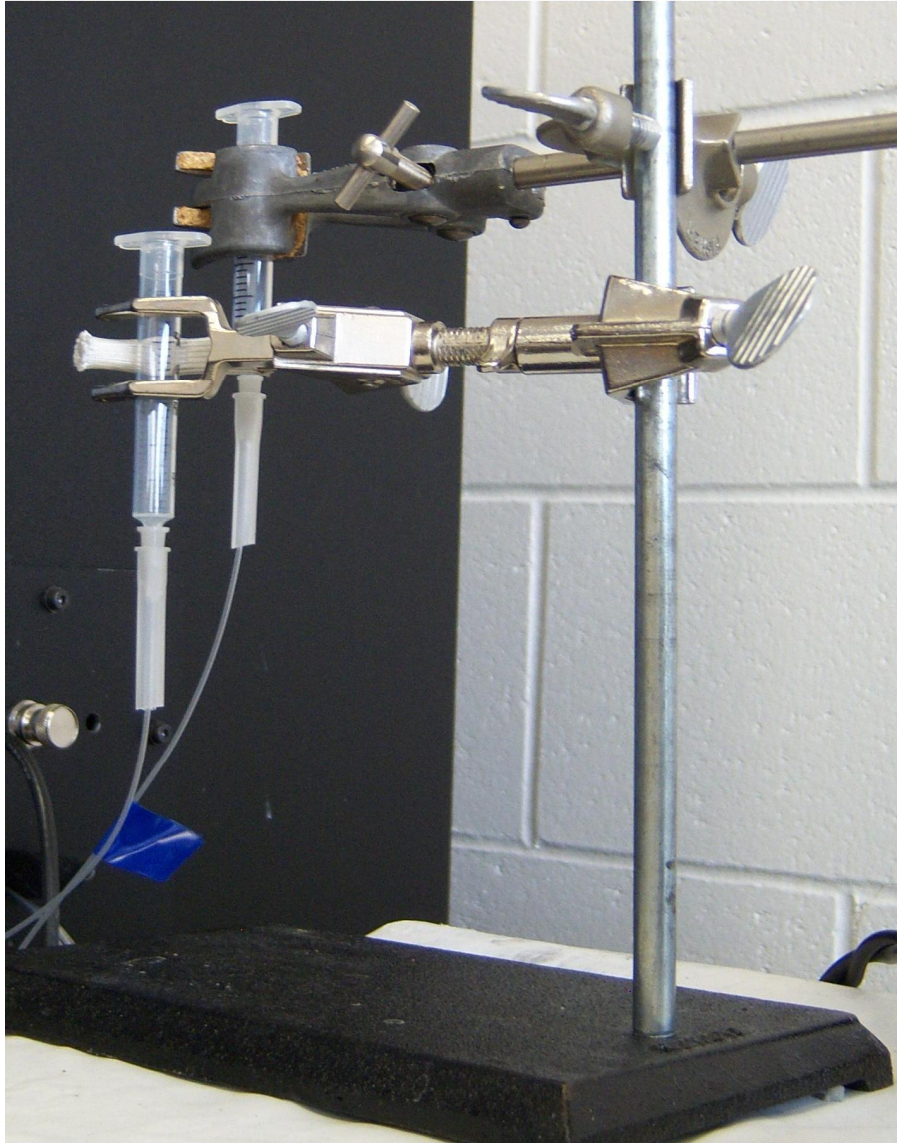
Figure 2-3: *The microflow cytometer assembly utilizes a gravity driven flow,*
in which the fluid flow within the 100 μm wide cross-channel
is controlled via the relative elevation of 3 mL syringes.

2.4   Optical Monitoring of the Microelectrode Array Detection Zone

The bonded assembly is clamped down inside a shielded probe station (SUSS SE1000), as shown in Figure 2-4. The principal MEA detection zone is monitored by a microscope (Motic PSM-1000). The detection zone is illuminated by: (1) white-light emitting diodes (LEDs; Lumex Opto Components SLX-LX5093UWC/G) directly above and below the MEA detection zone; and (2) the microscope's interior light.
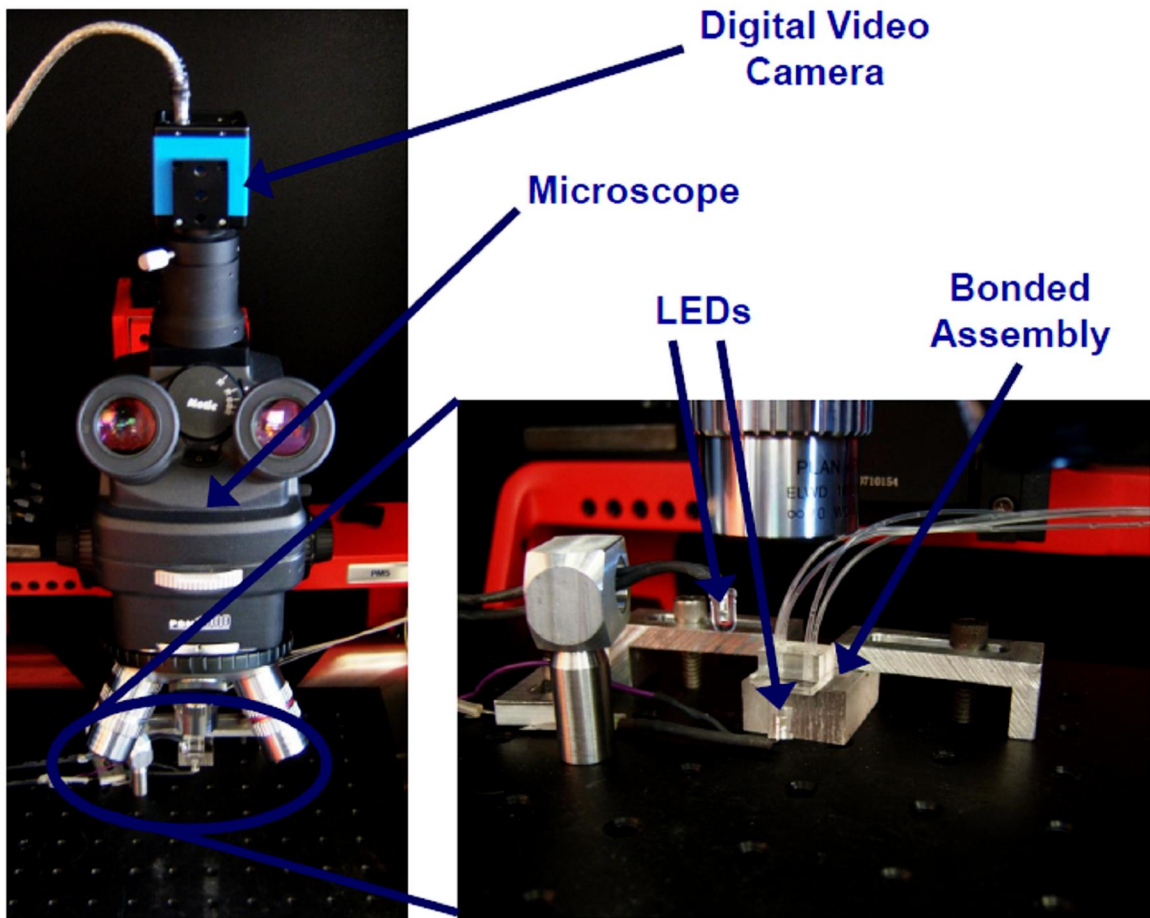
Figure 2-4: *The bonded assembly is clamped down within a shielded probe station and monitored by a microscope fitted with a digital video camera.*

A digital video camera (Imaging Source DFK 31AF03) fitted to the microscope captures 1024 pixel x 768 pixel UYVY formatted colour video at 15 frames per second. A FireWire cable connects the camera to the host personal computer (PC). Imaging Source's IC Easy Image Acquisition Capture 2.0 software displays and backlogs the captured video in real-time. Figure 2-5 presents a screen-shot of the IC Capture 2.0 interface monitoring the MEA detection zone. The backlogged video is encoded with the Digital Video (DV) Video Encoder codec and is saved as Audio Video Interleave (AVI) files.
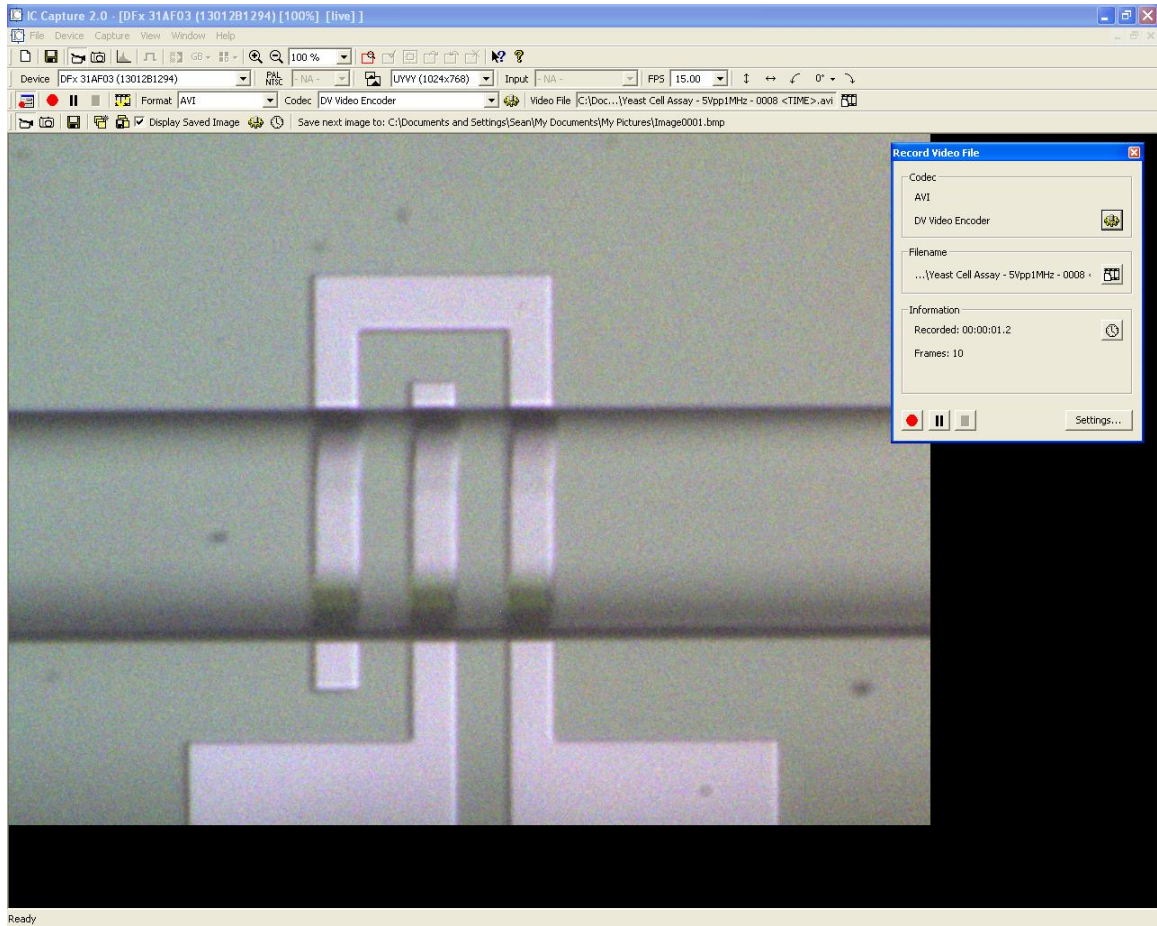
Figure 2-5: *The IC Capture 2.0 software as run on the host PC*
to display and backlog the captured UYVY video in real-time.

2.5   Coupled-Microstrip Resonator for Capacitive Sensing

To achieve capacitive cytometry, this work requires a capacitance sensor coupled to the MEA which produces a sense signal *S* proportional to the transient MEA capacitance perturbations ΔC_{MEA} induced by passing cells. The employed capacitance sensor is based upon a coupled transmission-line (T-line) sensor developed by Tran *et al.* for Scanning Capacitance Microscopy (SCM) applications [Tran01a, Tran01b].

The SCM resonator is itself based upon a coupled-stripline Radio Corporation of America (RCA) VideoDisc sensor, used to read audio and video data stored as depressions at the bottom of a fine spiral groove engraved into a plastic disc [Cle78]. A schematic of the RCA sensor is presented as Figure 2-6 (reproduced with permission graciously provided by Thang Duc Tran [Tran01b]). The groove guides a thin stylus

- 18 -

electrode loading the sensor's resonant center T-line with a capacitive load C, consisting of the disc-to-stylus capacitance C_{DS} and a stray capacitance C_S. This resonant T-line posses a bandpass transmission magnitude spectrum $|S_{2,1}|$ with a 900 MHz center frequency f_r and an unloaded quality factor (Q-factor) of 45. An edge-coupled shorted T-line driven at a fixed 915 MHz excites the resonant T-line at the maximum slope point within $|S_{2,1}|$. Changes in C_{DS}, ΔC_{DS}, on the order of 100 aF, shift f_r, modulating the amplitude of the resonator's output. ΔC_{DS} can thus be inferred from the output envelope, as measured by a peak detector and amplifier of gain A at the input of a second edge-coupled shorted T-line. To electronically tune the loaded resonance via bias voltage ϕ_{bias}, a grounded varactor diode was used as a variable capacitance loading the other end of the resonant T-line. The RCA sensor was determined to have a 1.15 MHz/fF frequency sensitivity and a 154 mV/MHz voltage sensitivity, yielding an 177 mV/fF overall sensitivity [Tran01b].
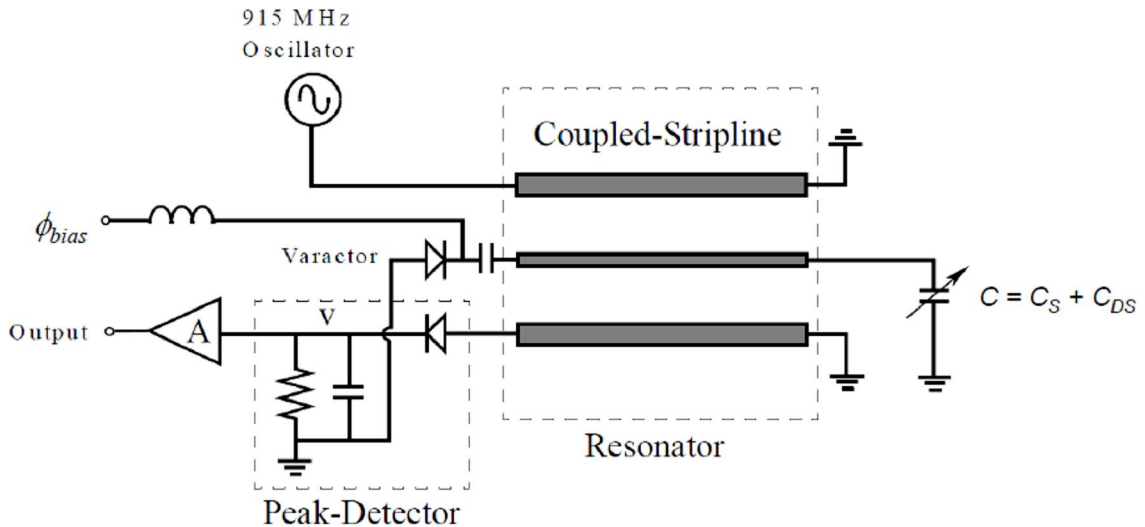
Figure 2-6: *Schematical diagram for the RCA capacitance sensor [Tran01b].*

The coupled-microstrip SCM sensor is functionally similar to the RCA VideoDisc sensor, with the stylus replaced by a scanning probe tip (and C_{DS} replaced by the scanning probe tip capacitance variance dC) [Tran01b]. A schematic of the SCM sensor is presented as Figure 2-7 (reproduced with permission graciously provided by Thang Duc Tran [Tran01b]). As a tuneable oscillator drives the SCM sensor, the varactor diode was replaced by an electrical short. The SCM sensor's resonant center T-line posses a

bandpass transmission magnitude spectrum $|S_{2,1}|$ with a 1.994 GHz center frequency and an unloaded Q-factor of 95. During operation, the resonant T-line was excited at 1.850-1.876 GHz, affording a superior 1.5 MHz/fF frequency sensitivity. Furthermore, a Schottky diode based peak detector afforded a superior 520 mV/MHz maximum voltage sensitivity. Together, these sensitivities imply a maximum 780 mV/fF overall sensitivity. The minimum detector output noise was measured within a 1 Hz bandwidth as 2.10 $\mu V/\sqrt{Hz}$, implying a 2.70 zF $/\sqrt{Hz}$ resolution. This resolution is suitable for SCM systems, which demand a resolution less than 32 zF $/\sqrt{Hz}$ [Tran01b].
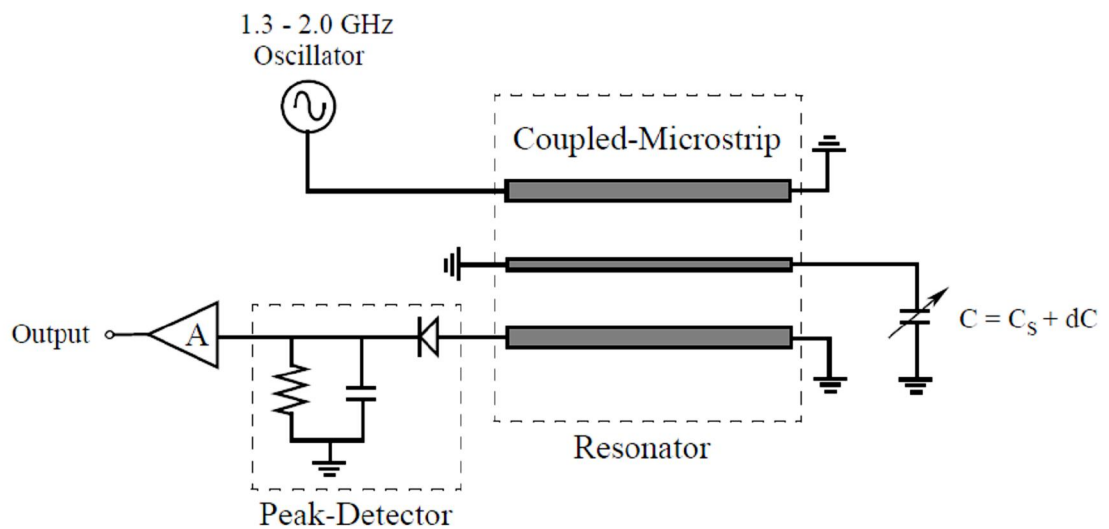
Figure 2-7: *Schematical diagram for the SCM capacitance sensor [Tran01b].*

Figure 2-8 presents the coupled-microstrip resonator used in this work, fabricated by milling copper (Cu) lines onto a Cu-clad, low-loss Rogers 5880 dielectric substrate. The 90 Ω center T-line is a quarter-wavelength resonator, edge-coupled on each side to a 50 Ω short-circuit terminated T-line. Each 50 Ω T-line input is fitted with a sub-miniature A (SMA) port, serving as the resonator's input and output ports 1-2. Due to symmetry, either port 1 or 2 can be used as the input or output port. 150 μm diameter brass wires are soldered onto the center T-line's open-circuit edge port. The brass wires are cut to a point using sharp wire cutters, ground with 600 grit fine grain silicon carbide (SiC) sandpaper, and subsequently rinsed with isopropanol (C_3H_7OH) and deionized water (DI H_2O). These brass wires contact the electrode pads within the electrode access trench, loading the resonant T-line with the MEA. The resonator's other port is

terminated with an 85 pF shunt capacitor. Port 3, used for applying the 10-1000 kHz DEP actuation potential ϕ_{DEP}, is coupled to the resonator's end using another SMA connector and a 750 Ω series resistor. The resulting resistor-and-capacitor (RC) circuit is a lowpass filter (LPF) with a 2.5 MHz cut-off frequency, shorting higher frequencies to ground through the shunt capacitor, thereby isolating the 1.478 GHz interferometer from the electronics generating ϕ_{DEP}.
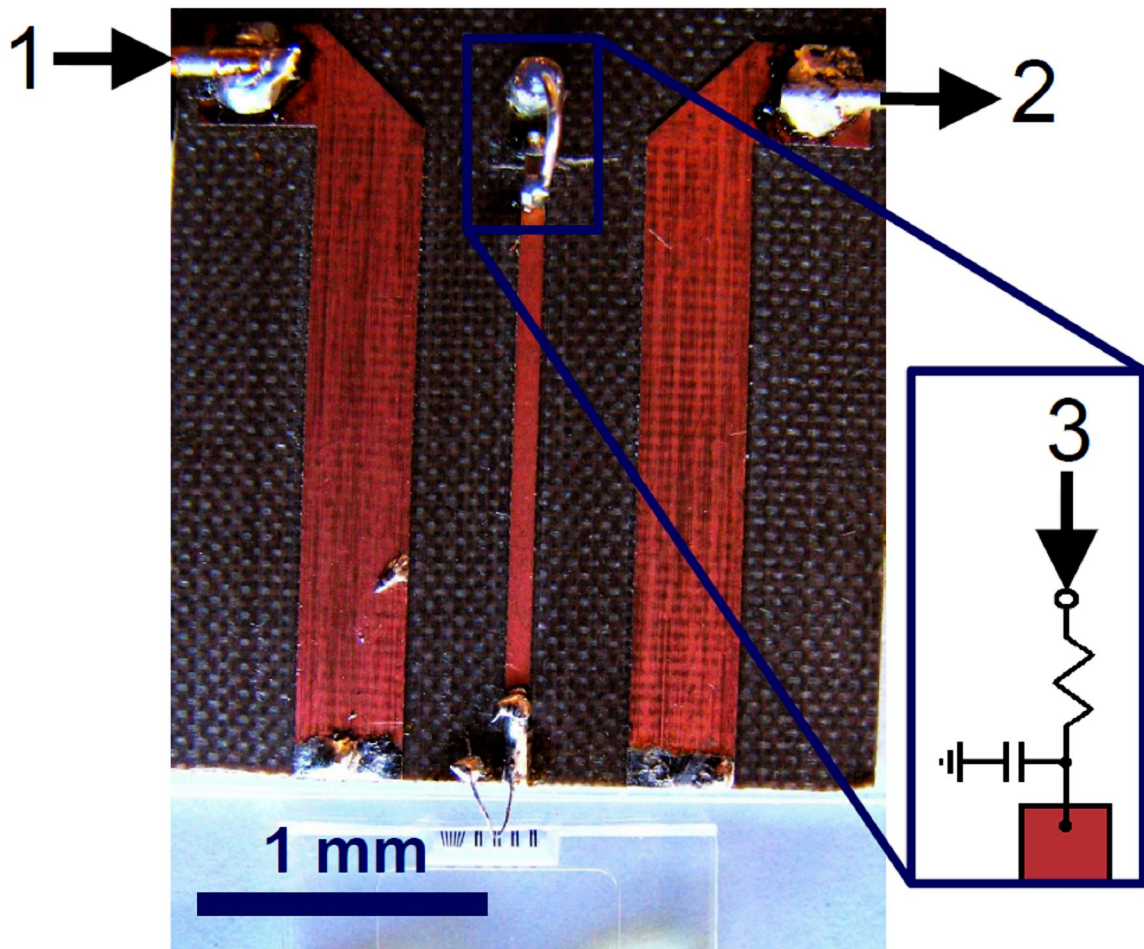
Figure 2-8: *The coupled-microstrip resonator loaded by the MEA.*

To facilitate loading the resonator with the MEA, the microstrip structure is mounted onto an XYZ positioner, as shown in Figure 2-9. The positioner is adjusted so that the brass wires firmly contact the MEA pads within the microflow cytometer's powder blasted trench, loading the resonator with the MEA.
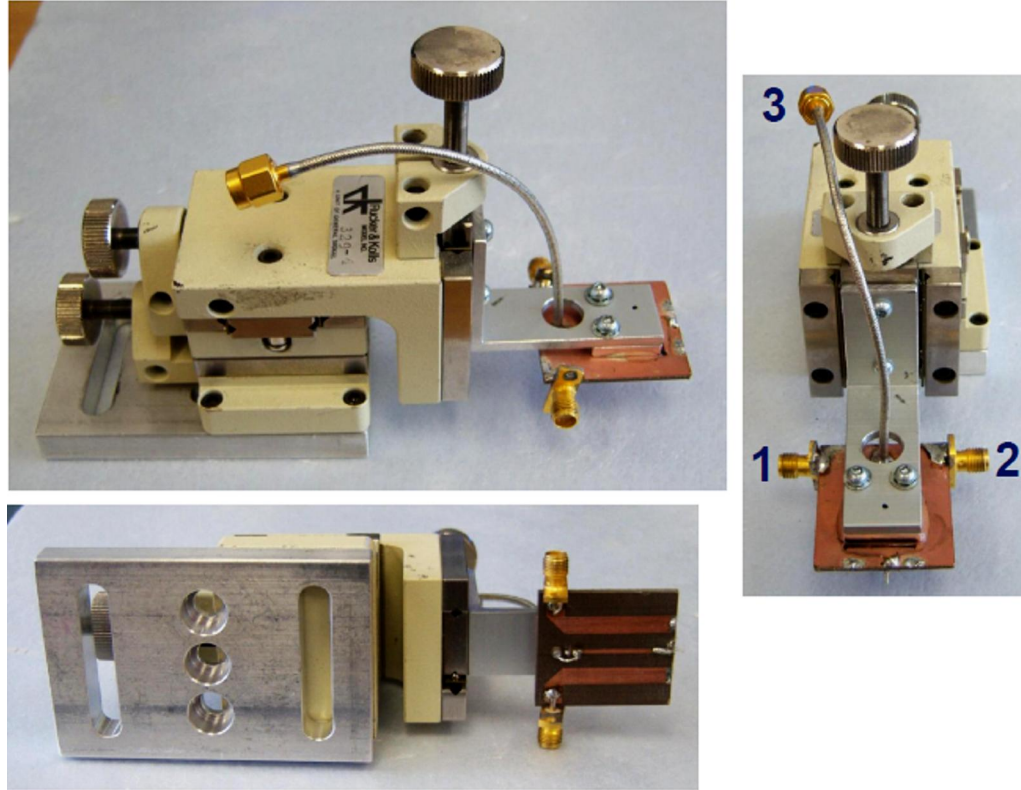
Figure 2-9: *The coupled-microstrip resonator mounted into an XYZ positioner.*

Figure 2-10 presents the coupled-microstrip resonator's port 1-2 transmission response $S_{2,1}$ (experimentally measured with a Hewlett Packard (HP) 8753E vector network analyzer) when: (1) unloaded and (2) loaded with the MEA. The microfluidic cross-channel is filled with a 33.4 μS/cm diluted methylene blue solution, as will be the case in Chapters 6, 8, and 9. The $|S_{2,1}|$ response shows that: (1) the unloaded resonator resonates at 1.826 GHz with a 7.3 dB insertion loss and a Q-factor of 54; and (2) the loaded resonator resonates at 1.478 GHz with a 15.9 dB insertion loss and a Q-factor of 20. The $|S_{2,1}|$ response thus demonstrates that: (i) the MEA's capacitive load shifts f_r by 349 MHz; (ii) an increased electrical loss reduces the resonant magnitude by 8.7 dB; and (iii) this increased electrical loss also diminishes the resonator's energy storage capability, as quantified by the Q-factor. The $\angle S_{2,1}$ response demonstrates that the capacitive MEA load increases the resonator's effective electrical length, thereby increasing the phase shift between ports 1 and 2. Moreover, the loaded $\angle S_{2,1}$ response shows that the rate of change of θ with f_r in the vicinity of 1.478 GHz, $d\theta/df_r$, is approximately -1.18 °/MHz. $d\theta/df_r$ is referred to as the sensor's phase sensitivity.
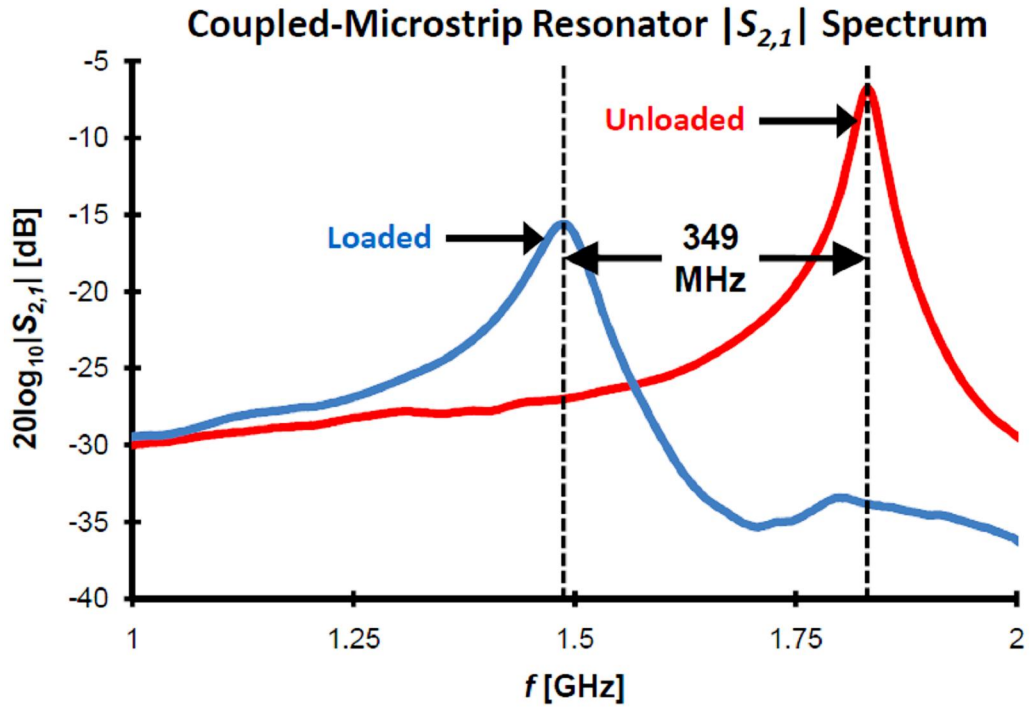
Figure 2-10a: *The resonator's $|S_{2,1}|$ response when:*
(1) unloaded and (2) loaded by the MEA.
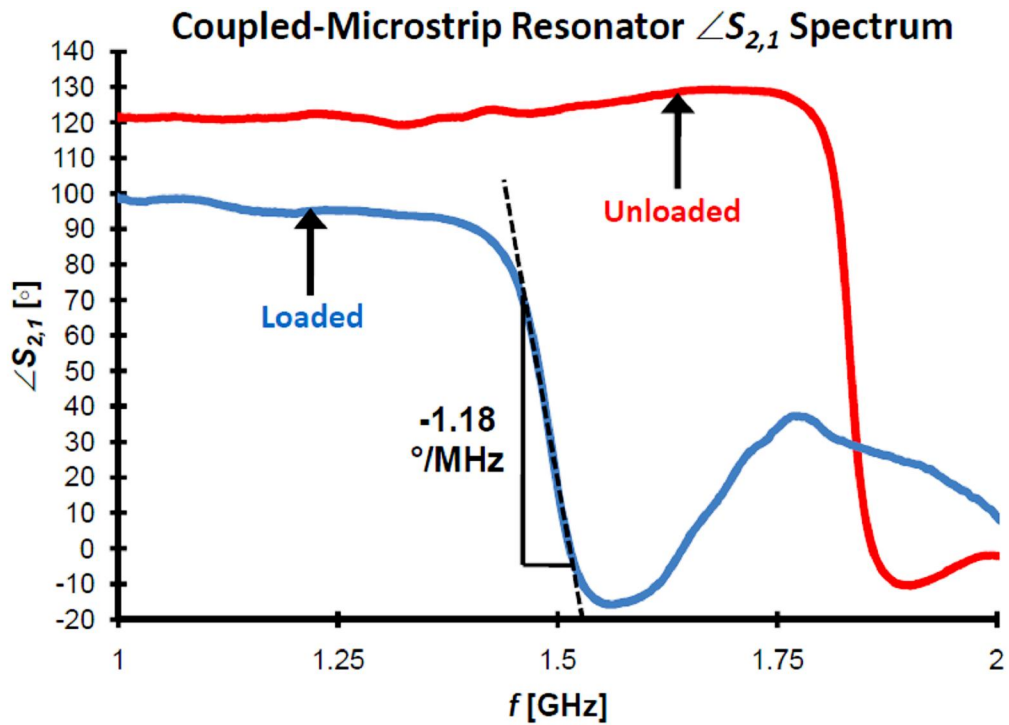
Figure 2-10b: *The resonator's $\angle S_{2,1}$ response when:*
(1) unloaded and (2) loaded by the MEA.

During capacitive cytometry, the resonator shall be driven at the 1.478 GHz loaded resonance f_r. The presence of a cell within the detection zone shall perturb the MEA capacitance C_{MEA} by ΔC_{MEA}, shifting the loaded resonance by Δf_r. The rate of change of f_r with C_{MEA} in the neighbourhood of 1.478 GHz is termed the frequency sensitivity, df_r/dC_{MEA}. This Δf_r shift in turn modifies $\angle S_{2,1}$ by $\Delta\theta$. Section 2.6 presents the microwave interferometer used to interrogate the resonator and generate a sense signal S proportional to ΔC_{MEA}.

2.6   Microwave Interferometer for Resonator Interrogation

Figure 2-11 presents a schematic of the microwave interferometer used to interrogate the coupled-microstrip resonator and generate a sense signal S proportional to ΔC_{MEA}.
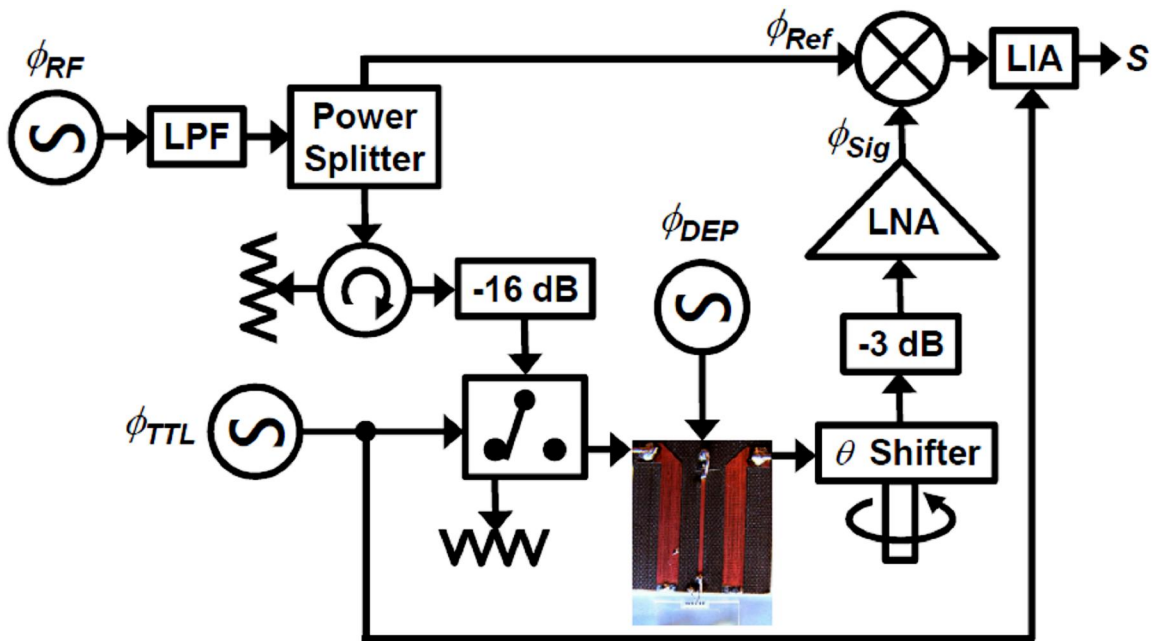
Figure 2-11:   *Schematic of the microwave interferometer interrogating the coupled-microstrip resonator loaded by the MEA.*

The radio frequency (RF) source ϕ_{RF} (Agilent E8663B) is lowpass filtered (Mini-Circuits SLP-2400) with a 2.4 GHz cut-off frequency and then split (Mini-Circuits ZAPDJ-2-S) into two paths. The signal path contains a high-isolation switch (Mini-

Circuits ZASWA-2-50DR), the coupled-microstrip resonator, an adjustable delay line (Advanced Technical Materials PNR P1213), and a low noise amplifier (LNA; Mini-Circuits ZHL-1724MLN). Attenuators (Mini-Circuits VAT-3+, VAT-6+, and VAT-10+) and a match-terminated circulator based isolator (SNT SN20113) are inserted throughout the signal path for isolation. The LNA output is denoted ϕ_{Sig}. The reference path contains no additional electronics and is denoted ϕ_{Ref}. ϕ_{Sig} and ϕ_{Ref} are multiplied using a mixer (Mini-Circuits ZEM-4300MH+). The switch's control signal ϕ_{TTL} is toggled on-and-off at 95 kHz, enabling narrow-band detection of the mixer's mean output, S, using a lock-in amplifier (LIA; Stanford SR380). During operation, the driving frequency is set near the 1.478 GHz reference state MEA loaded resonance f_r and the delay line is adjusted such that the reference phase, θ, between ϕ_{Sig} and ϕ_{Ref} is nominally 90°. When operating near f_r, a sufficiently small ΔC_{MEA} (less than 10 fF) affords utilizing the small angle approximation to express S as [Poz05]:

$$
\begin{aligned}
S \;&=\; G\,|\phi_{Ref}|\,|\phi_{Sig}|\,\cos(\,90° + \Delta\theta\,) \\[2mm]
&=\; G\,|\phi_{Ref}|\,|\phi_{Sig}|\,\sin(\,\Delta\theta\,) \\[2mm]
&\cong\; G\,|\phi_{Ref}|\,|\phi_{Sig}|\,\Delta\theta \\[2mm]
&\cong\; G\,|\phi_{Ref}|\,|\phi_{Sig}|\,(d\theta/df_r)\,(df_r/dC_{MEA})\,\Delta C_{MEA} \\[2mm]
&=\; (dS/dC_{MEA})\,\Delta C_{MEA}
\end{aligned}
\tag{2-1}
$$

where G is the combined mixer-and-LIA gain and dS/dC_{MEA} is the overall sensitivity, being the rate of change in S with C_{MEA} in the neighbourhood of 1.478 GHz. An experimental estimate of dS/dC_{MEA} is presented in Section 6.2.

As shown in Figure 2-12, the RF electronics were placed inside of the shielded probe station to reduce the coupled electromagnetic, thermal, and mechanical noise. Once the system is adjusted, S remains stable with only minor driving frequency adjustments required.
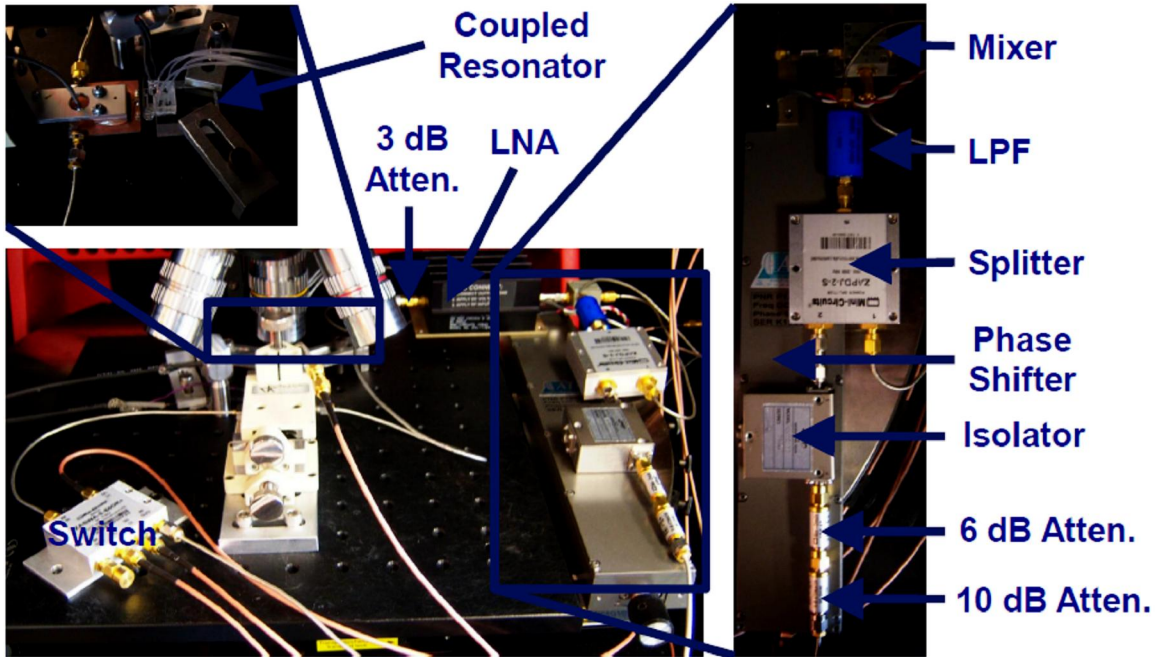
Figure 2-12: *The interferometer's RF electronics are placed inside of the shielded probe station.*

2.7 Capacitive Perturbation Data Acquisition & Parsing

The LIA's differential output, *S*, is supplied to the differential-input of a Peripheral Component Interconnect (PCI) slotted data acquisition (DAQ) board (Measurement Computing PCI-DAS6034 board with BNC-16DI connector box and a C100HD50-6 ribbon cable) internal to the host PC. The host PC runs a Graphical User Interface (GUI), entitled *GUI Controller*, which I wrote in National Instruments LabVIEW® 7.1 as a Virtual Instrument (VI). *GUI Controller* uses Measurement Computing's Universal Library of VIs to configure and control the DAQ board [Mea05]. A user's guide to *GUI Controller* is presented as Appendix A. Figure 2-13 presents a screen-shot of this GUI taken during a typical DAQ session.
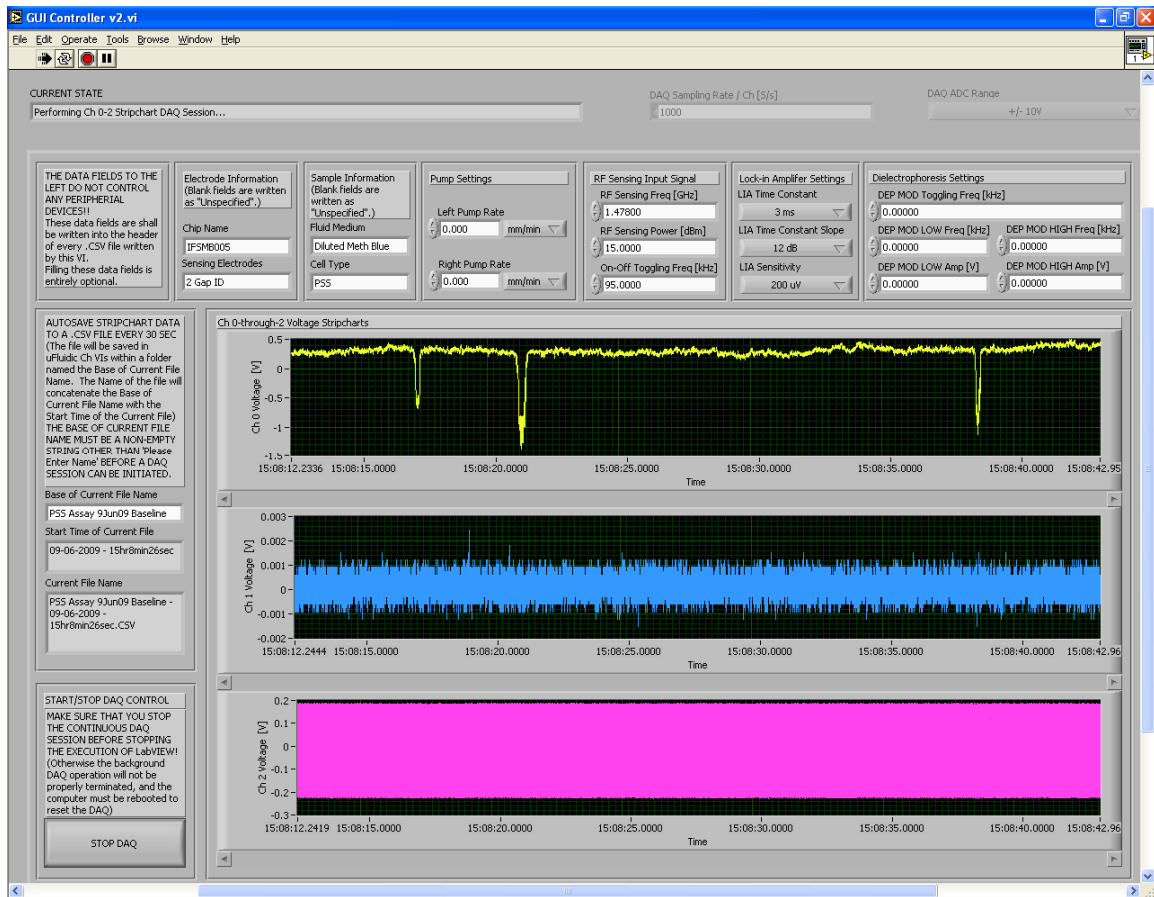
Figure 2-13: *The GUI Controller VI used to control data acquisition.*

During a given DAQ session, *GUI Controller* concurrently samples three different differential-input channels at 1 kS/s/Ch. *S* is sampled as channel 0. As *S* is bounded within ±10 V, the DAQ board is configured with a ±10 V dynamic range to take full advantage of its 16-bit uniform quantization. *S* is also frequently supplied to a digital oscilloscope (Tecktronix TDS 3012) for independent confirmation of proper measurement.

Each of the three sampled channels are displayed as real-time stripcharts. The two concurrently sampled channels afford the user the flexibility to record two additional real-time stripcharts. For example, the user may wish to toggle ϕ_{DEP} between negative and positive DEP (nDEP and pDEP) frequencies, to estimate the mechanical properties of an actuated cell. In this case, the user could use one of the concurrently sampled channels to record the actuation frequency modulation signal as a separate stripchart. In this work, both of the concurrently sampled channels are left floating.

The three concurrent stripcharts are backlogged as a sequence of 30 s long comma-separated value (CSV) files. The backlogged stripcharts are segmented into 30 s long CSV files to facilitate importing and plotting the data using Microsoft® Excel and RedRock® DeltaGraph, which limit plots to no more than 32 000 data points.

Before analyzing the backlogged CSV files, it is necessary to first parse out the individual capacitive signatures corresponding to a detected cell. I wrote a second VI, called *Event Parser & Analyzer*, to (1) indentify each individual capacitive signature within a backlogged CSV file, and (2) save each identified capacitive signature as its own CSV file. A user's guide to using *Event Parser & Analyzer* is presented as Appendix B. As suggested by its name, *Event Parser & Analyzer* also includes modules for analyzing the parsed capacitive signatures. These modules were not utilized in this thesis.

Chapter 3

The Time-Averaged Dielectrophoretic Force

3.1 The Dielectrophoretic Force Experienced by an Induced Electric Dipole Subjected to an Electric Field

When a dielectric particle is exposed to an external electric field E_{ext}, electric charge accumulates at the interface between the particle and the surrounding medium. The particle is said to have been polarized once it develops spatially distinct centers of positive and negative charge, $+Q$ and $-Q$, which are equal in magnitude and opposite in sign. These charge centers, separated by a vector distance d (directed from $-Q$ to $+Q$), are said to have formed a physical dipole moment $p = Q\,d$ [Jon95]. This physical dipole moment is illustrated in Figure 3-1.
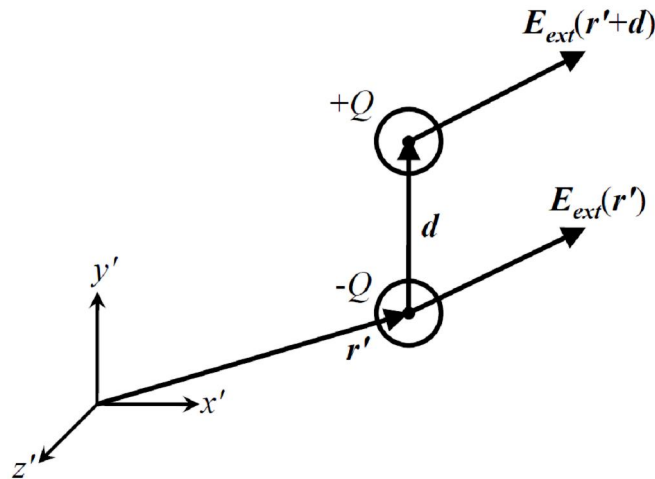
Figure 3-1: *A particle polarized by an external electric field forms a physical dipole.*

Each charge center experiences a Coulombic force, induced by E_{ext} as experienced at the respective charge center's spatial location. Together, the two Coulombic forces produce a net dipole force

$$F_{dipole} = Q\,E_{ext}(r'+d) - Q\,E_{ext}(r')$$ (3-1)

where r' is the position vector for $-Q$ [Jon95].

When d is small relative to the spatial non-uniformity of $\boldsymbol{E}_{ext}$, only the first two terms in the Taylor series expansion of $\boldsymbol{E}_{ext}(\boldsymbol{r'}+\boldsymbol{d})$ about $\boldsymbol{r'}$ need be considered [Jon95]:

$$\begin{aligned}
\boldsymbol{F}_{dipole} &= Q\,\boldsymbol{E}_{ext}(\boldsymbol{r'}+\boldsymbol{d}) \;–\; Q\,\boldsymbol{E}_{ext}(\boldsymbol{r'}) \\
&\approx Q\,[\,\boldsymbol{E}_{ext}(\boldsymbol{r'}) + \boldsymbol{d}\bullet\nabla\boldsymbol{E}_{ext}\,] \;–\; Q\,\boldsymbol{E}_{ext}(\boldsymbol{r'}) \\
&\approx Q\,\boldsymbol{d}\bullet\nabla\boldsymbol{E}_{ext} \qquad\qquad\qquad\qquad\qquad (3\text{-}2)
\end{aligned}$$

If the limit $d \to 0$ is taken such that $\boldsymbol{p} \equiv Q\,\boldsymbol{d}$ remain finite, then $\boldsymbol{F}_{dipole}$ is given as

$$\boldsymbol{F}_{dipole} \approx \boldsymbol{p}\bullet\nabla\boldsymbol{E}_{ext} \qquad\qquad\qquad\qquad (3\text{-}3)$$

Equation (3-3) is a general expression true for any dipole moment $\boldsymbol{p}$ [Jon95]. To determine the $\boldsymbol{F}_{dipole}$ acted upon a suspended particle by an external electric field $\boldsymbol{E}_{ext}$, I shall follow the effective dipole method prescribed by Jones and model the suspended particle as an equivalent effective dipole moment $\boldsymbol{p}_{eff}$ [Jon95]. When $\boldsymbol{F}_{dipole}$ is acting upon an effective dipole moment $\boldsymbol{p}_{eff}$ representing a suspended particle, Equation (3-3) is referred to as the dielectrophoretic approximation and $\boldsymbol{F}_{dipole}$ is referred to as the dielectrophoretic force denoted as $\boldsymbol{F}_{DEP}$ [Pohl78, Jon95]. The phenomenon of motion induced within suspended particles by $\boldsymbol{F}_{DEP}$ is referred to as dielectrophoresis (DEP) [Pohl78].

The interested reader may note that the effective dipole moment method of deriving $\boldsymbol{F}_{DEP}$ is used here for its conceptual and mathematical simplicity. A more rigorous derivation of $\boldsymbol{F}_{DEP}$, which involves integrating the Maxwell stress tensor over the particle's surface, can be found elsewhere in the literature [Sau85a, Sau85b].

$\boldsymbol{p}_{eff}$ is explicitly defined as the moment of an equivalent infinitesimal dipole, located at the particle's center, which produces the same dipolar electrostatic potential ϕ_{dipole} [Jon95]. Given this definition for $\boldsymbol{p}_{eff}$, it behoves me to first derive the electrostatic potential ϕ_{dipole} produced by an infinitesimal dipole. To do so, first consider Figure 3-2, which presents a finite dipole $\boldsymbol{p}_{eff}$ immersed in a homogeneous, isotropic dielectric medium of real absolute permittivity ε'_{med}. As the charge distribution of the depicted $\boldsymbol{p}_{eff}$ is axisymmetric: $\phi_{dipole} = \phi_{dipole}(r,\theta)$, where r is the radial component and θ is the zenith angle within a concentric spherical coordinate system.

- 30 -
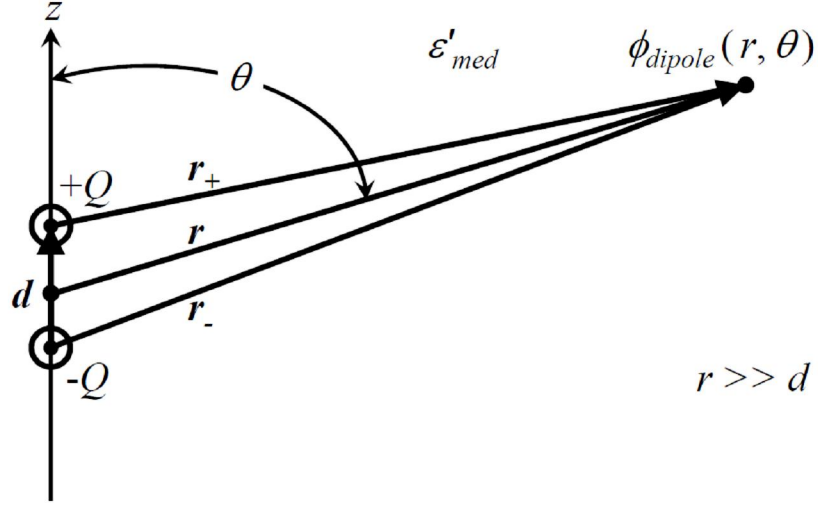
Figure 3-2: _A finite dipole along the z-axis of a concentric spherical coordinate system._

Via superposition, ϕ_{dipole} can be expressed as the sum of the electrostatic potentials due to each $\pm Q$ point charge [Jon95]:

$$\phi_{dipole}(r,\theta) = \frac{Q}{4\pi\varepsilon'_{med}\,r_+} - \frac{Q}{4\pi\varepsilon'_{med}\,r_-}$$

$$= \frac{Q}{4\pi\varepsilon'_{med}\,r}\left[\left(\frac{r}{r_+}\right)-\left(\frac{r}{r_-}\right)\right] \tag{3-4}$$

The ratios $r/r_\pm$ follow from the geometry of Figure 3-2:

$$\frac{r}{r_\pm} = \frac{r}{\sqrt{x^2 + y^2 + \left(z\mp\dfrac{d}{2}\right)^2}}$$

$$= \left\{\frac{1}{r^2}\left[r^2\sin^2(\theta)+\left(r\cos(\theta)\mp\frac{d}{2}\right)^2\right]\right\}^{-\frac{1}{2}}$$

$$= \left\{\frac{1}{r^2}\left[r^2\sin^2(\theta)+r^2\cos^2(\theta)\mp dr\cos(\theta)+\left(\frac{d}{2}\right)^2\right]\right\}^{-\frac{1}{2}}$$

$$= \left[1+\left(\frac{d}{2r}\right)^2\mp\left(\frac{d}{r}\right)\cos(\theta)\right]^{-\frac{1}{2}} \tag{3-5}$$

- 31 -

Equation (3-5) can be expanded via the Maclaurin series for $(1+x)^{-1/2}$:

$$\frac{1}{\sqrt{1+x}} = 1 - \frac{x}{2} + \frac{3x^2}{8} - \frac{5x^3}{16} + \ldots$$

$$\Rightarrow \quad \frac{r}{r_\pm} = 1 - \frac{1}{2}\left[\left(\frac{d}{2r}\right)^2 \mp 2\left(\frac{d}{2r}\right)\cos(\theta)\right]$$

$$+ \frac{3}{8}\left[\left(\frac{d}{2r}\right)^2 \mp 2\left(\frac{d}{2r}\right)\cos(\theta)\right]^2 - \frac{5}{16}\left[\left(\frac{d}{2r}\right)^2 \mp 2\left(\frac{d}{2r}\right)\cos(\theta)\right]^3 + \ldots$$

$$= 1 - \frac{1}{2}\left(\frac{d}{2r}\right)^2 \pm \left(\frac{d}{2r}\right)\cos(\theta) + \frac{3}{8}\left(\frac{d}{2r}\right)^4 \mp \frac{3}{2}\left(\frac{d}{2r}\right)^3\cos(\theta) + \frac{3}{2}\left(\frac{d}{2r}\right)^2\cos^2(\theta)$$

$$- \frac{5}{16}\left(\frac{d}{2r}\right)^6 \pm \frac{15}{8}\left(\frac{d}{2r}\right)^5\cos(\theta) - \frac{15}{4}\left(\frac{d}{2r}\right)^4\cos^2(\theta) \pm \frac{5}{2}\left(\frac{d}{2r}\right)^3\cos^3(\theta) + \ldots$$

$$= 1 \pm \left(\frac{d}{2r}\right)\cos(\theta) + \left(\frac{d}{2r}\right)^2\left[\frac{3\cos^2(\theta)-2}{2}\right] \pm \left(\frac{d}{2r}\right)^3\left[\frac{5\cos^3(\theta)-2\cos(\theta)}{2}\right] + \ldots$$

$$= P_0[\cos(\theta)] \pm \left(\frac{d}{2r}\right)P_1[\cos(\theta)] + \left(\frac{d}{2r}\right)^2 P_2[\cos(\theta)] \pm \left(\frac{d}{2r}\right)^3 P_3[\cos(\theta)] + \ldots \qquad (3\text{-}6)$$

where $P_n[\cos(\theta)]$ is the nth Legendre Polynomial in $\cos(\theta)$ [Jon95].

Substituting Equation (3-6) into Equation (3-4) yields

$$\phi_{dipole}(r,\theta) = \frac{QdP_1[\cos(\theta)]}{4\pi\varepsilon'_{med}r^2} + \frac{Qd^3 P_3[\cos(\theta)]}{16\pi\varepsilon'_{med}r^4} + \ldots \qquad (3\text{-}7)$$

The first term in Equation (3-7) is the $n = 1$ dipolar approximation of ϕ_{dipole}, which is sufficiently accurate when $r \gg d$ [Jon95]. The remaining terms in (3-7) are the higher-order multipolar terms, required to correct the dipolar approximation when $r \to d$ [Jon95]. Assuming that $r \gg d$, I shall retain only the dipolar approximation to express ϕ_{dipole} as

$$\phi_{dipole}(r,\theta) \approx \frac{p_{eff}\cos(\theta)}{4\pi\varepsilon'_{med}r^2} \qquad (3\text{-}8)$$

To determine the $\boldsymbol{p_{eff}}$ which models a bioparticle suspended in a fluid medium, I shall follow the lead of Jones and: (1) model the bioparticle as an equivalent lossless homogeneous dielectric sphere suspended in a lossless homogeneous dielectric medium (in Chapter 5 and Sections 7-3-7.4); (2) determine the $\boldsymbol{p_{eff}}$ which models the suspended sphere, as subjected to an external uniform time-invariant electric field $\boldsymbol{E_{ext}}$ (in Section 3.2); and (3) extend the lossless result to a lossy homogeneous dielectric sphere suspended within a lossy homogeneous dielectric medium, as subjected to an external non-uniform time-harmonis electric field $\boldsymbol{E_{ext}}$ (in Section 3.3) [Jon95].

3.2 The Dielectrophoretic Force Experienced by a Homogeneous Lossless Dielectric Sphere Subjected to a Uniform Time-Invariant Electric Field

Figure 3-3 depicts a lossless dielectric sphere of radius a and real absolute permittivity ε'_{cell} suspended in a lossless homogeneous isotropic dielectric medium of real absolute permittivity ε'_{med}. It is assumed that this system is exposed to an external spatially uniform linearly polarized electric field $\boldsymbol{E_{ext}} = E_{ext0}\,\boldsymbol{a_z}$.
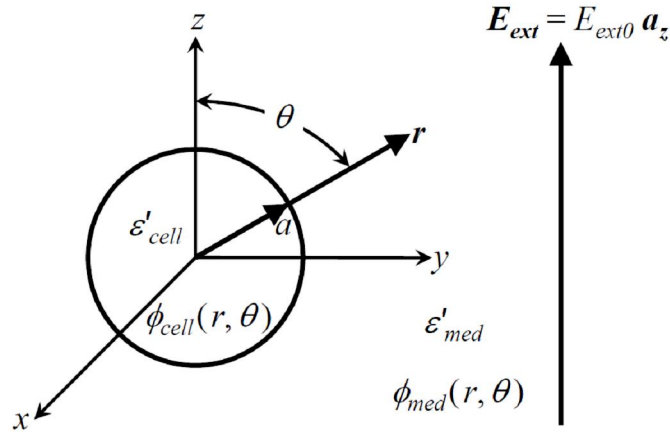
Figure 3-3: *A lossless dielectric sphere suspended in a lossless dielectric medium and subjected to a uniform time-invariant electric field.*

The electrostatic potentials within the particle and the external medium, ϕ_{cell} and ϕ_{med}, follow as the solution to Laplace's Equation, $\nabla^2 \phi = 0$. This second-order partial

differential equation shall be solved by assuming that $\phi(r,\theta) = R(r)\Theta(\theta)$, to yield a pair of uncoupled second-order ordinary differential equations [Zill01]. In spherical coordinates, Laplace's Equation follows as [Hayt01]:

$$\nabla^2\phi = \frac{1}{r^2}\frac{d}{dr}\left[r^2\frac{d}{dr}(R\Theta)\right] + \frac{1}{r^2\sin(\theta)}\frac{d}{d\theta}\left[\sin(\theta)\frac{d}{d\theta}(R\Theta)\right]$$

$$= \frac{\Theta}{r^2}\left[r^2\frac{d^2R}{dr^2} + 2r\frac{dR}{dr}\right] + \frac{R}{r^2\sin(\theta)}\left[\sin(\theta)\frac{d^2\Theta}{d\theta^2} + \cos(\theta)\frac{d\Theta}{d\theta}\right]$$

$$= \frac{R\Theta}{r^2}\left\{\frac{1}{R}\left[r^2\frac{d^2R}{dr^2} + 2r\frac{dR}{dr}\right] + \frac{1}{\Theta\sin(\theta)}\left[\sin(\theta)\frac{d^2\Theta}{d\theta^2} + \cos(\theta)\frac{d\Theta}{d\theta}\right]\right\}$$

$$= 0$$

$$\therefore \quad \frac{1}{R}\left[r^2\frac{d^2R}{dr^2} + 2r\frac{dR}{dr}\right] = -\frac{1}{\Theta\sin(\theta)}\left[\sin(\theta)\frac{d^2\Theta}{d\theta^2} + \cos(\theta)\frac{d\Theta}{d\theta}\right] = n(n+1) \quad , \quad n \in N \quad \text{(3-9)}$$

Consider the second-order ordinary differential equation for the radial component R embedded within Equation (3-9):

$$r^2\frac{d^2R}{dr^2} + 2r\frac{dR}{dr} - n(n+1)R = 0 \tag{3-10}$$

Equation (3-10) is a Cauchy-Euler Equation [Zill01], which is solved by assuming $R = r^m$ to yield a corresponding auxiliary equation whose roots yield m:

$$r^2\left(m(m-1)r^{m-2}\right) + 2r\left(mr^{m-1}\right) - n(n+1)r^m = 0$$

$$m(m-1)r^m + 2mr^m - n(n+1)r^m = 0$$

$$m(m-1) + 2m - n(n+1) = 0$$

$$m^2 + m - n(n+1) = 0$$

$$\therefore \quad m = n, -(n+1) \tag{3-11}$$

The general solution to (3-10) then follows a linear combination of r^n and $r^{-(n+1)}$:

$$R = c_1 r^n + c_2 r^{-(n+1)} \quad , \quad c_1, c_2 \in \Re \tag{3-12}$$

- 34 -

Consider the second-order ordinary differential equation for the zenith angle component Θ embedded within Equation (3-9):

$$\frac{d^2\Theta}{d\theta^2} + \cot(\theta)\frac{d\Theta}{d\theta} + n(n-1)\Theta = 0 \qquad (3\text{-}13)$$

Employing the substitution $x = \cos(\theta)$, where $0 \leq \theta \leq \pi$, Equation (3-13) becomes

$$\frac{d}{d\theta}\left[\frac{d\Theta}{dx}\frac{dx}{d\theta}\right] + \cot(\theta)\frac{d\Theta}{dx}\frac{dx}{d\theta} + n(n-1)\Theta = 0$$

$$\frac{d^2\Theta}{dxd\theta}\frac{dx}{d\theta} + \frac{d\Theta}{dx}\frac{d^2x}{d\theta^2} + \cot(\theta)\frac{d\Theta}{dx}\frac{dx}{d\theta} + n(n-1)\Theta = 0$$

$$\frac{d^2\Theta}{dx}\frac{1}{d\theta}\frac{dx}{d\theta} + \frac{d\Theta}{dx}\frac{d^2x}{d\theta^2} + \cot(\theta)\frac{d\Theta}{dx}\frac{dx}{d\theta} + n(n-1)\Theta = 0$$

$$\frac{d^2\Theta}{dx}\left[-\frac{\sin(\theta)}{dx}\right]\left[-\sin(\theta)\right] + \frac{d\Theta}{dx}\left[-\cos(\theta)\right] + \cot(\theta)\frac{d\Theta}{dx}\left[-\sin(\theta)\right] + n(n-1)\Theta = 0$$

$$\sin^2(\theta)\frac{d^2\Theta}{dx^2} - \cos(\theta)\frac{d\Theta}{dx} - \cos(\theta)\frac{d\Theta}{dx} + n(n-1)\Theta = 0$$

$$\therefore \quad (1-x^2)\frac{d^2\Theta}{dx^2} - 2x\frac{d\Theta}{dx} + n(n-1)\Theta = 0 \quad , \quad -1 \leq x \leq 1 \qquad (3\text{-}14)$$

Equation (3-14) is a Legendre Equation, for which the only solutions that are continuous and have continuous derivatives within the $-1 \leq x \leq 1$ interval are the Legendre Polynomials $P_n(x)$ corresponding to $n(n+1)$ [Zill01].

$\phi(r,\theta) = R(r)\Theta(\theta)$ thus follows as

$$\phi = [\, c_1 r^n + c_2 r^{-(n+1)} \,]\, P_n[\cos(\theta)] \qquad (3\text{-}15)$$

Equation (3-8) was obtained by retaining only the $P_1[\cos(\theta)]$ term in Equation (3-7). By analogy, the substitution $n = 1$ shall be employed in Equation (3-15) to yield

$$\phi = c_1 r \cos(\theta) + \frac{c_2 \cos(\theta)}{r^2} \qquad (3\text{-}16)$$

Equation (3-16) must be considered within the particle and the external medium separately:

$$\phi_{med}(r,\theta) = c_1 r \cos(\theta) + \frac{c_2 \cos(\theta)}{r^2} \quad , \quad r > a \tag{3-17a}$$

$$\phi_{cell}(r,\theta) = c_3 r \cos(\theta) + \frac{c_4 \cos(\theta)}{r^2} \quad , \quad r < a \tag{3-17b}$$

The first-term in Equation (3-17a) is attributed to ϕ_{ext}, the electrostatic potential associated with the external electric field $\boldsymbol{E_{ext}} = E_{ext0}\, \boldsymbol{a_z}$ alone. As $\boldsymbol{E_{ext}} = -\nabla \phi_{ext}$ must be satisfied [Hayt01]: $c_1 = -E_{ext0}$. Furthermore, ϕ_{cell} must be finite at all points within the particle, and thus $c_4 = 0$ (otherwise $\phi_{cell} \rightarrow \infty$ as $r \rightarrow 0$). Employing the substitutions $c_2 = A$ and $c_3 = -B$ (where $A, B \in \Re$), Equations (3-17a) and (3-17b) are expressed as

$$\phi_{med}(r,\theta) = -E_{ext0} r \cos(\theta) + \frac{A\cos(\theta)}{r^2} \quad , \quad r > a \tag{3-18a}$$

$$\phi_{cell}(r,\theta) = -Br \cos(\theta) \quad , \quad r < a \tag{3-18b}$$

The total electric fields within the particle and the external medium, $\boldsymbol{E_{cell}}$ and $\boldsymbol{E_{med}}$, follow from Equations (3-18a) and (3-18b) as [Hayt01]:

$$
\begin{aligned}
\boldsymbol{E_{med}} &= -\nabla \phi_{med} \\[2mm]
&= -\frac{\partial \phi_{med}}{\partial r}\boldsymbol{a_r} - \frac{1}{r}\frac{\partial \phi_{med}}{\partial \theta}\boldsymbol{a_\theta} \\[2mm]
&= \left[E_{ext0}\cos(\theta) + \frac{2A\cos(\theta)}{r^3}\right]\boldsymbol{a_r} + \left[-E_{ext0}\sin(\theta) + \frac{A\sin(\theta)}{r^3}\right]\boldsymbol{a_\theta} \\[2mm]
&= E_{ext0}[\cos(\theta)\,\boldsymbol{a_r} \; \acute{o} \; \sin(\theta)\,\boldsymbol{a_\theta}] + \frac{A}{r^3}[2\cos(\theta)\boldsymbol{a_r} + \sin(\theta)\boldsymbol{a_\theta}] \\[2mm]
&= E_{ext0}\,\boldsymbol{a_z} + \frac{A}{r^3}[2\cos(\theta)\boldsymbol{a_r} + \sin(\theta)\boldsymbol{a_\theta}] \\[2mm]
&= \boldsymbol{E_{ext}} + \frac{A}{r^3}[2\cos(\theta)\boldsymbol{a_r} + \sin(\theta)\boldsymbol{a_\theta}] \tag{3-19a}
\end{aligned}
$$

$$E_{cell} = -\nabla \phi_{cell}$$

$$= -\frac{\partial \phi_c}{\partial r} a_r - \frac{1}{r} \frac{\partial \phi_c}{\partial \theta} a_\theta$$

$$= B\cos(\theta) a_r - B\sin(\theta) a_\theta$$

$$= B\, a_z \quad\quad\quad\quad\quad\quad\quad\quad (3\text{-}19b)$$

The electrostatic boundary conditions at the surface of the particle yields a system of two coupled linear equations in A and B [Hayt01]:

$$D_{med}(r=a,\theta) \bullet a_{normal} = D_{cell}(r=a,\theta) \bullet a_{normal}$$

$$\varepsilon'_{med}\, E_{med}(r=a,\theta) \bullet a_r = \varepsilon'_{cell}\, E_{cell}(r=a,\theta) \bullet a_r$$

$$\varepsilon'_{med}\left[E_{ext0}\cos(\theta) + \frac{2A\cos(\theta)}{a^3} \right] = \varepsilon'_{cell} B\cos(\theta)$$

$$\therefore\quad B = \frac{\varepsilon'_{med}}{\varepsilon'_{cell}}\left[E_{ext0} + \frac{2A}{a^3} \right] \quad\quad (3\text{-}20a)$$

$$E_{med}(r=a,\theta) \bullet a_{tangent} = E_{cell}(r=a,\theta) \bullet a_{tangent}$$

$$E_{med}(r=a,\theta) \bullet (a_\theta + a_\varphi)/\sqrt{2} = E_{cell}(r=a,\theta) \bullet (a_\theta + a_\varphi)/\sqrt{2}$$

$$\frac{1}{\sqrt{2}}\left[-E_{ext0}\sin(\theta) + \frac{A\sin(\theta)}{a^3} \right] = -\frac{B\sin(\theta)}{\sqrt{2}}$$

$$\therefore\quad B = \left[E_{ext0} - \frac{A}{a^3} \right] \quad\quad\quad (3\text{-}20b)$$

Solving the linear system of Equations (3-20a) and (3-20b) yields A and B as

$$A = \left[\frac{\varepsilon'_{cell} - \varepsilon'_{med}}{\varepsilon'_{cell} + 2\varepsilon'_{med}} \right] a^3 E_{ext0} \quad\quad (3\text{-}21a)$$

$$B = \left[\frac{3\varepsilon'_{med}}{\varepsilon'_{cell} + 2\varepsilon'_{med}} \right] E_{ext0} \quad\quad\quad (3\text{-}21b)$$

The second term in Equation (3-18a) corresponds to the electrostatic potential produced by the induced electric dipole $\boldsymbol{p_{eff}}$. Comparing this term to Equation (3-8) suggests that

$$\boldsymbol{p_{eff}} = 4\,\pi\,\varepsilon'_{med}\,K\,a^3\,\boldsymbol{E_{ext}} \qquad (3\text{-}22)$$

where K is the Clausius-Mossotti factor [Jon95], a measure of the strength of the effective polarization of a spherical particle suspended in a fluid medium, given by

$$K = \frac{\varepsilon'_{cell} - \varepsilon'_{med}}{\varepsilon'_{cell} + 2\varepsilon'_{med}} \qquad (3\text{-}23)$$

3.3 The Time-Averaged Dielectrophoretic Force Experienced by a Homogeneous Lossy Dielectric Sphere Subjected to a Non-Uniform Time-Harmonic Electric Field

Figure 3-4 depicts a lossy dielectric sphere of radius a, real absolute permittivity ε'_{cell}, intrinsic absolute dielectric loss ε''_{cell}, and conductivity σ_{cell} suspended in a lossy dielectric medium of real absolute permittivity ε'_{med}, intrinsic absolute dielectric loss ε''_{med}, and conductivity σ_{med}.
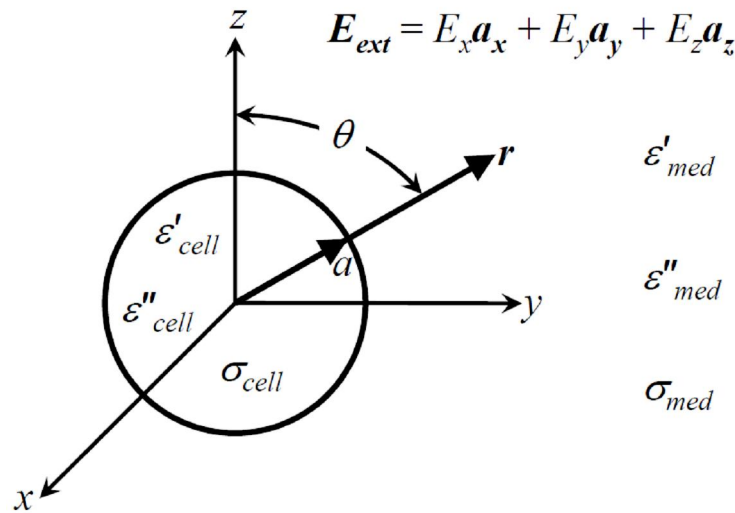
Figure 3-4: *A lossy dielectric sphere suspended in a lossy dielectric medium and subjected to an external time-harmonic electric field.*

I shall now allow for a spatially non-uniform external electric E_{ext}. However, I shall restrict the analysis to the special case of a time-harmonic E_{ext} as given by

$$
\begin{aligned}
E_{ext} &= E_x a_x + E_y a_y + E_z a_z \\
&= \quad E_{x0}(x,y,z)\cos(\omega t + \gamma_x(x,y,z))a_x \\
&\quad + E_{y0}(x,y,z)\cos(\omega t + \gamma_y(x,y,z))a_y \\
&\quad + E_{z0}(x,y,z)\cos(\omega t + \gamma_z(x,y,z))a_z \quad\quad\quad (3\text{-}24)
\end{aligned}
$$

where E_i is the linearly polarized component of E_{ext} pointing in the direction of a_i, E_{i0} is the spatially non-uniform magnitude of E_i, γ_i is the spatially non-uniform phase of E_i, and ω is the angular frequency at which E_{ext} oscillates [Hug03].

The effective dipole moment p_{eff} for this lossy time-harmonic case follows from Equations (3-22) and (3-24) as [Hug03]:

$$
\begin{aligned}
p_{eff} &= p_x a_x + p_y a_y + p_z a_z \\
&= 4\pi \varepsilon'_{med} a^3 \{ \quad E_{x0} [\, \mathrm{Re}\{\underline{K}\}\cos(\omega t + \gamma_x) - \mathrm{Im}\{\underline{K}\}\sin(\omega t + \gamma_x) \,]\, a_x \\
&\quad + E_{y0} [\, \mathrm{Re}\{\underline{K}\}\cos(\omega t + \gamma_y) - \mathrm{Im}\{\underline{K}\}\sin(\omega t + \gamma_y) \,]\, a_y \\
&\quad + E_{z0} [\, \mathrm{Re}\{\underline{K}\}\cos(\omega t + \gamma_z) - \mathrm{Im}\{\underline{K}\}\sin(\omega t + \gamma_z) \,]\, a_z \quad \} \quad (3\text{-}25)
\end{aligned}
$$

where p_i is the component of p_{eff} pointing in the direction of a_i and $\underline{K}$ is the complex Clausius-Mossotti factor obtained by replacing the ε' terms in Equation (3-23) by the complex absolute permittivities, $\underline{\varepsilon} = \varepsilon' - j\,\varepsilon'' \,\acute{o}\, j\,(\sigma/\omega)$ (where j is the unit imaginary number) [Jon95]:

$$
\begin{aligned}
\underline{K} &= \frac{\underline{\varepsilon}_{cell} - \underline{\varepsilon}_{med}}{\underline{\varepsilon}_{cell} + 2\underline{\varepsilon}_{med}} \\[2mm]
&= \frac{\varepsilon'_{cell} - j\varepsilon''_{cell} - j\left(\sigma_{cell}/\omega\right) - \varepsilon'_{med} + j\varepsilon''_{med} + j\left(\sigma_{med}/\omega\right)}{\varepsilon'_{cell} - j\varepsilon''_{cell} - j\left(\sigma_{cell}/\omega\right) + 2\varepsilon'_{med} - j2\varepsilon''_{med} - j2\left(\sigma_{med}/\omega\right)} \quad (3\text{-}26)
\end{aligned}
$$

The instantaneous dielectrophoretic force $F_{DEP}(t)$ for this lossy time-harmonic case follows from Equations (3-3), (3-24), and (3-25) as:

$$F_{DEP}(t) = p_{eff}(t) \bullet \nabla E_{ext}(t)$$

$$= [\, p_x a_x + p_y a_y + p_z a_z \,] \bullet [\quad \partial_x E_x a_{x,x} + \partial_y E_x a_{x,y} + \partial_z E_x a_{x,z}$$
$$+ \partial_x E_y a_{y,x} + \partial_y E_y a_{y,y} + \partial_z E_y a_{y,z}$$
$$+ \partial_x E_z a_{z,x} + \partial_y E_z a_{z,y} + \partial_z E_z a_{z,z} \quad]$$

$$= [\, p_x(\partial_x E_x) + p_y(\partial_x E_y) + p_z(\partial_x E_z) \,] \, a_x$$
$$+ [\, p_x(\partial_y E_x) + p_y(\partial_y E_y) + p_z(\partial_y E_z) \,] \, a_y$$
$$+ [\, p_x(\partial_z E_x) + p_y(\partial_z E_y) + p_z(\partial_z E_z) \,] \, a_z \qquad (3\text{-}27)$$

where the tensor definition for the gradient of a vector field [Spurk08] and the definition for the dot product between a vector and a tensor [Poly01] have been employed.

Consider the component of Equation (3-27) pointing in the direction of a_x:

$$F_{DEPx}(t) = p_x(\partial_x E_x) + p_y(\partial_x E_y) + p_z(\partial_x E_z)$$

$$= 4 \pi \varepsilon'_{med} a^3 \{ \quad E_{x0} [\, \mathrm{Re}\{\underline{K}\}\cos(\omega t + \gamma_x) - \mathrm{Im}\{\underline{K}\}\sin(\omega t + \gamma_x) \,]$$
$$\bullet [\, (\partial_x E_{x0})\cos(\omega t + \gamma_x) - E_{x0}\sin(\omega t + \gamma_x)\,(\partial_x \gamma_x) \,]$$
$$+ E_{y0} [\, \mathrm{Re}\{\underline{K}\}\cos(\omega t + \gamma_y) - \mathrm{Im}\{\underline{K}\}\sin(\omega t + \gamma_y) \,]$$
$$\bullet [\, (\partial_x E_{y0})\cos(\omega t + \gamma_y) - E_{y0}\sin(\omega t + \gamma_y)\,(\partial_x \gamma_y) \,]$$
$$+ E_{z0} [\, \mathrm{Re}\{\underline{K}\}\cos(\omega t + \gamma_z) - \mathrm{Im}\{\underline{K}\}\sin(\omega t + \gamma_z) \,]$$
$$\bullet [\, (\partial_x E_{z0})\cos(\omega t + \gamma_z) - E_{z0}\sin(\omega t + \gamma_z)\,(\partial_x \gamma_z) \,] \quad \}$$

$$= 4 \pi \varepsilon'_{med} a^3 \{ \quad E_{x0}(\partial_x E_{x0})\cos(\omega t + \gamma_x) [\, \mathrm{Re}\{\underline{K}\}\cos(\omega t + \gamma_x) - \mathrm{Im}\{\underline{K}\}\sin(\omega t + \gamma_x) \,]$$
$$+ E_{y0}(\partial_x E_{y0})\cos(\omega t + \gamma_y) [\, \mathrm{Re}\{\underline{K}\}\cos(\omega t + \gamma_y) - \mathrm{Im}\{\underline{K}\}\sin(\omega t + \gamma_y) \,]$$
$$+ E_{z0}(\partial_x E_{z0})\cos(\omega t + \gamma_z) [\, \mathrm{Re}\{\underline{K}\}\cos(\omega t + \gamma_z) - \mathrm{Im}\{\underline{K}\}\sin(\omega t + \gamma_z) \,]$$
$$- E_{x0}^2 (\partial_x \gamma_x) \sin(\omega t + \gamma_x) [\, \mathrm{Re}\{\underline{K}\}\cos(\omega t + \gamma_x) - \mathrm{Im}\{\underline{K}\}\sin(\omega t + \gamma_x) \,]$$
$$- E_{y0}^2 (\partial_x \gamma_y) \sin(\omega t + \gamma_y) [\, \mathrm{Re}\{\underline{K}\}\cos(\omega t + \gamma_y) - \mathrm{Im}\{\underline{K}\}\sin(\omega t + \gamma_y) \,]$$
$$- E_{z0}^2 (\partial_x \gamma_z) \sin(\omega t + \gamma_z) [\, \mathrm{Re}\{\underline{K}\}\cos(\omega t + \gamma_z) - \mathrm{Im}\{\underline{K}\}\sin(\omega t + \gamma_z) \,] \quad \}$$

$$= 4 \pi \varepsilon'_{med} a^3 \{ \quad E_{x0}(\partial_x E_{x0}) [\, \mathrm{Re}\{\underline{K}\}\cos^2(\omega t + \gamma_x) - \mathrm{Im}\{\underline{K}\}\sin(\omega t + \gamma_x)\cos(\omega t + \gamma_x) \,]$$
$$+ E_{y0}(\partial_x E_{y0}) [\, \mathrm{Re}\{\underline{K}\}\cos^2(\omega t + \gamma_y) - \mathrm{Im}\{\underline{K}\}\sin(\omega t + \gamma_y)\cos(\omega t + \gamma_y) \,]$$
$$+ E_{z0}(\partial_x E_{z0}) [\, \mathrm{Re}\{\underline{K}\}\cos^2(\omega t + \gamma_z) - \mathrm{Im}\{\underline{K}\}\sin(\omega t + \gamma_z)\cos(\omega t + \gamma_z) \,]$$
$$- E_{x0}^2 (\partial_x \gamma_x) [\, \mathrm{Re}\{\underline{K}\}\sin(\omega t + \gamma_x)\cos(\omega t + \gamma_x) - \mathrm{Im}\{\underline{K}\}\sin^2(\omega t + \gamma_x) \,]$$
$$- E_{y0}^2 (\partial_x \gamma_y) [\, \mathrm{Re}\{\underline{K}\}\sin(\omega t + \gamma_y)\cos(\omega t + \gamma_y) - \mathrm{Im}\{\underline{K}\}\sin^2(\omega t + \gamma_y) \,]$$
$$- E_{z0}^2 (\partial_x \gamma_z) [\, \mathrm{Re}\{\underline{K}\}\sin(\omega t + \gamma_z)\cos(\omega t + \gamma_z) - \mathrm{Im}\{\underline{K}\}\sin^2(\omega t + \gamma_z) \,] \quad \}$$

$$
\begin{aligned}
= \; 2\pi\varepsilon'_{med}\,a^3\{ \; & E_{x0}(\nabla_x E_{x0})\,[\,\mathrm{Re}\{\underline{K}\} + \mathrm{Re}\{\underline{K}\}\cos(2\omega t + 2\gamma_x) - \mathrm{Im}\{\underline{K}\}\sin(2\omega t + 2\gamma_x)\,] \\
+ & E_{y0}(\nabla_x E_{y0})\,[\,\mathrm{Re}\{\underline{K}\} + \mathrm{Re}\{\underline{K}\}\cos(2\omega t + 2\gamma_y) - \mathrm{Im}\{\underline{K}\}\sin(2\omega t + 2\gamma_y)\,] \\
+ & E_{z0}(\nabla_x E_{z0})\,[\,\mathrm{Re}\{\underline{K}\} + \mathrm{Re}\{\underline{K}\}\cos(2\omega t + 2\gamma_z) - \mathrm{Im}\{\underline{K}\}\sin(2\omega t + 2\gamma_z)\,] \\
- & E_{x0}{}^2\,(\nabla_x \gamma_x)\,[\,\mathrm{Re}\{\underline{K}\}\sin(2\omega t + 2\gamma_x) - \mathrm{Im}\{\underline{K}\} + \mathrm{Im}\{\underline{K}\}\cos(2\omega t + 2\gamma_x)\,] \\
- & E_{y0}{}^2\,(\nabla_x \gamma_y)\,[\,\mathrm{Re}\{\underline{K}\}\sin(2\omega t + 2\gamma_y) - \mathrm{Im}\{\underline{K}\} + \mathrm{Im}\{\underline{K}\}\cos(2\omega t + 2\gamma_y)\,] \\
- & E_{z0}{}^2\,(\nabla_x \gamma_z)\,[\,\mathrm{Re}\{\underline{K}\}\sin(2\omega t + 2\gamma_z) - \mathrm{Im}\{\underline{K}\} + \mathrm{Im}\{\underline{K}\}\cos(2\omega t + 2\gamma_z)\,] \;\} \quad (3\text{-}28)
\end{aligned}
$$

Equation (3-28) demonstrates that the components of the $\boldsymbol{F_{DEP}}(t)$ experienced by a suspended sphere within an external time-harmonic electric field $\boldsymbol{E_{ext}}(t)$ consist of a time-invariant average force and sinusoidal time-variant force which oscillates at twice the frequency of $\boldsymbol{E_{ext}}(t)$. When the spherical particle is on the order of 1-1000 μm in diameter, the oscillatory motion induced by the time-variant $F_{DEP}(t)$ terms is usually heavily dampened by the suspension medium's viscosity [Jon95]. As such, only the time-invariant average $F_{DEP}(t)$ terms are considered within this work. The time-averaged F_{DEPx} follows directly from Equation (3-28) as:

$$
\begin{aligned}
< F_{DEPx}(t) > \; = \; 2\pi\varepsilon'_{med}\,a^3\,\{ \quad & \mathrm{Re}\{\underline{K}\}\,[\,E_{x0}(\nabla_x E_{x0}) + E_{y0}(\nabla_x E_{y0}) + E_{z0}(\nabla_x E_{z0})\,] \\
& + \mathrm{Im}\{\underline{K}\}\,[\,E_{x0}{}^2(\nabla_x \gamma_x) + E_{y0}{}^2(\nabla_x \gamma_y) + E_{z0}{}^2(\nabla_x \gamma_z)\,] \;\} \\[4pt]
= \; 2\pi\varepsilon'_{med}\,a^3\,\{ \quad & \mathrm{Re}\{\underline{K}\}\,(1/2)\,[\,2E_{x0}(\nabla_x E_{x0}) + 2E_{y0}(\nabla_x E_{y0}) + 2E_{z0}(\nabla_x E_{z0})\,] \\
& + \mathrm{Im}\{\underline{K}\}\,[\,E_{x0}{}^2(\nabla_x \gamma_x) + E_{y0}{}^2(\nabla_x \gamma_y) + E_{z0}{}^2(\nabla_x \gamma_z)\,] \;\} \\[4pt]
= \; 2\pi\varepsilon'_{med}\,a^3\,\{ \quad & \mathrm{Re}\{\underline{K}\}\,(1/2)\,[\,\nabla_x E_{x0}{}^2 + \nabla_x E_{y0}{}^2 + \nabla_x E_{z0}{}^2\,] \\
& + \mathrm{Im}\{\underline{K}\}\,[\,E_{x0}{}^2(\nabla_x \gamma_x) + E_{y0}{}^2(\nabla_x \gamma_y) + E_{z0}{}^2(\nabla_x \gamma_z)\,] \;\} \\[4pt]
= \; 2\pi\varepsilon'_{med}\,a^3\,\{ \quad & \mathrm{Re}\{\underline{K}\}\,(1/2)\,\nabla_x E_{ext}{}^2 \\
& + \mathrm{Im}\{\underline{K}\}\,[\,E_{x0}{}^2(\nabla_x \gamma_x) + E_{y0}{}^2(\nabla_x \gamma_y) + E_{z0}{}^2(\nabla_x \gamma_z)\,] \;\} \quad (3\text{-}29)
\end{aligned}
$$

The components of $< \boldsymbol{F_{DEP}}(t) >$ pointing in the directions of $\boldsymbol{a_y}$ and $\boldsymbol{a_z}$, $< F_{DEPy}(t) >$ and $< F_{DEPz}(t) >$, follow in the same manner as $< F_{DEPx}(t) >$ to yield the total $< \boldsymbol{F_{DEP}}(t) >$ as:

$$\langle \boldsymbol{F_{DEP}}(t) \rangle = \langle F_{DEPx}(t)\rangle \boldsymbol{a_x} + \langle F_{DEPy}(t)\rangle \boldsymbol{a_y} + \langle F_{DEPz}(t)\rangle \boldsymbol{a_z}$$

$$= 2\pi\varepsilon'_{med}\,a^3 \{\ \text{Re}\{\underline{K}\}\,(1/2)\,[\,(\nabla_x E_{ext}^2)\boldsymbol{a_x} + (\nabla_y E_{ext}^2)\boldsymbol{a_y} + (\nabla_z E_{ext}^2)\boldsymbol{a_z}\,]$$

$$+\,\text{Im}\{\underline{K}\}\,[\quad E_{x0}^2(\nabla_x\gamma_x)\boldsymbol{a_x} + E_{y0}^2(\nabla_x\gamma_y)\boldsymbol{a_x} + E_{z0}^2(\nabla_x\gamma_z)\boldsymbol{a_x}$$

$$+\,E_{x0}^2(\nabla_y\gamma_x)\boldsymbol{a_y} + E_{y0}^2(\nabla_y\gamma_y)\boldsymbol{a_y} + E_{z0}^2(\nabla_y\gamma_z)\boldsymbol{a_y}$$

$$+\,E_{x0}^2(\nabla_z\gamma_x)\boldsymbol{a_z} + E_{y0}^2(\nabla_z\gamma_y)\boldsymbol{a_z} + E_{z0}^2(\nabla_z\gamma_z)\boldsymbol{a_z}\ ]\ \}$$

$$= 2\pi\varepsilon'_{med}\,a^3 \{\ \text{Re}\{\underline{K}\}\,(1/2)\,\nabla E_{ext}^2$$

$$+\,\text{Im}\{\underline{K}\}\,E_{x0}^2\,[\,(\nabla_x\gamma_x)\boldsymbol{a_x} + (\nabla_y\gamma_x)\boldsymbol{a_y} + (\nabla_z\gamma_x)\boldsymbol{a_z}\,]$$

$$+\,\text{Im}\{\underline{K}\}\,E_{y0}^2\,[\,(\nabla_x\gamma_y)\boldsymbol{a_x} + (\nabla_y\gamma_y)\boldsymbol{a_y} + (\nabla_z\gamma_y)\boldsymbol{a_z}\,]$$

$$+\,\text{Im}\{\underline{K}\}\,E_{z0}^2\,[\,(\nabla_x\gamma_z)\boldsymbol{a_x} + (\nabla_y\gamma_z)\boldsymbol{a_y} + (\nabla_z\gamma_z)\boldsymbol{a_z}\,]\ \}$$

$$= 2\pi\varepsilon'_{med}\,a^3 \{\ \text{Re}\{\underline{K}\}\,\nabla[(1/2)E_{ext}^2]$$

$$+\,\text{Im}\{\underline{K}\}\,[\,E_{x0}^2\nabla\gamma_x + E_{y0}^2\nabla\gamma_y + E_{z0}^2\nabla\gamma_z\,]\ \}$$

$$= 2\pi\varepsilon'_{med}\,a^3 \{\ \text{Re}\{\underline{K}\}\,\nabla E_{RMS}^2$$

$$+\,\text{Im}\{\underline{K}\}\,[\,E_{x0}^2\nabla\gamma_x + E_{y0}^2\nabla\gamma_y + E_{z0}^2\nabla\gamma_z\,]\ \} \qquad (3\text{-}30)$$

where E_{RMS} is the spatially non-uniform root-mean-squared magnitude (RMS) of $\boldsymbol{E_{ext}}$.

The Re$\{\underline{K}\}$ term within Equation (3-30) corresponds to the conventional DEP generated by the spatial non-uniformity of E_{RMS}^2, whereas the Im$\{\underline{K}\}$ terms correspond to the travelling-wave DEP (twDEP) generated by the spatial non-uniformity of γ_i [Hug03, Gasc04]. In this work, $\boldsymbol{E_{ext}}$ is generated by a single time-harmonic electric potential ϕ_{DEP} applied to the microelectrode array (MEA). As such, $\nabla\gamma_i = 0$ and the twDEP terms in Equation (3-30) vanish:

$$\langle \boldsymbol{F_{DEP}}(t) \rangle = 2\pi\varepsilon'_{med}\,a^3\,\text{Re}\{\underline{K}\}\,\nabla E_{RMS}^2 \qquad (3\text{-}31)$$

From this point onwards, $\boldsymbol{F_{DEP}}$ represents $\langle \boldsymbol{F_{DEP}}(t) \rangle$ as given by Equation (3-31). The validity of Equation (3-31) is confirmed by the more rigorous Maxwell stress tensor based derivation found elsewhere in the literature [Jon95, Sau85a, Sau85b].

The frequency dependence of $\boldsymbol{F_{DEP}}$ is solely determined by Re$\{\underline{K}\}$. This dependence, which depends upon the ε', ε'', and σ terms of the sphere and the medium, defines the DEP spectrum. As ε'' are typically neglected within the 10-1000 kHz band at which the DEP actuation potential ϕ_{DEP} oscillates, $\underline{K}$ is commonly written as [Jon95]:

$$\underline{K} \approx \frac{\varepsilon'_{cell} - \varepsilon'_{med} - j\left(\dfrac{\sigma_{cell} - \sigma_{med}}{\omega}\right)}{\varepsilon'_{cell} + 2\varepsilon'_{med} - j\left(\dfrac{\sigma_{cell} + 2\sigma_{med}}{\omega}\right)} \tag{3-32}$$

Equation (3-32) implies that the $\omega \rightarrow 0$ DEP behaviour is governed by the conductivities, and that the $\omega \rightarrow \infty$ DEP behaviour is governed by the real permittivities:

$$K_0 = \lim_{\omega \rightarrow 0}\{Re\{\underline{K}\}\} \approx \frac{\sigma_{cell} - \sigma_{med}}{\sigma_{cell} + 2\sigma_{med}} \tag{3-33a}$$

$$K_\infty = \lim_{\omega \rightarrow \infty}\{Re\{\underline{K}\}\} \approx \frac{\varepsilon'_{cell} - \varepsilon'_{med}}{\varepsilon'_{cell} + 2\varepsilon'_{med}} \tag{3-33b}$$

The real part of Equation (3-32) can be expressed via a partial fraction expansion as

$$Re\{\underline{K}\} \approx K_\infty - \left(\frac{K_\infty - K_0}{1 + \omega^2 \tau_{MW}^2}\right) \tag{3-34}$$

where τ_{MW} is the Maxwell-Wagner charge relaxation time of the material interface between the fluid medium and the sphere [Beng82, Jon95]. τ_{MW} is given as [Beng82, Jon95]:

$$\tau_{MW} = \frac{\varepsilon'_{cell} + 2\varepsilon'_{med}}{\sigma_{cell} + 2\sigma_{med}} \tag{3-35}$$

The bands within which the $\omega \rightarrow 0$ and $\omega \rightarrow \infty$ limits of $Re\{\underline{K}\}$, presented above as Equations (3-33a) and (3-33b), are valid approximations of the true $Re\{\underline{K}\}$ can be identified using τ_{MW} as follows: if $\omega\tau_{MW} << 1$, then $Re\{\underline{K}\}$ é K_0; and if $\omega\tau_{MW} >> 1$, then $Re\{\underline{K}\}$ é K_∞ [Jon95].

Equations (3-25) through (3-35) are valid only for the special case of a homogeneous lossy dielectric sphere suspended in a homogeneous isotropic lossy

dielectric medium and subjected to a non-uniform external electric field $\boldsymbol{E_{ext}}$ generated by a single time-harmonic electric potential ϕ_{DEP}. As the polystyrene microspheres (PSS) used in this work are essentially homogeneous lossy dielectric spheres, Equations (3-25) through (3-35) can be directly applied to predict the DEP spectra of PSS (as is done in Chapter 5). However, the *Saccharomyces cerevisiae* cells used in this work posses a highly heterogeneous internal structure, and thus must be represented as equivalent homogeneous lossy dielectric spheres before Equations (3-25) through (3-35) can be applied to predict their DEP spectra (as is done in Sections 7.3-7.4).

Chapter 4

Induced Microelectrode Array
Capacitance Perturbation Signatures
& Simulated Bioparticle Trajectories

4.1 Theoretical Microelectrode Array Capacitance Perturbation

First assume that the microfluidic cross-channel is filled with a homogeneous isotropic lossy dielectric of real absolute permittivity ε'_{med}, absolute intrinsic dielectric loss ε''_{med}, and conductivity σ_{med}. Also assume that a time-harmonic root-mean-squared (RMS) electrical potential ϕ_{RF} is applied to the coplanar microelectrode array (MEA), generating the following non-uniform external RMS electric field $\boldsymbol{E_{ext}}$ within the microfludic cross-channel detection zone directly above the MEA:

$$\boldsymbol{E_{ext}} \;=\; \mathrm{Re}\{\; \underline{\boldsymbol{E}}_{ext} \exp(j\,\omega t\,)\;\} \tag{4-1}$$

where $\underline{\boldsymbol{E}}_{ext}$ is the spatially non-uniform external electric field phasor, ω is the angular frequency at which $\boldsymbol{E_{ext}}$ oscillates, and j is the unit imaginary number.

The time-averaged electrical energy W_{elec0} stored in the detection zone follows as

$$W_{elec0} \;=\; \frac{1}{2}\, C_{MEA0}\, \phi_{RF}{}^{2} \tag{4-2}$$

where C_{MEA0} is the total MEA capacitance [Jar09].

A lossy dielectric sphere, with radius a, real absolute permittivity ε'_{cell}, absolute intrinsic dielectric loss ε''_{cell}, and conductivity σ_{cell}, is now inserted into the detection zone directly above the MEA. The time-averaged electrical energy of this region is now changed to a new value W_{elecf}, given by

$$W_{elecf} = \frac{1}{2} C_{MEAf}\, \phi_{RF}{}^{2}$$

$$= \frac{1}{2} C_{MEA0}\, \phi_{RF}{}^{2} + \frac{1}{2}\mathrm{Re}\{\textstyle\int_{V} \underline{\boldsymbol{E}}_{ext} \bullet \underline{\boldsymbol{P}}^{*}{}_{cell}\, dV\}$$

$$= \frac{1}{2} C_{MEA0}\, \phi_{RF}{}^{2} + \frac{1}{2}\mathrm{Re}\{\textstyle\int_{V_{cell}} \underline{\boldsymbol{E}}_{ext} \bullet \underline{\boldsymbol{P}}^{*}{}_{cell}\, dV\} \qquad (4\text{-}3)$$

where C_{MEAf} is the new total MEA capacitance, $\underline{\boldsymbol{P}}^{*}{}_{cell}$ is the complex conjugate of the RMS polarization of the sphere as induced by $\underline{\boldsymbol{E}}_{ext}$, V is the detection zone's volume, and V_{cell} is the sphere's volume [Jar09].

Equation (4-3) can be re-arranged so that the change in total MEA capacitance ΔC_{MEA} induced by the inserted sphere is proportional to the integral over V_{cell} [Jar09]:

$$W_{elecf} - W_{elec0} = \frac{1}{2}\mathrm{Re}\{\textstyle\int_{V_{cell}} \underline{\boldsymbol{E}}_{ext} \bullet \underline{\boldsymbol{P}}^{*}{}_{cell}\, dV\}$$

$$\frac{1}{2}(C_{MEAf} - C_{MEA0})\, \phi_{RF}{}^{2} = \frac{1}{2}\mathrm{Re}\{\textstyle\int_{V_{cell}} \underline{\boldsymbol{E}}_{ext} \bullet \underline{\boldsymbol{P}}^{*}{}_{cell}\, dV\}$$

$$\therefore \quad \Delta C_{MEA} = C_{MEAf} - C_{MEA0}$$

$$= \frac{1}{\phi_{RF}^{2}}\mathrm{Re}\{\textstyle\int_{V_{cell}} \underline{\boldsymbol{E}}_{ext} \bullet \underline{\boldsymbol{P}}^{*}{}_{cell}\, dV\} \qquad (4\text{-}4)$$

The sphere polarization $\underline{\boldsymbol{P}}_{cell}$ can be written as [Jar09]:

$$\underline{\boldsymbol{P}}_{cell} = (\underline{\varepsilon}_{cell} - \underline{\varepsilon}_{med})\, \underline{\boldsymbol{E}}_{cell} \qquad (4\text{-}5)$$

where $\underline{\boldsymbol{E}}_{cell}$ is the RMS phasor of the electric field induced within the sphere by the separation of electrical charges, $\underline{\varepsilon}_{med} = \varepsilon'_{med} - j\, \varepsilon''_{med} - j\,(\sigma_{med}/\omega)$ is the complex permittivity of the medium, and $\underline{\varepsilon}_{cell} = \varepsilon'_{cell} - j\, \varepsilon''_{cell} - j\,(\sigma_{cell}/\omega)$ is the complex permittivity of the sphere [Jar09]. If I assume that a is sufficiently small for the non-uniformity of $\underline{\boldsymbol{E}}_{ext}$ to be insignificant over V_{cell}, then $\underline{\boldsymbol{E}}_{cell}$ follows from Equations (3-19b) and (3-21b) as

$$\underline{E}_{cell} = \left[\frac{3\underline{\varepsilon}_{med}}{\underline{\varepsilon}_{cell} + 2\underline{\varepsilon}_{med}} \right] \underline{E}_{ext} \qquad (4\text{-}6)$$

ΔC_{MEA} then follows by substituting Equations (4-5) and (4-6) into Equation (4-4):

$$\Delta C_{MEA} = \frac{1}{\phi_{RF}^2} \, \text{Re}\{ \int_{V_{cell}} \underline{E}_{ext} \bullet \underline{P}^*_{cell} \, dV \}$$

$$= \frac{1}{\phi_{RF}^2} \, \text{Re}\left\{ \left[\left(\underline{\varepsilon}_{cell} - \underline{\varepsilon}_{med} \right) \left(\frac{3\underline{\varepsilon}_{med}}{\underline{\varepsilon}_{cell} + 2\underline{\varepsilon}_{med}} \right) \right]^* \underline{E}_{ext} \, \underline{E}^*_{ext} V_{cell} \right\}$$

$$= \frac{3\underline{E}_{ext}^2}{\phi_{RF}^2} \left(\frac{4\pi}{3} a^3 \right) \text{Re}\left\{ \left[\underline{\varepsilon}_{med} \left(\frac{\underline{\varepsilon}_{cell} - \underline{\varepsilon}_{med}}{\underline{\varepsilon}_{cell} + 2\underline{\varepsilon}_{med}} \right) \right]^* \right\}$$

$$= \frac{4\pi \, a^3 \, \text{Re}\{\underline{\varepsilon}_{med} \underline{K}\} E_{ext}^2}{\phi_{RF}^2} \qquad (4\text{-}7)$$

where $\underline{K}$ is the complex Clausius-Mossotti factor, given by [Jon95]:

$$\underline{K} = \frac{\underline{\varepsilon}_{cell} - \underline{\varepsilon}_{med}}{\underline{\varepsilon}_{cell} + 2\underline{\varepsilon}_{med}} \qquad (4\text{-}8)$$

In this work, the applied ϕ_{RF} shall oscillate in the neighbourhood of 1.478 GHz. Pethig indicates that the intrinsic dielectric loss of deionized water (DI H$_2$O), ε''_{med}, is at most $5\varepsilon_0$ in the vicinity of 1.478 GHz [Peth79]. ε''_{med} is assumed to be the same for the diluted methylene blue solution as for DI H$_2$O. The intrinsic dielectric loss of the polystyrene microspheres (PSS), ε''_{cell}, is at most $0.001\varepsilon_0$ in the vicinity of 1.478 GHz [Agil09, Wiki09, Poly09]. Unfortunately, data regarding the intrinsic dielectric loss of *Saccharomyces cerevisiae* cells, ε''_{cell}, is unavailable (and is consequently assumed to be negligible). As such, both ε''_{med} and ε''_{cell} are neglected throughout the entirety of this work. Moreover, at GHz frequencies, the real absolute permittivities dominate the conduction losses, $\varepsilon'_{med} \gg \sigma_{med}/\omega$ and $\varepsilon'_{cell} \gg \sigma_{cell}/\omega$. As such, Equation (4-8) can be approximated as [Jar09]:

$$\Delta C_{MEA} \approx \frac{4\pi\varepsilon'_{med}K_{\infty}a^3\underline{E}^2_{ext}}{\phi^2_{RF}} \tag{4-9}$$

where K_{∞} is the $\omega \to \infty$ limit of $\mathrm{Re}\{\underline{K}\}$, given by

$$K_{\infty} = \lim_{\omega \to \infty}\{\mathrm{Re}\{\underline{K}\}\} \approx \frac{\varepsilon'_{cell} - \varepsilon'_{med}}{\varepsilon'_{cell} + 2\varepsilon'_{med}} \tag{4-10}$$

Equation (4-9) demonstrates that a spherical cell, with a fixed radius a and fixed real absolute permittivity ε'_{cell}, shall produce a ΔC_{MEA} signature proportional to E_{ext}^2 / ϕ_{RF}^2 as encountered along its trajectory [Jar09].

Equation (4-9) is valid only for the special case of a homogeneous lossy dielectric sphere suspended in a homogeneous isotropic lossy dielectric medium and subjected to a non-uniform time-harmonic external electric field $\boldsymbol{E_{ext}}$. As the PSS used in this work are essentially homogeneous lossy dielectric spheres, Equation (4-9) can be directly applied to compute the scaling factor required to convert the E_{ext}^2 / ϕ_{RF}^2 encountered along the PSS trajectory to the associated ΔC_{MEA} signature (as is done in Chapter 5). However, the *S. cerevisiae* cells used in this work posses a highly heterogeneous internal structure, and thus must be represented as equivalent homogeneous lossy dielectric spheres before Equation (4-9) can be applied to compute the scaling factor required to convert the E_{ext}^2 / ϕ_{RF}^2 encountered along the cellular trajectory to the associated ΔC_{MEA} signature (as is done in Sections 7.3-7.4).

4.2   Simulated Microelectrode Array Electric Fields

COMSOL® Multiphysics was used to construct a two dimensional (2-D) finite element model of the detection zone, presented as Figure 4-1, as defined by the microfluidic cross-channel and the MEA. The microfluidic cross-channel was modeled as a 40 μm deep and a 1 mm long rectangular subdomain. To model the diluted methylene blue solution, the cross-channel subdomain was filled with a real absolute permittivity ε'_{med} of $78\varepsilon_0$ [Wang93a] and conductivity σ_{med} of 33.4 μS/cm (as measured with a Thermo Scientific Orion 3 Star portable conductivity meter with an Orion

01300SMD Conductivity Cell probe). The MEA was placed at the bottom of the cross-channel subdomain, centered along its length. Each microelectrode was infinitesimally thin, 25 µm wide, and given a 25 µm edge-to-edge separation. The innermost microelectrode was grounded, and a 1 V_p 1.5 GHz time-harmonic electric potential ϕ_{RF} was applied to the outer microelectrodes. As the remaining top and bottom subdomain boundaries represent the interface between the cross-channel interior and the electrically insulating Borofloat glass wafers, the electrical insulation Neumann boundary condition was assumed along these boundaries. Electrical insulation boundary conditions were also assumed along the leftmost and rightmost subdomain boundaries, where the electric field E_{ext} generated by the MEA is expected to be negligible as a consequence of the separation between these boundaries and the MEA.
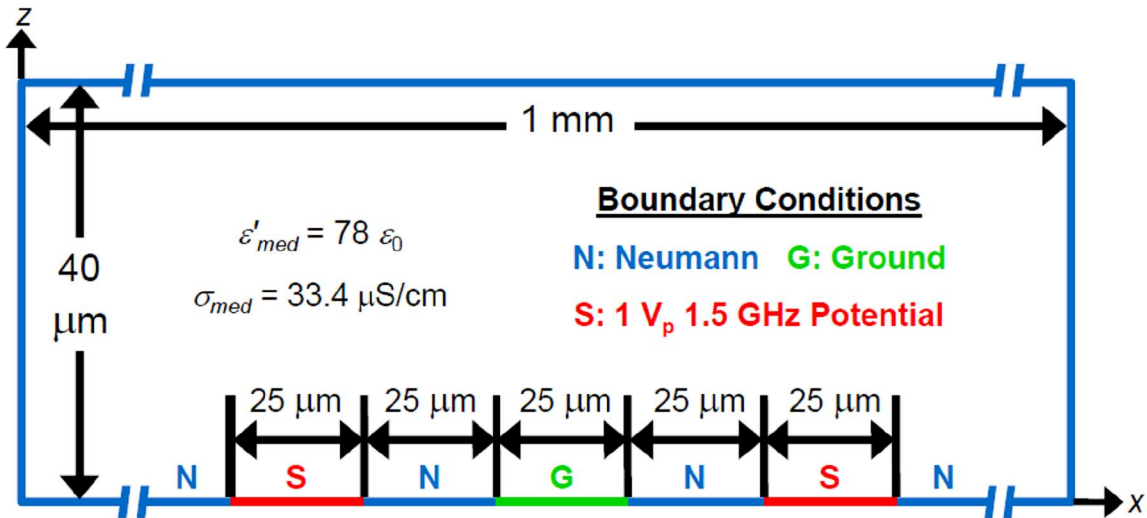
Figure 4-1: *Geometry of detection zone as simulated within COMSOL® Multiphysics.*

The Electric Currents module was then used to solve the complex form of Laplace's Equation, $\nabla \bullet (\underline{\varepsilon} \nabla \phi) = 0$, and subsequently compute the spatially non-uniform peak electric field $E_{ext} = -\nabla \phi$. As E_{ext} was generated by a simulated 1 V_p 1.5 GHz ϕ_{RF}, the solved E_{ext} represents E_{ext} as normalized to ϕ_{RF}. Figure 4-2 presents plots of E_{ext}^2 / ϕ_{RF}^2 along various constant elevation h_{cell} trajectories parallel with the bottom of Figure 4-1. The largest plot within Figure 4-2 corresponds to $h_{cell} = 4.0$ µm, whereas as the second largest plot corresponds to $h_{cell} = 5.0$ µm, and so on until the smallest plot

corresponds to h_{cell} = 40.0 μm. Depending upon the value of h_{cell}, the maximum of the E_{ext}^2 / ϕ_{RF}^2 along a constant elevation h_{cell} trajectory can vary from 5×10^7 to 1.4×10^9 m^{-2}.
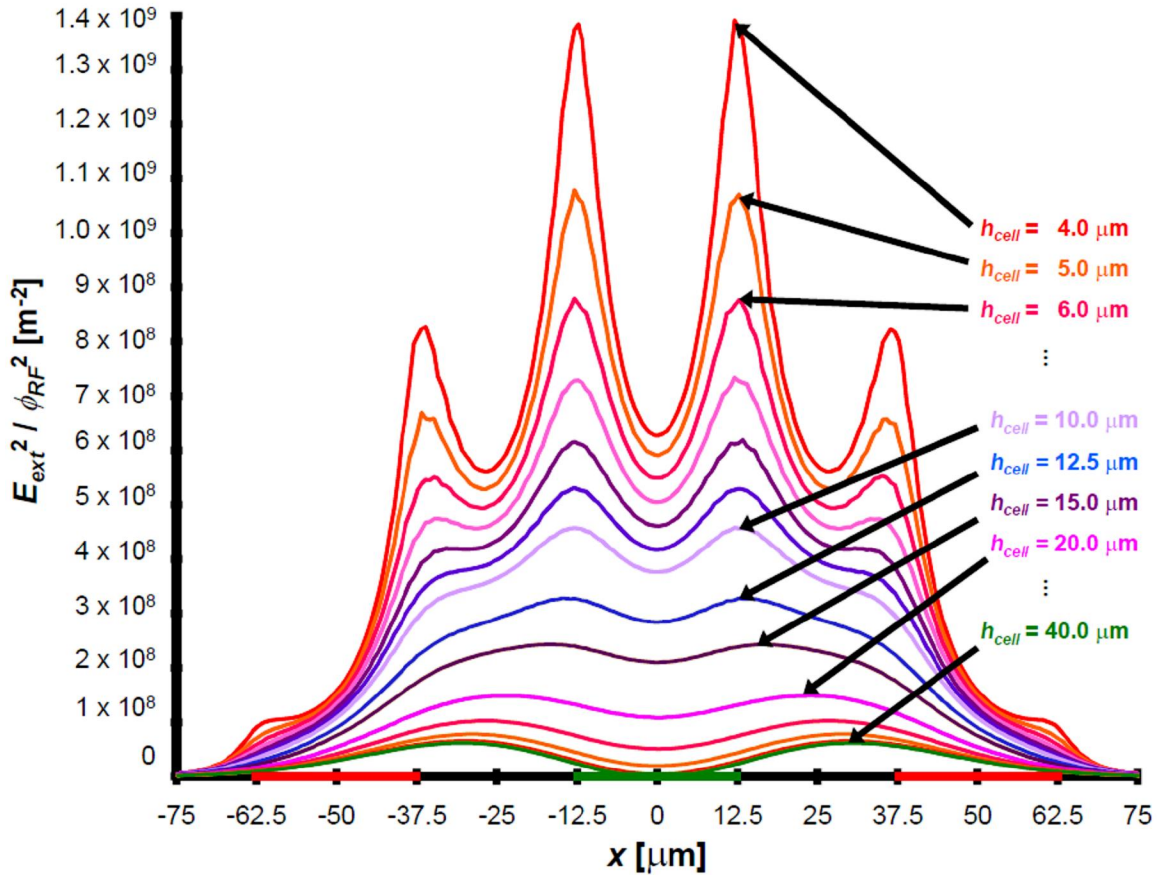
Figure 4-2: _E_{ext}^2 / ϕ_{RF}^2 along various constant elevation trajectories parallel to the bottom of the cross-channel subdomain._

As the MEA is much smaller than the simulated 1.5 GHz wavelength of ϕ_{RF}, Figure 4-2 is a good approximation of the peak E_{ext}^2 / ϕ_{RF}^2 produced by both the 1.478 GHz sensing potential ϕ_{RF} and the 10-1000 kHz dielectrophoretic (DEP) actuation potential ϕ_{DEP} in practice (with the substitution ϕ_{RF} ϕ_{DEP} employed in the latter case).

Figure 4-2 shows that: (1) at a given lateral position, E_{ext}^2 / ϕ_{RF}^2 decreases as h_{cell} increases; (2) near the MEA, local maxima in E_{ext}^2 / ϕ_{RF}^2 correspond to microelectrode edges; (3) the maxima at the outermost edges are much smaller than the other maxima; (4) near the MEA, local minima in E_{ext}^2 / ϕ_{RF}^2 correspond to the microelectrode and inter-microelectrode gap centers; (5) as h_{cell} increases, the maxima bordering each gap collapse

into maxima at each gap's center; (6) as h_{cell} increases, the maxima at the outermost microelectrode edges vanish; and (7) the location of the minima at the gap centers are independent of h_{cell}. A negative DEP (nDEP) force, $\boldsymbol{F_{DEP}}$, repels cells from the E_{ext}^2 / ϕ_{DEP}^2 maxima and attracts cells towards the E_{ext}^2 / ϕ_{DEP}^2 minima [Jon95]. Conversely, a positive DEP (pDEP) force, $\boldsymbol{F_{DEP}}$, attracts cells toward the E_{ext}^2 / ϕ_{DEP}^2 maxima and repels cells from the E_{ext}^2 / ϕ_{DEP}^2 minima [Jon95].

4.3   Simulated Bioparticle Trajectories

Once the peak $\boldsymbol{E_{ext}}$ produced by the 1 V_p 1.5 GHz ϕ_{RF} has been solved, the Particle Tracing post-processing module can then be used to simulate the trajectory of a spherical particle as it passes through the detection zone. Within these simulations, the particle is treated as a point particle (corresponding to the particle's center) subjected to user-specified forces directed along both Cartesian axes.

The particle is initially placed 125 μm to the left of the MEA center and given an initial velocity v_{cell} approximated by the fluid velocity v_{med}. As is typical within microfluidics, a Poiseuille v_{med} profile is assumed:

$$v_{med} \approx 6 < v_{med} > (h_{cell} / d_{Ch}) [1 - (h_{cell} / d_{Ch})] \qquad (4\text{-}11)$$

where $< v_{med} >$ is the mean v_{med}, h_{cell} is the particle's elevation, and d_{Ch} is the channel's 40 μm depth [Hua97,Whi03]. $< v_{med} >$ and the initial elevation h_{cell0} are matched to experimental observations.

A mass is also associated with the simulated point particle, given as

$$m_{cell} = (4 \pi / 3) a^3 \rho_{cell} \qquad (4\text{-}12)$$

where ρ_{cell} is the density of the particle (1050 kg m^{-3} for both PSS and *S. cerevisiae* [Poly09, Raf07]).

The first specified force is the DEP force $\boldsymbol{F_{DEP}}$, as given in Equation (3-31). To computed $\boldsymbol{F_{DEP}}$ using the simulated E_{ext}^2 / ϕ_{RF}^2 in conjunction with Equation (3-31), the simulated E_{ext}^2 / ϕ_{RF}^2 must be scaled by half the peak magnitude of ϕ_{DEP} to obtain the

RMS E_{ext}^2 produced by ϕ_{DEP}. The full DEP spectrum can be simulated by varying the specified value for Re{$\underline{K}$}. $\boldsymbol{F_{DEP}}$ is specified along both Cartesian axes.

The second specified force is the viscous fluid drag force $\boldsymbol{F_{drag}}$, given by Stoke's law as

$$\boldsymbol{F_{drag}} \; \acute{e} \; -6 \, \pi \, \eta_{med} \, a \, (\, v_{cell} - v_{med} \,) \qquad\qquad (4\text{-}13)$$

where η_{med} is the fluid medium's viscosity (known to be 1 mPa s for DI H_2O [Res02] and assumed to be 1 mPa s for the diluted methylene blue solution) and a is the particle's effective radius [Hua97]. $\boldsymbol{F_{drag}}$ is specified along both Cartesian axes.

$\boldsymbol{F_{DEP}}$ and $\boldsymbol{F_{drag}}$ are the most significant forces acting on passing particles, and are the only two forces considered within this particle tracing simulation. At the length scale of micrometers, Brownian motion is negligible [Hug03]. More significant, in practice, are the gravitational and hydrodynamic lift forces, $\boldsymbol{F_{grav}}$ and $\boldsymbol{F_{lift}}$ [Hua97]. $\boldsymbol{F_{grav}}$ acts to pull particles towards the bottom of the microfluidic cross-channel. $\boldsymbol{F_{lift}}$ acts to push particles away from the edges of the microfluidic cross-channel. Ideally, both $\boldsymbol{F_{grav}}$ and $\boldsymbol{F_{lift}}$ would be considered within this particle tracing simulation. However, the exact form for $\boldsymbol{F_{lift}}$ to be used in this application is unclear [Hua97, You03]. Although the exact form of $\boldsymbol{F_{grav}}$ is clear [Hua97], $\boldsymbol{F_{grav}}$ was also excluded from this particle tracing simulation. The exclusion of $\boldsymbol{F_{grav}}$ is sensible as: (1) $\boldsymbol{F_{grav}}$ and $\boldsymbol{F_{lift}}$ are opposing near the bottom of the cross-channel; and (2) ΔC_{MEA} signatures are relatively weak near the top of the cross-channel, and particles are thus rarely detected when h_{cell} is exceedingly high.

At each time-step, the particle's position $\boldsymbol{r_{cell}} = x_{cell} \, \boldsymbol{a_x} + h_{cell} \, \boldsymbol{a_y}$ and velocity v_{cell} are re-calculated via

$$m_{cell} \, (d\,v_{cell}/dt) = \boldsymbol{F_{DEP}}(\boldsymbol{r_{cell}}, v_{cell}, t) + \boldsymbol{F_{grav}}(\boldsymbol{r_{cell}}, v_{cell}, t) \qquad\qquad (4\text{-}14)$$

The short effective time response of $\boldsymbol{F_{drag}}$ necessitates that time steps no larger than 5 μs be used during the simulation, to ensure stability. The simulation runs until either 200 000 time steps have occurred or the particle contacts a subdomain boundary.

Chapter 5

The Dielectrophoretic Actuation & Capacitive Detection of Polystyrene Microspheres in This Work

Impedance based cytometers commonly use polystyrene microspheres (PSS) as model biological particles (bioparticles) [Che04, Wood07]; capitalizing on their well defined spherical shape, diameter, and homogeneous electrical parameters. Moreover, PSS can be utilized as a coated base adhering to other bioparticles via biochemical reactions (such that within a biotin-streptavidin complex [Dia91] and protein-ligand pair complexes [Pie06]) for various bioassays.

In this work, the capacitive cytometer shall be calibrated using the experimental sense signal, S, signatures generated by unactuated 5.68 ± 0.305 μm diameter PSS (from Polysciences, Inc. [Poly09]) suspended in deionized water (DI H_2O). This calibration, which estimates the capacitive cytometer's overall sensitivity dS/dC_{MEA} and resolution $|\delta C_{MEA}|$, is presented in Section 6.2.

Following the capacitive cytometer calibration, actuated PSS suspended in a diluted methylene blue solution shall be studied (to use the same fluid in which the *Saccharomyces cerevisiae* cells shall be suspended in Chapters 7-9). The initial PSS elevation, h_{cell0}, shall be estimated by comparing the measured microelectrode array (MEA) capacitance perturbation, ΔC_{MEA}, signatures to the simulated external electric field squared magnitude to MEA potential squared magnitude, E_{ext}^2 / ϕ_{RF}^2, plots. The initial and final lateral PSS velocities, v_{cellx0} and v_{cellxf}, shall be estimated from the optical assay video. A finite element simulation of the PSS trajectory, as subjected to the dielectrophoretic (DEP) force $\boldsymbol{F_{DEP}}$ and the viscous fluid drag force $\boldsymbol{F_{drag}}$, shall be compared to the experimentally observed PSS trajectories to verify the experimentally observed DEP spectrum. This analysis is presented in Section 6.3.

The PSS are readily modeled as homogeneous lossy dielectric spheres with radius $a = 2.84$ μm [Poly09], real absolute permittivity $\varepsilon'_{cell} = 2.5\varepsilon_0$ [Poly09], and conductivity $\sigma_{cell} = 2$ μS/cm [Che04]. The intrinsic dielectric loss of PSS, ε''_{cell}, is at most $0.001\varepsilon_0$ in the vicinity of 1.478 GHz and is consequently neglected [Agil09, Wiki09, Poly09].

The DI H_2O is modeled as a homogeneous isotropic lossy dielectric medium with real absolute permittivity $\varepsilon'_{med} = 78\varepsilon_0$ [Wang93a] and conductivity $\sigma_{med} = 18$ µS/cm (as measured with a Thermo Scientific Orion 3 Star portable conductivity meter with an Orion 01300SMD Conductivity Cell probe). Similarly, the diluted methylene blue solution is modeled as a homogeneous isotropic lossy dielectric medium with $\varepsilon'_{med} = 78\varepsilon_0$ (assumed to be the same as DI H_2O) and $\sigma_{med} = 33.4$ µS/cm (as measured with the aforementioned conductivity meter). Notably, the ε' of DI H_2O exhibits a relaxation centered about 10-20 GHz, in which the static $78\varepsilon_0$ drops to approximately $1.155\varepsilon_0$ [Peth79]. As the largest frequency applied to the MEA is less than 2 GHz, ε'_{med} can be safely assumed to be a constant $78\varepsilon_0$ throughout the entirety of this work. Moreover, Pethig indicates that the ε'' of DI H_2O is at most $5\varepsilon_0$ in the vicinity of 1.478 GHz [Peth79]. As the fluid medium's intrinsic dielectric loss ε''_{med} is assumed to be the same for the diluted methylene blue solution as for DI H_2O, ε''_{med} is neglected throughout this work.

The MATLAB® program of Appendix C.1 uses the aforementioned model parameters with Equation (3-32) to plot the DEP spectrum of PSS as suspended in each fluid. These DEP spectra plots are presented as Figure 5-1.
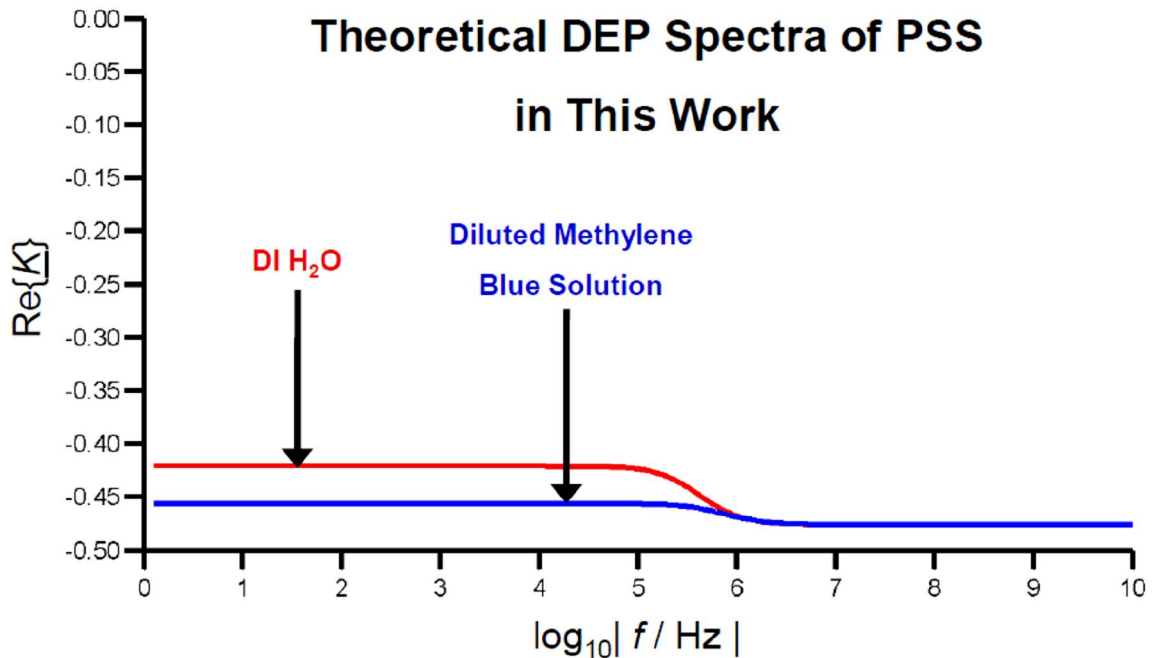
Figure 5-1: *Theoretical DEP spectra of PSS as used in this work.*

Equations (3-33a) through (3-35) predict that: (1) the DEP spectrum of PSS suspended in DI H_2O drops from a $\omega \rightarrow 0$ limit of K_0 é -0.42 to a $\omega \rightarrow \infty$ limit of K_∞ é -0.48 via a Maxwell-Wagner interfacial relaxation centered at $f_{MW} = 1/(2\pi\tau_{MW})$ é 430.95 kHz; and (2) the DEP spectrum of PSS suspended in the diluted methylene blue solution drops from K_0 é -0.46 to K_∞ é -0.48 via a Maxwell-Wagner interfacial relaxation centered at $f_{MW} = 1/(2\pi\tau_{MW})$ é 780.29 kHz. These predictions are clearly visible within Figure 5-1.

Assuming that $\varepsilon'_{med} = 78\varepsilon_0$, $a = 2.84$ µm, and $K_\infty = -0.48$: Equation (4-9) predicts a -9.54 x 10^{-26} F m^2 scaling factor for converting the 5×10^7 to 1.4×10^9 m^{-2} E_{ext}^2 / ϕ_{RF}^2 profiles of Figure 4-2 into the corresponding -5 to -134 aF MEA capacitance perturbation ΔC_{MEA} signatures induced by PSS as used in this work.

Chapter 6

Analysis of a Homogeneous
Polystyrene Microsphere Population

6.1   Polystyrene Microsphere Sample Preparation

In Section 6.2, the capacitive cytometer shall be calibrated using the experimental sense signal, S, signatures generated by unactuated 5.68 ± 0.305 μm diameter Polysciences, Inc. [Poly09] polystyrene microspheres (PSS) suspended in deionized water (DI H_2O).   As discussed in Chapter 5, the PSS are readily modeled as homogeneous lossy dielectric spheres with radius $a = 2.84$ μm [Poly09], real absolute permittivity $\varepsilon'_{cell} = 2.5\varepsilon_0$ [Poly09], negligible intrinsic dielectric loss ε''_{cell} [Agil09, Wiki09, Poly09], and conductivity $\sigma_{cell} = 2$ μS/cm [Che04].   As is also discussed in Chapter 5, the DI H_2O is modeled as a homogeneous isotropic lossy dielectric medium with $\varepsilon'_{med} = 78\varepsilon_0$ [Wang93a], negligible ε''_{med} [Peth79], and $\sigma_{med} = 18$ μS/cm (as measured with a Thermo Scientific Orion 3 Star portable conductivity meter with an Orion 01300SMD Conductivity Cell probe).

In Section 6.3, actuated PSS suspended in a diluted methylene blue solution are studied (to use the same fluid in which *Saccharomyces cerevisiae* cells shall be suspended in Chapters 7-9).   To prepare the solution: (1) 10 mg of methylene blue trihydrate ($C_{16}H_{18}ClN_3S \bullet 3H_2O$) was stirred into 10 mL of DI H_2O; (2) the solution was filtered and further diluted with DI H_2O, yielding a total 100 mL volume; (3) 5 mg of sodium citrate dihydrate ($Na_3C_6H_5O_7 \bullet 2H_2O$) was mixed into this solution; and (4) this solution was further diluted with 300 mL of DI H_2O. The final solution's conductivity σ_{med} is 33.4 μS/cm (as measured with the aforementioned conductivity meter). The real absolute permittivity of the solution is assumed to be that of DI H_2O, $\varepsilon'_{med} = 78\varepsilon_0$. The intrinsic dielectric loss of the solution, ε''_{med}, is also assumed to be that of DI H_2O and is neglected.

6.2   Capacitive Cytometer Calibration Using Unactuated Polystyrene Microspheres

Figure 6-1 presents the experimental S signature of an unactuated PSS suspended in DI H_2O (measured using a 3 ms lock-in amplifier (LIA) time constant with a 12 dB/octave roll off). By comparing the shape of Figure 6-1 to the simulated external electric field squared magnitude to squared microelectrode array (MEA) potential, E_{ext}^2 / ϕ_{MEA}^2, plots of Figure 4-2: the elevation, h_{cell}, of the detected PSS was estimated as 6±1 µm. Using the -9.54 x 10^{-26} F m^2 scaling factor computed in Chapter 5, the h_{cell} = 6 µm plot of Figure 4-2 was converted into the theoretical h_{cell} = 6 µm MEA capacitance perturbation, ΔC_{MEA}, signature. The h_{cell} = 6 µm ΔC_{MEA} signature is -46 aF at the outermost inter-microelectrode gap (the feature most insensitive to h_{cell}), whilst the S signature is -2.64 V at this point. It thus follows that the capacitive cytometer's overall sensitivity dS/dC_{MEA} é 57 mV/aF. The mean-subtracted root mean squared (RMS) background noise voltage V_{RMS} was measured within the 0-1 s window of Figure 6-1 as 51 mV. The capacitive cytometer's resolution $|\delta C_{MEA}|$ thus follows as approximately 900 zF (at this particular LIA setting; as V_{RMS} is not strictly white noise, a zF $/\sqrt{Hz}$ resolution cannot be quoted). This $|\delta C_{MEA}|$ is acceptable when detecting the -2 to -46 aF ΔC_{MEA} induced by *Saccharomyces cerevisiae* cells (as estimated in Section 7.4).
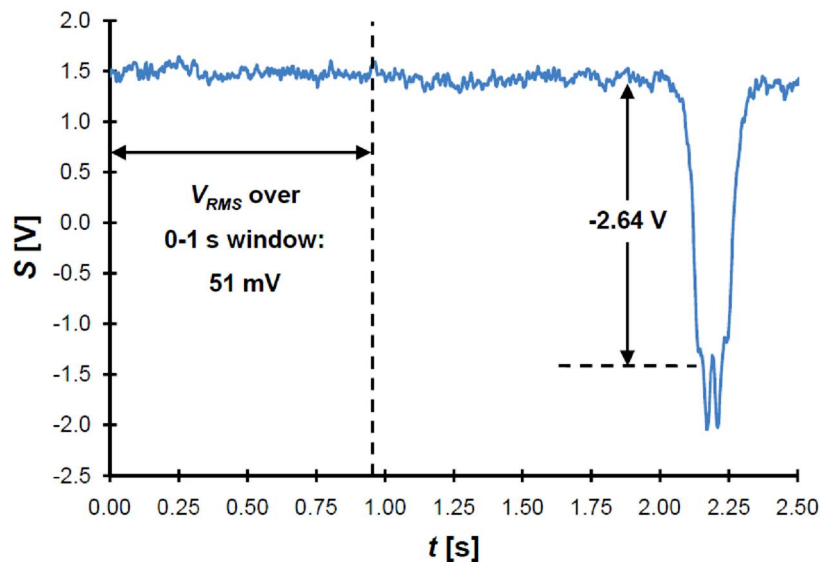
Figure 6-1: *Experimental PSS S signature used for capacitive cytometry calibration.*

6.3   Analysis of Actuated Polystyrene Microspheres

A sample of PSS suspended in the diluted methylene blue solution was prepared as outlined in Section 6.1. This sample was injected into the microflow cytometer, which was simultaneously operated as both an optical assay and a capacitive cytometer. The relative elevation of the syringes was adjusted until the PSS were observed to pass over the MEA with an average cross-over time of approximately 400 ms. The time-harmonic dielectrophoretic (DEP) actuation potential ϕ_{DEP} was set to: 0 V_p and 1 V_p 10 kHz. Approximately 20 minutes of data was gathered at each ϕ_{DEP} setting. Each experimental dataset was then examined to select five S signatures, with no bias as to the initial PSS elevation h_{cell0}, which were visually confirmed to correspond to individual PSS passing over the MEA. Each S signature was converted into a ΔC_{MEA} signature using the capacitive cytometer's dS/dC_{MEA} é 57 mV/aF overall sensitivity (as computed in Section 6.2).

6.3.A   Analysis of $\phi_{DEP} = 0$ V_p Data

Figure 6-2 presents the five experimental ΔC_{MEA} signatures selected from the baseline $\phi_{DEP} = 0$ V_p dataset. Visual inspection of these ΔC_{MEA} signatures suggests that they correspond to low elevation crossings, with h_{cell0} on the order of 4-6 μm (as is consistent with the observation of my colleague Marija Nikolic-Jaric that over 90% of PSS pass over the MEA with a 3-7 μm h_{cell0} [Jar09]).
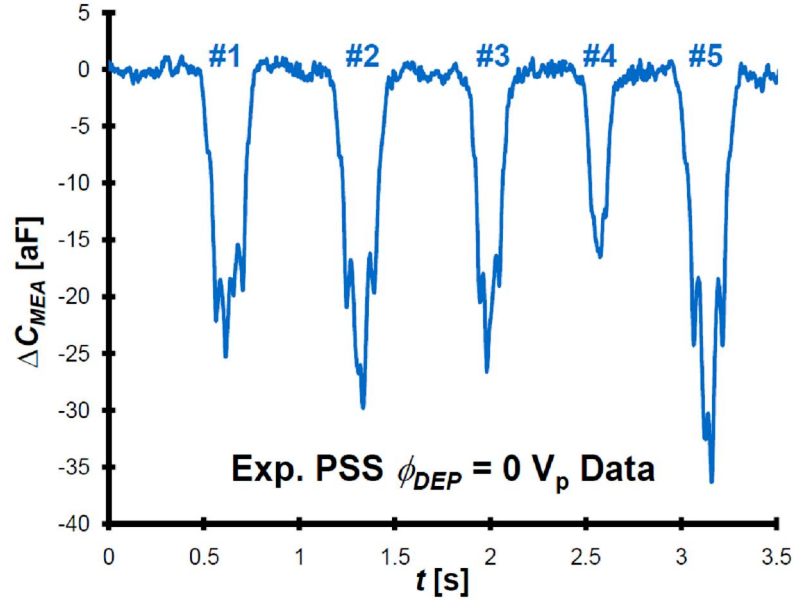
Figure 6-2: *Experimental ΔC_{MEA} signatures induced by passing PSS with $\phi_{DEP} = 0\ V_p$.*

The Open Source Physics program Tracker 2.60 [Track09] was then used to analyze the captured MEA detection zone video corresponding to the ΔC_{MEA} signatures of Figure 6-2. Once a given Audio Video Interleave (AVI) file was loaded: (1) a resize filter, set with a 720 width x 480 height input and a 640 width x 480 height output, was applied to compensate for Digital Video (DV) formatted video spatial distortions; (2) a brightness filter, set with a brightness of -14 and a contrast of 77.0, was applied to facilitate the identification of PSS; and (3) a x2 zoom was employed to improve the accuracy in identifying the center of a given PSS. The known 125 μm distance between the MEAøs outermost edges was used as a dimensional reference. An orthogonal set of coordinate axes were defined such that the *y*-axis runs down the MEAøs center and the *x*-axis is in the general direction of the PSS velocity v_{cell}. The AVI video was scanned until an individual PSS crossing corresponding to an experimental ΔC_{MEA} signature was identified. A point mass track was then employed, in which the spatial position of the said PSSøs center is manually identified in each frame of its recorded passage. Figure 6-3 presents an example of this Tracker analysis.
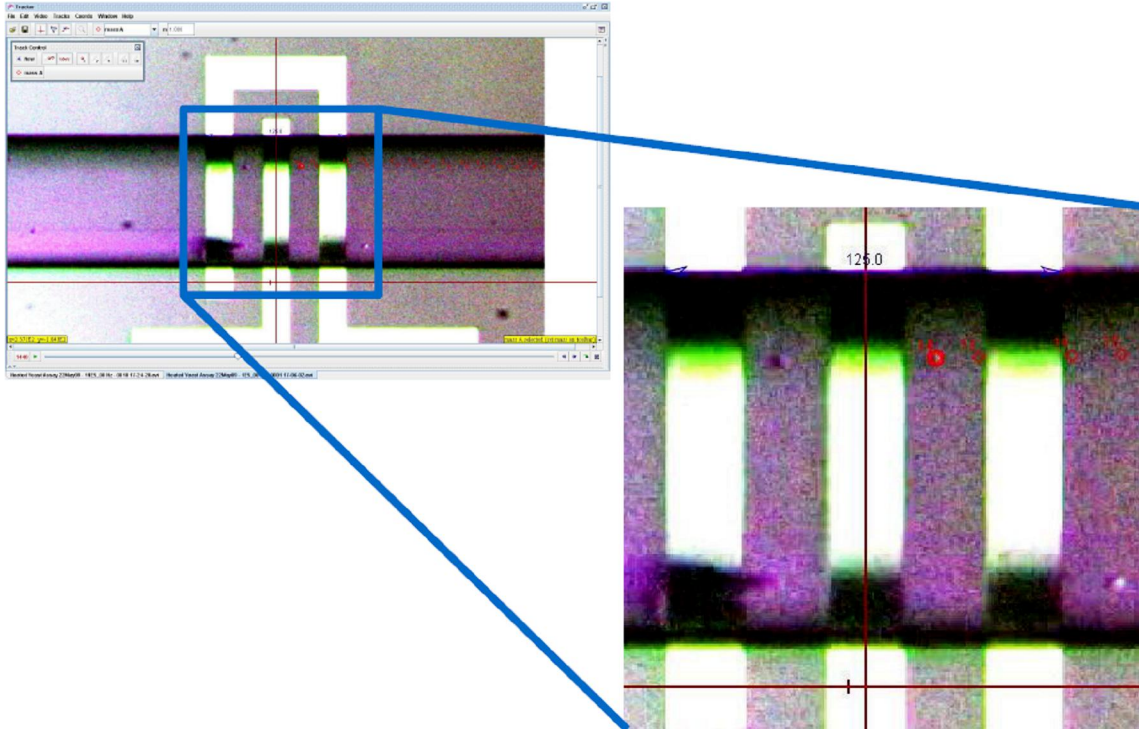
Figure 6-3: *A point mass track is used within Tracker 2.60*
to yield the experimental $x_{cell}(t)$ profile of a passing PSS with $\phi_{DEP} = 0\ V_p$.

The point mass track yields a lateral position x_{cell} versus elapsed time t dataset which can be exported into other programs for further analysis. Specifically, these $x_{cell}(t)$ profiles were exported in Microsoft® Excel 2007 to produce comma separated value (CSV) files which can be read by MATLAB® for further analysis.

The MATLAB® program presented in Appendix D reads in the CSV file containing the $x_{cell}(t)$ profiles corresponding to the ΔC_{MEA} signatures of Figure 6-2. Figure 6-4 presents these five $x_{cell}(t)$ profiles.
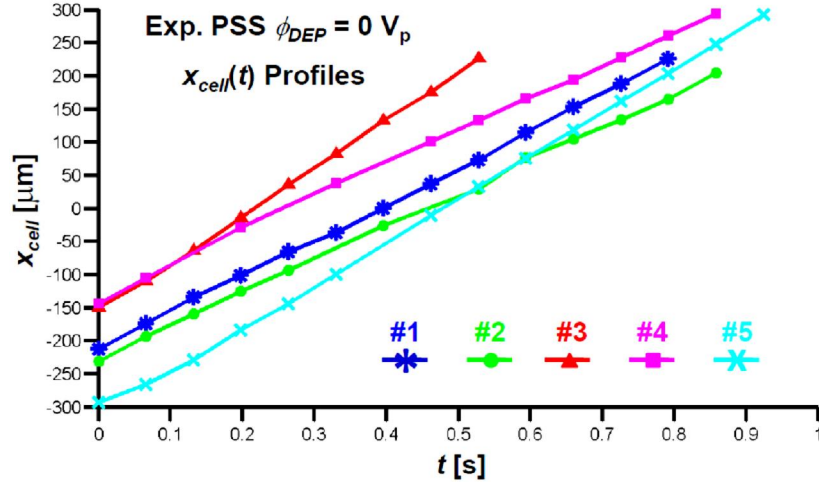
Figure 6-4: *Experimental $x_{cell}(t)$ profiles of passing PSS with $\phi_{DEP} = 0\ V_p$.*

The MATLAB[®] program of Appendix D estimated the lateral PSS velocity $v_{cellx}(t)$ profiles corresponding to the ΔC_{MEA} signatures of Figure 6-2 via the first-order backward finite difference approximation. Linear interpolation was then employed to fit each $v_{cellx}(t)$ profile to a uniformly spaced x_{cell} line spanning ±125 μm in 0.5 μm steps. Figure 6-5 presents these fitted $v_{cellx}(x_{cell})$ profiles.
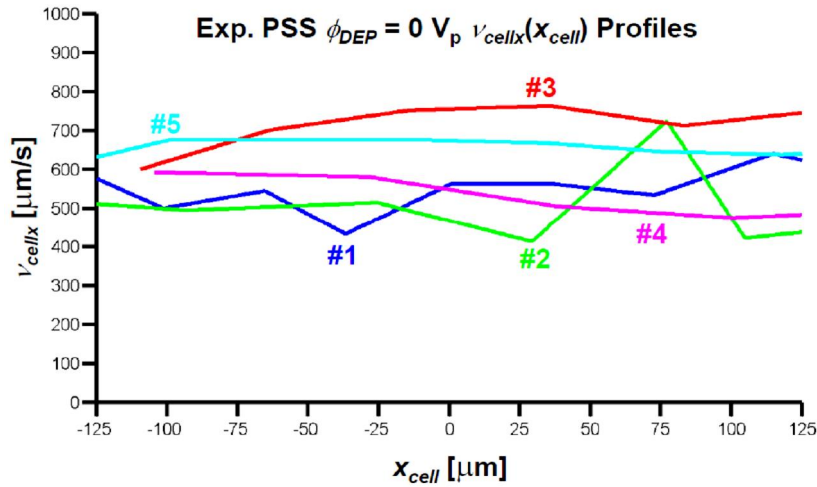
Figure 6-5: *Experimental $v_{cellx}(x_{cell})$ profiles of passing PSS with $\phi_{DEP} = 0\ V_p$.*

The initial v_{cellx}, v_{cellx0}, of each profile was estimated as the mean v_{cellx} within the -125 μm Ö x_{cell} Ö -75 μm interval. The final v_{cellx}, v_{cellxf}, of each profile was estimated as the mean v_{cellx} within the 75 μm Ö x_{cell} Ö 125 μm interval. The relative percent change in

v_{cellx}, $\%\Delta v_{cellx}$, is then estimated using v_{cellx0} and v_{cellxf}. Table 6-1 summarizes the results of this $\%\Delta v_{cellx}$ analysis.

Table 6-1: $\%\Delta v_{cellx}$ Analysis of Experimental v_{cellx} Profiles of Passing PSS with $\phi_{DEP} = 0\ V_p$			
Signature	v_{cellx0} [μm/s]	v_{cellxf} [μm/s]	$\%\Delta v_{cellx}$
1	526.92	598.10	13.5
2	500.37	521.34	4.2
3	637.70	726.44	13.9
4	589.27	479.34	-18.7
5	663.68	640.68	-3.5
$E\{\ \}$	583.59	593.18	1.9
$\sigma\{\ \}$	69.8	97.7	13.6

Table 6-1: $\%\Delta v_{cellx}$ analysis of experimental v_{cellx} profiles of passing PSS with $\phi_{DEP} = 0\ V_p$.

The expectation and standard deviation of each of the v_{cellx} profiles, $E\{v_{cellx}\}$ and $\sigma\{v_{cellx}\}$, was then computed at each point along x_{cell}. Figure 6-6 presents the computed $E\{v_{cellx}\}$ and $E\{v_{cellx}\} \pm \sigma\{v_{cellx}\}$ profiles. Table 6-2 presents the corresponding $\%\Delta v_{cellx}$ analysis of these three statistical profiles.
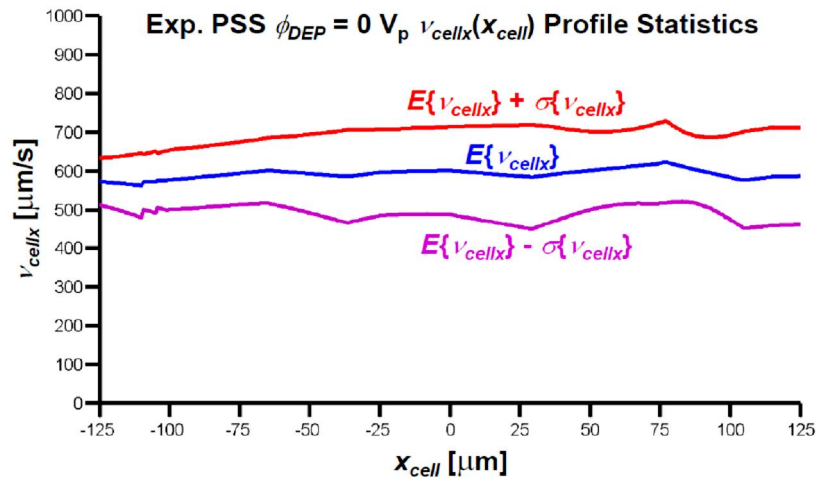
Figure 6-6: Experimental v_{cellx} profile statistics of passing PSS with $\phi_{DEP} = 0\ V_p$.

Table 6-2: %Δ v_{cellx} Analysis of Experimental $E\{v_{cellx}\}$ and $E\{v_{cellx}\} \pm \sigma\{v_{cellx}\}$ Profiles of Passing PSS with $\phi_{DEP} = 0$ V$_p$			
Signature	v_{cellx0} [μm/s]	v_{cellxf} [μm/s]	%Δ v_{cellx}
$E\{v_{cellx}\} + \sigma\{v_{cellx}\}$	652.99	702.88	7.6
$E\{v_{cellx}\}$	577.63	593.18	2.7
$E\{v_{cellx}\} - \sigma\{v_{cellx}\}$	502.28	483.47	-2.9

Table 6-2: *%Δv_{cellx} analysis of experimental $E\{v_{cellx}\}$ and $E\{v_{cellx}\} \pm \sigma\{v_{cellx}\}$ profiles of passing PSS with $\phi_{DEP} = 0$ V$_p$.*

The particle tracing simulation of Section 4.3 then attempted to reproduce the $E\{v_{cellx}\}$ profile of Figure 6-6. In this simulation, the particle was initially placed at (x_{cell0}, h_{cell0}) = (-125, 5) μm and given an initial velocity of v_{cell0} = 583.59 a_x μm/s (referring to Table 6-1). Equation (4-11) was employed to estimate the mean of the parabolic fluid velocity profile as < v_{med} > = 889.28 a_x μm/s. The particle tracing simulation proceeded to compute the trajectory of the PSS as subjected to the vicious fluid drag force, F_{drag}, computed using Equation (4-13). Both the elapsed time t and E_{ext}^2 / ϕ_{RF}^2 were plotted along the computed trajectory, yielding text files containing: (1) x_{cell}, h_{cell}, and t; and (2) x_{cell}, h_{cell}, and E_{ext}^2 / ϕ_{RF}^2.

The MATLAB® program of Appendix D was re-run, with additional code for the analysis of the particle tracing simulation executed. This additional code proceeds to read in the text file containing the simulated $x_{cell}(t)$ profile. The corresponding $v_{cellx}(t)$ profile was computed via the first-order backward finite difference approximation. Linear interpolation was employed to fit this $v_{cellx}(t)$ profile to a uniformly spaced x_{cell} line spanning ±125 μm in 0.5 μm steps. Figure 6-7 presents this fitted $v_{cellx}(x_{cell})$ profile along with the computed $E\{v_{cellx}\}$ and $E\{v_{cellx}\} \pm \sigma\{v_{cellx}\}$ profiles of Figure 6-6. Figure 6-7 Figure 8-9 shows that the simulated v_{cellx} profile reasonably approximates the experimental $E\{v_{cellx}\}$ profile. As this simulation did not include a DEP actuation force F_{DEP}, the simulated h_{cell} and v_{cellx} remained constant.
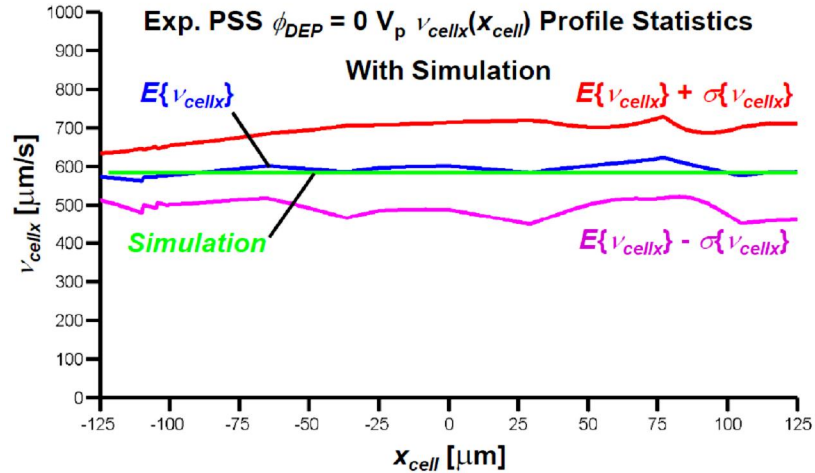
Figure 6-7: *The simulated v_{cellx} profile reasonably approximates the experimental $E\{v_{cellx}\}$ profile of passing PSS with $\phi_{DEP} = 0\ V_p$.*

Figure 6-8 presents the ΔC_{MEA} signature produced by scaling the simulated $E_{ext}^2(t) / \phi_{RF}^2$ profile with the -9.54 x 10^{-26} F m² scaling factor computed in Chapter 5. Curiously, Figure 6-8 depicts a significantly larger ΔC_{MEA} signature than those featured in Figure 6-2. However, the similarity in the shape of Figure 6-8 and Figure 6-2 verifies that $h_{cell0} = 5$ µm was a reasonable assumption within the particle tracing simulation.
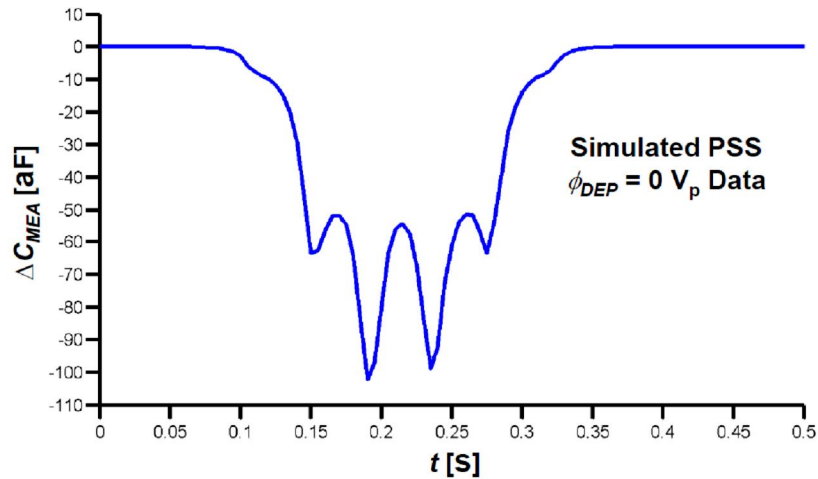
Figure 6-8: *Simulated ΔC_{MEA} signature induced by passing PSS with $\phi_{DEP} = 0\ V_p$.*

6.3.B Analysis of $\phi_{DEP} = 1$ V$_p$ 10 kHz Data

Figure 6-9 presents the five experimental ΔC_{MEA} signatures selected from the $\phi_{DEP} = 1$ V$_p$ 10 kHz dataset. Visual inspection of these ΔC_{MEA} signatures suggests that they correspond to low initial elevation crossings, with h_{cell0} on the order of 4-6 μm.
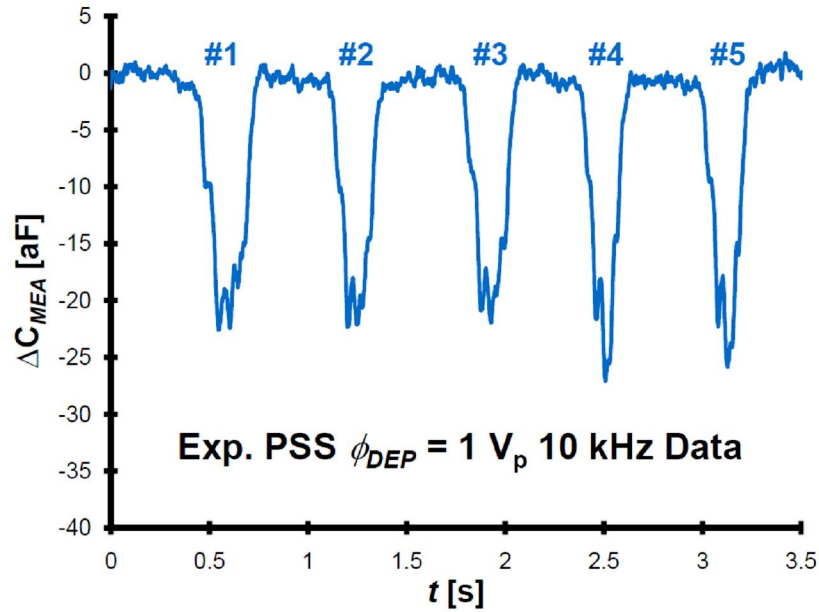
Figure 6-9: *Experimental ΔC_{MEA} signatures induced by passing PSS with $\phi_{DEP} = 1$ V$_p$ 10 kHz.*

The Tracker 2.60 analysis of Section 6.3.A was then repeated to analyze the captured MEA detection zone video corresponding to the ΔC_{MEA} signatures of Figure 6-9, yielding an $x_{cell}(t)$ dataset saved as a CSV file. The MATLAB® program of Appendix D analyzes this CSV file. Figure 6-10 presents these five $x_{cell}(t)$ profiles.
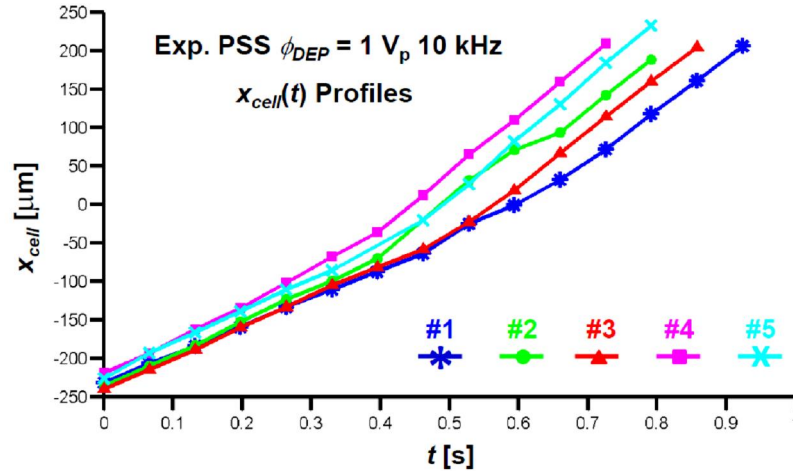
Figure 6-10: _Experimental $x_{cell}(t)$ profiles of passing PSS with $\phi_{DEP} = 1\ V_p$ 10 kHz._

The MATLAB® program of Appendix D estimated the $v_{cellx}(t)$ profiles corresponding to the ΔC_{MEA} signatures of Figure 6-9 via the first-order backward finite difference approximation. Linear interpolation was employed to fit each $v_{cellx}(t)$ profile to a uniformly spaced x_{cell} line spanning ±125 μm in 0.5 μm steps. Figure 6-11 presents these fitted $v_{cellx}(x_{cell})$ profiles.
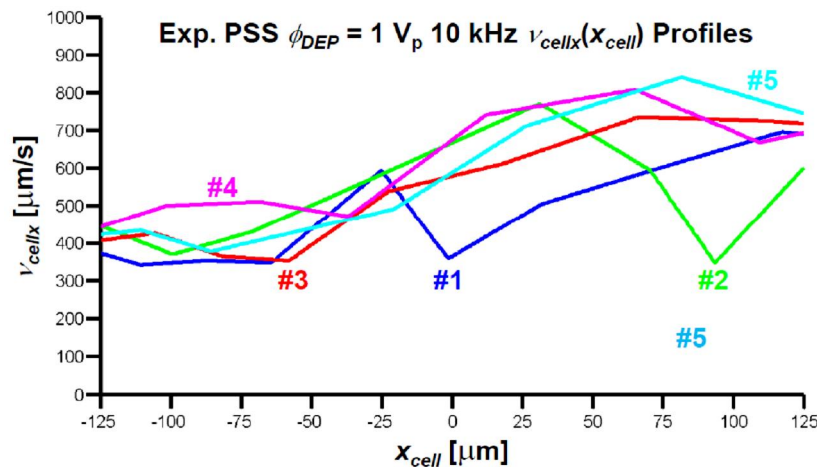
Figure 6-11: _Experimental $v_{cellx}(x_{cell})$ profiles of passing PSS with $\phi_{DEP} = 1\ V_p$ 10 kHz._

The initial v_{cellx}, v_{cellx0}, of each profile was estimated as the mean v_{cellx} within the -125 μm Ö x_{cell} Ö-75 μm interval. The final v_{cellx}, v_{cellxf}, of each profile was estimated as the mean v_{cellx} within the 75 μm Ö x_{cell} Ö125 μm interval. The relative percent change in

v_{cellx}, %Δv_{cellx}, is then estimated using v_{cellx0} and v_{cellxf}. Table 6-3 summarizes the results of this %Δv_{cellx} analysis.

Table 6-3: %Δv_{cellx} Analysis of Experimental v_{cellx} Profiles of Passing PSS with $\phi_{DEP} = 1$ V$_p$ 10 kHz			
Signature	v_{cellx0} [μm/s]	v_{cellxf} [μm/s]	%Δv_{cellx}
1	352.15	656.76	86.5
2	403.34	465.86	15.5
3	399.68	727.17	81.9
4	489.29	710.09	45.1
5	409.09	798.80	95.3
E{ }	*410.71*	*671.73*	*64.9*
σ{ }	*49.45*	*125.8*	*33.6*

Table 6-3: *%Δv_{cellx} analysis of experimental v_{cellx} profiles of passing PSS with $\phi_{DEP} = 1$ V$_p$ 10 kHz.*

The expectation and standard deviation of each of the v_{cellx} profiles, $E\{v_{cellx}\}$ and $\sigma\{v_{cellx}\}$, was then computed at each point along x_{cell}. Figure 6-12 presents the computed $E\{v_{cellx}\}$ and $E\{v_{cellx}\} \pm \sigma\{v_{cellx}\}$ profiles. Table 6-4 presents the corresponding %Δv_{cellx} analysis of these three statistical profiles.
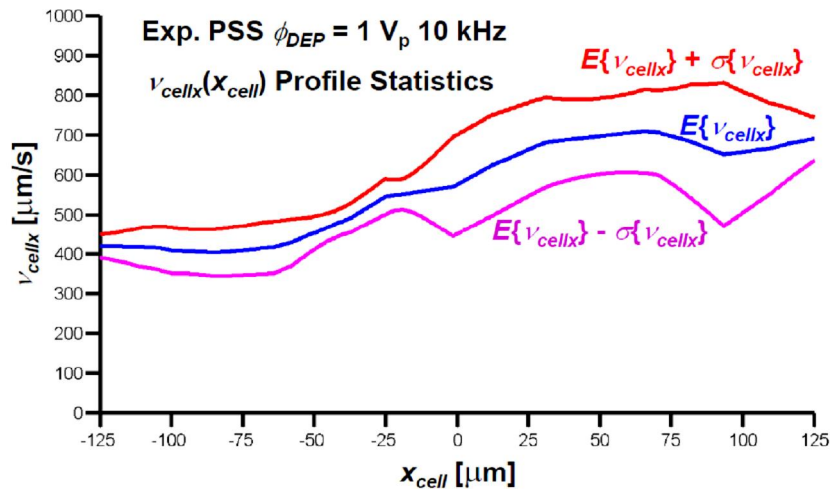
Figure 6-12: *Experimental v_{cellx} profile statistics of passing PSS with $\phi_{DEP} = 1$ V$_p$ 10 kHz.*

Table 6-4: %Δv_{cellx} Analysis of Experimental $E\{v_{cellx}\}$ and $E\{v_{cellx}\} \pm \sigma\{v_{cellx}\}$ Profiles of Passing PSS with $\phi_{DEP} = 1$ V_p 10 kHz			
Signature	v_{cellx0} [μm/s]	v_{cellxf} [μm/s]	%Δv_{cellx}
$E\{v_{cellx}\} + \sigma\{v_{cellx}\}$	462.86	799.49	72.7
$E\{v_{cellx}\}$	410.71	671.73	63.6
$E\{v_{cellx}\} - \sigma\{v_{cellx}\}$	358.56	543.98	40.1

Table 6-4: *%Δv_{cellx} analysis of experimental $E\{v_{cellx}\}$*

and $E\{v_{cellx}\} \pm \sigma\{v_{cellx}\}$ profiles of passing PSS with $\phi_{DEP} = 1$ V_p 10 kHz.

The particle tracing simulation of Section 4.3 then attempted to reproduce the $E\{v_{cellx}\}$ profile of Figure 6-12. In this simulation, the particle was initially placed at (x_{cell0}, h_{cell0}) = (-125, 5) μm and given an initial velocity of $v_{cell0} = 410.71$ a_x μm/s (referring to Table 6-3). Equation (4-11) was employed to estimate $< v_{med} >$ as 625.84 a_x μm/s. The real part of the complex Clausius-Mossotti factor, Re$\{\underline{K}\}$, was assumed to be -0.46 (referring to Figure 5-1). The particle tracing simulation then proceeded to compute the trajectory of the particle as subjected to $\boldsymbol{F_{DEP}}$ and $\boldsymbol{F_{drag}}$, computed using Equations (3-31) and (4-13), respectively. Both the elapsed time t and E_{ext}^2 / ϕ_{RF}^2 were plotted along the computed trajectory, yielding text files containing: (1) x_{cell}, h_{cell}, and t; and (2) x_{cell}, h_{cell}, and E_{ext}^2 / ϕ_{RF}^2.

The MATLAB® program of Appendix D was re-run, with additional code for the analysis of the particle tracing simulation executed. This additional code proceeds to read in the text file containing the simulated $x_{cell}(t)$ profile. The corresponding $v_{cellx}(t)$ profile was computed via the first-order backward finite difference approximation. Linear interpolation was employed to fit this $v_{cellx}(t)$ profile to a uniformly spaced x_{cell} line spanning ±125 μm in 0.5 μm steps. Figure 6-13 presents this fitted $v_{cellx}(x_{cell})$ profile along with the computed $E\{v_{cellx}\}$ and $E\{v_{cellx}\} \pm \sigma\{v_{cellx}\}$ profiles of Figure 6-12. Figure 6-13 Figure 8-9 shows that the simulated v_{cellx} profile reasonably approximates the experimental $E\{v_{cellx}\}$ profile. Table 6-5 presents the corresponding %Δv_{cellx} analysis of this simulated profile.
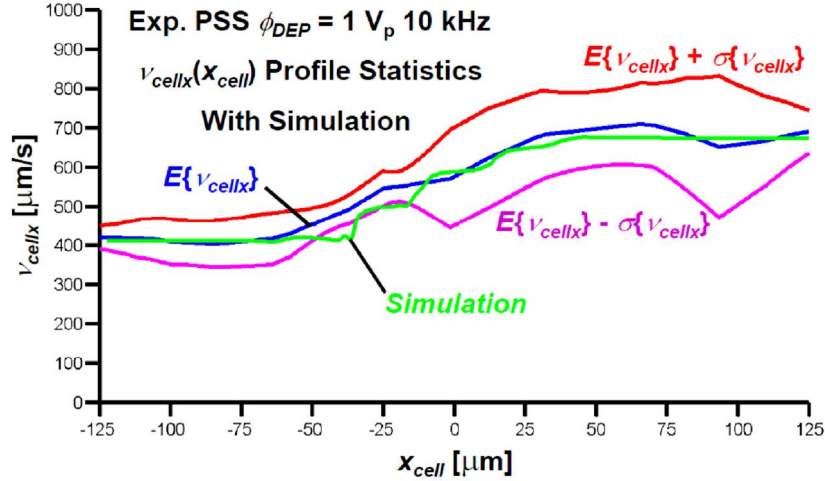
Figure 6-13: *The simulated v_{cellx} profile reasonably approximates the experimental $E\{v_{cellx}\}$ profile of passing PSS with $\phi_{DEP} = 1\ V_p$ 10 kHz.*

Table 6-5: %Δv_{cellx} Analysis of Simulated v_{cellx}		
Profile of Passing PSS with $\phi_{DEP} = 1\ V_p$ 10 kHz		
Signature	v_{cellx0} [μm/s]	v_{cellxf} [μm/s]	%Δv_{cellx}
Simulation	410.67	673.58	64.0

Table 6-5: *%Δv_{cellx} analysis of simulated v_{cellx} profile of passing PSS with $\phi_{DEP} = 1\ V_p$ 10 kHz.*

Figure 6-14 presents the ΔC_{MEA} signature produced by scaling the simulated $E_{ext}^2(t)\ /\ \phi_{RF}^2$ profile with the -9.54 x 10^{-26} F m^2 scaling factor computed in Chapter 5. Curiously, Figure 6-14 depicts a significantly larger ΔC_{MEA} signature than those featured in Figure 6-9. However, the similarity in the shape of Figure 6-14 and Figure 6-9 verifies that $h_{cell0} = 5$ μm was a reasonable assumption within the particle tracing simulation.
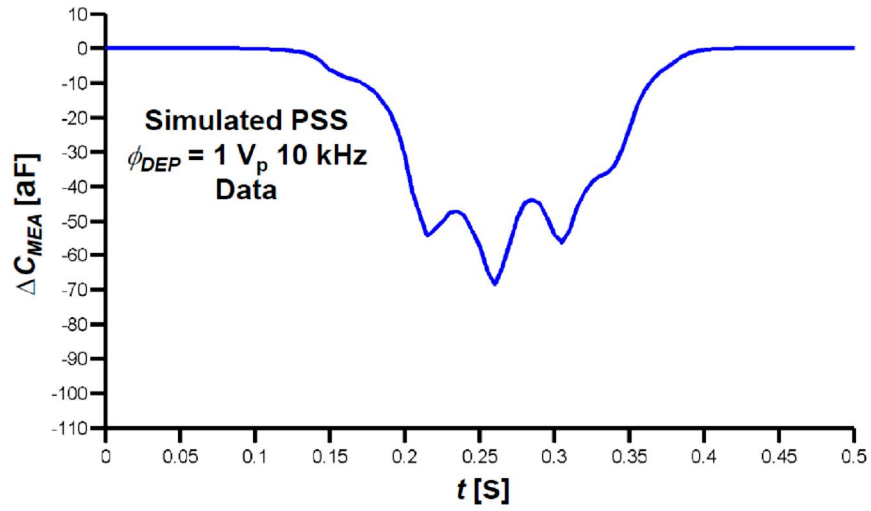
Figure 6-14: *Simulated ΔC$_{MEA}$ signature induced by passing PSS with ϕ$_{DEP}$ = 1 V$_p$ 10 kHz.*

Chapter 7

The Dielectrophoretic Actuation & Capacitive Detection of *Saccharomyces cerevisiae* in This Work

7.1   *Saccharomyces cerevisiae* as the Model Eukaryote

In the 3.5-3.9 billion years since life on Earth originated as prokaryotes, evolution has yielded a grand myriad of cells [Campb02]. Basic cellular mechanism studies have pragmatically focused on a few specific species that serve as representative models [Phil09, Karp05]. In particular, the bacterium *Escherichia coli* (abbr. *E. coli*) posses several ideal properties: (1) procurement and isolation is simple; (2) grow is rapid, with division as frequent as every 20 minutes; (3) plated colonies afford grouping a cell's descendants; (4) mutation is straightforward; and (5) a wide variety of alternative metabolisms are exhibited, including aerobic or anaerobic growth and the ability to self-synthesize metabolites absent from the environment [Phil09, Campb02]. This metabolic flexibility affords the isolation of auxotrophic mutants (unable to synthesize an essential metabolite), facilitating the identification of major metabolic pathway enzymes [Phil09].

All animal, plant, and fungus cells are eukaryotes, containing their deoxyribonucleic acid (DNA) within a membrane-bound nucleus. Many eukaryotes also posses other elaborate intracellular membrane-bound structures absent within other cells. As a bacterium, *E. coli* is profoundly different from a eukaryote. To study eukaryotic specific processes, a eukaryotic model must be selected. Ideally, this model should be closely related, or directly useful, to humans. Among single-celled eukaryotes, fungi are most closely related to animal cells (as proved by ribosomal ribonucleic acid (RNA)) [Phil09]. The fungus *Saccharomyces cerevisiae* (abbr. *S. cerevisiae*), known as baker's, brewer's, or budding yeast, serves as the representative eukaryotic model [Phil09, Karp05]. *S. cerevisiae* was domesticated millennia ago and aerobically acts as the agent releasing CO_2 bubbles to level bread or anaerobically converts sugars into alcohol during fermentation [Campb02, Phil09]. Like *E. coli*, *S. cerevisiae* exhibits a variety of alternative metabolisms and affords auxotrophic mutant isolation [Phil09]. *S. cerevisiae*

also grows remarkably fast for a eukaryote, doubling as frequently as every 90 minutes [Phil09]. *S. cerevisiae* shares many specific metabolic pathways with animal cells, including many absent in *E. coli* [Phil09]. As the complete genomes of two parents are blended and recombined within offspring, *S. cerevisiae* has traditional eukaryotic sex [Phil09]. Moreover, *S. cerevisiae* can grow as a haploid, with one copy of every chromosome, or as a diploid, with copies of every chromosome from both parents [Phil09]. As such, *S. cerevisiae* has been used for the genetic and molecular dissection of eukaryotic-specific behaviours [Phil09].

7.2   Subcellular Structure of *Saccharomyces cerevisiae*

Figure 7-1 presents a cross-sectional scanning electron micrograph (SEM) of a *S. cerevisiae* cell engaged in budding (produced by Dr. O. Mueller and graciously provided by Dr. I. Walther of the Space Biology Group, Swiss Federal Institute of Technology, Zürich, Switzerland) [SACE09]. It is observed that *S. cerevisiae* is roughly ellipsoidal, and is comprised of a complex cytoplasmic interior enclosed by a thin cytoplasmic membrane (cm) and a thicker cell wall (cw). The cell wall is possessed of narrow pores impermeable to molecules with a molecular weight in excess of 4500, but permeable to smaller molecules including inorganic ions, amino acids, and sugars [Asa76]. The cytoplasmic membrane acts as a selectively permeable barrier to these smaller molecules, with porous channels that can be actively opened and closed to maintain the concentrations within the cytoplasmic interior necessary to sustain life [Asa76]. The heterogeneous cytoplasmic interior of *S. cerevisiae* is unquestionably eukaryotic, possessing a nucleus (n) bounded by a nuclear membrane (nm), a vacuole (v) bounded by a vacuole membrane (vm), mitochondria (m), storage granules (sg), and various other organelles.
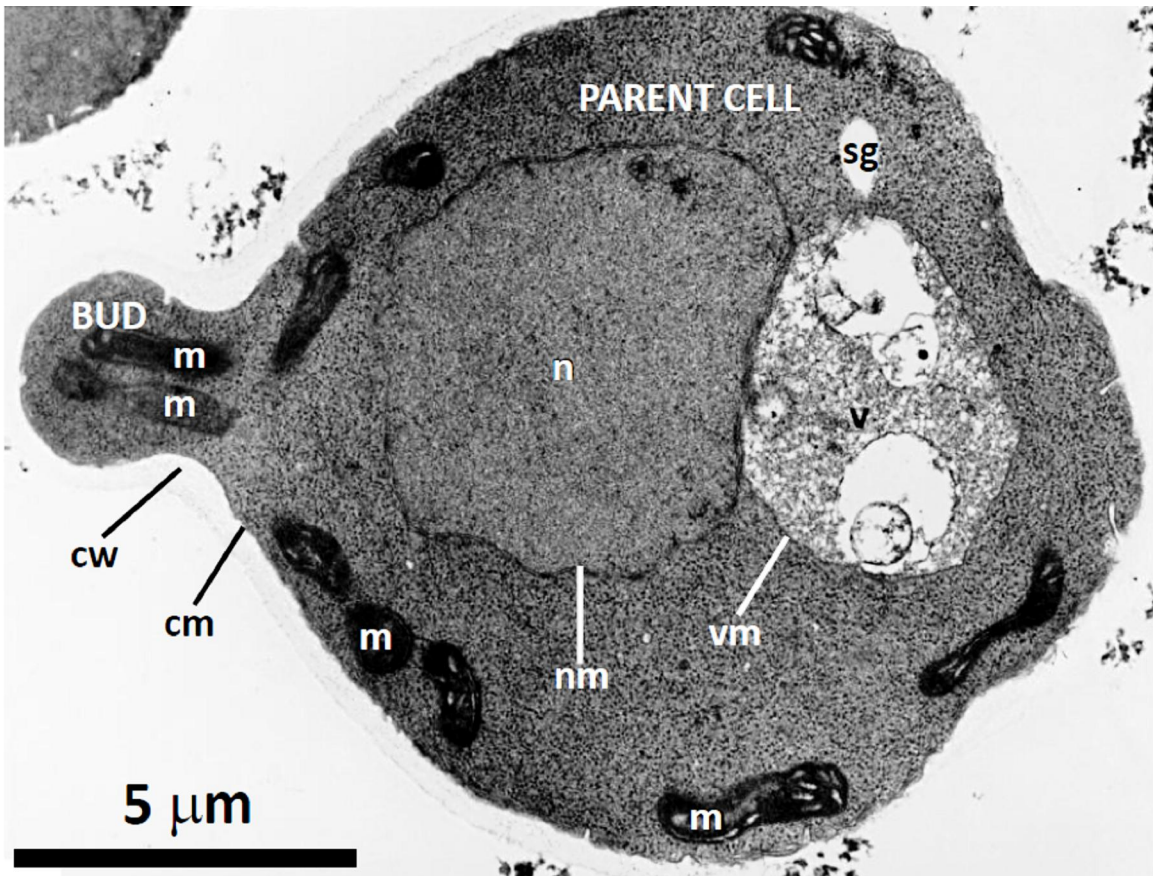
Figure 7-1: *Cross-sectional SEM of a budding S. cerevisiae cell [SACE09].*

7.3 Lossy Dielectric Models of *Saccharomyces cerevisiae* Cells as Used in This Work

The constitutive subcellular electrical parameters of *S. cerevisiae* have been inferred using electrorotation (ROT) data [Fuhr85, Wang93a, Höl90, Höl92, Höl97, Asa76, Asa96]. The complex heterogeneous cytoplasmic interior of *S. cerevisiae* necessitates that experimental ROT data be fitted to simplified cellular models. Frequently, the subcellular electrical properties of *S. cerevisiae* are extracted by fitting experimental ROT spectra to a cellular model comprised of a homogeneous cytoplasmic sphere surrounded by concentric homogeneous spherical shells representing the cytoplasmic membrane and the cell wall [Fuhr85, Wang93a]. Unfortunately, Hölzel found that this two-shelled model failed to accurately simulate his experimentally observed ROT spectra under 3 kHz [Höl97]. However, Hölzel was able to obtain an

excellent agreement with his experimental ROT spectra over a broad 100 Hz to 1.6 GHz bandwidth by using a four-shelled model [Höl97]. These additional shells are not an arbitrary increase in the model's complexity so as to improve the fit to the experimental ROT spectrum, as SEMs of *S. cerevisiae* suggest a three-layered structure beyond the cytoplasmic membrane [Vit61, Moo92, Mulh94]. Immediately beyond the cytoplasmic membrane is a localized electron-opaque layer referred to as the periplasmic space [Gan95]. This periplasmic space is then followed by a more transparent inner cell wall layer and a highly opaque outer cell wall layer. Notably, Asami *et al.* also presented a four-shelled model for *S. cerevisiae*, in which the vacuole is modeled as a homogeneous sphere, followed by concentric homogeneous spherical shells representing the vacuole membrane, the cytoplasmic space beyond the vacuole, the cytoplasmic membrane, and the cell wall [Asa96]. This model facilitated Asami *et al.*'s comparison between the ROT spectrum of wild and vacuole-deficient mutant *S. cerevisiae* strains [Asa96]. Raicu *et al.* also present a multi-shelled cellular model for *S. cerevisiae* which considers the vacuole and its membrane as separate layers [Rai96]. Hölzel attempted a least-squares error (LSE) fit based upon a model which also included the vacuole and its membrane as separate layers, but found that this model yielded unrealistic parameter values [Höl97]. This failure demonstrates that the conditions of a biological model constrain its correspondence to experimental data [Höl97].

As subcellular conductivities vary with the external medium conductivity σ_{med}, Hölzel measured the ROT spectra for a single viable *S. cerevisiae* cell using σ_{med} é 0.7, 20, 90, and 550 μS/cm [Höl97]. Notably, Hölzel found that the four-shell model was only required to simulate the low frequency ROT spectrum at a low σ_{med} é 0.7 μS/cm. The traditional two-shelled model yielded a fair agreement at a moderate σ_{med} é 20 μS/cm and σ_{med} é 90 μS/cm, and an excellent agreement at a high σ_{med} é 550 μS/cm.

Each layer within the multi-shelled spherical cellular model for *S. cerevisiae* is defined by three distinct parameters: thickness (or radius), real relative permittivity ε', and conductivity σ. To estimate subcellular conductivities using his ROT data, Hölzel used cellular dimensions derived from SEMs [Vit61, Moo92, Mulh94], and ε' values reported elsewhere in the literature [Asa76, Peth79, Fuhr85, Höl90, Asa96]. The subcellular dimensions and ε' values used by Hölzel are summarized in Table 7-1a. Data

regarding the intrinsic dielectric loss, ε'', of *S. cerevisiae* is unavailable and is consequently assumed to be negligible.

In Table 7-1a, the fluid medium's real absolute permittivity ε'_{med} is assumed to be that of deionized water (DI H$_2$O), $\varepsilon'_{med} = 78\varepsilon_0$ [Wang93a]. Notably, the real absolute permittivity of DI H$_2$O exhibits a relaxation centered about 10-20 GHz, in which the static $78\varepsilon_0$ drops to approximately $1.155\varepsilon_0$ [Peth79]. As the largest frequency applied to the microelectrode array (MEA) is less than 2 GHz, ε'_{med} can be safely assumed to be a constant $78\varepsilon_0$ throughout the entirety of this work. Moreover, Pethig indicates that the ε'' of DI H$_2$O is at most $5\varepsilon_0$ in the vicinity of 1.478 GHz [Peth79]. As the fluid medium's intrinsic dielectric loss ε''_{med} is assumed to be the same for the diluted methylene blue solution as for DI H$_2$O, ε''_{med} is neglected throughout this work.

Table 7-1a: Subcellular Viable *S. cerevisiae* Dimensions and Real Relative Permittivities Used by Hölzel		
Layer	*Radius or Thickness*	ε'_r
Cytoplasm (cyt)	3.0 µm Radius	51
Membrane (mem)	3.5 nm Thick	3
Periplasmic space (pps)	25 nm Thick	14.4
Inner Cell Wall (icw)	110 nm Thick	60
Outer Cell Wall (ocw)	50 nm Thick	5.9
Medium (med)	N/A	78

Table 7-1a: *Subcellular viable S. cerevisiae dimension and real relative permittivities used by Hölzel [Höl97].*

The subcellular conductivities were then obtained via a combined LSE fit of the ROT spectrum at each σ_{med} [Höl97]. Hölzel's results are summarized in Table 7-1b.

Table 7-1b: Subcellular Viable *S. cerevisiae* Conductivities Computed by Hölzel					
σ_{med} [μS/cm]	σ_{cyt} [μS/cm]	σ_{mem} [μS/cm]	σ_{pps} [μS/cm]	σ_{icw} [μS/cm]	σ_{ocw} [μS/cm]
0.7	9400	0.0058	11	6.1	100
20	12 000	0.029	41	29	200
90	12 000	0.046	41	62	200
550	12 000	0.037	41	240	200

Table 7-1b: *Subcellular viable S. cerevisiae conductivities computed by Hölzel [Höl97].*

Hölzeløs dataset suggests that only σ_{mem} and σ_{icw} vary with σ_{med}, provided that $\sigma_{med} \times 20$ μS/m. As such, σ_{cyt}, σ_{pps}, and σ_{ocw} were assumed to be independent of σ_{med} at the σ_{med} é 33.4 mS/cm of this work. The invariability of σ_{cyt} with σ_{med} is unsurprising, as the cell is actively maintaining the concentrations of ionic species, amino acids, and sugars within its cytoplasmic interior that are necessary to sustain life [Asa76]. σ_{mem} and σ_{icw} were plotted using Microsoft® Excel 2007 to yield LSE fits to Hölzeløs data. Figure 7-2a shows a logarithmic LSE fit to Hölzeløs σ_{mem} data that can be used to estimate σ_{mem} given σ_{med}. Hölzel and Lamprecht suggest that the nonlinear turn-off behaviour in σ_{mem} at exceedingly low σ_{med} values corresponds to the tight closure of the membraneøs ionic channels to prevent the loss of cytoplasmic electrolytes to the surrounding environment [Höl92]. Figure 7-2b shows a linear LSE fit to Hölzeløs σ_{icw} data that can be used to estimate σ_{icw} given σ_{med}. The linear behaviour of σ_{icw} with σ_{med} is unsurprising, as the cell wall is permeable to ions, amino acids, and sugars [Asa76]. Given the stated permeability of the cell wall [Asa76], the invariability of σ_{ocw} and σ_{pps} with σ_{med} suggested by Hölzeløs data is curious.
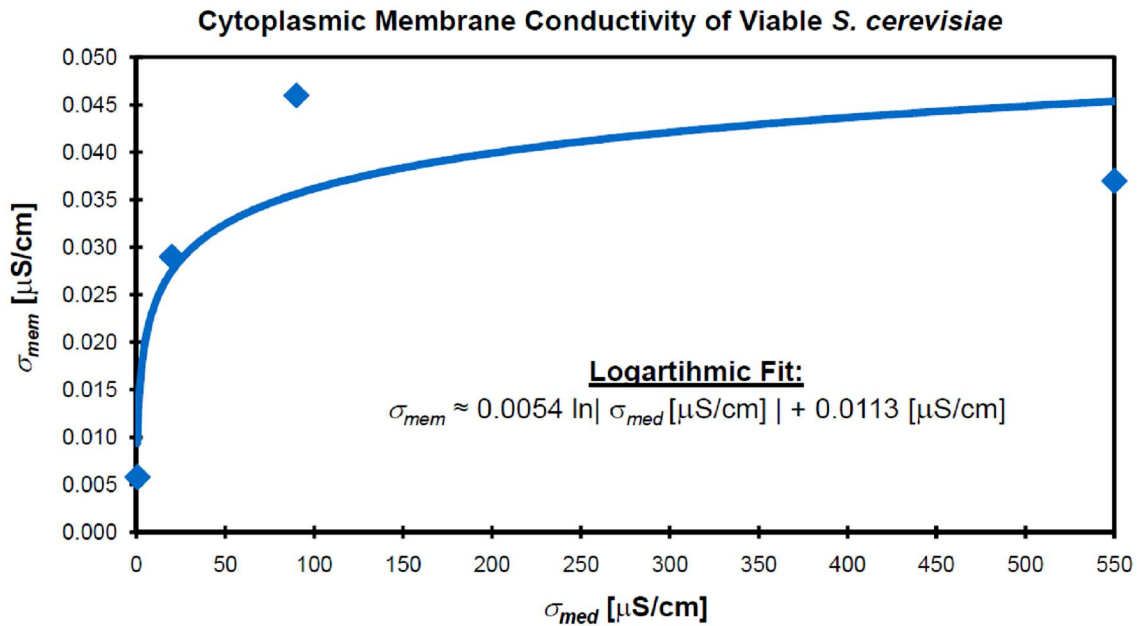
Figure 7-2a: _Logarithmic fit to Hölzel's viable S. cerevisiae $\sigma_{mem}(\sigma_{med})$ data [Höl97]._
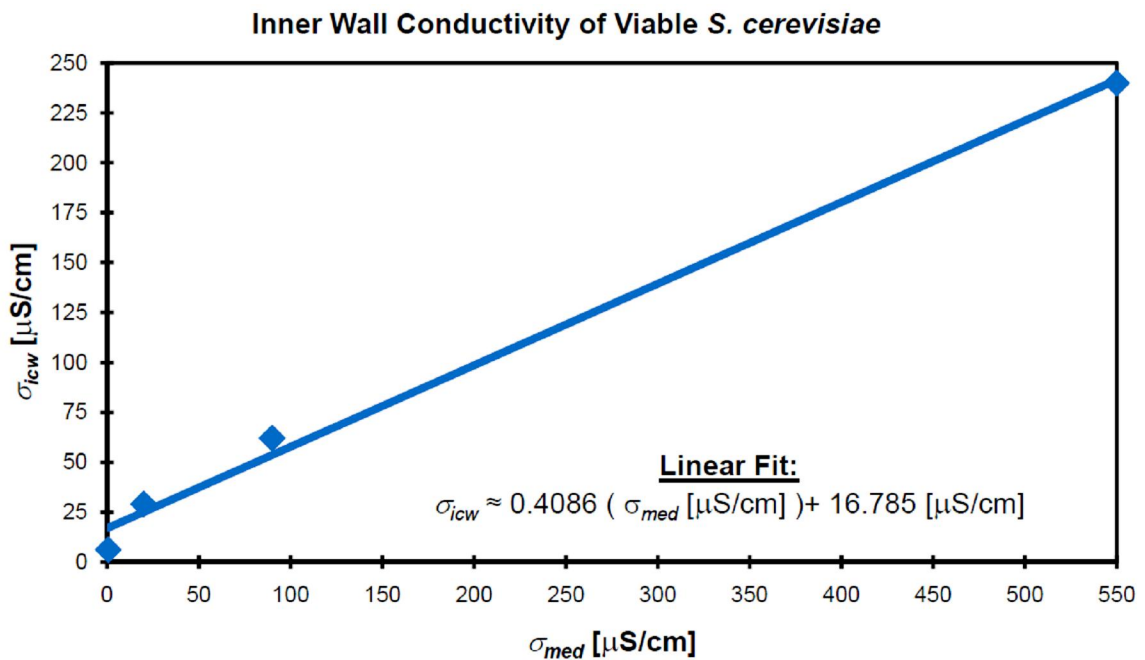
Figure 7-2b: _Linear fit to Hölzel's viable S. cerevisiae $\sigma_{icw}(\sigma_{med})$ data [Höl97]._

In this work, *S. cerevisiae* cells shall be suspended within a diluted methylene blue solution with a σ_{med} é 33.4 μS/cm conductivity. Using the LSE fits of Figures 7-2a and 7-2b, the subcellular parameters at this σ_{med} value were estimated as presented in Table 7-2.

Table 7-2: Subcellular Viable *S. cerevisiae* Properties Inferred from Hölzel			
Layer	*Radius or Thickness*	ε'_r	σ [μS/cm]
Cytoplasm (cyt)	3.0 μm Radius	51	12 000
Membrane (mem)	3.5 nm Thick	3	0.0302
Periplasmic space (pps)	25 nm Thick	14.4	41
Inner Cell Wall (icw)	110 nm Thick	60	30.4322
Outer Cell Wall (ocw)	50 nm Thick	5.9	200
Medium (med)	N/A	78	33.4

Table 7-2: *Subcellular viable S. cerevisiae properties inferred from Hölzel.*

Unfortunately, Hölzel did not measure the ROT spectra of a single nonviable *S. cerevisiae* cell using the distinct σ_{med} values of Table 7-1b [Höl97]. However, Hölzel and Lamprecht measured the ROT spectra of a single heat shocked (heated to 75 °C for 5 minutes) *S. cerevisiae* cell using σ_{med} é 25 μS/cm [Höl92]. In this paper, Hölzel and Lamprecht used a cellular model comprised of a homogeneous cytoplasmic sphere surrounded by concentric homogeneous spherical shells representing the cytoplasmic membrane and the cell wall. Using subcellular dimension and real relative permittivity assumptions, Hölzel and Lamprecht obtained subcellular conductivities via a combined LSE fit of the ROT spectrum [Höl92]. Hölzel and Lamprechtøs results are summarized in Table 7-3.

Table 7-3: Subcellular Heat Shocked *S. cerevisiae* Properties Presented by Hölzel and Lamprecht			
Layer	*Radius or Thickness*	ε'_r	$\sigma\,[\mu S/cm]$
Cytoplasm (cyt)	3.0 μm Radius	51	100-800
Membrane (mem)	3.5 nm Thick	6	> 0.1
Cell Wall (cw)	110 nm Thick	60	300
Medium (med)	N/A	78	25

Table 7-3: *Subcellular heat shocked S. cerevisiae*
properties presented by Hölzel and Lamprecht [Höl92].

In this work, heat shocked *S. cerevisiae* cells shall be suspended in a diluted methylene blue solution with a σ_{med} é 33.4 μS/cm conductivity. The subcellular parameters at this σ_{med} value were estimated from Table 7-3, as presented in Table 7-4. As the subcellular parameters in Table 7-4 are being approximated using the Table 7-3 data measured at σ_{med} é 25 μS/cm, the deviation between Table 7-4 and experimental heat shocked *S. cerevisiae* cell observations is expected to be more significant than the deviation between Table 7-2 and experimental viable *S. cerevisiae* cell observations.

Table 7-4: Subcellular Heat Shocked *S. cerevisiae* Properties Inferred from Hölzel and Lamprecht			
Layer	*Radius or Thickness*	ε'_r	$\sigma\,[\mu S/cm]$
Cytoplasm (cyt)	3.0 μm Radius	51	100
Membrane (mem)	3.5 nm Thick	6	0.1
Cell Wall (cw)	110 nm Thick	60	300
Medium (med)	N/A	78	33.4

Table 7-4: *Subcellular heat shocked S. cerevisiae*
properties inferred from Hölzel and Lamprecht.

7.4 Theoretical Dielectrophoretic Behaviour of *Saccharomyces cerevisiae* Cells as Used in This Work

When deriving the induced MEA capacitance perturbation ΔC_{MEA}, Equation (4-9), and the time-averaged dielectrophoretic (DEP) force $\boldsymbol{F_{DEP}}$ experienced by a cell, Equation (3-31): the cell was assumed to be a single homogeneous sphere to reduce the complexity of the considered biological system. As such, it is necessary to replace Hölzel's four-shelled spherical model with a single homogenous dielectric sphere. Fortunately, Jones provides an iterative method specifically designed to model a multi-shelled dielectric sphere as an equivalent homogeneous dielectric sphere [Jon95]. Consider a sphere with radius r_{sphere} and complex absolute permittivity $\underline{\varepsilon}_{sphere}$ surrounded by a single concentric spherical shell with thickness d_{shell} and complex permittivity $\underline{\varepsilon}_{shell}$. Using Jones' method, this single-shelled sphere can be replaced with an equivalent homogeneous sphere with radius $r_{eq} = r_{sphere} + d_{shell}$ and complex absolute permittivity $\underline{\varepsilon}_{eq}$, given as [Jon95]:

$$\underline{\varepsilon}_{eq} = \underline{\varepsilon}_{shell} \left[\frac{\left(\dfrac{r_{sphere} + d_{shell}}{r_{sphere}}\right)^3 + 2\left(\dfrac{\underline{\varepsilon}_{sphere} - \underline{\varepsilon}_{shell}}{\underline{\varepsilon}_{sphere} + 2\underline{\varepsilon}_{shell}}\right)}{\left(\dfrac{r_{sphere} + d_{shell}}{r_{sphere}}\right)^3 - \left(\dfrac{\underline{\varepsilon}_{sphere} - \underline{\varepsilon}_{shell}}{\underline{\varepsilon}_{sphere} + 2\underline{\varepsilon}_{shell}}\right)} \right] \tag{7-1}$$

The effective real absolute permittivity ε'_{eq} and effective conductivity σ_{eq} of the equivalent homogeneous sphere can also be computed using Equation (7-1) by replacing the $\underline{\varepsilon}$ terms with the associated ε' and σ terms, respectively.

Equation (7-1) is first used to replace the cytoplasmic sphere and the cytoplasmic membrane shell with an equivalent homogeneous sphere. Equation (7-1) is then used iteratively from the inside out until the entire multi-shelled model is replaced by an equivalent homogeneous sphere. The effective complex permittivity $\underline{\varepsilon}_{cell}$, effective conductivity σ_{cell}, and effective real absolute permittivity ε'_{cell} of the final equivalent homogeneous sphere which replaces the entire multi-shelled model are denoted with the subscript *cell*.

Although the multi-shelled spherical model has been replaced with an equivalent homogeneous sphere, the Maxwell-Wagner interfaces between each layer are embedded within the repeated applications of Equation (7-1). As such, the real part of the complex Clausius-Mossotti factor, Re{$\underline{K}$}, can be expressed via a partial fraction expansion as

$$\text{Re}\{\underline{K}\} \approx K_\infty - \sum_{i=1}^{N} \left\{ \frac{\Delta K_{MWi}}{1 + \omega^2 \tau_{MWi}^2} \right\} \tag{7-2}$$

where ω is the angular frequency of the applied DEP actuation potential ϕ_{DEP}, τ_{MWi} is the Maxwell-Wagner charge relaxation time of material interface i, ΔK_{MWi} is the change in Re{$\underline{K}$} which occurs when the applied frequency $f = \omega / (2\pi)$ of ϕ_{DEP} drops below the interfacial Maxwell-Wagner dispersion $f_{MWi} = 1 / (2\pi\tau_{MWi})$, N is the number of material layers within the multi-shelled spherical model, and K_∞ is the $f \quad \infty$ limit of Re{$\underline{K}$} as given by Equation (3-33b) [Jon95]. Analytical computation of each τ_{MWi} and ΔK_{MWi} is difficult when multiple interfaces are present and all τ_{MWi} values are not sufficiently disparate [Jon95]. Furthermore, Equation (7-2) does not include additional dispersions within the fluid medium or the cell that are not associated with an interfacial polarization, such as the 10-20 GHz relaxation exhibited by DI H_2O [Peth79].

The MATLAB® program presented in Appendix C.2 uses the data tabulated in Tables 7-2 and 7-4 in conjunction with Equations (3-32) and (7-1) to compute and plot Figure 7-3, the DEP spectra for viable and heat shocked *S. cerevisiae* cells as used in this work.
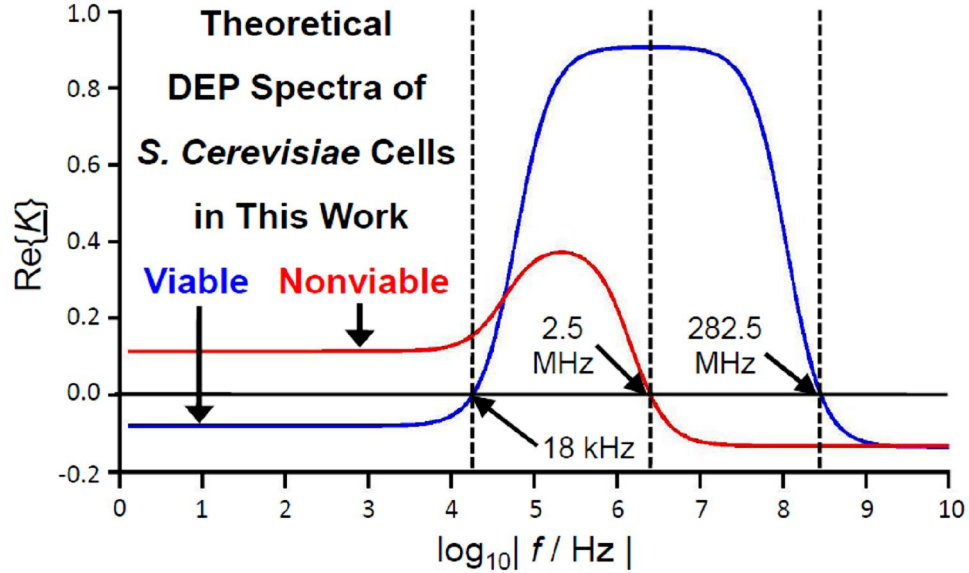
Figure 7-3: *Theoretical DEP spectra of viable and nonviable S. cerevisiae cells suspended in the 33.4 μS/cm diluted methylene blue solution.*

Figure 7-3 demonstrates that there are two distinct bands in which the viable and nonviable DEP spectra have opposing polarities: (1) the 0-18 kHz band, in which viable and nonviable cells experience negative DEP (nDEP) and positive DEP (pDEP) forces, respectively; and (2) the 2.5-282.5 MHz band, in which viable and nonviable cells experience pDEP and nDEP forces, respectively. A ϕ_{DEP} operating in either of these bands is well suited for distinguishing between viable and nonviable *S. cerevisiae* cells suspended in a fluid medium with a conductivity σ_{med} é 33.4 μS/cm. In this work, ϕ_{DEP} shall be limited to the 10-1000 kHz band. This constraint on ϕ_{DEP} is necessary to: (1) prevent the accumulation of ions at the MEA which may occur if ϕ_{DEP} oscillated below 10 kHz, and (2) stay below the 2.5 MHz cut-off frequency of the single time-constant filter isolating the electronics generating ϕ_{DEP} from the 1.478 GHz radio frequency (RF) sensing potential ϕ_{RF}.

Figure 7-3 also demonstrates that both DEP spectra have K_∞ é -0.14. Assuming that $\varepsilon'_{med} = 78\varepsilon_0$, $a = 3$ μm, and $K_\infty = -0.14$: Equation (4-9) predicts a -3.28 x 10^{-26} F m^2 scaling factor for converting the E_{ext}^2 / ϕ_{RF}^2 profiles of Figure 4-2 into the corresponding -2 to -46 aF ΔC_{MEA} signatures induced by both viable and nonviable *S. cerevisiae* cells as used in this work.

Figure 7-3 shows that the viable and nonviable DEP spectra each consist of two effective Maxwell-Wagner interfacial dispersions, f'_{MW1} and f'_{MW2}. As all of the τ_{MWi} terms of Equation (7-2) are not sufficiently disparate in either case: exact analytical expressions for the various features within each DEP spectrum, from which their dependence upon the various subcellular and medium conductivities and real absolute permittivities could be directly inferred, cannot be presented [Jon95].

When a biological cell structurally similar to *S. cerevisiae* is exposed to an external electric field $\boldsymbol{E_{ext}}$ oscillating at GHz frequencies: the cytoplasmic membrane is electrically transparent, exposing the cytoplasmic interior to $\boldsymbol{E_{ext}}$ [Jon95, Cost03]. As the diameter of the cytoplasmic sphere is much larger than the thickness of any of the surrounding spherical shells of similar real absolute permittivity, it follows that K_∞ is dominated by ε'_{cyt} and ε'_{med}. A first-order approximation for K_∞ thus follows from Equation (3-33b) as:

$$K_\infty = \lim_{f \to \infty} \{\underline{K}\} \approx \frac{\varepsilon'_{cyt} - \varepsilon'_{med}}{\varepsilon'_{cyt} + 2\varepsilon'_{med}} \tag{7-3}$$

In both the viable and nonviable cases, Equation (7-3) predicts K_∞ é -0.13. The relative percent error between the K_∞ é -0.14 presented within Figure 7-3 and the K_∞ é -0.13 predicted by Equation (7-3) is 7.14%. As such, Equation (7-3) is a reasonable first-order approximation for K_∞. As ε'_{cyt} is the same in both the viable and nonviable cases, the viable and nonviable K_∞ are virtually identical. Moreover, as the dielectric contrast between ε'_{cyt} and ε'_{med} is relatively low: $|K_\infty|$ is relatively low.

When a biological cell structurally similar to *S. cerevisiae* is exposed to a medium frequency (MF) $\boldsymbol{E_{ext}}$: the electrical impedance of the cytoplasmic membrane is relatively low [Cost03]. MF $\boldsymbol{E_{ext}}$ are thus able to enter the cytoplasmic membrane [Cost03]. However, as the cytoplasmic interior is highly conductive: MF $\boldsymbol{E_{ext}}$ are prevented from entering the cytoplasmic interior [Cost03]. It thus follows that the MF value of Re$\{\underline{K}\}$, Re$\{\underline{K}_{MF}\}$, is dominated by σ_{cyt} and σ_{med}. A first-order approximation for Re$\{\underline{K}_{MF}\}$ thus follows from Equation (3-33a) as:

$$\mathrm{Re}\{\underline{K}_{MF}\} = \mathrm{Re}\{\underline{K}|_{f'_{MW1}<<f<<f'_{MW2}}\} \approx \frac{\sigma_{cyt} - \sigma_{med}}{\sigma_{cyt} + 2\sigma_{med}} \qquad (7\text{-}4)$$

The relative percent error between the viable case $\mathrm{Re}\{\underline{K}_{MF}\}$ é 0.91 presented within Figure 7-3 and the viable case $\mathrm{Re}\{\underline{K}_{MF}\}$ é 0.99 predicted by Equation (7-4) is 8.79%. Similarly, the relative percent error between the nonviable case $\mathrm{Re}\{\underline{K}_{MF}\}$ é 0.37 presented within Figure 7-3 and the nonviable case $\mathrm{Re}\{\underline{K}_{MF}\}$ é 0.40 predicted by Equation (7-4) is 8.11%. As such, Equation (7-4) is a reasonable first-order approximation for $\mathrm{Re}\{\underline{K}_{MF}\}$. As σ_{cyt} is 120 times greater in the viable case than in the nonviable case, the nonviable cellø cytoplasmic interior is more susceptible to MF $\boldsymbol{E}_{ext}$ than the viable cellø cytoplasmic interior. Consequently, the viable case $\mathrm{Re}\{\underline{K}_{MF}\}$ is significantly greater than the nonviable case $\mathrm{Re}\{\underline{K}_{MF}\}$.

Equation (7-3) was obtained by employing the substitution $\varepsilon'_{cell} \quad \varepsilon'_{cyt}$ in Equation (3-33b). Similarly, Equation (7-4) was obtained by employing the substitution $\sigma_{cell} \quad \sigma_{cyt}$ in Equation (3-33a). It thus seems reasonable that a first-order approximation for the second effective Maxwell-Wagner charge relaxation time, τ'_{MW2}, can be obtained by employing the substitutions $\varepsilon'_{cell} \quad \varepsilon'_{cyt}$ and $\sigma_{cell} \quad \sigma_{cyt}$ in Equation (3-35):

$$\tau'_{MW2} \approx \frac{\varepsilon'_{cyt} + 2\varepsilon'_{med}}{\sigma_{cyt} + 2\sigma_{med}} \qquad (7\text{-}5)$$

In the viable case, Equation (7-5) predicts $f'_{MW2} = 1 / (2 \pi \tau'_{MW2})$ é 104.79 MHz. In the nonviable case, Equation (7-5) predicts $f'_{MW2} = 1 / (2 \pi \tau'_{MW2})$ é 1.45 MHz. Both of these predictions are reasonable first-order approximations to f'_{MW2} as observed in Figure 7-3. As σ_{cyt} is 120 times greater in the viable case than in the nonviable case, the nonviable cellø cytoplasmic interior is more susceptible to MF $\boldsymbol{E}_{ext}$ than the viable cellø cytoplasmic interior. Consequently, the viable case f'_{MW2} is significantly higher than the nonviable case f'_{MW2}.

When a biological cell structurally similar to *S. cerevisiae* is exposed to a low frequency (LF) $\boldsymbol{E}_{ext}$: the cytoplasmic membrane acts as a very low loss capacitor, excluding $\boldsymbol{E}_{ext}$ from the cytoplasmic membrane and interior [Jon95, Cost03]. As σ_{mem} is

greater within a nonviable cell than in a viable cell, it is expected that a nonviable cell's cytoplasm would be more susceptible to LF $\boldsymbol{E_{ext}}$ than a viable cell's cytoplasm.

Unfortunately, there appears to be no first-order approximations for the LF features of the DEP spectra presented in Figure 7-3. To compute the $f \to 0$ limit of $\underline{K}$, K_0: the σ_{cell} of the equivalent homogeneous sphere must be employed within Equation (3-33a). Equation (3-33a) demonstrates that: the sign of K_0 is given by the contrast between σ_{cell} and σ_{med}, K_0 decreases as σ_{med} is increased, and K_0 increases as σ_{med} is decreased. As such, σ_{med} is a critical material parameter in determining the LF and MF regimes of a fluid-suspended biological cell's DEP spectrum. Fortunately, σ_{med} is the material parameter that an experimenter is most easily able to tune so as to optimize the DEP spectrum of his or her experiment. For example, the methylene blue solution of this work was diluted with DI H_2O to obtain the desired $\sigma_{med} \approx 33.4$ μS/cm conductivity.

Given the lack of reasonable first-order approximations for the LF features of a fluid-suspended biological cell's DEP spectrum, it is recommended that an experimenter simulate their DEP spectra using a complete multi-shelled cellular model and observe the change in the LF and MF regimes as σ_{med} is varied. In this manner, the said experimenter can select the physically realizable σ_{med} which yields the DEP spectra best suited for studying the said cell. In this work, this strategy resulted in the selection of 33.4 μS/cm as the optimal σ_{med}, as the viable and nonviable *S. cerevisiae* DEP spectra presented in Figure 7-3 have opposing polarities within the 0-18 kHz band when $\sigma_{med} \approx 33.4$ μS/cm.

By varying the value for σ_{med} used within the MATLAB® program presented in Appendix C.2: the strong dependence of K_0 and $Re\{\underline{K}_{MF}\}$ with σ_{med}, and the virtual independence of K_∞ and f'_{MW2} with σ_{med}, were empirically confirmed. Moreover, it was observed that the first effective Maxwell-Wagner interfacial dispersion, f'_{MW1}, is strongly dependent upon σ_{med}: increasing as σ_{med} increases and decreasing as σ_{med} decreases. Furthermore, it was observed that if σ_{med} is sufficiently small: K_0 shall approximate $Re\{\underline{K}_{MF}\}$ and consequently f'_{MW1} shall not be observed. Notably, it was observed that the DEP spectra are confined to the range $-0.5 \leq Re\{\underline{K}\} \leq 1.0$ regardless of the value of σ_{med} employed in the computation.

Chapter 8

Analysis of a Homogeneous Heat Shocked
Saccharomyces cerevisiae Cell Population

8.1   Heat Shocked *Saccharomyces cerevisiae* Sample Preparation

For this work, a 113 g jar of Fleischmann's® Traditional active dry yeast was purchased from the local supermarket. In this product, dehydrated *Saccharomyces cerevisiae* cells are stored within a sorbitan monostearate ($C_{24}H_{46}O_6$) matrix, forming granules. These granules are depicted in Figure 8-1.

Figure 8-1: *Fleischmann's® Traditional active dry yeast granules.*

In this work, individual active dry yeast granules are rehydrated and mixed into a diluted methylene blue solution (prepared as outlined in Section 6.1). Methylene blue was selected as it preferentially stains *S. cerevisiae* cells whose cytoplasmic membranes have been compromised, thus labelling only nonviable cells.

To confirm that the diluted methylene blue solution only labels nonviable cells, a sample of rehydrated *S. cerevisiae* was heat shocked to comprise the cytoplasmic membrane of every cell within the sample. The heat shocking apparatus is presented in Figure 8-2. A single active dry yeast granule was rehydrated in 20 mL of the diluted methylene blue solution within a 50 mL graduated glass beaker. A 500 mL graduated

glass beaker filled with 400 mL of deionized water (DI H$_2$O) was then heated with a hot plate (Thermodyne Type 1900) set to 175 °C. A multimeter (Fluke 116 True RMS) equipped with a thermocouple probe was used to monitor the heated DI H$_2$O bath's temperature. Once the monitored bath temperature reached 70 °C, the 50 mL glass beaker was partially submerged into the bath. The thermocouple was then used to monitor the temperature of the *S. cerevisiae* sample. Once the monitored *S. cerevisiae* sample temperature reached 60 °C, the 50 mL glass beaker was heated for an additional 4 minutes before being removed from the heated bath and allowed to cool for 30 minutes.
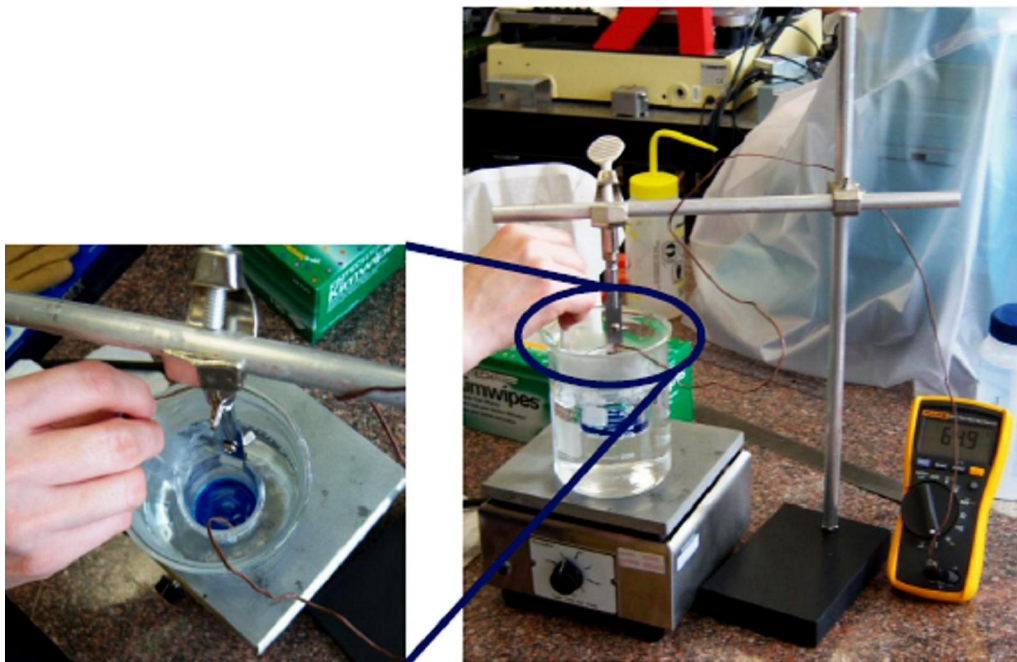
Figure 8-2: A sample of S. cerevisiae cells rehydrated in a diluted methylene blue solution being heat shocked.

A disposable syringe (BD 3 mL Slip Tip) was then used to deposit a single drop of the heat shocked *S. cerevisiae* sample onto a 3ö x 1ö x 1.0 mm glass slide (Fisherbrand Microscope Slide). A second glass slide (Magna No. 1 Microscope Cover Glass) was then placed on top of the droplet. The heat shocked *S. cerevisiae* sample slide was then examined using an optical microscope (Olympus BX51) fitted with a digital camera (Diagnostic Instruments RT Color SPOT). A micropictograph of heat shocked *S. cerevisiae* sample under study is presented as Figure 8-3. Figure 8-3 demonstrates that all of the heat shocked *S. cerevisiae* cells were permeable to the methylene blue dye.
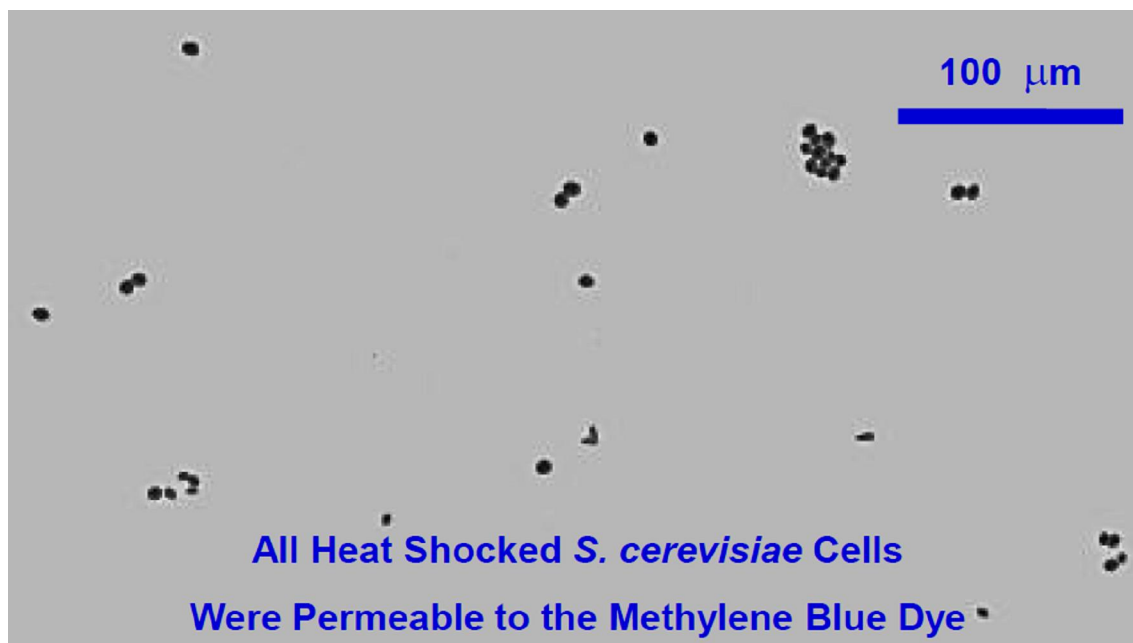
Figure 8-3: *Micropictograph demonstrating that all of the heat shocked S. cerevisiae cells were permeable to the methylene blue dye.*

A second active dry yeast granule was then rehydrated in another 20 mL of the diluted methylene blue solution. No further undue stress (such as being heat shocked) was applied to this second *S. cerevisiae* sample. Another disposable syringe (BD 3 mL Slip Tip) was then used to deposit a single drop of this unstressed *S. cerevisiae* sample onto another 3ö x 1ö x 1.0 mm glass slide (Fisherbrand Microscope Slide). Another glass slide (Magna No. 1 Microscope Cover Glass) was then placed on top of the droplet. The unstressed *S. cerevisiae* sample slide was then examined using the optical microscope. A micropictograph of the unstressed *S. cerevisiae* sample under study is presented as Figure 8-4. Figure 8-4 demonstrates that a high percentage of the unstressed *S. cerevisiae* cells were permeable to the methylene blue dye. However, not all of the unstressed *S. cerevisiae* cells have been stained, as was the case with the heat shocked *S. cerevisiae* sample. This suggests that a high percentage of the rehydrated *S. cerevisiae* cells from this batch of Fleischmann's[®] Traditional active dry yeast are nonviable, with compromised cytoplasmic membranes, prior to the application of any further undue stress. However, as (1) the microflow cytometer analyzes cells on a cell-by-cell basis and (2) the methylene blue dye labels the nonviable cells, the Fleischmann's[®] Traditional active dry yeast granules are suitable for this work.
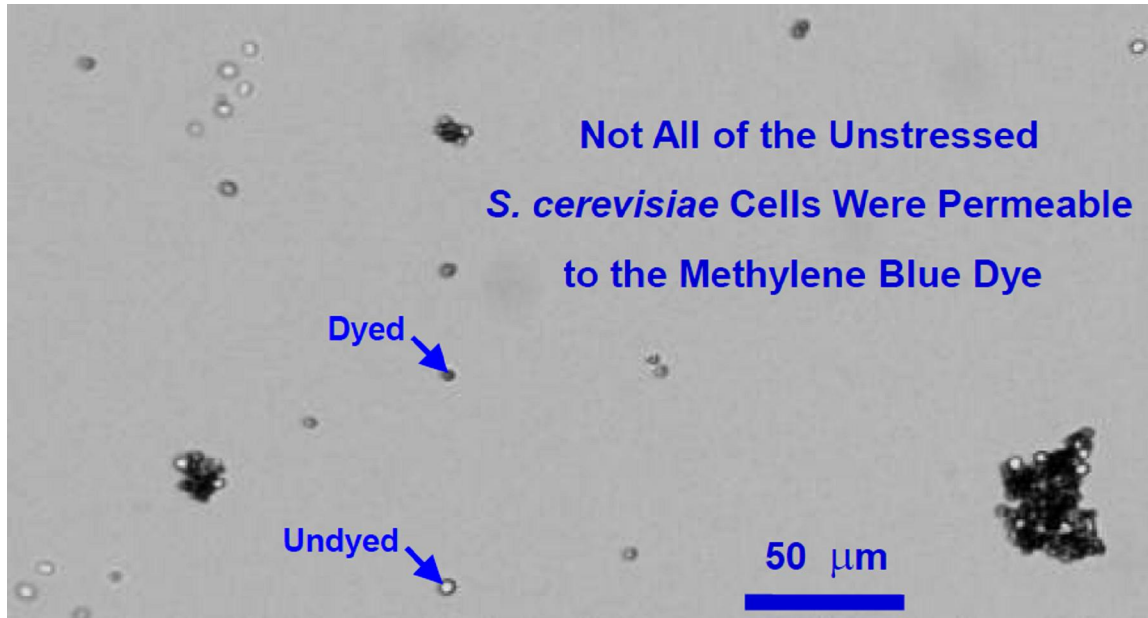
Figure 8-4: *Micropictograph demonstrating that not all of the unstressed S. cerevisiae cells were permeable to the methylene blue dye.*

8.2   Analysis of Actuated Heat Shocked *Saccharomyces cerevisiae*

A homogeneous population of heat shocked *S. cerevisiae* cells suspended in the diluted methylene blue solution was prepared as outlined in Section 8.1. This *S. cerevisiae* sample was injected into the microflow cytometer, which was simultaneously operated as both an optical assay and a capacitive cytometer. The relative elevation of the syringes was adjusted until the *S. cerevisiae* cells were observed to pass over the microelectrode array (MEA) with an average cross-over time of approximately 400 ms. The time-harmonic dielectrophoretic (DEP) actuation ϕ_{DEP} potential was then set to: 0 V_p, 1 V_p 10 kHz, 0.5 V_p 100 kHz, and 0.5 V_p 1 MHz. $|\phi_{DEP}|$ was halved in the 100 kHz and 1 MHz cases so as to reduce the cellular adhesion to the MEA observed when $|\phi_{DEP}| = 1$ V_p. Approximately 20 minutes of data was gathered at each ϕ_{DEP} setting. Each experimental dataset was then examined to select five S signatures, with no bias as to the initial cellular elevation h_{cell0}, which were visually confirmed to correspond to individual stained *S. cerevisiae* cells passing over the MEA. Each S signature was converted into a ΔC_{MEA} signature using the capacitive cytometer's dS/dC_{MEA} ≈ 57 mV/aF overall sensitivity (as computed in Section 6.2).

8.2.A Analysis of $\phi_{DEP} = 0$ V_p Data

Figure 8-5 presents the five experimental ΔC_{MEA} signatures selected from the baseline $\phi_{DEP} = 0$ V_p dataset. Visual inspection of these ΔC_{MEA} signatures suggests that they correspond to low elevation crossings, with h_{cell0} on the order of 4-6 µm (as is consistent with the polystyrene microsphere (PSS) observations of Section 6.3).
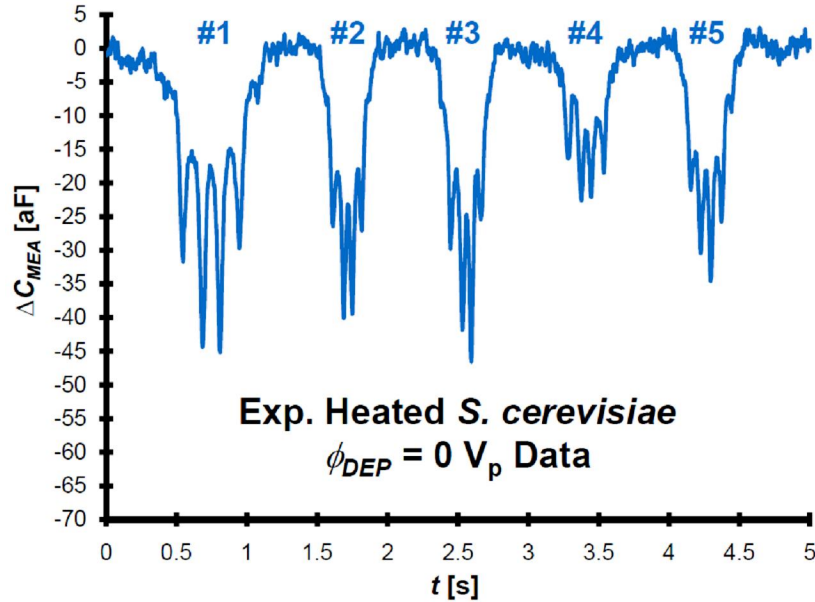
Figure 8-5: *Experimental ΔC_{MEA} signatures induced by passing heat shocked S. cerevisiae cells with $\phi_{DEP} = 0$ V_p.*

The Tracker 2.60 analysis of Section 6.3.A was then repeated to analyze the captured MEA detection zone video corresponding to the ΔC_{MEA} signatures of Figure 8-5, yielding an $x_{cell}(t)$ dataset saved as a comma separated value (CSV) file. The MATLAB® program of Appendix D analyzes this CSV file. Figure 8-6 presents these five $x_{cell}(t)$ profiles.
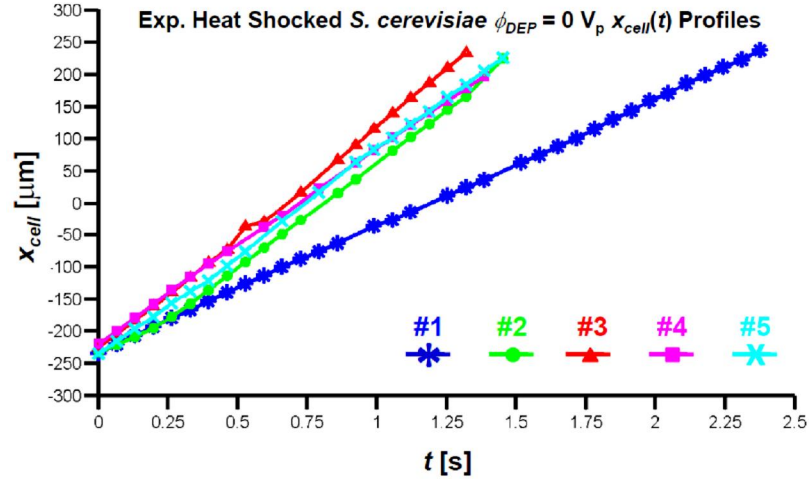
Figure 8-6: *Experimental $x_{cell}(t)$ profiles of passing heat shocked S. cerevisiae cells with $\phi_{DEP} = 0 \; V_p$.*

The MATLAB® program of Appendix D estimated the lateral cellular velocity $v_{cellx}(t)$ profiles corresponding to the ΔC_{MEA} signatures of Figure 8-5 via the first-order backward finite difference approximation. Linear interpolation was then employed to fit each $v_{cellx}(t)$ profile to a uniformly spaced x_{cell} line spanning ±125 μm in 0.5 μm steps. Figure 8-7 presents these fitted $v_{cellx}(x_{cell})$ profiles.
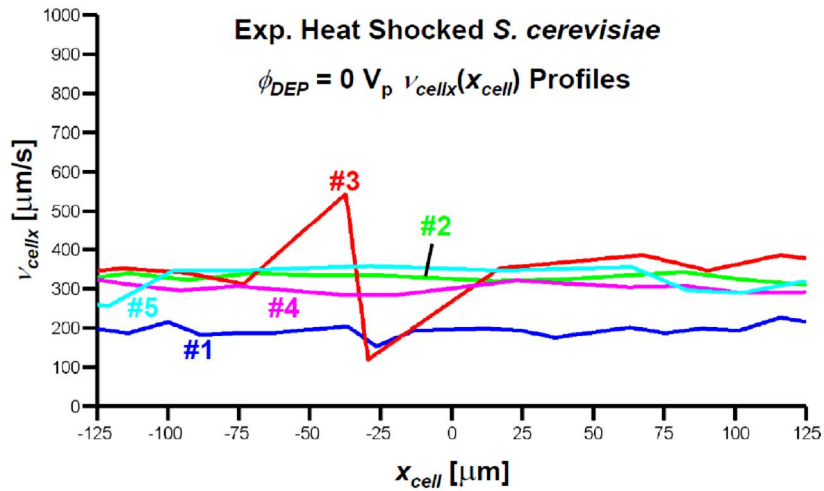
Figure 8-7: *Experimental $v_{cellx}(x_{cell})$ profiles of passing heat shocked S. cerevisiae cells with $\phi_{DEP} = 0 \; V_p$.*

The initial v_{cellx}, v_{cellx0}, of each profile was estimated as the mean v_{cellx} within the -125 μm Öx_{cell} Ö-75 μm interval. The final v_{cellx}, v_{cellxf}, of each profile was estimated as the mean v_{cellx} within the 75 μm Öx_{cell} Ö125 μm interval. The relative percent change in v_{cellx}, %Δv_{cellx}, is then estimated using v_{cellx0} and v_{cellxf}. Table 8-1 summarizes the results of this %Δv_{cellx} analysis.

Table 8-1: %Δv_{cellx} Analysis of Experimental v_{cellx} Profiles of Passing Heat Shocked *S. cerevisiae* Cells with $\phi_{DEP} = 0$ V_p			
Signature	v_{cellx0} [μm/s]	v_{cellxf} [μm/s]	%Δv_{cellx}
1	193.47	202.89	4.9
2	330.47	326.12	-1.3
3	338.88	366.34	8.1
4	304.80	294.91	-3.2
5	317.91	300.10	-5.6
E{ }	*297.11*	*298.07*	*0.6*
σ{ }	*59.35*	*60.25*	*5.7*

Table 8-1: *%Δv_{cellx} analysis of experimental v_{cellx} profiles of passing heat shocked S. cerevisiae cells with $\phi_{DEP} = 0$ V_p.*

The expectation and standard deviation of each of the v_{cellx} profiles, $E\{v_{cellx}\}$ and $\sigma\{v_{cellx}\}$, was then computed at each point along x_{cell}. Figure 8-8 presents the computed $E\{v_{cellx}\}$ and $E\{v_{cellx}\} \pm \sigma\{v_{cellx}\}$ profiles. Table 8-2 presents the corresponding %Δv_{cellx} analysis of these three statistical profiles.
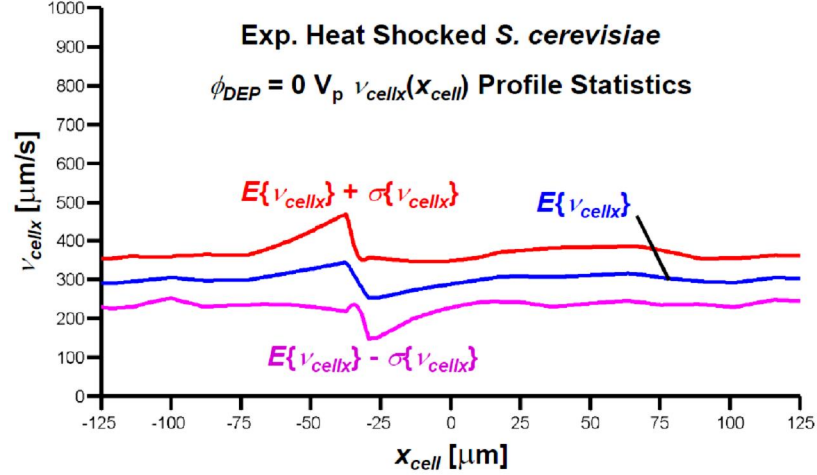
Figure 8-8: *Experimental v_{cellx} profile statistics of passing heat shocked S. cerevisiae cells with $\phi_{DEP} = 0$ V_p.*

Table 8-2: %Δv_{cellx} Analysis of Experimental $E\{v_{cellx}\}$ and $E\{v_{cellx}\} \pm \sigma\{v_{cellx}\}$ Profiles of Passing Heat Shocked *S. cerevisiae* Cells with $\phi_{DEP} = 0$ V_p			
Signature	v_{cellx0} [μm/s]	v_{cellxf} [μm/s]	%Δv_{cellx}
$E\{v_{cellx}\} + \sigma\{v_{cellx}\}$	359.02	359.11	0.0
$E\{v_{cellx}\}$	297.11	298.07	0.3
$E\{v_{cellx}\} - \sigma\{v_{cellx}\}$	235.19	237.03	0.5

Table 8-2: *%Δv_{cellx} analysis of experimental $E\{v_{cellx}\}$ and $E\{v_{cellx}\} \pm \sigma\{v_{cellx}\}$ profiles of passing heat shocked S. cerevisiae cells with $\phi_{DEP} = 0$ V_p.*

The particle tracing simulation of Section 4.3 then attempted to reproduce the $E\{v_{cellx}\}$ profile of Figure 8-8. In this simulation, the particle was initially placed at (x_{cell0}, h_{cell0}) = (-125, 5) μm and given an initial velocity of $v_{cell0} = 297.11$ a_x μm/s (referring to Table 8-1). Equation (4-11) was employed to estimate the mean of the parabolic fluid velocity profile as $< v_{med} > = 452.74$ a_x μm/s. The particle tracing simulation proceeded to compute the trajectory of the cell as subjected to the vicious fluid drag force, F_{drag}, computed using Equation (4-13). Both the elapsed time t and E_{ext}^2 / ϕ_{RF}^2 were plotted along the computed trajectory, yielding text files containing: (1) x_{cell}, h_{cell}, and t; and (2) x_{cell}, h_{cell}, and E_{ext}^2 / ϕ_{RF}^2.

The MATLAB® program of Appendix D was re-run, with additional code for the analysis of the particle tracing simulation executed. This additional code proceeds to read in the text file containing the simulated $x_{cell}(t)$ profile. The corresponding $v_{cellx}(t)$ profile was computed via the first-order backward finite difference approximation. Linear interpolation was employed to fit this $v_{cellx}(t)$ profile to a uniformly spaced x_{cell} line spanning ±125 μm in 0.5 μm steps. Figure 8-9 presents this fitted $v_{cellx}(x_{cell})$ profile along with the computed $E\{v_{cellx}\}$ and $E\{v_{cellx}\} \pm \sigma\{v_{cellx}\}$ profiles of Figure 8-8. Figure 8-9 shows that the simulated v_{cellx} profile reasonably approximates the experimental $E\{v_{cellx}\}$ profile. As this simulation did not include a DEP actuation force $\boldsymbol{F_{DEP}}$, the simulated h_{cell} and v_{cellx} remained constant.
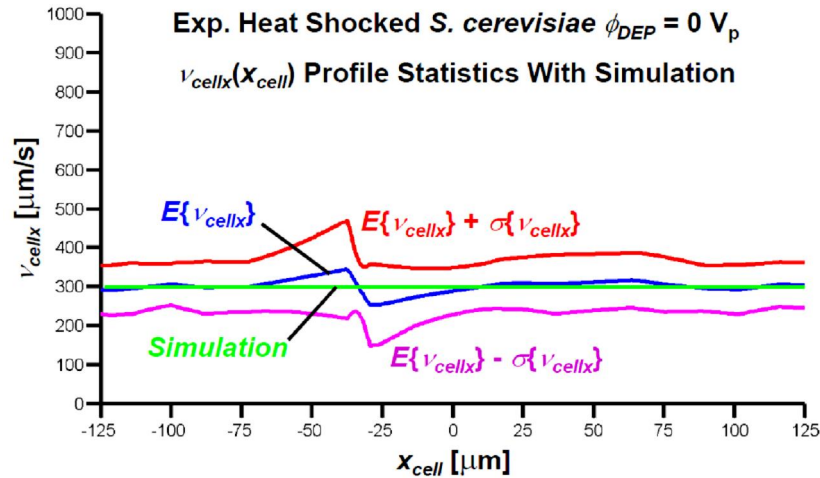
Figure 8-9: *The simulated v_{cellx} profile reasonably approximates the experimental $E\{v_{cellx}\}$ profile of passing heat shocked S. cerevisiae cells with $\phi_{DEP} = 0\ V_p$.*

Figure 8-10 presents the ΔC_{MEA} signature produced by scaling the simulated $E_{ext}^2(t)\ /\ \phi_{RF}^2$ profile with the -3.28 x 10^{-26} F m^2 scaling factor computed in Section 7.4. Figure 8-10 resembles the ΔC_{MEA} signatures of Figure 8-5 in both shape and peak magnitude, verifying that $h_{cell0} = 5$ μm was a reasonable assumption within the particle tracing simulation.
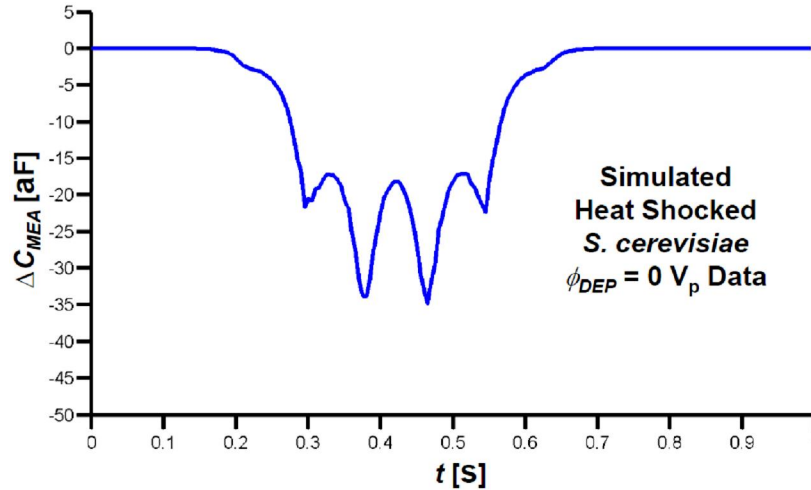
Figure 8-10: *Simulated ΔC_{MEA} signature induced by passing heat shocked S. cerevisiae cell with $\phi_{DEP} = 0\ V_p$.*

8.2.B   Analysis of $\phi_{DEP} = 1\ V_p$ 10 kHz Data

Figure 8-11 presents the five experimental ΔC_{MEA} signatures selected from the $\phi_{DEP} = 1\ V_p$ 10 kHz dataset. Visual inspection of these ΔC_{MEA} signatures suggests that they correspond to low initial elevation crossings, with h_{cell0} on the order of 4-6 μm.
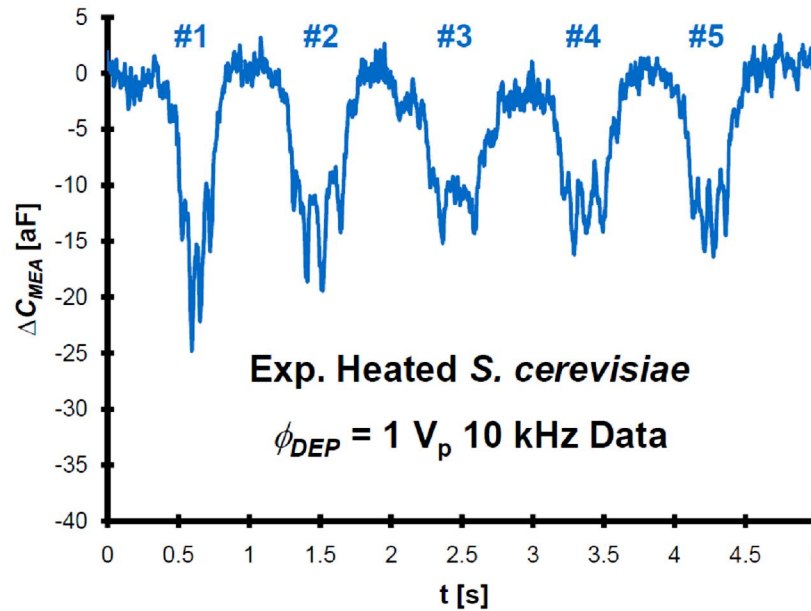
Figure 8-11: *Experimental ΔC_{MEA} signatures induced by passing heat shocked S. cerevisiae cells with $\phi_{DEP} = 1\ V_p$ 10 kHz.*

- 95 -

The Tracker 2.60 analysis of Section 6.3.A was then repeated to analyze the captured MEA detection zone video corresponding to the ΔC_{MEA} signatures of Figure 8-11, yielding an $x_{cell}(t)$ dataset saved as a CSV file. The MATLAB® program of Appendix D analyzes this CSV file. Figure 8-12 presents these five $x_{cell}(t)$ profiles.
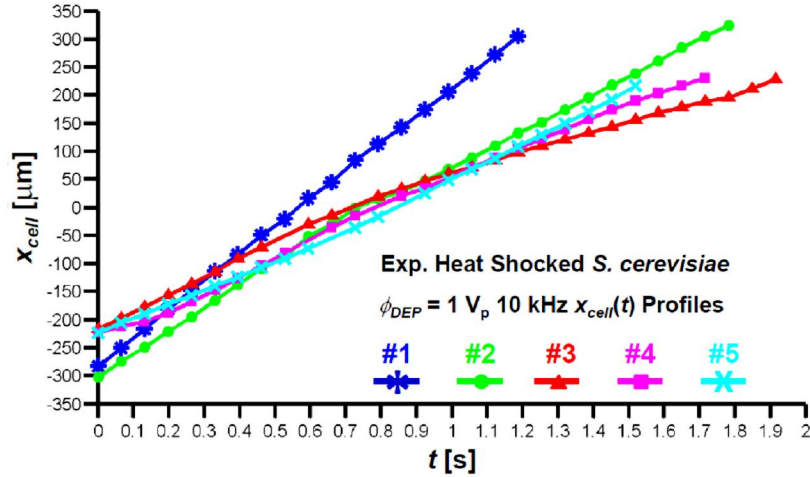
Figure 8-12: *Experimental $x_{cell}(t)$ profiles of passing heat shocked S. cerevisiae cells with ϕ_{DEP} = 1 V_p 10 kHz.*

The MATLAB® program of Appendix D estimated the $v_{cellx}(t)$ profiles corresponding to the ΔC_{MEA} signatures of Figure 8-12 via the first-order backward finite difference approximation. Linear interpolation was employed to fit each of these $v_{cellx}(t)$ profiles to a uniformly spaced x_{cell} line spanning ±125 µm in 0.5 µm steps. Figure 8-13 presents these fitted $v_{cellx}(x_{cell})$ profiles.
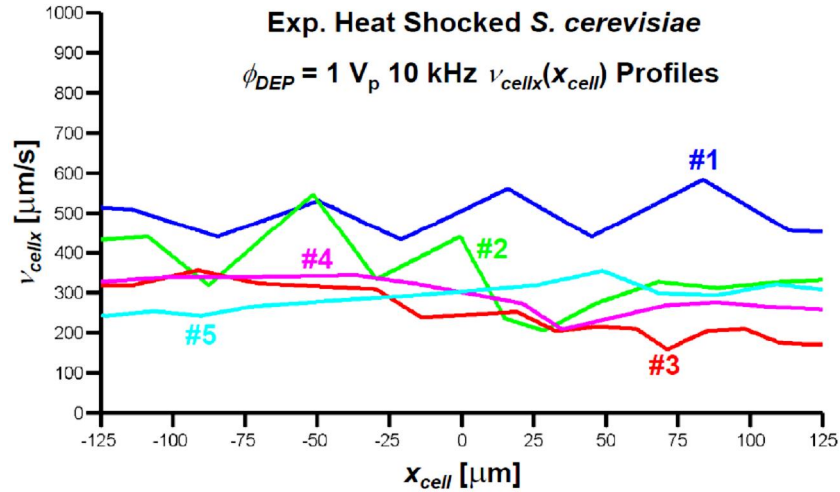
Figure 8-13: *Experimental $v_{cellx}(x_{cell})$ profiles of passing*

heat shocked S. cerevisiae cells with $\phi_{DEP} = 1\ V_p$ 10 kHz.

The initial v_{cellx}, v_{cellx0}, of each profile was estimated as the mean v_{cellx} within the -125 μm Ö x_{cell} Ö -75 μm interval. The final v_{cellx}, v_{cellxf}, of each profile was estimated as the mean v_{cellx} within the 75 μm Ö x_{cell} Ö 125 μm interval. The relative percent change in v_{cellx}, %Δv_{cellx}, is then estimated using v_{cellx0} and v_{cellxf}. Table 8-3 summarizes the results of this %Δv_{cellx} analysis.

Signature	v_{cellx0} [μm/s]	v_{cellxf} [μm/s]	%Δv_{cellx}
Table 8-3: %Δv_{cellx} Analysis of Experimental v_{cellx} Profiles of Passing Heat Shocked *S. cerevisiae* Cells with $\phi_{DEP} = 1\ V_p$ 10 kHz			
1	478.32	512.75	7.2
2	392.65	320.92	-18.3
3	334.14	188.65	-43.5
4	334.88	267.01	-20.3
5	248.51	305.45	22.9
E{ }	*357.70*	*318.96*	*-10.39*
σ{ }	*84.81*	*119.82*	*25.87*

Table 8-3: *%Δv_{cellx} analysis of experimental v_{cellx} profiles*

of passing heat shocked S. cerevisiae cells with $\phi_{DEP} = 1\ V_p$ 10 kHz.

The expectation and standard deviation of each of the v_{cellx} profiles, $E\{v_{cellx}\}$ and $\sigma\{v_{cellx}\}$, was then computed at each point along x_{cell}. Figure 8-14 presents the computed $E\{v_{cellx}\}$ and $E\{v_{cellx}\} \pm \sigma\{v_{cellx}\}$ profiles. Table 8-4 presents the corresponding $\%\Delta v_{cellx}$ analysis of these three statistical profiles.

Figure 8-14: _Experimental v_{cellx} profile statistics of passing heat shocked S. cerevisiae cells with $\phi_{DEP} = 1\ V_p$ 10 kHz._

Table 8-4: $\%\Delta v_{cellx}$ Analysis of Experimental $E\{v_{cellx}\}$ and $E\{v_{cellx}\} \pm \sigma\{v_{cellx}\}$ Profiles of Passing Heat Shocked _S. cerevisiae_ Cells with $\phi_{DEP} = 1\ V_p$ 10 kHz			
Signature	v_{cellx0} [μm/s]	v_{cellxf} [μm/s]	$\%\Delta v_{cellx}$
$E\{v_{cellx}\} + \sigma\{v_{cellx}\}$	444.25	439.89	-1.0
$E\{v_{cellx}\}$	357.70	318.96	-10.8
$E\{v_{cellx}\} - \sigma\{v_{cellx}\}$	271.15	198.03	-16.5

Table 8-4: _$\%\Delta v_{cellx}$ analysis of experimental $E\{v_{cellx}\}$ and $E\{v_{cellx}\} \pm \sigma\{v_{cellx}\}$ profiles of passing heat shocked S. cerevisiae cells with $\phi_{DEP} = 1\ V_p$ 10 kHz._

The particle tracing simulation of Section 4.3 then attempted to reproduce the $E\{v_{cellx}\}$ profile of Figure 8-14. In an initial simulation, the particle was initially placed at (x_{cell0}, h_{cell0}) = (-125, 5) μm and given an initial velocity of $v_{cell0} = 357.70\ a_x$ μm/s (referring to Table 8-3). Equation (4-11) was employed to estimate $< v_{med} >$ as 545.07 a_x μm/s. The real part of the complex Clausius-Mossotti factor, Re$\{\underline{K}\}$, was assumed to be

0.13 (referring to Figure 7-3). The particle tracing simulation then proceeded to compute the trajectory of the cell as subjected to F_{DEP} and F_{drag}, computed using Equations (3-31) and (4-13), respectively. In this initial simulation, the particle adhered to the MEA. As such, the simulation was repeated with a raised initial position of (x_{cell0}, h_{cell0}) = (-125, 8.5) μm. The v_{cell0} = 357.70 a_x μm/s assumption was maintained, and < v_{med} > was re-computed as 356.25 a_x μm/s. In this second simulation, the particle did not adhere to the MEA. Both the elapsed time t and E_{ext}^2 / ϕ_{RF}^2 were plotted along the computed trajectory, yielding text files containing: (1) x_{cell}, h_{cell}, and t; and (2) x_{cell}, h_{cell}, and E_{ext}^2 / ϕ_{RF}^2.

The MATLAB® program of Appendix D was re-run, with additional code for the analysis of the particle tracing simulation executed. This additional code proceeds to read in the text file containing the simulated $x_{cell}(t)$ profile. The corresponding $v_{cellx}(t)$ profile was computed via the first-order backward finite difference approximation. Linear interpolation was employed to fit this $v_{cellx}(t)$ profile to a uniformly spaced x_{cell} line spanning ±125 μm in 0.5 μm steps. Figure 8-15 presents this fitted $v_{cellx}(x_{cell})$ profile along with the computed $E\{v_{cellx}\}$ and $E\{v_{cellx}\} \pm \sigma\{v_{cellx}\}$ profiles of Figure 8-14. Figure 8-15 shows that the simulated v_{cellx} profile reasonably approximates the experimental $E\{v_{cellx}\}$ profile. Table 8-5 presents the corresponding %Δv_{cellx} analysis of this simulated profile.

Figure 8-15: *The simulated v_{cellx} profile reasonably approximates the experimental $E\{v_{cellx}\}$ profile of passing heat shocked S. cerevisiae cells with ϕ_{DEP} = 1 V_p 10 kHz.*

Table 8-5: %Δv_{cellx} Analysis of Simulated v_{cellx} Profile of Passing Heat Shocked *S. cerevisiae* Cell with ϕ_{DEP} = 1 V$_p$ 10 kHz			
Signature	v_{cellx0} [μm/s]	v_{cellxf} [μm/s]	%Δv_{cellx}
Simulation	357.71	279.74	-21.8

Table 8-5: *%Δv_{cellx} analysis of simulated v_{cellx} profile*

of passing heat shocked S. cerevisiae cell with ϕ_{DEP} = 1 V$_p$ 10 kHz.

Figure 8-16 presents the ΔC_{MEA} signature produced by scaling the simulated $E_{ext}^2(t)$ / ϕ_{RF}^2 profile with the -3.28 x 10^{-26} F m^2 scaling factor computed in Section 7.4. The peak magnitude of Figure 8-16 matches the ΔC_{MEA} signatures featured in Figure 8-11. Notably, the shape of Figure 8-16 suggests that the h_{cell0} = 8.5 μm assumption used within the particle tracing simulation was higher than experimentally observed. However, the h_{cell0} = 8.5 μm assumption was necessary to prevent adhesion of the simulated particle to the MEA. This may indicate that the experimentally observed Re{$\underline{K}$} is within the interval 0 < Re{$\underline{K}$} < 0.13. However, it is worth noting that the error within the simulation as a result of neglecting the hydrodynamic lift force F_{lift} is most prominent when the point particle is close to the bottom of the microfluidic cross-channel subdomain.
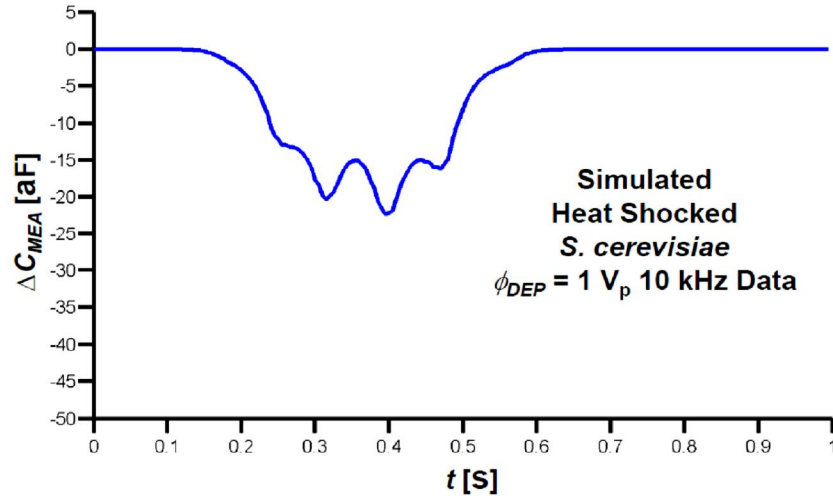
Figure 8-16: *Simulated ΔC_{MEA} signature induced by*

passing heat shocked S. cerevisiae cell with ϕ_{DEP} = 1 V$_p$ 10 kHz.

8.2.C   Analysis of $\phi_{DEP} = 0.5$ V$_\text{p}$ 100 kHz Data

Figure 8-17 presents the five experimental ΔC_{MEA} signatures selected from the $\phi_{DEP} = 0.5$ V$_\text{p}$ 100 kHz dataset. Visual inspection of these ΔC_{MEA} signatures suggests that they correspond to low initial elevation crossings, with h_{cell0} on the order of 4-6 μm.
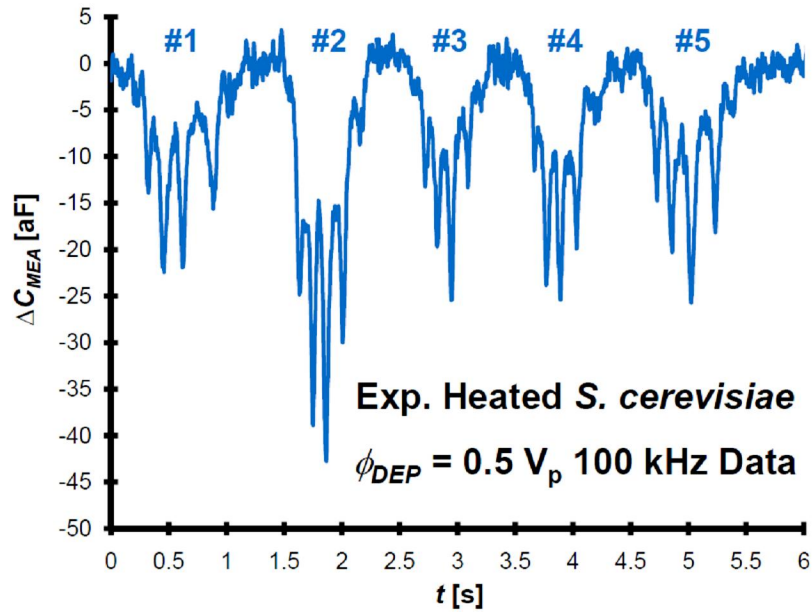
Figure 8-17: *Experimental ΔC_{MEA} signatures induced by passing heat shocked S. cerevisiae cells with $\phi_{DEP} = 0.5$ V$_p$ 100 kHz.*

The Tracker 2.60 analysis of Section 6.3.A was then repeated to analyze the captured MEA detection zone video corresponding to the ΔC_{MEA} signatures of Figure 8-17, yielding an $x_{cell}(t)$ dataset saved as a CSV file. The MATLAB® program of Appendix D analyzes this CSV file. Figure 8-18 presents these five $x_{cell}(t)$ profiles.

Figure 8-18: *Experimental xcell(t) profiles of passing heat shocked S. cerevisiae cells with ϕ_{DEP} = 0.5 V_p 100 kHz.*

The MATLAB® program of Appendix D estimated the $v_{cellx}(t)$ profiles corresponding to the ΔC_{MEA} signatures of Figure 8-17 via the first-order backward finite difference approximation. Linear interpolation was employed to fit each $v_{cellx}(t)$ profile to a uniformly spaced x_{cell} line spanning ±125 μm in 0.5 μm steps. Figure 8-19 presents these fitted $v_{cellx}(x_{cell})$ profiles.
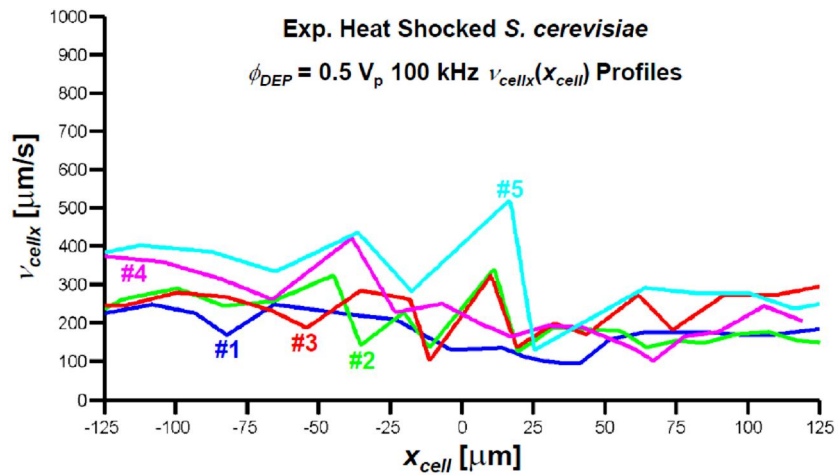
Figure 8-19: *Experimental vcellx(xcell) profiles of passing heat shocked S. cerevisiae cells with ϕ_{DEP} = 0.5 V_p 100 kHz.*

The initial v_{cellx}, v_{cellx0}, of each profile was estimated as the mean v_{cellx} within the -125 μm $\ddot{\text{O}} x_{cell}$ Ö-75 μm interval. The final v_{cellx}, v_{cellxf}, of each profile was estimated as the mean v_{cellx} within the 75 μm $\ddot{\text{O}} x_{cell}$ Ö125 μm interval. The relative percent change in v_{cellx}, %Δv_{cellx}, is then estimated using v_{cellx0} and v_{cellxf}. Table 8-6 summarizes the results of this %Δv_{cellx} analysis.

Table 8-6: %Δv_{cellx} Analysis of Experimental v_{cellx} Profiles of Passing Heat Shocked *S. cerevisiae* Cells with ϕ_{DEP} = 0.5 V$_p$ 100 kHz			
Signature	v_{cellx0} [μm/s]	v_{cellxf} [μm/s]	%Δv_{cellx}
1	221.07	173.90	-21.3
2	265.25	161.18	-39.2
3	263.40	262.42	-0.4
4	342.73	200.94	-41.4
5	387.90	265.87	-31.5
E{ }	*296.07*	*212.86*	*-26.8*
σ{ }	*67.55*	*48.98*	*16.7*

**Table 8-6:** *%Δv_{cellx} analysis of experimental v_{cellx} profiles of passing heat shocked S. cerevisiae cells with ϕ_{DEP} = 0.5 V$_p$ 100 kHz.*

The expectation and standard deviation of each of the v_{cellx} profiles, $E\{v_{cellx}\}$ and $\sigma\{v_{cellx}\}$, was then computed at each point along x_{cell}. Figure 8-20 presents the computed $E\{v_{cellx}\}$ and $E\{v_{cellx}\} \pm \sigma\{v_{cellx}\}$ profiles. Table 8-7 presents the corresponding %Δv_{cellx} analysis of these three statistical profiles.
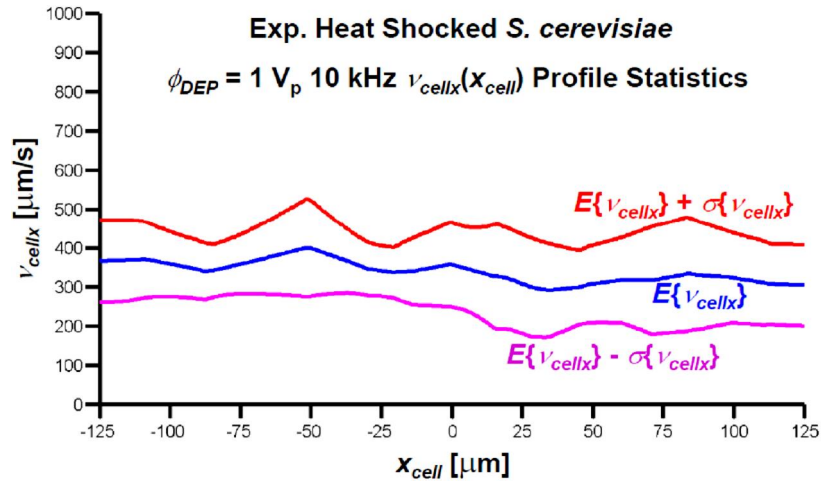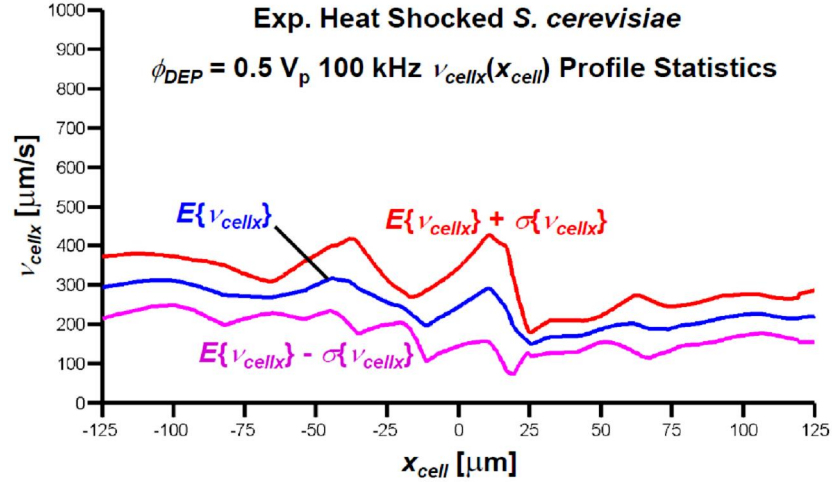
Figure 8-20: *Experimental v_{cellx} profile statistics of passing heat shocked S. cerevisiae cells with $\phi_{DEP} = 0.5\ V_p$ 100 kHz.*

Signature	v_{cellx0} [μm/s]	v_{cellxf} [μm/s]	%Δv_{cellx}
Table 8-7: %Δv_{cellx} Analysis of Experimental $E\{v_{cellx}\}$ and $E\{v_{cellx}\} \pm \sigma\{v_{cellx}\}$ Profiles of Passing Heat Shocked S. cerevisiae Cells with $\phi_{DEP} = 0.5\ V_p$ 100 kHz			
$E\{v_{cellx}\} + \sigma\{v_{cellx}\}$	364.80	266.36	-27.0
$E\{v_{cellx}\}$	296.07	213.26	-28.0
$E\{v_{cellx}\} - \sigma\{v_{cellx}\}$	227.34	160.15	-18.4

Table 8-7: *%Δv_{cellx} analysis of experimental $E\{v_{cellx}\}$ and $E\{v_{cellx}\} \pm \sigma\{v_{cellx}\}$ profiles of passing heat shocked S. cerevisiae cells with $\phi_{DEP} = 0.5\ V_p$ 100 kHz.*

The particle tracing simulation of Section 4.3 then attempted to reproduce the $E\{v_{cellx}\}$ profile of Figure 8-20. In an initial simulation, the particle was initially placed at (x_{cell0}, h_{cell0}) = (-125, 5) μm and given an initial velocity of v_{cell0} = 296.07 a_x μm/s (referring to Table 8-6). Equation (4-11) was employed to estimate $< v_{med} >$ as 451.15 a_x μm/s. Re$\{\underline{K}\}$ was assumed to be 0.35 (referring to Figure 7-3). The particle tracing simulation then proceeded to compute the trajectory of the cell as subjected to F_{DEP} and F_{drag}, computed using Equations (3-31) and (4-13), respectively. In this initial simulation, the particle adhered to the MEA. As such, the simulation was repeated with a raised initial position of (x_{cell0}, h_{cell0}) = (-125, 8) μm. The v_{cell0} = 296.07 a_x μm/s assumption was maintained, and $< v_{med} >$ was re-computed as 308.41 a_x μm/s. In this second

- 104 -

simulation, the particle did not adhere to the MEA. Both the elapsed time t and E_{ext}^2 / ϕ_{RF}^2 were plotted along the computed trajectory, yielding text files containing: (1) x_{cell}, h_{cell}, and t; and (2) x_{cell}, h_{cell}, and E_{ext}^2 / ϕ_{RF}^2.

The MATLAB® program of Appendix D was re-run, with additional code for the analysis of the particle tracing simulation executed. This additional code proceeds to read in the text file containing the simulated $x_{cell}(t)$ profile. The corresponding $v_{cellx}(t)$ profile was computed via the first-order backward finite difference approximation. Linear interpolation was employed to fit this $v_{cellx}(t)$ profile to a uniformly spaced x_{cell} line spanning ±125 µm in 0.5 µm steps. Figure 8-21 presents this fitted $v_{cellx}(x_{cell})$ profile along with the computed $E\{v_{cellx}\}$ and $E\{v_{cellx}\} \pm \sigma\{v_{cellx}\}$ profiles of Figure 8-21. Figure 8-21 shows that the simulated v_{cellx} profile reasonably approximates the experimental $E\{v_{cellx}\}$ profile. Table 8-8 presents the corresponding %Δv_{cellx} analysis of this simulated profile.
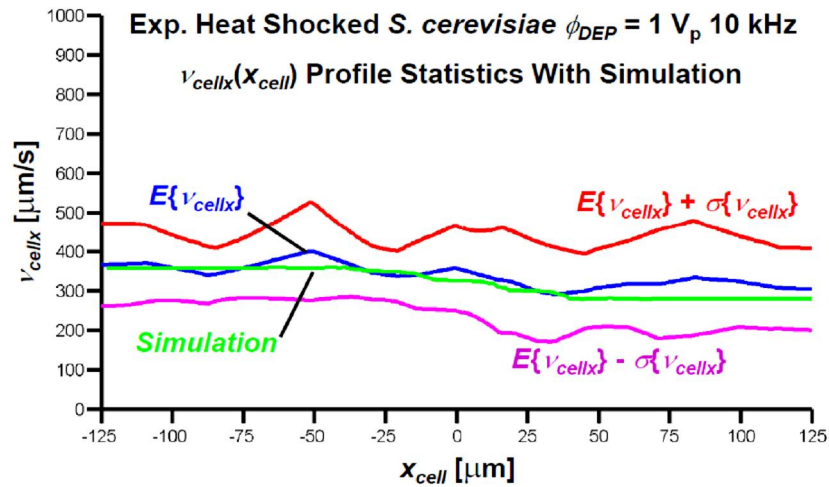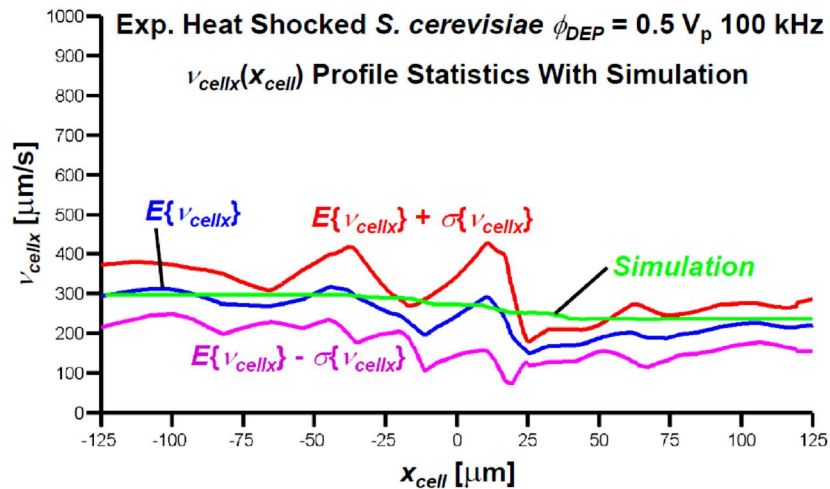

Figure 8-21: *The simulated v_{cellx} profile reasonably approximates the experimental $E\{v_{cellx}\}$ profile of passing heat shocked S. cerevisiae cells with ϕ_{DEP} = 0.5 V_p 100 kHz.*

Table 8-8: %Δv_{cellx} Analysis of Simulated v_{cellx} Profile of Passing Heat Shocked *S. cerevisiae* Cell with ϕ_{DEP} = 0.5 V$_p$ 100 kHz			
Signature	v_{cellx0} [μm/s]	v_{cellxf} [μm/s]	%Δv_{cellx}
Simulation	296.08	235.70	-20.4

Table 8-8: *%Δv_{cellx} analysis of simulated v_{cellx} profile of passing heat shocked S. cerevisiae cell with ϕ_{DEP} = 0.5 V$_p$ 100 kHz.*

Figure 8-22 presents the ΔC_{MEA} signature produced by scaling the simulated $E_{ext}^2(t)$ / ϕ_{RF}^2 profile with the -3.28 x 10^{-26} F m^2 scaling factor computed in Section 7.4. The peak magnitude of Figure 8-22 matches the ΔC_{MEA} signatures featured in Figure 8-17. Notably, the shape of Figure 8-22 suggests that the h_{cell0} = 8.0 μm assumption used within the particle tracing simulation was higher than experimentally observed. However, the h_{cell0} = 8.0 μm assumption was necessary to prevent adhesion of the simulated particle to the MEA. This may indicate that the experimentally observed Re{$\underline{K}$} is within the interval 0 < Re{$\underline{K}$} < 0.35. However, it is worth noting that the error within the simulation as a result of neglecting $\boldsymbol{F}_{lift}$ is most prominent when the point particle is close to the bottom of the microfluidic cross-channel subdomain.
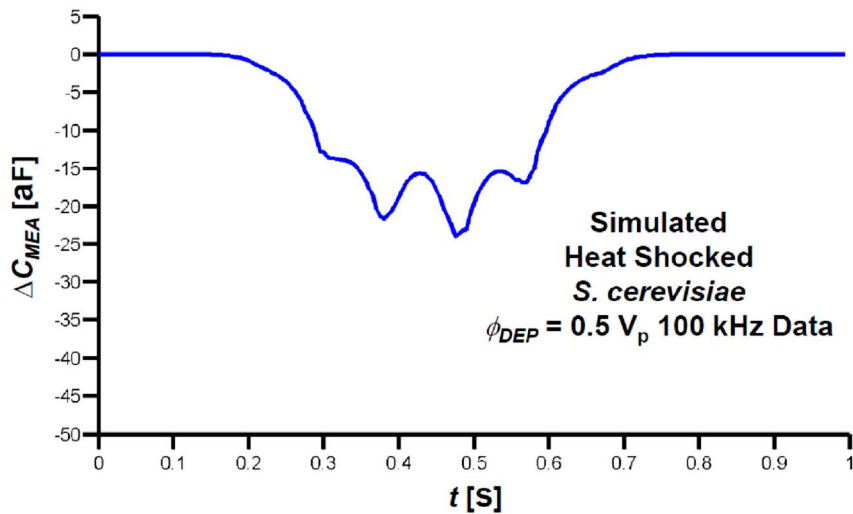
Figure 8-22: *Simulated ΔC_{MEA} signature induced by passing heat shocked S. cerevisiae cell with ϕ_{DEP} = 0.5 V$_p$ 100 kHz.*

8.2.D Analysis of $\phi_{DEP} = 0.5\ V_p$ 1 MHz Data

Figure 8-23 presents the five experimental ΔC_{MEA} signatures selected from the $\phi_{DEP} = 0.5\ V_p$ 1 MHz dataset. Visual inspection of these ΔC_{MEA} signatures suggests that they correspond to low initial elevation crossings, with h_{cell0} on the order of 4-6 µm.
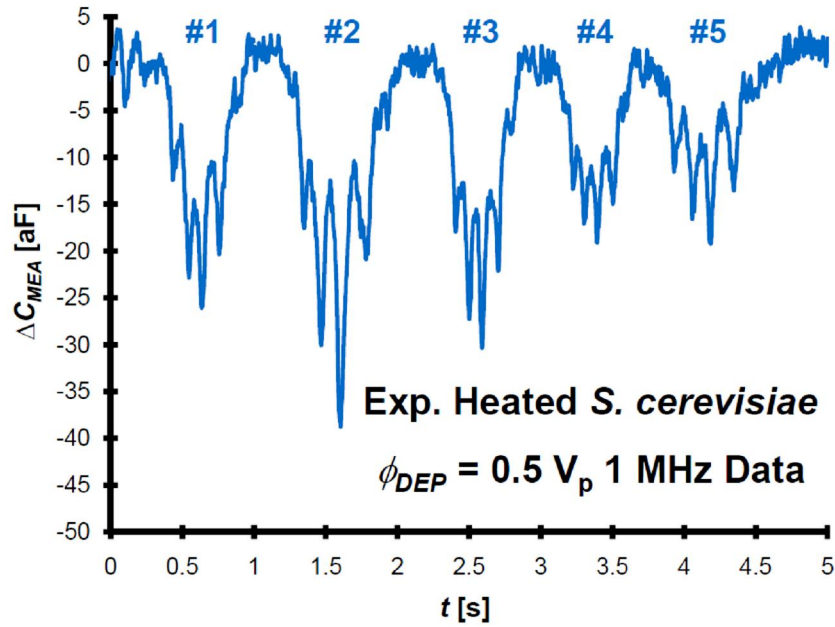
Figure 8-23: *Experimental ΔC_{MEA} signatures induced by passing heat shocked S. cerevisiae cells with $\phi_{DEP} = 0.5\ V_p$ 1 MHz.*

The Tracker 2.60 analysis of Section 6.3.A was then repeated to analyze the captured MEA detection zone video corresponding to the ΔC_{MEA} signatures of Figure 8-23, yielding an $x_{cell}(t)$ dataset saved as a CSV file. The MATLAB® program of Appendix D analyzes this CSV file. Figure 8-24 presents these five $x_{cell}(t)$ profiles.

Figure 8-24: *Experimental x_cell(t) profiles of passing heat shocked S. cerevisiae cells with ϕ_DEP = 0.5 V_p 1 MHz.*

The MATLAB® program of Appendix D estimated the $v_{cellx}(t)$ profiles corresponding to the ΔC_{MEA} signatures of Figure 8-23 via the first-order backward finite difference approximation. Linear interpolation was employed to fit each $v_{cellx}(t)$ profile to a uniformly spaced x_{cell} line spanning ±125 μm in 0.5 μm steps. Figure 8-25 presents these fitted $v_{cellx}(x_{cell})$ profiles.

Figure 8-25: *Experimental v_cellx(x_cell) profiles of passing heat shocked S. cerevisiae cells with ϕ_DEP = 0.5 V_p 1 MHz.*

The initial v_{cellx}, v_{cellx0}, of each profile was estimated as the mean v_{cellx} within the -125 μm Ö x_{cell} Ö -75 μm interval. The final v_{cellx}, v_{cellxf}, of each profile was estimated as the mean v_{cellx} within the 75 μm Ö x_{cell} Ö 125 μm interval. The relative percent change in v_{cellx}, $\%\Delta v_{cellx}$, is then estimated using v_{cellx0} and v_{cellxf}. Table 8-9 summarizes the results of this $\%\Delta v_{cellx}$ analysis.

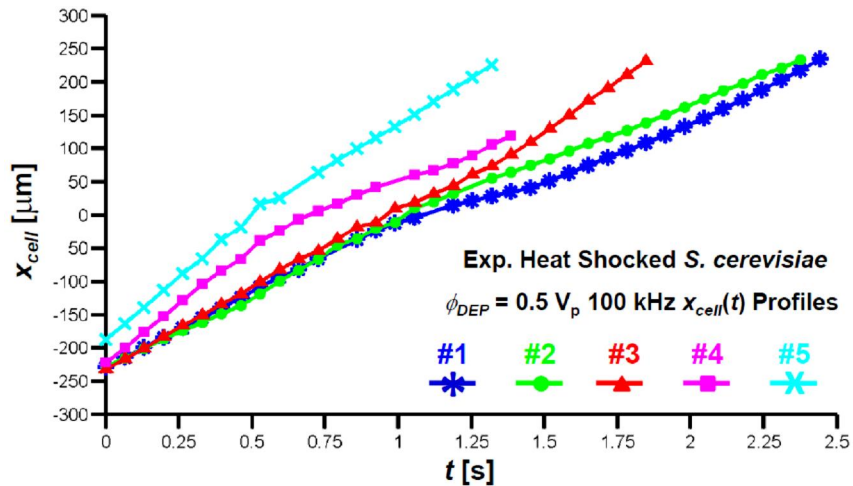| Table 8-9: $\%\Delta v_{cellx}$ Analysis of Experimental v_{cellx} Profiles of Passing Heat Shocked *S. cerevisiae* Cells with $\phi_{DEP} = 0.5\ V_p$ 1 MHz			
Signature	v_{cellx0} [μm/s]	v_{cellxf} [μm/s]	$\%\Delta v_{cellx}$
1	195.37	175.14	-10.4
2	231.53	178.38	-23.0
3	327.79	246.19	-24.9
4	341.87	192.35	-43.7
5	209.75	173.77	-17.2
E{ }	*261.26*	*193.17*	*-23.8*
σ{ }	*68.56*	*30.55*	*12.5*

Table 8-9: *$\%\Delta v_{cellx}$ analysis of experimental v_{cellx} profiles of passing heat shocked S. cerevisiae cells with $\phi_{DEP} = 0.5\ V_p$ 1 MHz.*

The expectation and standard deviation of each of the v_{cellx} profiles, $E\{v_{cellx}\}$ and $\sigma\{v_{cellx}\}$, was then computed at each point along x_{cell}. Figure 8-26 presents the computed $E\{v_{cellx}\}$ and $E\{v_{cellx}\} \pm \sigma\{v_{cellx}\}$ profiles. Table 8-10 presents the corresponding $\%\Delta v_{cellx}$ analysis of these three statistical profiles.

Figure 8-26: *Experimental v_{cellx} profile statistics of passing heat shocked S. cerevisiae cells with ϕ_{DEP} = 0.5 V_p 1 MHz.*

Table 8-10: %Δv_{cellx} Analysis of Experimental $E\{v_{cellx}\}$ and $E\{v_{cellx}\} \pm \sigma\{v_{cellx}\}$ Profiles of Passing Heat Shocked *S. cerevisiae* Cells with ϕ_{DEP} = 0.5 V_p 1 MHz			
Signature	v_{cellx0} [μm/s]	v_{cellxf} [μm/s]	%Δv_{cellx}
$E\{v_{cellx}\} + \sigma\{v_{cellx}\}$	330.33	225.57	-31.7
$E\{v_{cellx}\}$	261.26	193.17	-26.1
$E\{v_{cellx}\} - \sigma\{v_{cellx}\}$	192.19	160.76	-9.5

Table 8-10: *%Δv_{cellx} analysis of experimental $E\{v_{cellx}\}$ and $E\{v_{cellx}\} \pm \sigma\{v_{cellx}\}$ profiles of passing heat shocked S. cerevisiae cells with ϕ_{DEP} = 0.5 V_p 1 MHz.*

The particle tracing simulation of Section 4.3 then attempted to reproduce the $E\{v_{cellx}\}$ profile of Figure 8-26. In an initial simulation, the particle was initially placed at (x_{cell0}, h_{cell0}) = (-125, 5) μm and given an initial velocity of v_{cell0} = 261.26 a_x μm/s (referring to Table 8-9). Equation (4-11) was employed to estimate $< v_{med} >$ as 398.11 a_x μm/s. Re$\{\underline{K}\}$ was assumed to be 0.22 (referring to Figure 7-3). The particle tracing simulation then proceeded to compute the trajectory of the cell as subjected to F_{DEP} and F_{drag}, computed using Equations (3-31) and (4-13), respectively. In this initial simulation, the particle adhered to the MEA. As such, the simulation was repeated with a raised initial position of (x_{cell0}, h_{cell0}) = (-125, 7) μm. The v_{cell0} = 261.26 a_x μm/s assumption was maintained, and $< v_{med} >$ was re-computed as 301.60 a_x μm/s. In this second

simulation, the particle did not adhere to the MEA. Both the elapsed time t and E_{ext}^2 / ϕ_{RF}^2 were plotted along the computed trajectory, yielding text files containing: (1) x_{cell}, h_{cell}, and t; and (2) x_{cell}, h_{cell}, and E_{ext}^2 / ϕ_{RF}^2.

The MATLAB® program of Appendix D was re-run, with additional code for the analysis of the particle tracing simulation executed. This additional code proceeds to read in the text file containing the simulated $x_{cell}(t)$ profile. The corresponding $v_{cellx}(t)$ profile was computed via the first-order backward finite difference approximation. Linear interpolation was employed to fit this $v_{cellx}(t)$ profile to a uniformly spaced x_{cell} line spanning ±125 µm in 0.5 µm steps. Figure 8-27 presents this fitted $v_{cellx}(x_{cell})$ profile along with the computed $E\{v_{cellx}\}$ and $E\{v_{cellx}\} \pm \sigma\{v_{cellx}\}$ profiles of Figure 8-26. Figure 8-27 shows that the simulated v_{cellx} profile reasonably approximates the experimental $E\{v_{cellx}\}$ profile. Table 8-11 presents the corresponding %Δv_{cellx} analysis of this simulated profile.

***Figure 8-27:*** *The simulated v_{cellx} profile reasonably approximates the experimental $E\{v_{cellx}\}$ profile of passing heat shocked S. cerevisiae cells with ϕ_{DEP} = 0.5 V_p 1 MHz.*

Table 8-11: %Δ v_{cellx} Analysis of Simulated v_{cellx} Profile of Passing Heat Shocked *S. cerevisiae* Cell with ϕ_{DEP} = 0.5 V$_p$ 1 MHz			
Signature	v_{cellx0} [μm/s]	v_{cellxf} [μm/s]	%Δv_{cellx}
Simulation	261.27	209.76	-19.7

Table 8-11: *%Δv_{cellx} analysis of simulated v_{cellx} profile of passing heat shocked S. cerevisiae cell with ϕ_{DEP} = 0.5 V$_p$ 1 MHz.*

Figure 8-28 presents the ΔC_{MEA} signature produced by scaling the simulated $E_{ext}^2(t) / \phi_{RF}^2$ profile with the -3.28 x 10^{-26} F m^2 scaling factor computed in Section 7.4. The peak magnitude of Figure 8-28 matches the ΔC_{MEA} signatures featured in Figure 8-23. Notably, the shape of Figure 8-28 suggests that the h_{cell0} = 7.0 μm assumption used within the particle tracing simulation was higher than experimentally observed. However, the h_{cell0} = 7.0 μm assumption was necessary to prevent adhesion of the simulated particle to the MEA. This may indicate that the experimentally observed Re{$\underline{K}$} is within the interval 0 < Re{$\underline{K}$} < 0.22. However, it is worth noting that the error within the simulation as a result of neglecting F_{lift} is most prominent when the point particle is close to the bottom of the microfluidic cross-channel subdomain.
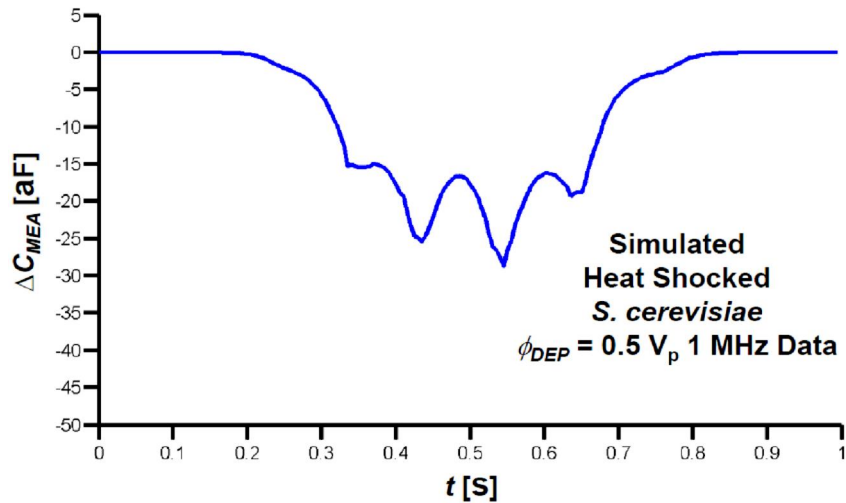
Figure 8-28: *Simulated ΔC_{MEA} signature induced by passing heat shocked S. cerevisiae cell with ϕ_{DEP} = 0.5 V$_p$ 1 MHz.*

Chapter 9

Analysis of a Homogeneous Viable
Saccharomyces cerevisiae Cell Subpopulation

9.1   *Saccharomyces cerevisiae* Sample Preparation

A single granule of Fleischmann's® Traditional active dry yeast (presented in Section 8.1) was rehydrated and mixed into 20 mL of the diluted methylene blue solution (prepared as outlined in Section 6.1). Methylene blue was selected as it preferentially stains *Saccharomyces cerevisiae* cells whose cytoplasmic membranes have been compromised, thus labelling only nonviable cells. As discussed in Section 8.1, a high percentage of the rehydrated *S. cerevisiae* cells from this batch of Fleischmann's® Traditional active dry yeast are nonviable, with compromised membranes, prior to the application of any further undue stress (such as being heat shocked). However, as (1) the microflow cytometer analyzes cells on a cell-by-cell basis and (2) the methylene blue dye labels the nonviable cells: the Fleischmann's® Traditional active dry yeast granules are suitable for this work.

9.2   Analysis of Actuated Viable *Saccharomyces cerevisiae*

A heterogeneous population of viable and nonviable *S. cerevisiae* cells suspended in the diluted methylene blue solution was prepared as outlined in Section 9.1. This *S. cerevisiae* sample was injected into the microflow cytometer, which was simultaneously operated as both an optical assay and a capacitive cytometer. The relative elevation of the syringes was adjusted until the *S. cerevisiae* cells were observed to pass over the microelectrode array (MEA) with an average cross-over time of approximately 400 ms. The time-harmonic dielectrophoretic (DEP) actuation ϕ_{DEP} potential was then set to: 0 V_p, 1 V_p 10 kHz, 1 V_p 18 kHz, and 0.5 V_p 100 kHz. $|\phi_{DEP}|$ was halved in the 100 kHz case so as to reduce the cellular adhesion to the MEA observed with $|\phi_{DEP}| = 1$ V_p. Approximately 60 minutes of data was gathered at each ϕ_{DEP} setting. Each experimental

dataset was then examined to select five S signatures, with no bias as to the initial cellular elevation h_{cell0}, which were visually confirmed to correspond to individual unstained *S. cerevisiae* cells passing over the MEA. Each S signature was converted into a ΔC_{MEA} signature using the capacitive cytometer's dS/dC_{MEA} ≈ 57 mV/aF overall sensitivity (as computed in Section 6.2).

9.2.A   Analysis of $\phi_{DEP} = 0$ V_p Data

Figure 9-1 presents the five experimental ΔC_{MEA} signatures selected from the baseline $\phi_{DEP} = 0$ V_p dataset. Visual inspection of these ΔC_{MEA} signatures suggests that they correspond to low elevation crossings, with $h_{cell0}$ on the order of 4-6 μm (as is consistent with the polystyrene microsphere (PSS) observations of Section 6.3 and the heat shocked *S. cerevisiae* cell observations of Section 8.2).
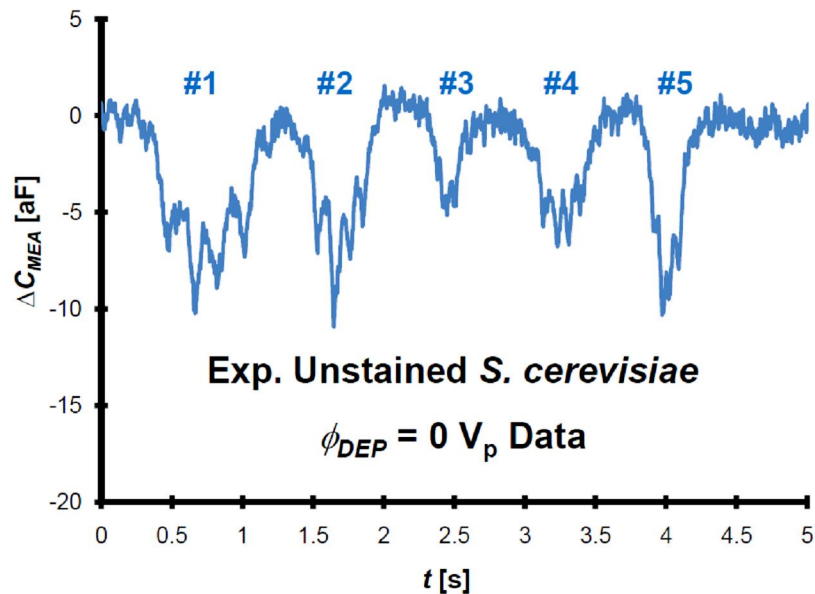
Figure 9-1: *Experimental ΔC_{MEA} signatures induced by passing viable S. cerevisiae cells with $\phi_{DEP} = 0$ V_p.*

The Tracker 2.60 analysis of Section 6.3.A was then repeated (with a refined brightness of 50) to analyze the captured MEA detection zone video corresponding to the ΔC_{MEA} signatures of Figure 9-1, yielding an $x_{cell}(t)$ dataset saved as a comma separated

value (CSV) file. The MATLAB® program of Appendix D analyzes this CSV file. Figure 9-2 presents these five $x_{cell}(t)$ profiles.
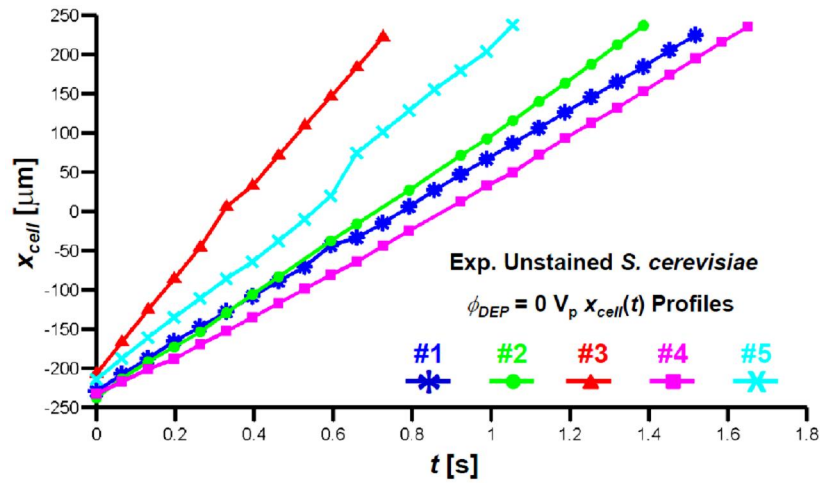
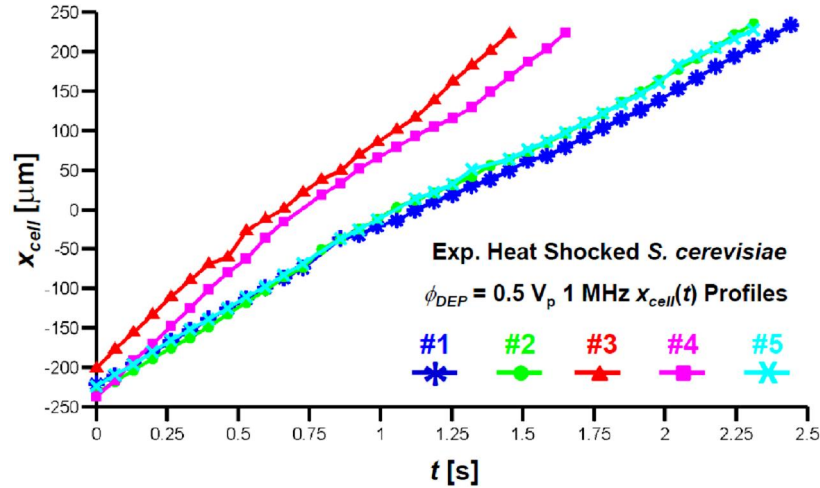***Figure 9-2:*** *Experimental $x_{cell}(t)$ profiles of passing viable S. cerevisiae cells with $\phi_{DEP} = 0$ V_p.*

The MATLAB® program of Appendix D estimated the lateral cellular velocity $v_{cellx}(t)$ profiles corresponding to the ΔC_{MEA} signatures of Figure 9-1 via the first-order backward finite difference approximation. Linear interpolation was then employed to fit each $v_{cellx}(t)$ profile to a uniformly spaced x_{cell} line spanning ± 125 μm in 0.5 μm steps. Figure 9-3 presents these fitted $v_{cellx}(x_{cell})$ profiles.
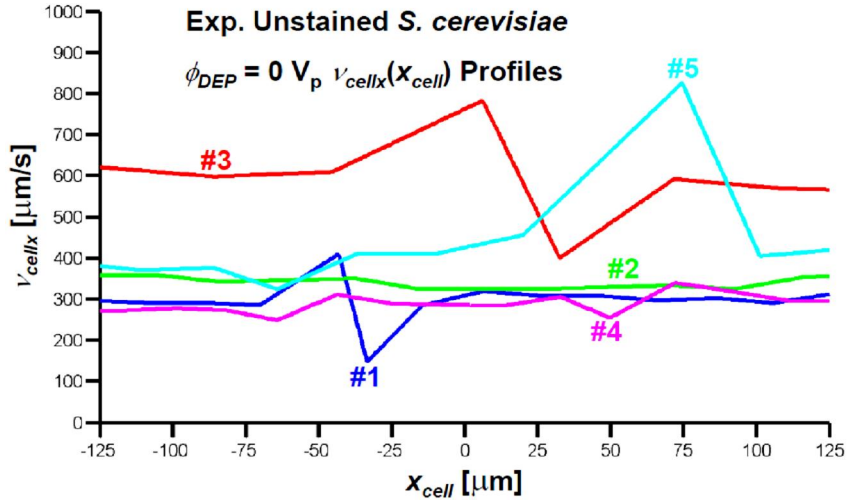
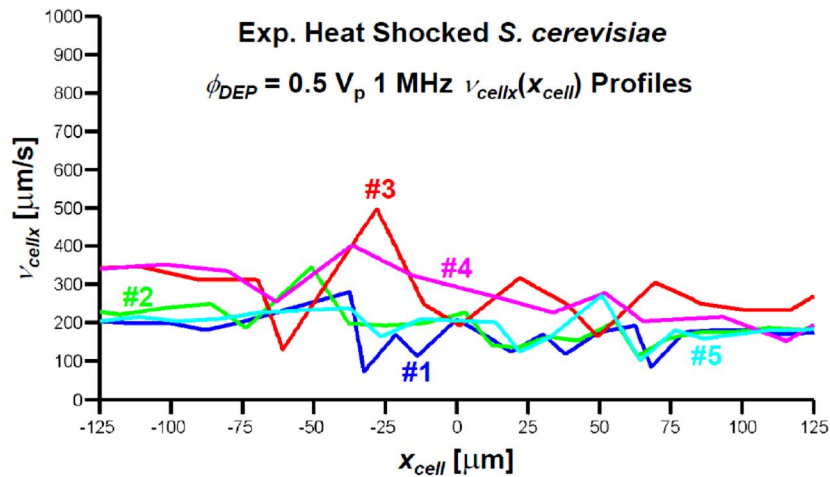***Figure 9-3:*** *Experimental $v_{cellx}(x_{cell})$ profiles*

of passing viable S. cerevisiae cells with $\phi_{DEP} = 0\ V_p$.

The initial v_{cellx}, v_{cellx0}, of each profile was estimated as the mean v_{cellx} within the -125 μm $\ddot{O}x_{cell}$ $\ddot{O}$-75 μm interval. The final v_{cellx}, v_{cellxf}, of each profile was estimated as the mean v_{cellx} within the 75 μm $\ddot{O}x_{cell}$ $\ddot{O}$125 μm interval. The relative percent change in v_{cellx}, $\%\Delta v_{cellx}$, is then estimated using v_{cellx0} and v_{cellxf}. Table 9-1 summarizes the results of this $\%\Delta v_{cellx}$ analysis.

Table 9-1: $\%\Delta v_{cellx}$ Analysis of Experimental v_{cellx} Profiles of Passing Viable *S. cerevisiae* Cells with $\phi_{DEP} = 0\ V_p$			
Signature	v_{cellx0} [μm/s]	v_{cellxf} [μm/s]	$\%\Delta v_{cellx}$
1	290.88	299.26	2.9
2	352.41	338.20	-4.0
3	607.23	575.65	-5.2
4	273.47	310.79	13.7
5	371.70	517.43	39.2
E{ }	*379.14*	*408.27*	*9.3*
σ{ }	*133.93*	*128.67*	*18.3*

Table 9-1: *$\%\Delta v_{cellx}$ analysis of experimental v_{cellx} profiles*

of passing viable S. cerevisiae cells with $\phi_{DEP} = 0\ V_p$.

The expectation and standard deviation of each of the v_{cellx} profiles, $E\{v_{cellx}\}$ and $\sigma\{v_{cellx}\}$, was then computed at each point along x_{cell}. Figure 9-4 presents the computed $E\{v_{cellx}\}$ and $E\{v_{cellx}\} \pm \sigma\{v_{cellx}\}$ profiles. Table 9-2 presents the corresponding $\%\Delta v_{cellx}$ analysis of these three statistical profiles.
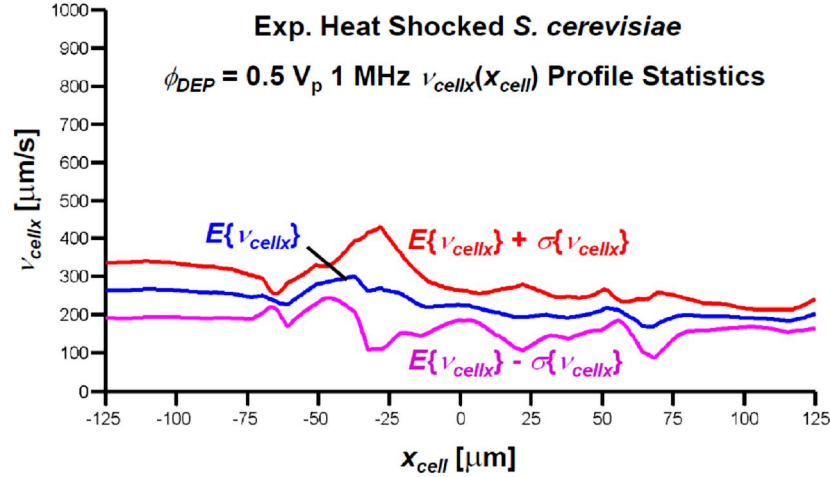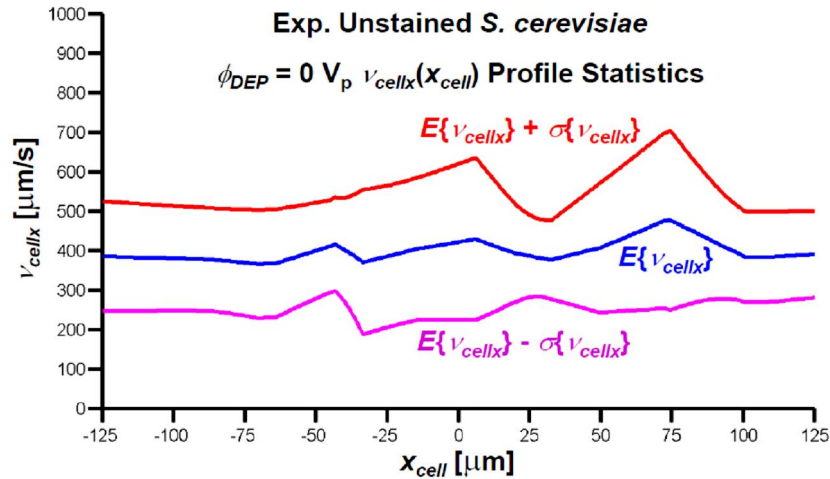

Figure 9-4: *Experimental v_{cellx} profile statistics of passing viable S. cerevisiae cells with $\phi_{DEP} = 0\ V_p$.*

Table 9-2: $\%\Delta v_{cellx}$ Analysis of Experimental $E\{v_{cellx}\}$ and $E\{v_{cellx}\} \pm \sigma\{v_{cellx}\}$ Profiles of Passing Viable *S. cerevisiae* Cells with $\phi_{DEP} = 0\ V_p$			
Signature	v_{cellx0} [μm/s]	v_{cellxf} [μm/s]	$\%\Delta v_{cellx}$
$E\{v_{cellx}\} + \sigma\{v_{cellx}\}$	513.11	545.61	6.3
$E\{v_{cellx}\}$	379.14	408.27	7.7
$E\{v_{cellx}\} - \sigma\{v_{cellx}\}$	245.18	270.93	5.0

Table 9-2: *$\%\Delta v_{cellx}$ analysis of experimental $E\{v_{cellx}\}$ and $E\{v_{cellx}\} \pm \sigma\{v_{cellx}\}$ profiles of passing viable S. cerevisiae cells with $\phi_{DEP} = 0\ V_p$.*

The particle tracing simulation of Section 4.3 then attempted to reproduce the $E\{v_{cellx}\}$ profile of Figure 9-4. In this simulation, the particle was initially placed at (x_{cell0}, h_{cell0}) = (-125, 5) μm and given an initial velocity of v_{cell0} = 379.14 a_x μm/s (referring to Table 9-1). Equation (4-11) was employed to estimate the mean of the parabolic fluid velocity profile as $< v_{med} > = 577.74\ a_x$ μm/s. The particle tracing

simulation proceeded to compute the trajectory of the cell as subjected to the vicious fluid drag force, F_{drag}, computed using Equation (4-13). Both the elapsed time t and E_{ext}^2 / ϕ_{RF}^2 were plotted along the computed trajectory, yielding text files containing: (1) x_{cell}, h_{cell}, and t; and (2) x_{cell}, h_{cell}, and E_{ext}^2 / ϕ_{RF}^2.

The MATLAB® program of Appendix D was re-run, with additional code for the analysis of the particle tracing simulation executed. This additional code proceeds to read in the text file containing the simulated $x_{cell}(t)$ profile. The corresponding $v_{cellx}(t)$ profile was computed via the first-order backward finite difference approximation. Linear interpolation was employed to fit this $v_{cellx}(t)$ profile to a uniformly spaced x_{cell} line spanning ±125 μm in 0.5 μm steps. Figure 9-5 presents this fitted $v_{cellx}(x_{cell})$ profile along with the computed $E\{v_{cellx}\}$ and $E\{v_{cellx}\} \pm \sigma\{v_{cellx}\}$ profiles of Figure 9-4. Figure 9-5 shows that the simulated v_{cellx} profile reasonably approximates the experimental $E\{v_{cellx}\}$ profile. As this simulation did not include a DEP actuation force F_{DEP}, the simulated h_{cell} and v_{cellx} remained constant.
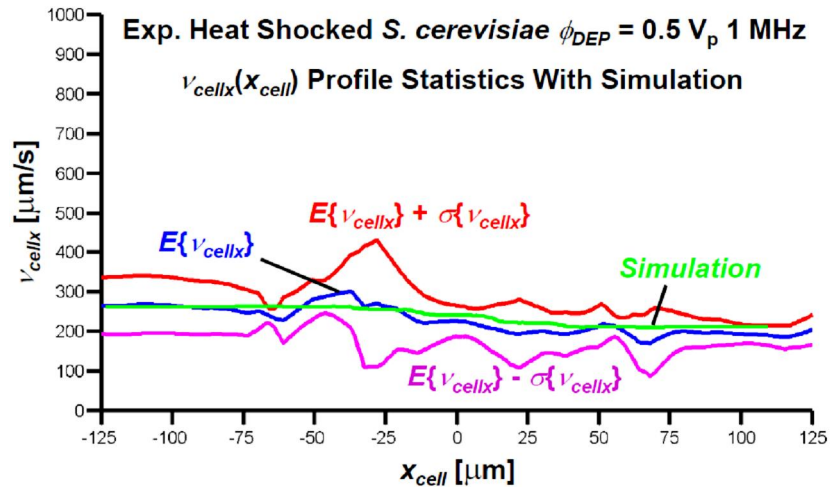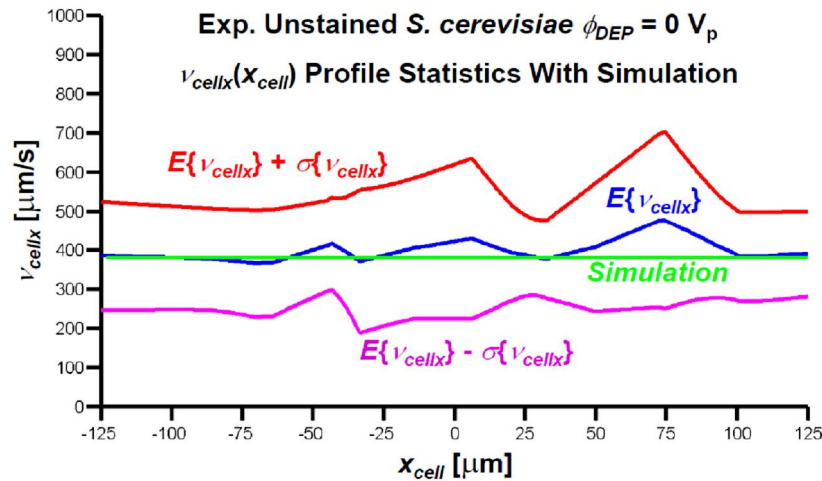

Figure 9-5: _The simulated v_{cellx} profile reasonably approximates the experimental $E\{v_{cellx}\}$ profile of passing viable S. cerevisiae cells with $\phi_{DEP} = 0$ V_p._

Figure 9-6 presents the ΔC_{MEA} signature produced by scaling the simulated $E_{ext}^2(t) / \phi_{RF}^2$ profile with the -3.28 x 10^{-26} F m^2 scaling factor computed in Section 7.4. The shape of Figure 9-6 resembles the ΔC_{MEA} signatures of Figure 9-1, verifying that h_{cell0} = 5 μm was a reasonable assumption within the particle tracing simulation.

However, the peak magnitude of Figure 9-6 is larger than the ΔC_{MEA} signatures of Figure 9-1.
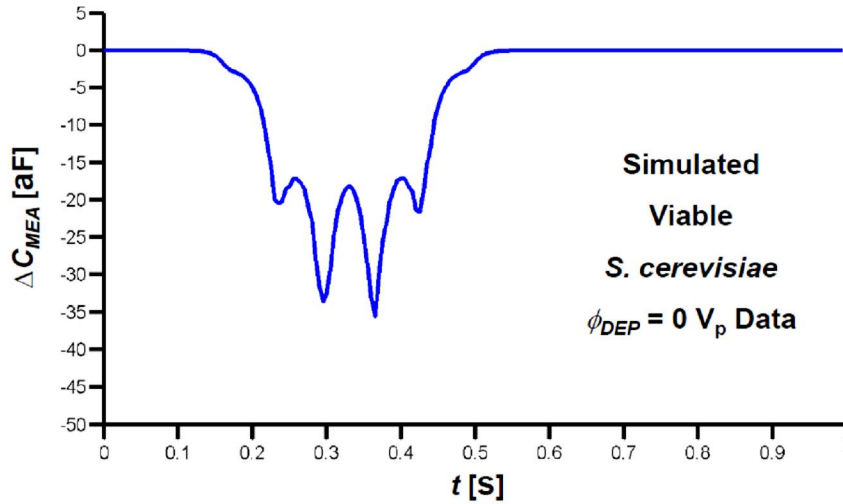
Figure 9-6: *Simulated ΔC_{MEA} signature induced by passing viable S. cerevisiae cell with $\phi_{DEP} = 0\ V_p$.*

9.2.B   Analysis of $\phi_{DEP} = 1\ V_p$ 10 kHz Data

Figure 9-7 presents the five experimental ΔC_{MEA} signatures selected from the $\phi_{DEP} = 1\ V_p$ 10 kHz dataset. Visual inspection of these ΔC_{MEA} signatures suggests that they correspond to low initial elevation crossings, with h_{cell0} on the order of 4-6 μm.
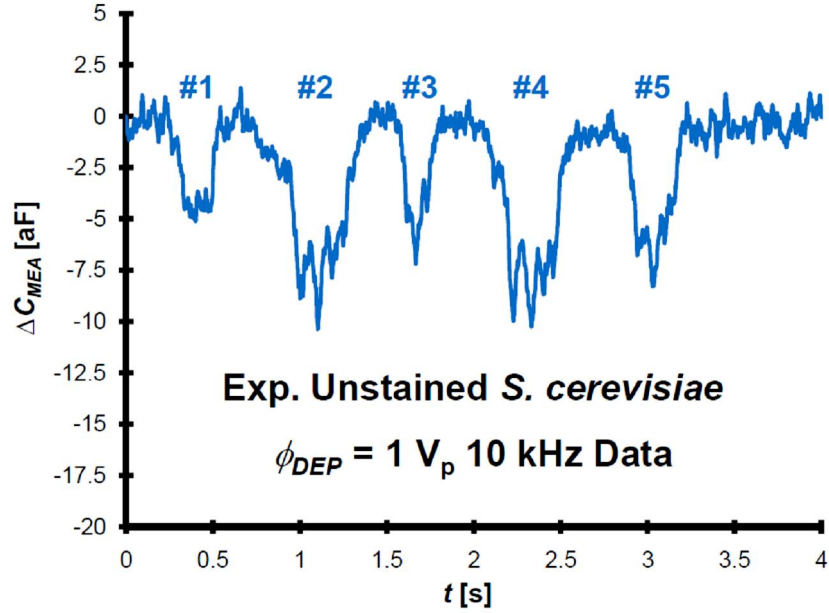
Figure 9-7: *Experimental ΔC$_{MEA}$ signatures induced by passing viable S. cerevisiae cells with ϕ_{DEP} = 1 V$_p$ 10 kHz.*

The Tracker 2.60 analysis of Section 6.3.A was then repeated (with a refined brightness of 50) to analyze the captured MEA detection zone video corresponding to the ΔC$_{MEA}$ signatures of Figure 9-7, yielding an $x_{cell}(t)$ dataset saved as a CSV file. The MATLAB® program of Appendix D analyzes this CSV file. Figure 9-8 presents these five $x_{cell}(t)$ profiles.
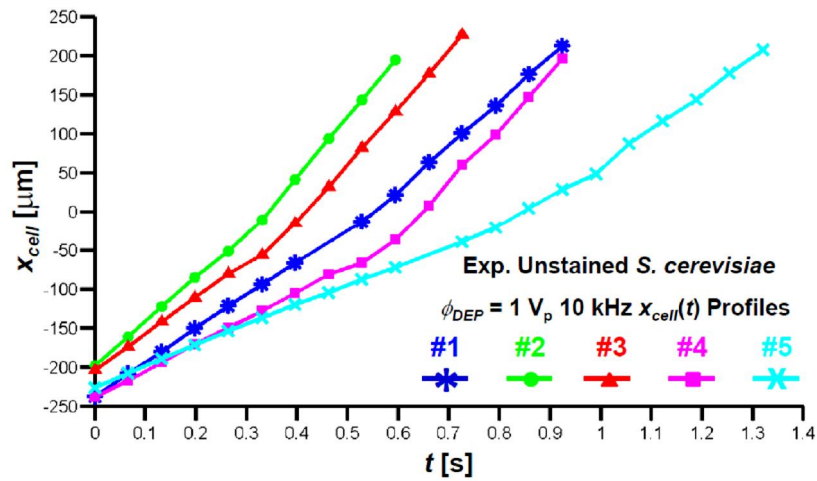
Figure 9-8: *Experimental x$_{cell}$(t) profiles of passing viable S. cerevisiae cells with ϕ_{DEP} = 1 V$_p$ 10 kHz.*

The MATLAB® program of Appendix D estimated the $v_{cellx}(t)$ profiles corresponding to the ΔC_{MEA} signatures of Figure 9-7 via the first-order backward finite difference approximation. Linear interpolation was employed to fit each $v_{cellx}(t)$ profile to a uniformly spaced x_{cell} line spanning ± 125 μm in 0.5 μm steps. Figure 9-9 presents these fitted $v_{cellx}(x_{cell})$ profiles.
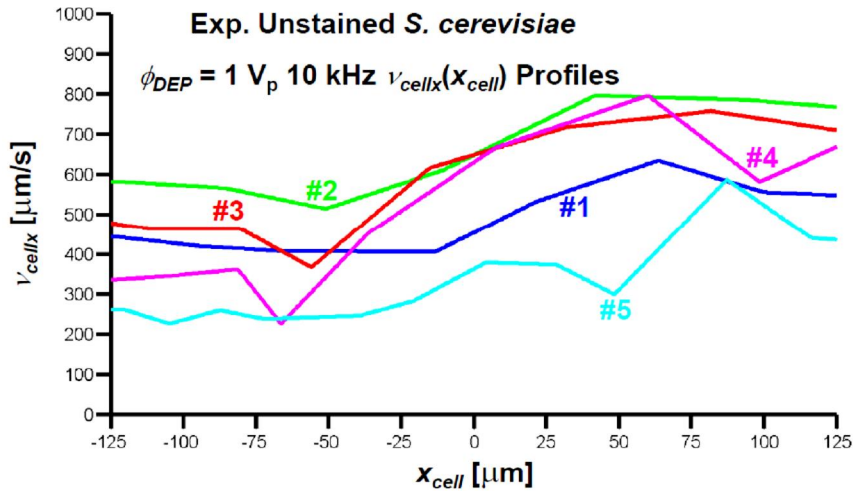
Figure 9-9: _Experimental $v_{cellx}(x_{cell})$ profiles of passing viable S. cerevisiae cells with ϕ_{DEP} = 1 V_p 10 kHz._

The initial v_{cellx}, v_{cellx0}, of each profile was estimated as the mean v_{cellx} within the -125 μm Ö x_{cell} Ö -75 μm interval. The final v_{cellx}, v_{cellxf}, of each profile was estimated as the mean v_{cellx} within the 75 μm Ö x_{cell} Ö 125 μm interval. The relative percent change in v_{cellx}, %Δv_{cellx}, is then estimated using v_{cellx0} and v_{cellxf}. Table 9-3 summarizes the results of this %Δv_{cellx} analysis.

Table 9-3: %Δv_{cellx} Analysis of Experimental v_{cellx} Profiles of Passing Viable *S. cerevisiae* Cells with $\phi_{DEP} = 1$ V_p 10 kHz			
Signature	v_{cellx0} [μm/s]	v_{cellxf} [μm/s]	%Δv_{cellx}
1	425.61	567.11	33.2
2	570.50	780.26	36.8
3	463.95	736.27	58.7
4	344.92	635.86	84.3
5	246.70	507.20	105.6
E{ }	410.34	645.34	63.7
σ{ }	122.29	113.76	31.1

Table 9-3: *%Δv_{cellx} analysis of experimental v_{cellx} profiles of passing viable S. cerevisiae cells with $\phi_{DEP} = 1$ V_p 10 kHz.*

The expectation and standard deviation of each of the v_{cellx} profiles, $E\{v_{cellx}\}$ and $\sigma\{v_{cellx}\}$, was then computed at each point along x_{cell}. Figure 9-10 presents the computed $E\{v_{cellx}\}$ and $E\{v_{cellx}\} \pm \sigma\{v_{cellx}\}$ profiles. Table 9-4 presents the corresponding %Δv_{cellx} analysis of these three statistical profiles.
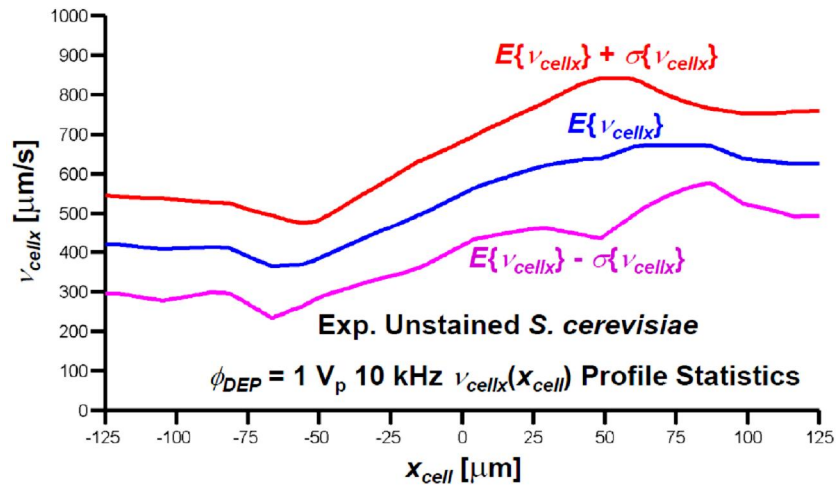
Figure 9-10: *Experimental v_{cellx} profile statistics of passing viable S. cerevisiae cells with $\phi_{DEP} = 1$ V_p 10 kHz.*

Table 9-4: %Δv_{cellx} Analysis of Experimental $E\{v_{cellx}\}$ and $E\{v_{cellx}\} \pm \sigma\{v_{cellx}\}$ Profiles of Passing Viable *S. cerevisiae* Cells with ϕ_{DEP} = 1 V_p 10 kHz			
Signature	v_{cellx0} [μm/s]	v_{cellxf} [μm/s]	%Δv_{cellx}
$E\{v_{cellx}\} + \sigma\{v_{cellx}\}$	532.79	760.97	42.8
$E\{v_{cellx}\}$	410.34	645.34	57.3
$E\{v_{cellx}\} - \sigma\{v_{cellx}\}$	287.88	529.71	45.4

Table 9-4: *%Δv_{cellx} analysis of experimental $E\{v_{cellx}\}$ and $E\{v_{cellx}\} \pm \sigma\{v_{cellx}\}$*

profiles of passing viable S. cerevisiae cells with ϕ_{DEP} = 1 V_p 10 kHz.

The particle tracing simulation of Section 4.3 then attempted to reproduce the $E\{v_{cellx}\}$ profile of Figure 9-10. In an initial simulation, the particle was initially placed at (x_{cell0}, h_{cell0}) = (-125, 5) μm and given an initial velocity of v_{cell0} = 410.34 a_x μm/s (referring to Table 9-3). Equation (4-11) was employed to estimate $< v_{med} >$ as 625.28 a_x μm/s. The real part of the complex Clausius-Mossotti factor, Re{$\underline{K}$}, was assumed to be -0.06 (referring to Figure 7-3). The particle tracing simulation then proceeded to compute the trajectory of the particle as subjected to F_{DEP} and F_{drag}, computed using Equations (3-31) and (4-13), respectively. The initial simulated trajectory yielded v_{cellxf} = 480.71 μm/s, which is significantly lower than the v_{cellxf} corresponding to the experimentally observed $E\{v_{cellx}\}$ - $\sigma\{v_{cellx}\}$ profile, as reported in Table 9-4. As such, the simulation was repeated with a lowered initial position of (x_{cell0}, h_{cell0}) = (-125, 3) μm. The v_{cell0} = 410.34 a_x μm/s assumption was maintained, and $< v_{med} >$ was re-computed as 985.80 a_x μm/s. The second simulated trajectory yielded v_{cellxf} = 578.22 μm/s, which is within the bounds of the v_{cellxf} values corresponding to the experimentally observed $E\{v_{cellx}\} \pm \sigma\{v_{cellx}\}$ profiles, as reported in Table 9-4. Both the elapsed time t and E_{ext}^2 / ϕ_{RF}^2 were plotted along the computed trajectory, yielding text files containing: (1) x_{cell}, h_{cell}, and t; and (2) x_{cell}, h_{cell}, and E_{ext}^2 / ϕ_{RF}^2.

The MATLAB® program of Appendix D was re-run, with additional code for the analysis of the particle tracing simulation executed. This additional code proceeds to read in the text file containing the simulated $x_{cell}(t)$ profile. The corresponding $v_{cellx}(t)$ profile was computed via the first-order backward finite difference approximation.

Linear interpolation was employed to fit this $v_{cellx}(t)$ profile to a uniformly spaced x_{cell} line spanning ± 125 μm in 0.5 μm steps. Figure 9-11 presents this fitted $v_{cellx}(x_{cell})$ profile along with the computed $E\{v_{cellx}\}$ and $E\{v_{cellx}\} \pm \sigma\{v_{cellx}\}$ profiles of Figure 9-10. Figure 9-11 shows that the simulated v_{cellx} profile reasonably approximates the experimental $E\{v_{cellx}\}$ profile. Table 9-5 presents the corresponding %Δv_{cellx} analysis of this simulated profile.
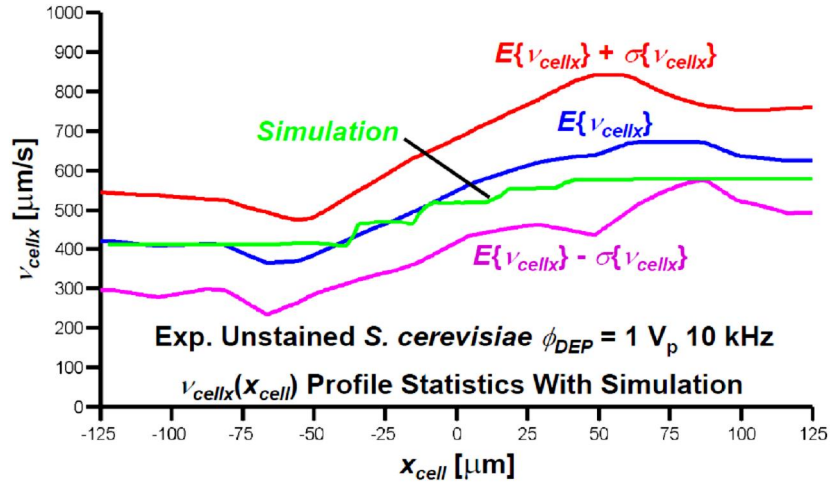
Figure 9-11: *The simulated v_{cellx} profile reasonably approximates the experimental $E\{v_{cellx}\}$ profile of passing viable S. cerevisiae cells with $\phi_{DEP} = 1\ V_p$ 10 kHz.*

Table 9-5: %Δv_{cellx} Analysis of Simulated v_{cellx} Profile of Passing Viable *S. cerevisiae* Cell with $\phi_{DEP} = 1\ V_p$ 10 kHz			
Signature	v_{cellx0} [μm/s]	v_{cellxf} [μm/s]	%Δv_{cellx}
Simulation	410.33	578.22	40.9

Table 9-5: *%Δv_{cellx} analysis of simulated v_{cellx} profile of passing viable S. cerevisiae cell with $\phi_{DEP} = 1\ V_p$ 10 kHz.*

Figure 9-12 presents the ΔC_{MEA} signature produced by scaling the simulated $E_{ext}^2(t) / \phi_{RF}^2$ profile with the -3.28 x 10^{-26} F m^2 scaling factor computed in Section 7.4. The shape of Figure 9-12 suggests that the $h_{cell0} = 3$ μm assumption used within the particle tracing simulation was slightly lower than experimentally observed. However, the $h_{cell0} = 3$ μm assumption was necessary to obtain a simulated v_{cellx} profile which was

bounded by the experimental $E\{v_{cellx}\} \pm \sigma\{v_{cellx}\}$ profiles. This may indicate that the experimentally observed $\text{Re}\{\underline{K}\}$ is within the interval $-0.06 < \text{Re}\{\underline{K}\} < 0$. Curiously, Figure 9-12 depicts a significantly larger ΔC_{MEA} signature than those featured in Figure 9-7.
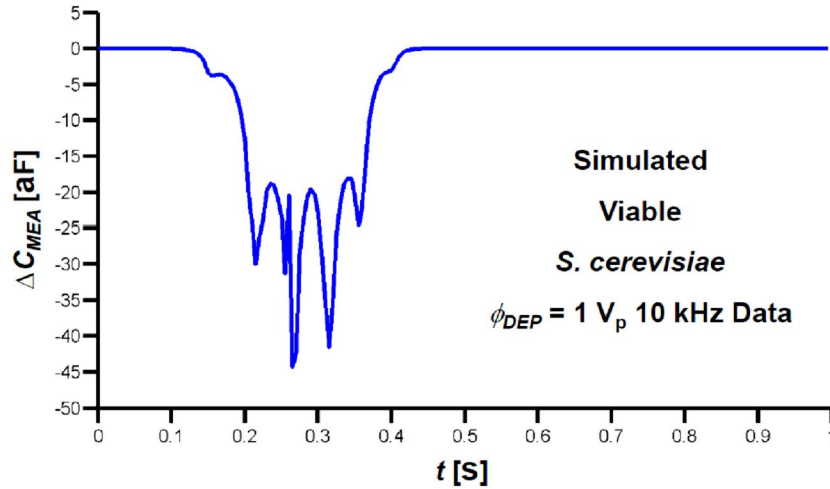
Figure 9-12: *Simulated ΔC_{MEA} signature induced by passing viable S. cerevisiae cell with $\phi_{DEP} = 1\ V_p$ 10 kHz.*

9.2.C Analysis of $\phi_{DEP} = 1\ V_p$ 18 kHz Data

Figure 9-13 presents the five experimental ΔC_{MEA} signatures selected from the $\phi_{DEP} = 1\ V_p$ 18 kHz dataset. Visual inspection of these ΔC_{MEA} signatures suggests that they correspond to low initial elevation crossings, with h_{cell0} on the order of 4-6 μm.
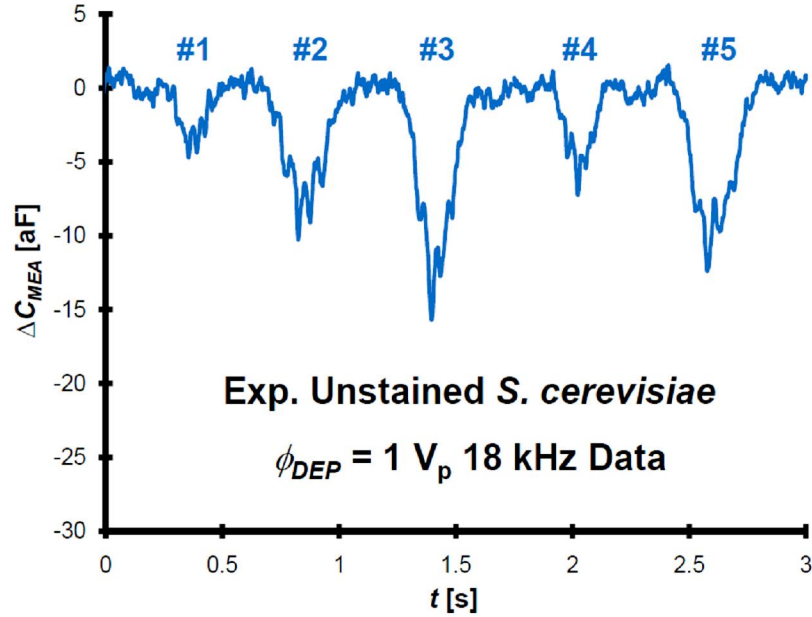
Figure 9-13: *Experimental ΔC_{MEA} signatures induced*
by passing viable S. cerevisiae cells with ϕ_{DEP} = 1 V_p 18 kHz.

The Tracker 2.60 analysis of Section 6.3.A was then repeated (with a refined brightness of 50) to analyze the captured MEA detection zone video corresponding to the ΔC_{MEA} signatures of Figure 9-13, yielding an $x_{cell}(t)$ dataset saved as a CSV file. The MATLAB® program of Appendix D analyzes this CSV file. Figure 9-14 presents these five $x_{cell}(t)$ profiles.
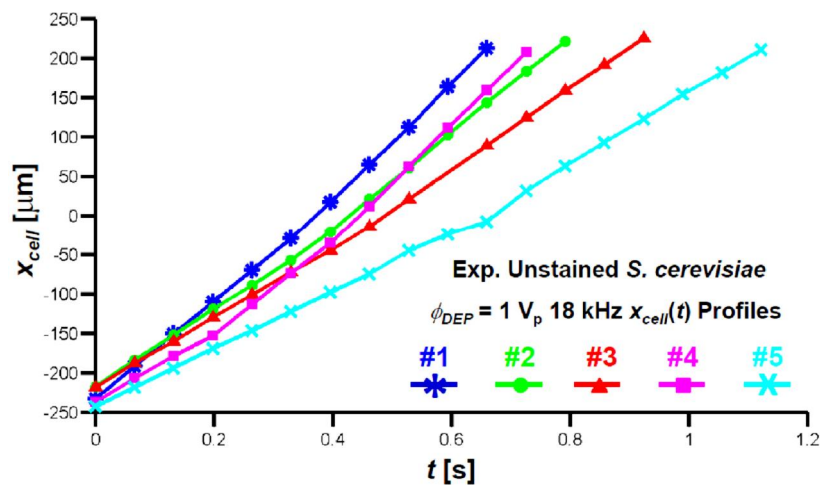
Figure 9-14: *Experimental $x_{cell}(t)$ profiles of passing*
viable S. cerevisiae cells with ϕ_{DEP} = 1 V_p 18 kHz.

The MATLAB® program of Appendix D estimated the $v_{cellx}(t)$ profiles corresponding to the ΔC_{MEA} signatures of Figure 9-13 via the first-order backward finite difference approximation. Linear interpolation was employed to fit each $v_{cellx}(t)$ profile to a uniformly spaced x_{cell} line spanning ±125 μm in 0.5 μm steps. Figure 9-15 presents these fitted $v_{cellx}(x_{cell})$ profiles.
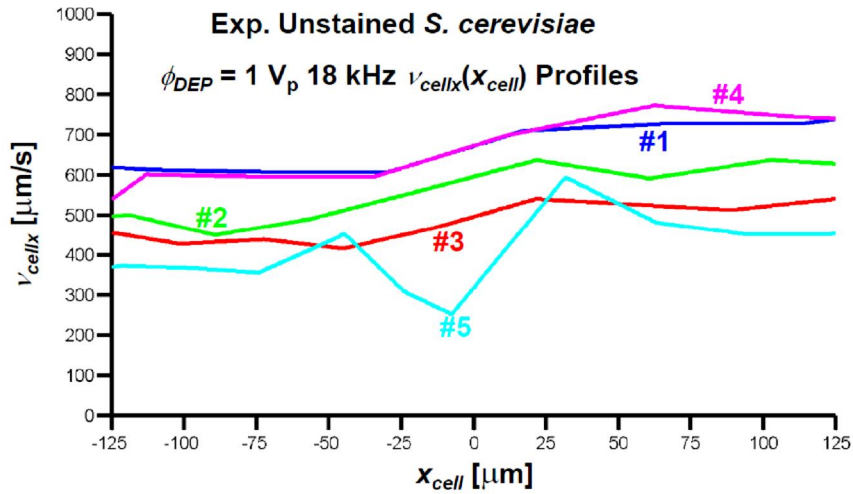
Figure 9-15: *Experimental $v_{cellx}(x_{cell})$ profiles of passing viable S. cerevisiae cells with ϕ_{DEP} = 1 V_p 18 kHz.*

The initial v_{cellx}, v_{cellx0}, of each profile was estimated as the mean v_{cellx} within the -125 μm Ö x_{cell} Ö -75 μm interval. The final v_{cellx}, v_{cellxf}, of each profile was estimated as the mean v_{cellx} within the 75 μm Ö x_{cell} Ö 125 μm interval. The relative percent change in v_{cellx}, %Δv_{cellx}, is then estimated using v_{cellx0} and v_{cellxf}. Table 9-6 summarizes the results of this %Δv_{cellx} analysis.

	Table 9-6: %Δv_{cellx} Analysis of Experimental v_{cellx} Profiles of Passing Viable *S. cerevisiae* Cells with ϕ_{DEP} = 1 V_p 18 kHz		
Signature	v_{cellx0} [μm/s]	v_{cellxf} [μm/s]	%Δv_{cellx}
1	610.93	727.53	19.1
2	472.63	625.91	32.4
3	435.81	522.67	19.9
4	590.61	750.39	27.1
5	364.92	454.87	24.6
E{ }	*494.98*	*616.27*	*24.6*
σ{ }	*104.29*	*127.74*	*5.5*

Table 9-6: *%Δv_{cellx} analysis of experimental v_{cellx} profiles of passing viable S. cerevisiae cells with ϕ_{DEP} = 1 V_p 18 kHz.*

The expectation and standard deviation of each of the v_{cellx} profiles, $E\{v_{cellx}\}$ and $\sigma\{v_{cellx}\}$, was then computed at each point along x_{cell}. Figure 9-16 presents the computed $E\{v_{cellx}\}$ and $E\{v_{cellx}\} \pm \sigma\{v_{cellx}\}$ profiles. Table 9-7 presents the corresponding %Δv_{cellx} analysis of these three statistical profiles.

Figure 9-16: *Experimental v_{cellx} profile statistics of passing viable S. cerevisiae cells with ϕ_{DEP} = 1 V_p 18 kHz.*

Table 9-7: $\%\Delta v_{cellx}$ Analysis of Experimental $E\{v_{cellx}\}$ and $E\{v_{cellx}\} \pm \sigma\{v_{cellx}\}$			
Profiles of Passing Viable *S. cerevisiae* Cells with $\phi_{DEP} = 1\ V_p\ 18\ kHz$			
Signature	v_{cellx0} [μm/s]	v_{cellxf} [μm/s]	$\%\Delta v_{cellx}$
$E\{v_{cellx}\} + \sigma\{v_{cellx}\}$	599.78	744.23	24.1
$E\{v_{cellx}\}$	494.98	616.27	24.5
$E\{v_{cellx}\} - \sigma\{v_{cellx}\}$	390.19	488.31	16.4

Table 9-7: *$\%\Delta v_{cellx}$ analysis of experimental $E\{v_{cellx}\}$ and $E\{v_{cellx}\} \pm \sigma\{v_{cellx}\}$*

profiles of passing viable S. cerevisiae cells with $\phi_{DEP} = 1\ V_p\ 18\ kHz$.

Notably, the 16.4-24.1% range of Table 9-7 is closer to the 5.0-7.7% range of Table 9-2 than the 42.8-57.3% range of Table 9-4. These $\%\Delta v_{cellx}$ analyses thus imply that the Re$\{\underline{K}\}$ associated with the experimentally observed $\boldsymbol{F_{DEP}}$ when $\phi_{DEP} = 1\ V_p\ 18$ kHz is closer to 0.00 than -0.06.

The particle tracing simulation of Section 4.3 then attempted to reproduce the $E\{v_{cellx}\}$ profile of Figure 9-16. In an initial simulation, the particle was initially placed at (x_{cell0}, h_{cell0}) = (-125, 5) μm and given an initial velocity of v_{cell0} = 494.98 $\boldsymbol{a_x}$ μm/s (referring to Table 9-6). Equation (4-11) was employed to estimate $<v_{med}>$ as 754.26 $\boldsymbol{a_x}$ μm/s. Re$\{\underline{K}\}$ was assumed to be 0.00 (referring to Figure 7-3). The particle tracing simulation then proceeded to compute the trajectory of the particle as subjected to $\boldsymbol{F_{drag}}$, computed using Equation (4-13). Both the elapsed time t and E_{ext}^2 / ϕ_{RF}^2 were plotted along the computed trajectory, yielding text files containing: (1) x_{cell}, h_{cell}, and t; and (2) x_{cell}, h_{cell}, and E_{ext}^2 / ϕ_{RF}^2.

The MATLAB® program of Appendix D was re-run, with additional code for the analysis of the particle tracing simulation executed. This additional code proceeds to read in the text file containing the simulated $x_{cell}(t)$ profile. The corresponding $v_{cellx}(t)$ profile was computed via the first-order backward finite difference approximation. Linear interpolation was employed to fit this $v_{cellx}(t)$ profile to a uniformly spaced x_{cell} line spanning ±125 μm in 0.5 μm steps. Figure 9-17 presents this fitted $v_{cellx}(x_{cell})$ profile along with the computed $E\{v_{cellx}\}$ and $E\{v_{cellx}\} \pm \sigma\{v_{cellx}\}$ profiles of Figure 9-16. As this simulation did not include $\boldsymbol{F_{DEP}}$, the simulated h_{cell} and v_{cellx} remained constant. The

v_{cellxf} = 494.94 μm/s of the simulated trajectory closely matches the v_{cellxf} = 488.31 μm/s of the $E\{v_{cellx}\}$ - $\sigma\{v_{cellx}\}$, confirming that the Re$\{\underline{K}\}$ associated with the experimentally observed $\boldsymbol{F_{DEP}}$ may not be entirely negligible, but is certainly closer to 0.00 than -0.06.
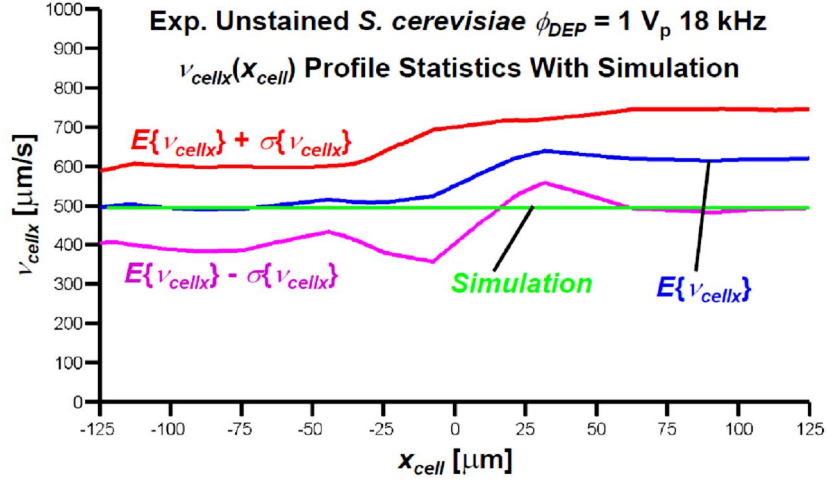
Figure 9-17: _The simulated v_{cellx} profile approximates the experimental_
_$E\{v_{cellx}\} \pm \sigma\{v_{cellx}\}$ profiles of passing viable S. cerevisiae cells with ϕ_{DEP} = 1 V_p 18 kHz._

Figure 9-18 presents the ΔC_{MEA} signature produced by scaling the simulated $E_{ext}^2(t)$ / ϕ_{RF}^2 profile with the -3.28 x 10^{-26} F m^2 scaling factor computed in Section 7.4. Comparing the shape of Figure 9-18 to Figure 9-13 suggests that the h_{cell0} = 5 μm assumption used within the particle tracing simulation was reasonable. Curiously, Figure 9-18 depicts a significantly larger ΔC_{MEA} signature than those featured in Figure 9-7.
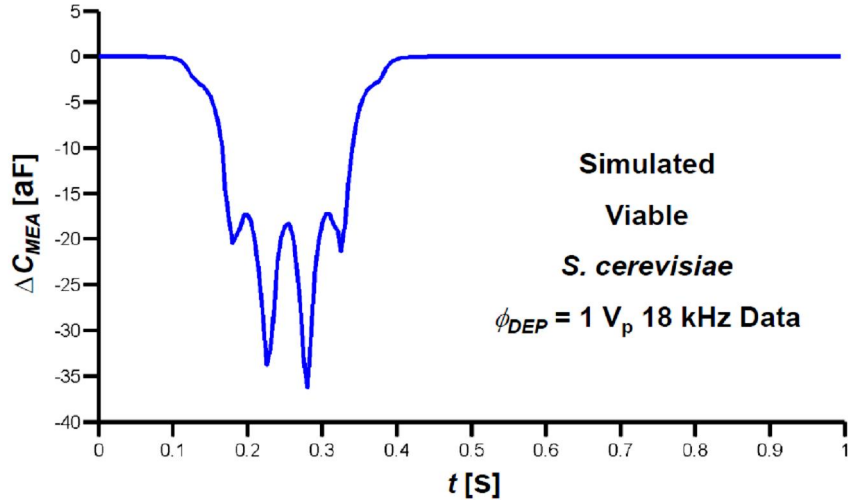
Figure 9-18: *Simulated ΔC_{MEA} signature induced by passing viable S. cerevisiae cell with $\phi_{DEP} = 1\ V_p$ 18 kHz.*

9.2.D   Analysis of $\phi_{DEP} = 0.5\ V_p$ 100 kHz Data

Figure 9-19 presents the five experimental ΔC_{MEA} signatures selected from the $\phi_{DEP} = 0.5\ V_p$ 100 kHz dataset. Visual inspection of these ΔC_{MEA} signatures suggests that they correspond to low initial elevation crossings, with h_{cell0} on the order of 4-6 µm.
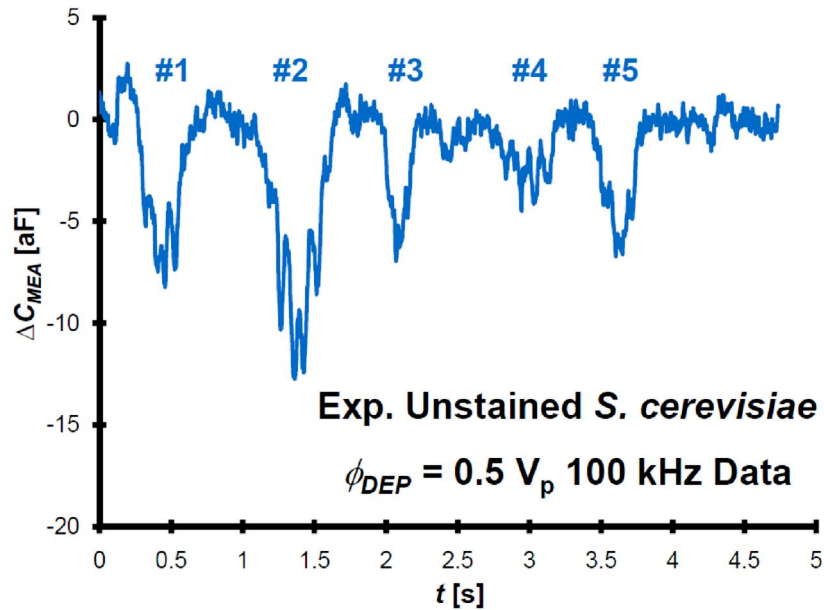
Figure 9-19: *Experimental ΔC_{MEA} signatures induced by passing viable S. cerevisiae cells with $\phi_{DEP} = 0.5\ V_p$ 100 kHz.*

The Tracker 2.60 analysis of Section 6.3.A was then repeated (with a refined brightness of 50) to analyze the captured MEA detection zone video corresponding to the ΔC_{MEA} signatures of Figure 9-19, yielding an $x_{cell}(t)$ dataset saved as a CSV file. The MATLAB® program of Appendix D analyzes this CSV file. Figure 9-20 presents these five $x_{cell}(t)$ profiles.
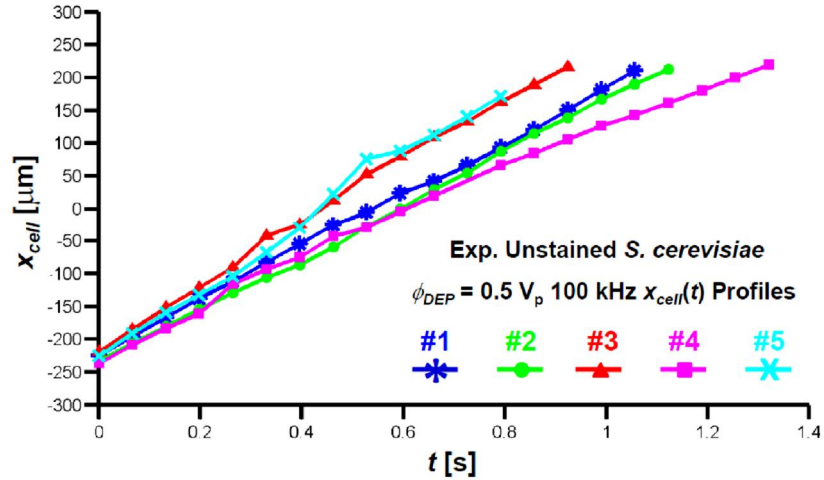
Figure 9-20: *Experimental $x_{cell}(t)$ profiles of passing viable S. cerevisiae cells with ϕ_{DEP} = 0.5 V_p 100 kHz.*

The MATLAB® program of Appendix D estimated the $v_{cellx}(t)$ profiles corresponding to the ΔC_{MEA} signatures of Figure 9-19 via the first-order backward finite difference approximation. Linear interpolation was employed to fit each $v_{cellx}(t)$ profile to a uniformly spaced x_{cell} line spanning ±125 μm in 0.5 μm steps. Figure 9-21 presents these fitted $v_{cellx}(x_{cell})$ profiles.
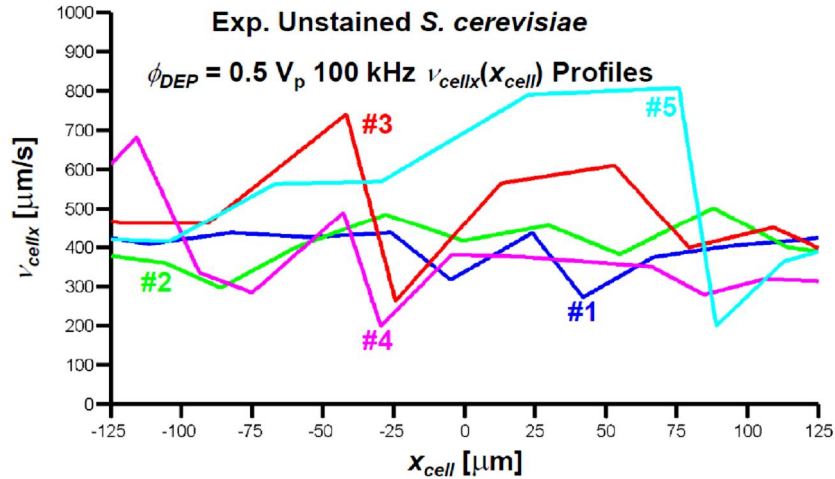
Figure 9-21: *Experiemental $v_{cellx}(x_{cell})$ profiles of passing viable S. cerevisiae cells with ϕ_{DEP} = 0.5 V_p 100 kHz.*

The initial v_{cellx}, v_{cellx0}, of each profile was estimated as the mean v_{cellx} within the -125 µm Öx_{cell} Ö-75 µm interval. The final v_{cellx}, v_{cellxf}, of each profile was estimated as the mean v_{cellx} within the 75 µm Öx_{cell} Ö125 µm interval. The relative percent change in v_{cellx}, %Δv_{cellx}, is then estimated using v_{cellx0} and v_{cellxf}. Table 9-8 summarizes the results of this %Δv_{cellx} analysis.

Table 9-8: %Δv_{cellx} Analysis of Experimental v_{cellx} Profiles of Passing Viable *S. cerevisiae* Cells with ϕ_{DEP} = 0.5 V_p 100 kHz			
Signature	v_{cellx0} [µm/s]	v_{cellxf} [µm/s]	%Δv_{cellx}
1	422.13	405.06	-4.0
2	341.42	445.27	30.4
3	476.22	423.71	-11.0
4	459.15	304.85	-33.6
5	450.01	372.59	-17.2
E{ }	429.79	390.29	-7.1
σ{ }	53.14	54.71	23.6

Table 9-8: *%Δv_{cellx} analysis of experimental v_{cellx} profiles of passing viable S. cerevisiae cells with ϕ_{DEP} = 0.5 V_p 100 kHz.*

The expectation and standard deviation of each of the v_{cellx} profiles, $E\{v_{cellx}\}$ and $\sigma\{v_{cellx}\}$, was then computed at each point along x_{cell}. Figure 9-22 presents the computed $E\{v_{cellx}\}$ and $E\{v_{cellx}\} \pm \sigma\{v_{cellx}\}$ profiles. Table 9-9 presents the corresponding $\%\Delta v_{cellx}$ analysis of these three statistical profiles.
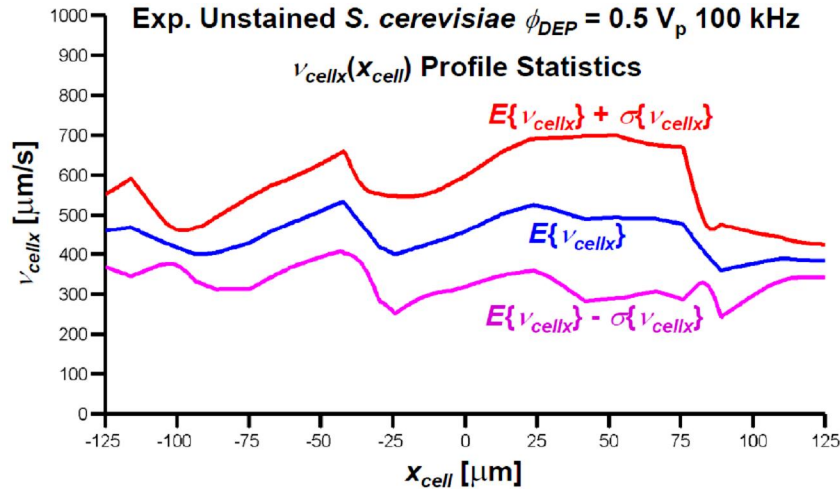
Figure 9-22: *Experimental v_{cellx} profile statistics of passing viable S. cerevisiae cells with $\phi_{DEP} = 0.5 \ V_p$ 100 kHz.*

Table 9-9: $\%\Delta v_{cellx}$ Analysis of Experimental $E\{v_{cellx}\}$ and $E\{v_{cellx}\} \pm \sigma\{v_{cellx}\}$ Profiles of Passing Viable *S. cerevisiae* Cells with $\phi_{DEP} = 0.5 \ V_p$ 100 kHz			
Signature	v_{cellx0} [μm/s]	v_{cellxf} [μm/s]	$\%\Delta v_{cellx}$
$E\{v_{cellx}\} + \sigma\{v_{cellx}\}$	515.88	471.00	-8.7
$E\{v_{cellx}\}$	429.79	390.29	-9.2
$E\{v_{cellx}\} - \sigma\{v_{cellx}\}$	343.69	309.59	-6.6

Table 9-9: *$\%\Delta v_{cellx}$ analysis of experimental $E\{v_{cellx}\}$ and $E\{v_{cellx}\} \pm \sigma\{v_{cellx}\}$ profiles of passing viable S. cerevisiae cells with $\phi_{DEP} = 0.5 \ V_p$ 100 kHz.*

The particle tracing simulation of Section 4.3 then attempted to reproduce the $E\{v_{cellx}\}$ profile of Figure 9-22. In an initial simulation, the particle was initially placed at (x_{cell0}, h_{cell0}) = (-125, 5) μm and given an initial velocity of $v_{cell0} = 429.79 \ a_x$ μm/s (referring to Table 9-8). Equation (4-11) was employed to estimate $< v_{med} >$ as 654.92 a_x μm/s. Re$\{\underline{K}\}$ was assumed to be 0.64 (referring to Figure 7-3). The particle tracing

simulation then proceeded to compute the trajectory of the particle as subjected to F_{DEP} and F_{drag}, computed using Equations (3-31) and (4-13), respectively. In this initial simulation, the particle adhered to the MEA. As such, the simulation was repeated with a raised initial position of (x_{cell0}, h_{cell0}) = (-125, 9) μm. The v_{cell0} = 429.79 a_x μm/s assumption was maintained, and < v_{med} > was re-computed as 410.79 a_x μm/s. In this second simulation, the particle did not adhere to the MEA. Both the elapsed time t and $E_{ext}{}^2 / \phi_{RF}{}^2$ were plotted along the computed trajectory, yielding text files containing: (1) x_{cell}, h_{cell}, and t; and (2) x_{cell}, h_{cell}, and $E_{ext}{}^2 / \phi_{RF}{}^2$.

The MATLAB$^{®}$ program of Appendix D was re-run, with additional code for the analysis of the particle tracing simulation executed. This additional code proceeds to read in the text file containing the simulated $x_{cell}(t)$ profile. The corresponding $v_{cellx}(t)$ profile was computed via the first-order backward finite difference approximation. Linear interpolation was employed to fit this $v_{cellx}(t)$ profile to a uniformly spaced x_{cell} line spanning ±125 μm in 0.5 μm steps. Figure 9-23 presents this fitted $v_{cellx}(x_{cell})$ profile along with the computed $E\{v_{cellx}\}$ and $E\{v_{cellx}\} \pm \sigma\{v_{cellx}\}$ profiles of Figure 9-22. Figure 9-23 shows that the simulated v_{cellx} profile is bounded by the experimental $E\{v_{cellx}\} \pm \sigma\{v_{cellx}\}$ profiles. Table 9-10 presents the corresponding %Δv_{cellx} analysis of this simulated profile.
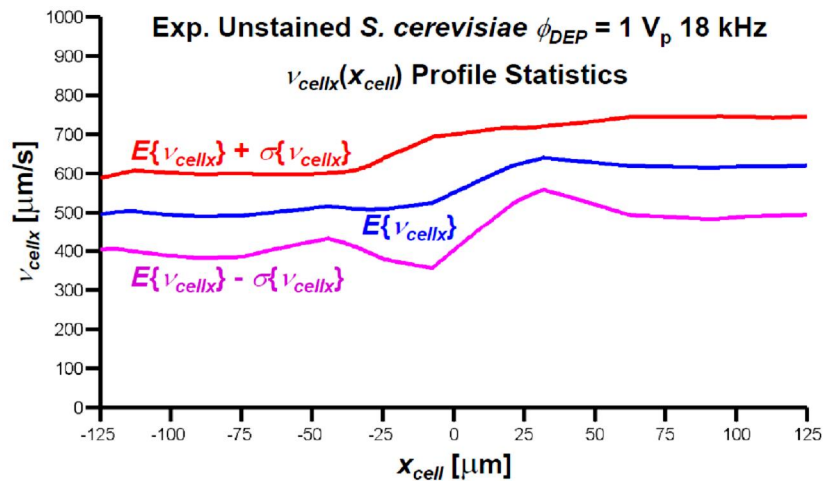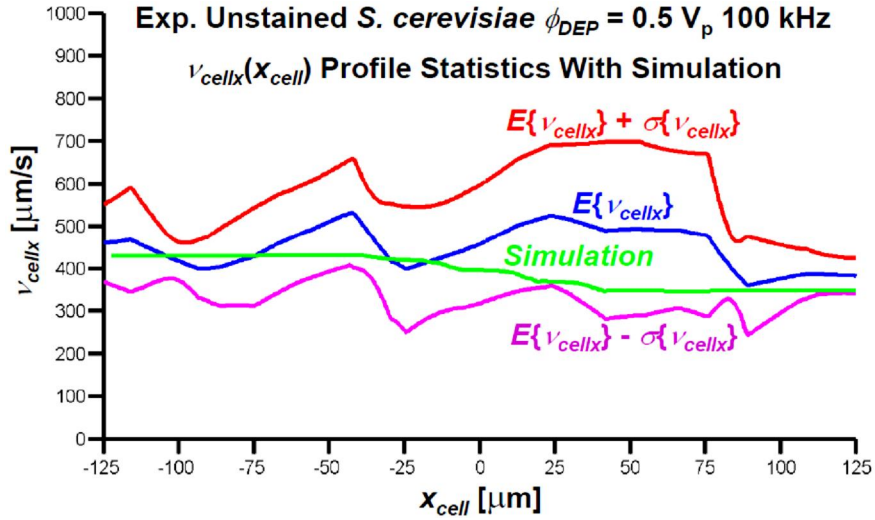
Figure 9-23: *The simulated v_{cellx} profile is bounded by the experimental $E\{v_{cellx}\} \pm \sigma\{v_{cellx}\}$ profiles of passing viable S. cerevisiae cells with $\phi_{DEP} = 0.5\ V_p$ 100 kHz.*

Table 9-10: %Δv_{cellx} Analysis of Simulated v_{cellx} Profile		
of Passing Viable *S. cerevisiae* Cell with $\phi_{DEP} = 0.5\ V_p$ 100 kHz		
Signature	v_{cellx0} [μm/s]	v_{cellxf} [μm/s]	%Δv_{cellx}
Simulation	429.80	346.58	-19.4

Table 9-10: *%Δv_{cellx} analysis of simulated v_{cellx} profile of passing viable S. cerevisiae cell with $\phi_{DEP} = 0.5\ V_p$ 100 kHz.*

Figure 9-24 presents the ΔC_{MEA} signature produced by scaling the simulated $E_{ext}^2(t)\ /\ \phi_{RF}^2$ profile with the -3.28 x 10^{-26} F m^2 scaling factor computed in Section 7.4. The peak magnitude of Figure 9-24 is larger than the ΔC_{MEA} signatures featured in Figure 9-19. Notably, the shape of Figure 9-24 suggests that the $h_{cell0} = 9.0\ \mu$m assumption used within the particle tracing simulation was higher than experimentally observed. However, the $h_{cell0} = 9.0\ \mu$m assumption was necessary to produce a simulated trajectory which was bounded by the experimental $E\{v_{cellx}\} \pm \sigma\{v_{cellx}\}$ profiles. This may indicate that the experimentally observed Re$\{\underline{K}\}$ is within the interval $0 < $ Re$\{\underline{K}\} < 0.64$. However, it is worth noting that the error within the simulation as a result of neglecting the

hydrodynamic lift force F_{lift} is most prominent when the point particle is close to the bottom of the microfluidic cross-channel subdomain.
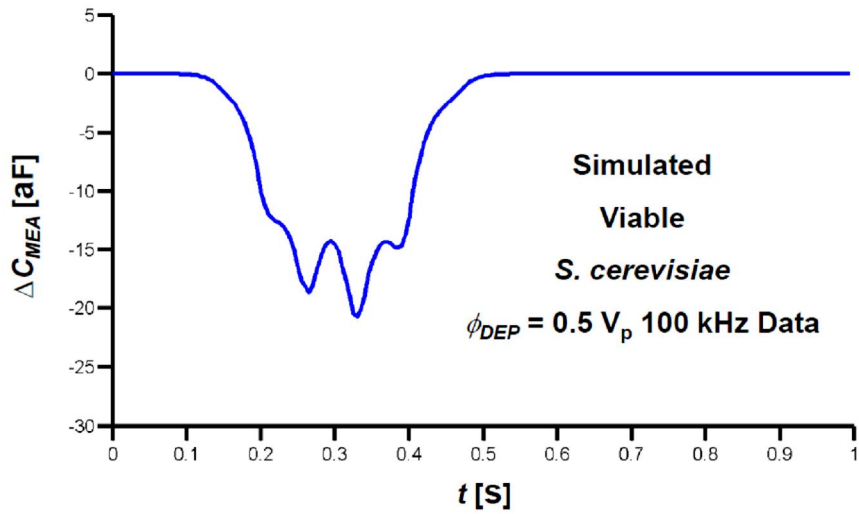
Figure 9-24: *Simulated ΔC_{MEA} signature induced by passing viable S. cerevisiae cell with $\phi_{DEP} = 0.5 V_p$ 100 kHz.*

Chapter 10
Conclusions & Recommended Future Work

The microflow cytometer presented in this work affords two independent methods for simultaneously detecting the response of actuated biological particles (bioparticles): (1) an optical assay, in which the change in the lateral velocity v_{cellx} of passing bioparticles is estimated from digital video of the microelectrode array (MEA) detection zone; and (2) a capacitive cytometer, in which a capacitance sensor coupled to the MEA produces a sense signal S proportional to the transient MEA capacitance perturbations ΔC_{MEA} induced by passing bioparticles. Chapters 6, 8, and 9 demonstrated the simultaneous operation of the microflow cytometer as both an optical assay and a capacitive cytometer in the study of dielectrophoretically (DEP) actuated polystyrene microspheres (PSS), heat shocked *Saccharomyces cerevisiae* cells, and viable *S. cerevisiae* cells, respectively. In each case: (1) the initial bioparticle elevation h_{cell0} was estimated by comparing the experimentally observed ΔC_{MEA} signatures to the squared external electric field magnitude to squared MEA potential, E_{ext}^2 / ϕ_{RF}^2, plots simulated using COMSOL® Multiphysics; and (2) the initial and final lateral bioparticle velocities, v_{cellx0} and v_{cellxf}, were estimated from the captured optical assay video. A particle tracing simulation of the bioparticle trajectory, as subjected to the DEP actuation force $\boldsymbol{F_{DEP}}$ and the viscous fluid drag force $\boldsymbol{F_{drag}}$, was compared to the experimentally observed bioparticle trajectories to verify the experimentally observed DEP spectrum. In each case, the polarity and cross-over frequencies of the theoretically predicted DEP spectrum were confirmed. However, obtaining a reasonable match when $\boldsymbol{F_{DEP}}$ was not negligible often required modifying h_{cell0} to the point that the shape of the simulated ΔC_{MEA} signatures differed from the experimentally observed ΔC_{MEA} signatures. This may indicate that the theoretically predicted values for the Clausius-Mossotti factor's real part, Re{$\underline{K}$}, (being the frequency dependent factor within $\boldsymbol{F_{DEP}}$) as used within the particle tracing simulation differs from experimental observations. However, it is worth noting that the error within the particle tracing simulation as a result of neglecting the hydrodynamic lift force $\boldsymbol{F_{lift}}$ is most prominent when the simulated point particle is close to the bottom of the

microfluidic cross-channel subdomain. As such, it is prudent to find a form for F_{lift} which affords incorporating both F_{lift} and the gravitational force F_{grav} into the particle tracing simulation. Moreover, the peak magnitudes of the simulated ΔC_{MEA} signatures often differed from the experimentally observed ΔC_{MEA} signatures. This may indicate that a re-calibration of the microflow cytometer, as per Section 6.2, is required.

Although the capacitive sensor is implemented using bench scale electronics, it could be miniaturized as a monolithic microwave integrated circuit (MMIC) and integrated on-chip with the microflow cytometer. As such, this work essentially serves as the developmental prototype of a capacitive cytometer with DEP actuation which could be miniaturized and integrated on-chip as a laboratory-on-a-chip (LoC) or micro-total-analysis-system (μTAS). The optical assay aspect of this microflow cytometer is merely to provide an independent confirmation of the viability and experimental DEP response of the actuated bioparticles. If Re$\{\underline{K}\}$ could be estimated from the experimental ΔC_{MEA} signatures alone, than the optical assay would not be required. The elimination of the optical assay components would facilitate the eventual miniaturization and on-chip integration of this microflow cytometer, as optical components are difficult to miniaturize and integrate on-chip. As such, it is prudent that algorithms be developed for the inference of Re$\{\underline{K}\}$ from the experimental ΔC_{MEA} data alone.

In this work, only PSS and *S. cerevisiae* cells were studied. If this work is to serve as the developmental prototype of a microflow cytometer for biomedical applications, it is necessary to demonstrate the applicability of our device in the analysis of mammalian cells. To that end: my colleague Graham Ferrier is currently using the microflow cytometer of this work to study the ΔC_{MEA} signatures induced by DEP actuated Chinese Hamster Ovary (CHO) cells transfected with the gene for human β-Interferon (IFN-β). CHO cells are mammalian cells commonly used for transfection and expression, and have been adopted as an industrial standard for large-scale recombinant protein production [Thar08]. Moreover, a lighter, portable version of the apparatus presented in Chapter 2 is being developed so that the microflow cytometer presented in this work can be utilized to study biohazardous bioparticles in such locations as the laboratories at Cancer Care Manitoba and the National Research Counciløs (NRC) Institute for Biodiagnostics.

Appendix A:

User's Guide to the *GUI Controller* Virtual Instrument

A.1   Data Acquisition Using *GUI Controller*

Before collecting data via the *GUI Controller* virtual instrument (VI), it is necessary to run InstaCal32 to calibrate the PCI-DAS6034 data acquisition (DAQ) board. As shown in Figure A-1, a short-cut to execute InstaCal is located on the desktop of the host personal computer (PC) (step 1). Once InstaCal has been opened, õBoard #0 ó PCI-DAS6034 (dev# 0)ö must be selected (step 2). The õBoard Calibration: PCI-DAS6034 (slot# 0)ö dialog is then opened by clicking on the button labelled õOK A/Dö (step 3). Once opened, the dialog automatically begins to calibrate the DAQ board. Once the õBoard Calibration: PCI-DAS6034 (slot# 0)ö dialog indicates that the calibration is complete, click on the button labelled õOKö. The InstaCal32 window can now be closed.
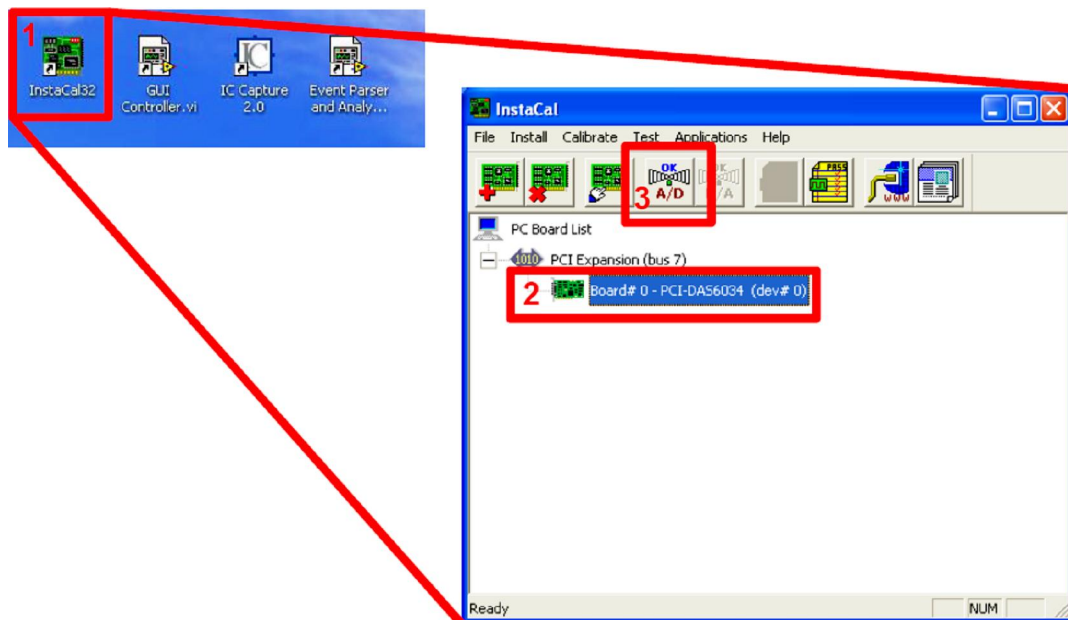
Figure A-1: *Steps to open InstaCal32 and calibrate the DAQ board.*

Once the DAQ board has been calibrated, the *GUI Controller* VI can now be executed. As shown in Figure A-2, a short-cut to execute LabVIEW® 7.1 and open the *GUI Controller* VI is located on the host PCøs desktop (step 4). When first opened, the

GUI Controller VI is in the õDAQ Ch 0-through-2 Stripchartsö tab. The *GUI Controller* VI is to first be run by clicking on the button labelled with an arrow icon (step 5).
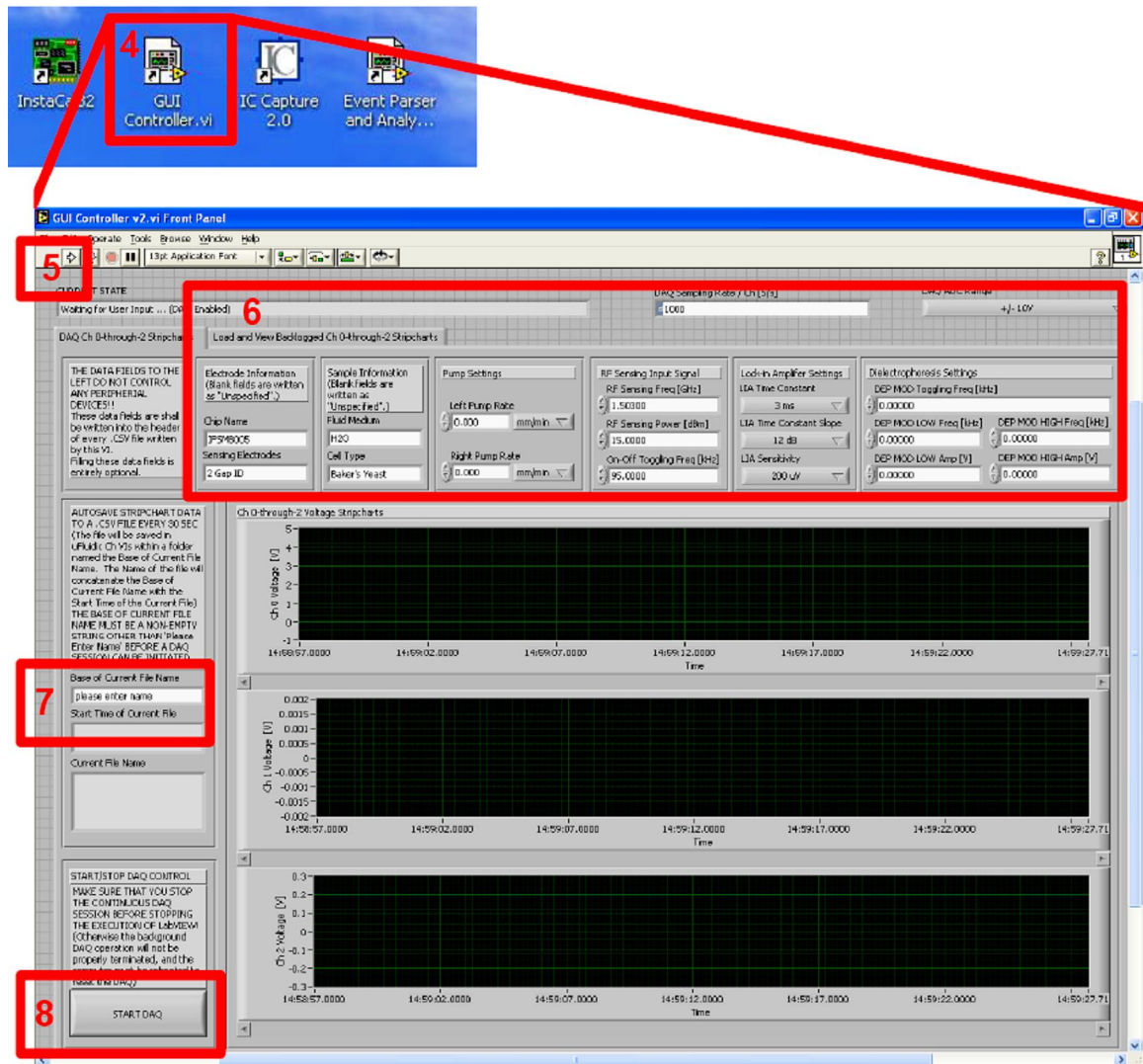
Figure A-2: *Steps to open the GUI Controller VI and begin a DAQ session.*

Before beginning a given DAQ session, the user is free to specify: (i) the header fields that are to be appended to each backlogged comma separated value (CSV) file generated during the said DAQ session, via the various associated controls; (ii) the rate at which the DAQ board samples the three channels, via the õDAQ Sampling Rate / Ch [S/s]ö numerical control; and (iii) the dynamic rage of the DAQ boardøs internal analog-to-digital converter (ADC), via the õDAQ ADC Rangeö droplist control (step 6). By default, õDAQ Sampling Rate / Ch [S/s]ö is set to 1 kS/s/Ch and õDAQ ADC Rangeö is

set to ±10 V. Unlike õDAQ Sampling Rate / Ch [S/s]ö and õDAQ ADC Rangeö: the various header fields neither control nor read any peripheral devices; their values are specified manually by the user. Moreover, the user is free to leave the header fields unspecified and to disregard them during analysis of the backlogged CSV files.

When the *GUI Controller* VI is first run, the button to begin a DAQ session (labelled õSTART DAQö) is disabled. The õSTART DAQö button will remain disabled until the user specifies a õBase of Current File Nameö field (step 7) which is neither an empty string nor õplease enter nameö. Notably, any trailing white space within a specified õBase of Current File Nameö string will be removed. Although the õBase of Current File Nameö string is case sensitive, the check to determine whether or not the õBase of Current File Nameö string is õplease enter nameö is case insensitive. Once a suitable õBase of Current File Nameö string has been provided by the user, the õSTART DAQö button will be enabled. Notably, the user may have to click on a point outside of the õBase of Current File Nameö field to enable the õSTART DAQö button after specifying a õBase of Current File Nameö string. The user may now initiate a DAQ session by clicking on the button labelled õSTART DAQö (step 8). The *GUI Controller* VI then begins to concurrently sample the three differential-input channels (as described in Section 2.7). Each of the three sampled channels are displayed as real-time stripcharts within the waveform charts immediately below the header field controls. Notably, the user may notice that the initial seconds of data are immediately reproduced within the stripcharts. This anomalous behaviour only occurs during the immediate start of a given DAQ session, and the user need not be concerned that data is being erroneously reproduced beyond the first few seconds of a given DAQ session.

The three concurrent stripcharts are also simultaneously backlogged as a sequence of 30 s long CSV files. These CSV files are saved within the directory specified by the õBase of Current File Nameö string. If this directory did not exist at the start of the DAQ session, the *GUI Controller* VI created it within the directory immediately prior to the directory containing the *GUI Controller* VI. These CSV files are given the name specified by the õBase of Current File Nameö string, as concatenated with the current date and system time of the host PC at the time that the first datum point within the given CSV file was sampled. The start time of the current file to which the

stripcharts are being written to is displayed within the õStart Time of Current Fileö indicator below the õBase of Current File Nameö control. The name of the current file to which the stripcharts are being written to is displayed within the õCurrent File Nameö indicator below the õStart Time of Current Fileö indicator.

The moment that the user depressed the õSTART DAQö button to initiate a DAQ session, this button became re-labelled as the õSTOP DAQö button, as shown in Figure A-3. During a DAQ session, the õSTOP DAQö button is the only enabled control within the *GUI Controller* VI. To stop a given DAQ session, the user must click on the õSTOP DAQö button (step 9). The DAQ board will then cease to sample the three channels and the various controls within the *GUI Controller* VI shall become enabled. The user is then free to cease execution of the *GUI Controller* VI by depressing the button labelled with a stop sign at the top left of the VI (step 10). It should be noted that the stop sign button should not be depressed before the õSTOP DAQö button has been used to terminate the DAQ session, as this would require that the host PC be rebooted before the DAQ board can sample data again.
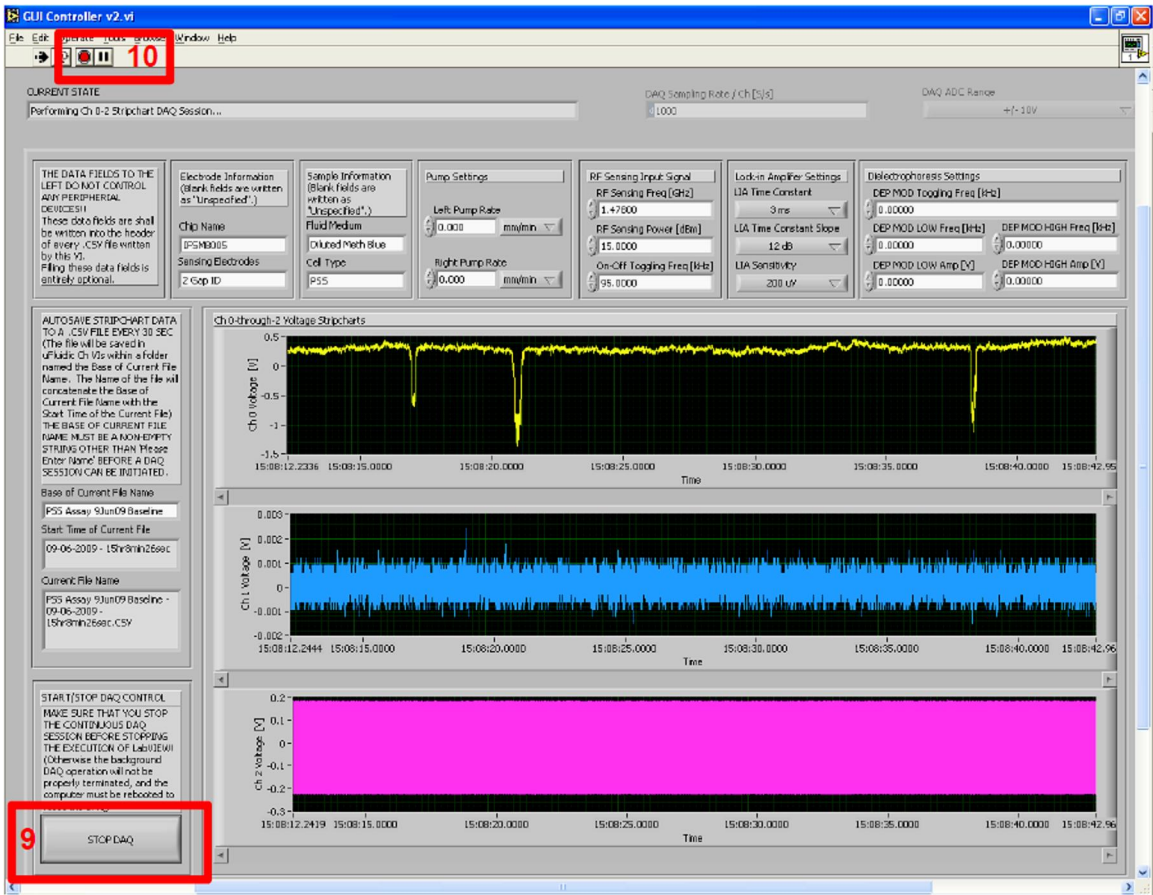
Figure A-3: *Steps to end a DAQ session*
and cease execution of the GUI Controller VI.

A.2 Displaying Backlogged Data Using *GUI Controller*

As shown in Figure A-4, the *GUI Controller* VI posses a second tab, labelled õLoad and View Backlogged Ch 0-through-2 Stripchartsö. In this tab, the user may examine the backlogged CSV files of an earlier DAQ session. To do so, the user first depresses the button labelled õLOAD DATA FROM .CSV FILEö to open a dialog in which the CSV file to be displayed is selected. Once a given CSV file has been selected, the three stripcharts are displayed in the bottom center of the VI and the header is displayed in the various indicators above and to the left of the stripcharts. The user may select another CSV file by once again using the õLOAD DATA FROM .CSV FILEö button, or by using the õLOAD PREV. FILEö and õLOAD NEXT FILEö buttons to the right of the stripcharts. The õLOAD PREV. FILEö button loads the CSV file

- 144 -

immediately prior to the currently displayed CSV file within the same directory. The õLOAD NEXT FILEö button loads the CSV file immediately after the currently displayed CSV file within the same directory. These buttons should automatically become disabled when there is no previous or next file to display, respectively. Notably, a dialog requesting that a file be selected may appear once either õLOAD PREV. FILEö or õLOAD NEXT FILEö are depressed. This is indicative of a fatal error, which requires that LabVIEW® be closed.

Figure A-4: *Loading backlogged CSV file using the GUI Controller VI.*

Appendix B:

User's Guide to the

Event Parser & Analyzer Virtual Instrument

B.1   Parsing Backlogged Data Using *Event Parser & Analyzer*

As shown in Figure B-1, a short-cut to execute LabVIEW® 7.1 and open the *Event Parser & Analyzer* virtual instrument (VI) is located on the desktop of the host personal computer (PC) (step 1). The *Event Parser & Analyzer* VI is to first be run by clicking on the button labelled with an arrow icon (step 2).
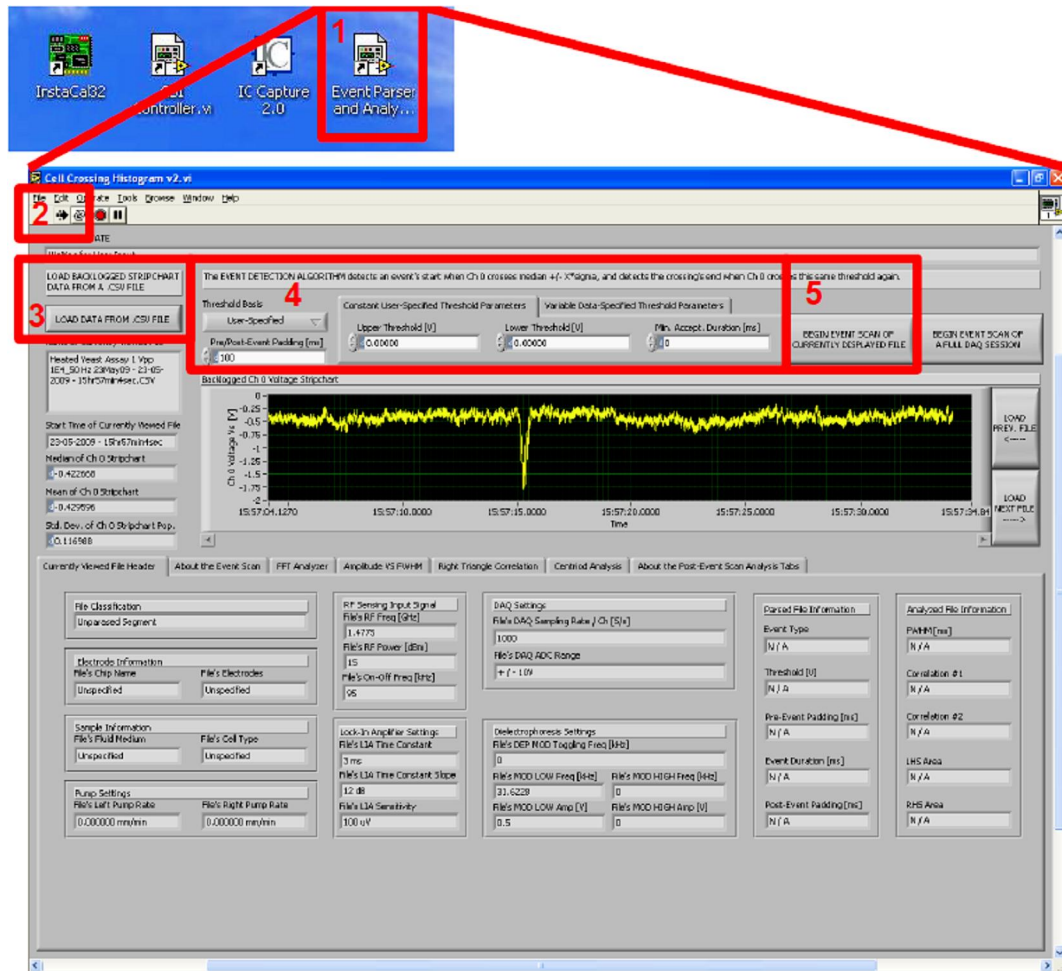
Figure B-1: *Steps to open the Event Parser & Analyzer VI, display a backlogged CSV file, and parse out events from the displayed CSV file.*

- 146 -

To parse out events from a single comma separated value (CSV) file, the user first depresses the button labelled õLOAD DATA FROM .CSV FILEö to open a dialog in which the CSV file to be displayed is selected (step 3). Once a given CSV file has been selected, the Channel 0 stripchart is displayed in the waveform graph in the center of the VI. The õCurrently Viewed File Headerö tab at the bottom of the VI displays all of the header information associated with the currently displayed CSV file. The user may select another CSV file by once again using the õLOAD DATA FROM .CSV FILEö button, or by using the õLOAD PREV. FILEö and õLOAD NEXT FILEö buttons to the right of the stripchart. The õLOAD PREV. FILEö button loads the CSV file immediately prior to the currently displayed CSV file within the same directory. The õLOAD NEXT FILEö button loads the CSV file immediately after the currently displayed CSV file within the same directory. These buttons should automatically become disabled when there is no previous or next file to display, respectively. Notably, a dialog requesting that a file be selected may appear once either õLOAD PREV. FILEö or õLOAD NEXT FILEö are depressed. This is indicative of a fatal error, which requires that LabVIEW® be closed.

To parse out events from the currently displayed CSV file, the user must confirm that the õThreshold Basisö droplist control is set to õUser-Specifiedö and specify the various numerical controls within the õConstant User-Specified Threshold Parametersö tab (step 4). The user is then to begin an event scan of the currently displayed Channel 0 stripchart by depressing the õBEGIN EVENT SCAN OF CURRENTLY DISPLAYED FILEö button (step 5). Once this button is depressed, the currently displayed Channel 0 stripchart is scanned from start to finish. When the currently displayed Channel 0 stripchart either drops below the lower threshold specified within the õLower Threshold [V]ö control or rises above the upper threshold specified within the õUpper Threshold [V]ö control, the time of the threshold crossing is noted as t_0. When the currently displayed Channel 0 stripchart subsequently rises above the lower threshold or drops below the upper threshold, this second threshold crossing time is noted as t_f. If the duration between these two threshold crossing times is not less than the minimum acceptable duration specified within the õMin. Accept. Duration [ms]ö control, then the data between these two threshold crossings has been identified as an event to be parsed. The currently displayed Channel 0 stripchart data from t_0 ó t_{pad} to $t_f + t_{pad}$, where t_{pad} is

the pre/post-event padding specified within the õPre/Post-Event Padding [ms]ö control, is then written as a new CSV file within a new directory called õSingle Eventsö created in the same directory as the currently displayed CSV file. Once the scan of the currently displayed Channel 0 stripchart is complete, a dialog appears indicating the number of detected events. (It should be noted that the displayed count may be erroneous.)

As an alternative to the user-specified upper and lower thresholds, the user could set the õThreshold Basisö droplist to õData-Specifiedö and have the upper and lower threshold be computed using the median and population standard deviation of the currently displayed Channel 0 stripchart. If this option is selected, then the upper and lower thresholds are set to the median of the currently displayed Channel 0 stripchart ± a computed deviation, respectively. This deviation is computed as the population standard deviation of the currently displayed Channel 0 stripchart as scaled by a multiplicative factor specified via the õX of Threshold = Median +/- X*Sigmaö control within the õVariable Data-Specified Threshold Parametersö tab. Once the õBEGIN EVENT SCAN OF CURRENTLY DISPLAYED FILEö button is depressed, the currently displayed Channel 0 stripchart is scanned from start to finish to identify threshold crossings in the same manner as described above. However, in addition to the minimum acceptable duration requirement, the computed deviation must also exceed a minimum acceptable deviation before a pair of threshold crossings is considered to be a detected event. This minimum acceptable deviation is specified using the õMin. Acceptable |X*Sigma| [V]ö control within the õVariable Data-Specified Threshold Parametersö tab. Moreover, the user must specify the minimum acceptable duration using the õMin. Acceptable Duration [ms]ö control within the õVariable Data-Specified Threshold Parametersö tab. To assist the user in selecting appropriate values for the õX of Threshold = Median +/- X*Sigmaö and õMin. Acceptable |X*Sigma| [V]ö controls, the median, mean, and population standard deviation of the currently displayed Channel 0 stripchart are provided in the indicators to the left of the Channel 0 stripchart.

As an alternative to scanning the currently displayed Channel 0 stripchart, the user can scan each CSV file within a given directory by depressing the õBEGIN EVENT SCAN OF A FULL DAQ SESSIONö button. Once this button is depressed, a dialog appears asking the user to select the directory containing the CSV files to scan. Once the

directory has been selected, each file is scanned in the same manner as discussed above for a single CSV file. The progress of the scan is indicated in the õCURRENT STATEö indicator at the top of the VI. Once the scan of the CSV files is complete, a dialog appears indicating the number of detected events. (It should be noted that the displayed count may be erroneous.)

B.2 Analyzing Backlogged Data Using *Event Parser & Analyzer*

The user can examine the amplitude and phase spectra of the currently displayed Channel 0 stripchartøs Fast Fourier Transform (FFT) by selecting the õFFT Analyzerö tab at the bottom of the VI. Moreover, the user can save the amplitude and phase FFT spectra as a new CSV file by depressing the õSAVE FFT DATA TO .CSV FILEö button. This new CSV file is given the same file name as the currently displayed CSV file, with the prefix õFFT of ö. This new CSV file is saved within a new directory called õSingle Eventsö created in the same directory as the currently displayed CSV file.

By selecting the õAmplitude VS FWHMö tab at the bottom of the VI, the user can generate a chart plotting the peak amplitude of a set of parsed events versus the full width half maximum (FWHM) of the said events. Once the user depresses the õCREATE AMPLITUDE VS FWHM CHARTö button, a dialog appears prompting the user to select the directory containing the parsed events to be analyzed. It is assumed that each CSV file within the selected directory contains a single parsed event. Moreover, any and all subdirectories within the selected directory are ignored. A graph within the õAmplitude VS FWHMö tab then plots the peak amplitude versus FWHM of each CSV file within the selected directory. The file name, duration (between the threshold crossings originally used to parse the file), peak amplitude, and FWHM of each point within the graph are displayed to the right of the graph. Moreover, a new CSV file is saved containing the displayed data. This CSV is named õAmplitude VS FWHM Dataö, and is saved within a new subdirectory called õCharacteristic Dataö within the directory containing the analyzed CSV files.

By selecting the õRight Triangle Correlationö tab at the bottom of the VI, the user can analyze a directory containing parsed CSV files using a correlation based algorithm. Once the user depresses the õCOMPUTE RIGHT TRIANGLE CORRELATIONSö

button, a dialog appears prompting the user to select the directory containing the parsed events to be analyzed. It is assumed that each CSV file within the selected directory contains a single parsed event. Moreover, any and all subdirectories within the selected directory are ignored. Each CSV file within the selected directory is correlated with a positively slopped linear ramp of a height and duration matched to the given CSV file, yielding the c_{inc} correlation coefficient. Each CSV file within the selected directory is also correlated with a negatively slopped linear ramp of a height and duration matched to the given CSV file, yielding the c_{dec} correlation coefficient. The following test parameter is then computed for each CSV file:

$$tp_{corr} = \frac{|c_{inc}| - |c_{dec}|}{|c_{inc}| + |c_{dec}|}$$ (B-1)

A graph within the õRight Triangle Correlationö tab then plots a histogram displaying the number of occurrences of each tp_{corr} value computed for each CSV file within the selected directory using Equation (B-1). The file name, c_{inc}, c_{dec}, and tp_{corr} of each point within the graph are displayed to the right of the graph. New CSV files containing the displayed data and the histogram are saved. The CSV file containing the displayed data is named õRight Triangle Coefficientsö. The CSV file containing the histogram is named õDiff Over Sum Correlation Histogramö. Both CSV files are saved within a new subdirectory called õCharacteristic Dataö within the directory containing the analyzed CSV files.

By selecting the õCentroid Analysisö tab at the bottom of the VI, the user can analyze a directory containing parsed CSV files using an area-under-the-curve based algorithm. Once the user depresses the õEXECUTE CENTROID ANALYSIS OF Ch 0 STRIPCHARTö button, a dialog appears prompting the user to select the directory containing the parsed events to be analyzed. It is assumed that each CSV file within the selected directory contains a single parsed event. Moreover, any and all subdirectories within the selected directory are ignored. Each CSV file within the selected directory is read in and copied by the VI. This internal copy is shifted so that no element is below zero. The area under the left-side of the curve, A_{LHS}, from t_0 to $(t_f$ ó $t_0)/2$ is then computed.

The area under the right-side of the curve, A_{RHS}, from $(t_f – t_0)/2$ to t_f is also computed. The following test parameter is then computed for each CSV file:

$$tp_{area} = \frac{\left| A_{RHS} \right| - \left| A_{LHS} \right|}{\left| A_{RHS} \right| + \left| A_{LHS} \right|}$$ (B-2)

A graph within the "Centroid Analysis" tab then plots a histogram displaying the number of occurrences of each tp_{area} value computed for each CSV file within the selected directory using Equation (B-2). The file name, A_{LHS}, A_{RHS}, and tp_{area} of each point within the graph are displayed to the right of the graph. New CSV files containing the displayed data and the histogram are saved. The CSV file containing the displayed data is named "LHS and RHS Areas". The CSV file containing the histogram is named "Diff Over Sum Centroid Histogram". Both CSV files are saved within a new subdirectory called "Characteristic Data" within the directory containing the analyzed CSV files.

Appendix C:

MATLAB® Code for the Computation

of Dielectrophoretic Spectra

C.1   Theoretical Polystyrene Microsphere Dielectrophoretic Spectra

```matlab
% PSS_DEP_Spectra.m
% Written by Sean Forrest Romanuik
% Aug. 24, 2009
% Dept of Electrical & Computer Engineering - University of Manitoba
clear all
close all
clc


% =======================================================================
% UNIVERSAL CONSTANT INITIALIZATION
% =======================================================================


eps_0 = 8.854e-12;          % permittivity of free space [F/m]
j = sqrt(-1);               % unit imaginary number


% =======================================================================
% FREQUENCY VARIABLE INITIALIZATION
% =======================================================================


f = 10.^(0.1:0.001:10);     % radial frequency [Hz]
w = (2*pi).*f;              % angular frequency [rad/s]


% =======================================================================
% FLUID MEDIUM INITIALIZATION
% =======================================================================


eps_prime_fm = 78*eps_0;    % real abs. fluid permittivity [F/m]
cond_DI_H2O = 18e-4;        % DI H2O conductivity [S/m]
cond_meth_blue = 33.4e-4;   % diluted meth blue conductivity [S/m]

% complex abs. DI H2O permittivity [F/m]
eps_bar_DI_H2O = eps_prime_fm - j.*cond_DI_H2O./w;

% complex abs. diluted meth blue permittivity [F/m]
eps_bar_meth_blue = eps_prime_fm - j.*cond_meth_blue./w;


% =======================================================================
% PSS INITIALIZATION
% =======================================================================


eps_prime_pss = 2.5*eps_0;  % real abs. PSS permittivity [F/m]
cond_pss = 2e-4;            % PSS conductivity [S/m]
```

```
% complex abs. PSS permittivity [F/m]
eps_bar_pss = eps_prime_pss - j.*cond_pss./w;


% ====================================================================
% Re{K} CALCULATION
% ====================================================================


K_bar_DI_H2O = ( eps_bar_pss - eps_bar_DI_H2O ) ...
                ./ ( eps_bar_pss + 2.*eps_bar_DI_H2O );
Re_K_bar_DI_H2O = real(K_bar_DI_H2O);

K_bar_meth_blue = ( eps_bar_pss - eps_bar_meth_blue ) ...
                ./ ( eps_bar_pss + 2.*eps_bar_meth_blue );
Re_K_bar_meth_blue = real(K_bar_meth_blue);


% ====================================================================
% Re{K} PLOTTING
% ====================================================================


plot(log10(f),Re_K_bar_DI_H2O,'color','r');
hold on
plot(log10(f),Re_K_bar_meth_blue,'color','b');
xlabel('log_1_0 | \itf\rm / Hz |')
ylabel('Re\{\itK\rm\}')
title('PSS DEP Spectra')
legend('DI H_2O','Diluted Meth Blue Soln')
% save('C:\Documents and Settings\Administrator\My
Documents\MSc\Thesis\Yeast DEP
Sim\NV_DEP.txt','freq','Re_K_bar_nonvia','-ASCII','-double', '-tabs')
```

C.2   Theoretical *Saccharomyces cerevisiae* Dielectrophoretic Spectra

```
% Yeast_DEP_Spectra.m
% Written by Sean Forrest Romanuik
% Aug. 24, 2009
% Dept of Electrical & Computer Engineering - University of Manitoba
clear all
close all
clc


% ====================================================================
% UNIVERSAL CONSTANT INITIALIZATION
% ====================================================================


eps_0 = 8.854e-12;          % permittivity of free space [F/m]
j = sqrt(-1);               % unit imaginary number


% ====================================================================
% FREQUENCY VARIABLE INITIALIZATION
% ====================================================================


f = 10.^(0.1:0.001:10);     % radial frequency [Hz]
w = (2*pi).*f;              % angular frequency [rad/s]
```

```matlab
% =====================================================================
% FLUID MEDIUM INITIALIZATION
% =====================================================================


eps_prime_fm = 78*eps_0;     % real abs. fluid permittivity [F/m]
cond_fm = 33.4e-4;           % fluid conductivity [S/m]

% complex abs. fluid permittivity [F/m]
eps_bar_fm = eps_prime_fm - j.*cond_fm./w;


% =====================================================================
% VIABLE YEAST COMPUTATIONS
% =====================================================================


% yeast cell dimensions [m]
r_cyt = 3e-6;                % cytoplasmic sphere radius
d_mem = 3.5e-9;             % cytoplasmic membrane thickness
d_pss = 25e-9;             % periplasmic space thickness
d_icw = 110e-9;            % inner cell wall thickness
d_ocw = 50e-9;             % inner cell wall thickness

% yeast cell real absolute permittivities [F/m]
eps_prime_cyt = 51*eps_0;   % cytoplasmic sphere
eps_prime_mem = 3*eps_0;    % cytoplasmic membrane
eps_prime_pss = 14.4*eps_0; % periplasmic space
eps_prime_icw = 60*eps_0;   % inner cell wall
eps_prime_ocw = 5.9*eps_0;  % outer cell wall

% yeast cell conductivities [S/m]
cond_cyt = 12000e-4;        % cytoplasmic sphere
cond_mem = 0.0302e-4;       % cytoplasmic membrane
cond_pss = 41e-4;           % periplasmic space
cond_icw = 30.4322e-5;      % inner cell wall
cond_ocw = 200e-4;          % outer cell wall

% yeast cell complex absolute permittivities [F/m]
eps_bar_cyt = eps_prime_cyt - j.*cond_cyt./w; % cytoplasmic sphere
eps_bar_mem = eps_prime_mem - j.*cond_mem./w; % plasma membrane
eps_bar_pss = eps_prime_pss - j.*cond_pss./w; % periplasmic space
eps_bar_icw = eps_prime_icw - j.*cond_icw./w; % inner cell wall
eps_bar_ocw = eps_prime_ocw - j.*cond_ocw./w; % outer cell wall

% combine the cytoplasmic sphere & the plasma
% membrane into equivalent homogeneous sphere a
a = ( r_cyt + d_mem ) / r_cyt;
K_bar_a = ( eps_bar_cyt - eps_bar_mem ) ...
          ./ ( eps_bar_cyt + 2.*eps_bar_mem );
eps_bar_a = eps_bar_mem .* ( a^3 + 2.*K_bar_a ) ./ ( a^3 - K_bar_a );

% combine sphere a & the periplasmic space
% layer into equivalent homogeneous sphere b
b = ( a + d_pss ) / a;
K_bar_b = ( eps_bar_a - eps_bar_pss ) ...
          ./ ( eps_bar_a + 2.*eps_bar_pss );
eps_bar_b = eps_bar_pss .* ( b^3 + 2.*K_bar_b ) ./ ( b^3 - K_bar_b );
```

```matlab
% combine sphere b & the inner cell
% wall into equivalent homogeneous sphere c
c = ( b + d_icw ) / b;
K_bar_c = ( eps_bar_b - eps_bar_icw ) ...
          ./ ( eps_bar_b + 2.*eps_bar_icw );
eps_bar_c = eps_bar_icw .* ( c^3 + 2.*K_bar_c ) ./ ( c^3 - K_bar_c );

% combine sphere c & the outer cell wall into
% equivalent homogeneous sphere d (the final sphere)
d = ( c + d_ocw ) / c;
K_bar_d = ( eps_bar_c - eps_bar_ocw ) ...
          ./ ( eps_bar_c + 2.*eps_bar_ocw );
eps_bar_d = eps_bar_ocw .* ( d^3 + 2.*K_bar_d ) ...
                           ./ ( d^3 - K_bar_d );

% compute the complex Clausius-Mossotti factor & its real part
K_bar_via = ( eps_bar_d - eps_bar_fm ) ...
            ./ ( eps_bar_d + 2.*eps_bar_fm );
Re_K_bar_via = real(K_bar_via);

% estimate the cross-over frequencies
i_co1 = find( abs(Re_K_bar_via)<0.0002, 1, 'first' );
i_co2 = find( abs(Re_K_bar_via)<0.0002, 1, 'last' );
disp('Viable DEP Spectrum Cross-Over Frequencies [GHz]:')
f_co1 = f(i_co1)
f_co2 = f(i_co2)

% compute and display the approximated RF features
% under the cytoplasmic simplification
disp('1st-Order Approx. of Viable DEP Spectrum Features:')
K_inf = ( eps_prime_cyt - eps_prime_fm ) ./ ( eps_prime_cyt +
2.*eps_prime_fm )
tau_prime_MW2 = ( eps_prime_cyt + 2.*eps_prime_fm ) ./ ( cond_cyt +
2.*cond_fm );
f_prime_MW2 = 1./(2.*pi.*tau_prime_MW2)
Re_K_MF = ( cond_cyt - cond_fm ) ./ ( cond_cyt + 2.*cond_fm )


% ====================================================================
% NONVIABLE YEAST COMPUTATIONS
% ====================================================================

% yeast cell dimensions [m]
r_cyt = 3e-6;                   % cytoplasmic sphere radius
d_mem = 3.5e-9;                 % cytoplasmic membrane thickness
d_cw = 110e-9;                  % inner cell wall thickness

% yeast cell real absolute permittivities [F/m]
eps_prime_cyt = 51*eps_0;       % cytoplasmic sphere
eps_prime_mem = 6*eps_0;        % cytoplasmic membrane
eps_prime_cw = 60*eps_0;        % cell wall

% yeast cell conductivities [S/m]
cond_cyt = 100e-4;              % cytoplasmic sphere
cond_mem = 0.1e-4;              % cytoplasmic membrane
cond_cw = 300e-4;              % cell wall
```

- 155 -

```matlab
% yeast cell complex absolute permittivities [F/m]
eps_bar_cyt = eps_prime_cyt - j.*cond_cyt./w; % cytoplasmic sphere
eps_bar_mem = eps_prime_mem - j.*cond_mem./w; % cytoplasmic membrane
eps_bar_cw = eps_prime_cw - j.*cond_cw./w;    % cell wall

% combine the cytoplasmic sphere & the plasma
% membrane into equivalent homogeneous sphere a
a = ( r_cyt + d_mem ) / r_cyt;
K_bar_a = ( eps_bar_cyt - eps_bar_mem ) ...
          ./ ( eps_bar_cyt + 2.*eps_bar_mem );
eps_bar_a = eps_bar_mem .* ( a^3 + 2.*K_bar_a ) ...
                        ./ ( a^3 - K_bar_a );

% combine sphere a & the outer cell wall into
% equivalent homogenoeus sphere b (the final sphere)
b = ( a + d_cw ) / a;
K_bar_b = ( eps_bar_a - eps_bar_cw ) ...
          ./ ( eps_bar_a + 2.*eps_bar_cw );
eps_bar_b = eps_bar_cw .* ( b^3 + 2.*K_bar_b ) ...
                        ./ ( b^3 - K_bar_b );

% compute the complex Clausius-Mossotti factor & its real part
K_bar_nonvia = ( eps_bar_b - eps_bar_fm ) ...
               ./ ( eps_bar_b + 2.*eps_bar_fm );
Re_K_bar_nonvia = real(K_bar_nonvia);

% estimate the cross-over frequency
i_co = find( abs(Re_K_bar_nonvia)<0.0002, 1, 'last' );
disp('Nonviable DEP Spectrum Cross-Over Frequency [GHz]:')
f_2 = f(i_co)

% compute and display the approximated RF features
% under the cytoplasmic simplification
disp('1st-Order Approx. of Nonviable DEP Spectrum Features:')
K_inf = ( eps_prime_cyt - eps_prime_fm ) ./ ( eps_prime_cyt +
2.*eps_prime_fm )
tau_prime_MW2 = ( eps_prime_cyt + 2.*eps_prime_fm ) ./ ( cond_cyt +
2.*cond_fm );
f_prime_MW2 = 1./(2.*pi.*tau_prime_MW2)
Re_K_MF = ( cond_cyt - cond_fm ) ./ ( cond_cyt + 2.*cond_fm )

% ======================================================================
% DEP Spectra Plotting
% ======================================================================

% plot the real part of the complex Clausius-Mossotti factor
plot(log10(f),Re_K_bar_via,'color','b');
hold on
plot(log10(f),Re_K_bar_nonvia,'color','r');
xlabel('log_1_0 | \itf\rm / Hz |')
ylabel('Re\{\itK\rm\}')
title('Yeast DEP Spectrum')
legend('Viable','Nonviable')
```

Appendix D:

MATLAB® Code for the Lateral Cellular

Velocity Analysis of Detected Bioparticles

```matlab
% Tracker_Data_Analysis_with_Sim_Comp.m
% Written by Sean Forrest Romanuik
% Aug. 24, 2009
% Dept of Electrical & Computer Engineering - University of Manitoba
clc
clear all
close all


% =======================================================================
% GLOBAL VARIABLES
% =======================================================================

% Boolean controls
inc_sim = 0; % Include COMSOL simulation data
is_PSS = 0; % Selects the scaling factor convert E^2 into dC

if inc_sim == 1

    % =======================================================================
    % READ IN COMSOL SIMULATION DATA FROM TEXT FILES
    % =======================================================================

    % Read data from the COMSOL-generated files
    [x_data,y_data,partt_data] = textread('C:\Documents and
      Settings\Administrator\My Documents\MSc\Unheated Yeast Assay\400
      ms\COMSOL Sims\Viable Yeast - 1 Vpp 100 kHz DEP - 9 um h0 -
      t.txt','%f %f %f','headerlines',13);
    [x_data,y_data,E2_data] = textread('C:\Documents and
      Settings\Administrator\My Documents\MSc\Unheated Yeast Assay\400
      ms\COMSOL Sims\Viable Yeast - 1 Vpp 100 kHz DEP - 9 um h0 -
      E^2.txt','%f %f %f','headerlines',13);

    % Read data from COMSOL-generated files every d_data points,
    % skipping over the headers and channel boundary data

    d_data = 1000;

    x_sim = x_data(1:d_data:end).*1e6;
    t_sim = partt_data(1:d_data:end);

    if is_PSS == 1
        dC_sim = E2_data(1:d_data:end).*-9.54E-8;
    else
        dC_sim = E2_data(1:d_data:end).*-3.28E-8;
    end
```

```matlab
    end

% ========================================================================
% READ IN x(t) TRACKER DATA FROM CSV FILE
% ========================================================================

exp_data = csvread('C:\Documents and Settings\Administrator\My
        Documents\MSc\PSS Assay\400 ms\PSS Lateral Velocities -
        Baseline.csv',1,0);

t1 = exp_data(:,1);
t1 = t1(1:find(abs(t1)>0,1,'last'));

x1 = exp_data(:,2);
x1 = x1(1:find(abs(x1)>0,1,'last'));

t2 = exp_data(:,3);
t2 = t2(1:find(abs(t2)>0,1,'last'));

x2 = exp_data(:,4);
x2 = x2(1:find(abs(x2)>0,1,'last'));

t3 = exp_data(:,5);
t3 = t3(1:find(abs(t3)>0,1,'last'));

x3 = exp_data(:,6);
x3 = x3(1:find(abs(x3)>0,1,'last'));

t4 = exp_data(:,7);
t4 = t4(1:find(abs(t4)>0,1,'last'));

x4 = exp_data(:,8);
x4 = x4(1:find(abs(x4)>0,1,'last'));

t5 = exp_data(:,9);
t5 = t5(1:find(abs(t5)>0,1,'last'));

x5 = exp_data(:,10);
x5 = x5(1:find(abs(x5)>0,1,'last'));

% ========================================================================
% COMPUTE v(t)
% ========================================================================

if inc_sim == 1
    v_sim = diff(x_sim)./diff(t_sim);
end

v1 = diff(x1)./diff(t1);
v2 = diff(x2)./diff(t2);
v3 = diff(x3)./diff(t3);
v4 = diff(x4)./diff(t4);
v5 = diff(x5)./diff(t5);
```

```
% ========================================================================
% FIT v(t) TO A UNIFORMLY SPACED x-AXIS
% ========================================================================

xi = -125:0.5:125;

if inc_sim == 1
    v_sim_i = interp1(x_sim(2:end),v_sim,xi);
end

v1i = interp1(x1(2:end),v1,xi);
v2i = interp1(x2(2:end),v2,xi);
v3i = interp1(x3(2:end),v3,xi);
v4i = interp1(x4(2:end),v4,xi);
v5i = interp1(x5(2:end),v5,xi);


% ========================================================================
% COMPUTE THE MEAN AND STANDARD DEVIATION OF v(x) AT EACH x POINT
% ========================================================================

v_mean = zeros(1,length(xi));
v_std = zeros(1,length(xi));

for i = 1:length(xi)
    v_mean(i) = nanmean( [ v1i(i), v2i(i), v3i(i), v4i(i), v5i(i) ] );
    v_std(i) = nanstd( [ v1i(i), v2i(i), v3i(i), v4i(i), v5i(i) ] );
end


% ========================================================================
% COMPUTE THE RELATIVE PERCENT CHANGE IN v AFTER CROSSING THE MEA
% ========================================================================

% define initial lateral velocity as the mean lateral velocity
% within the x = [ -125, -75 ] um interval

% define final lateral velocity as the mean lateral velocity
% within the x = [ 75, 125 ] um interval

v1i_0 = nanmean( v1i(1:101) )
v1i_f = nanmean( v1i(401:end) )
v1i_rpc = 100 * ( v1i_f - v1i_0 ) / v1i_0

v2i_0 = nanmean( v2i(1:101) )
v2i_f = nanmean( v2i(401:end) )
v2i_rpc = 100 * ( v2i_f - v2i_0 ) / v2i_0

v3i_0 = nanmean( v3i(1:101) )
v3i_f = nanmean( v3i(401:end) )
v3i_rpc = 100 * ( v3i_f - v3i_0 ) / v3i_0

v4i_0 = nanmean( v4i(1:101) )
v4i_f = nanmean( v4i(401:end) )
v4i_rpc = 100 * ( v4i_f - v4i_0 ) / v4i_0
```

```matlab
v5i_0 = nanmean( v5i(1:101) )
v5i_f = nanmean( v5i(401:end) )
v5i_rpc = 100 * ( v5i_f - v5i_0 ) / v5i_0

mean_vi_0 = nanmean( [ v1i_0, v2i_0, v3i_0, v4i_0, v5i_0 ] )

std_vi_0 = nanstd( [ v1i_0, v2i_0, v3i_0, v4i_0, v5i_0 ] )

mean_vi_f = nanmean( [ v1i_f, v2i_f, v3i_f, v4i_f, v5i_f ] )

std_vi_f = nanstd( [ v1i_f, v2i_f, v3i_f, v4i_f, v5i_f ] )

mean_vi_rpc = nanmean( [ v1i_rpc, v2i_rpc, ...
                         v3i_rpc, v4i_rpc, v5i_rpc ] )

std_vi_rpc = nanstd( [ v1i_rpc, v2i_rpc, v3i_rpc, v4i_rpc, v5i_rpc ] )

v_mu_plus_std_0 = nanmean( v_mean(1:101) + v_std(1:101) )
v_mu_plus_std_f = nanmean( v_mean(401:end) + v_std(401:end) )
v_mu_plus_std_rpc = 100 * ( v_mu_plus_std_f - v_mu_plus_std_0 ) / ...
v_mu_plus_std_0

v_mu_0 = nanmean( v_mean(1:101) )
v_mu_f = nanmean( v_mean(401:end) )
v_mu_rpc = 100 * ( v_mu_f - v_mu_0 ) / v_mu_0

v_mu_minus_std_0 = nanmean( v_mean(1:101) - v_std(1:101) )
v_mu_minus_std_f = nanmean( v_mean(401:end) - v_std(401:end) )
v_mu_minus_std_rpc = 100 * ( v_mu_minus_std_f - v_mu_minus_std_0 ) / ...
v_mu_plus_std_0

if inc_sim == 1
    v_sim_0 = nanmean( v_sim_i(1:101) )
    v_sim_f = nanmean( v_sim_i(401:end) )
    v_sim_rpc = 100 * ( v_sim_f - v_sim_0 ) / v_sim_0
end

% ========================================================================
% PLOT EXP. x(t), v(x), v(x) STATISTICS & SIM. v(x) & dC(t)
% ========================================================================

plot(t1,x1,'b')
hold on
plot(t2,x2,'g')
plot(t3,x3,'r')
plot(t4,x4,'m')
plot(t5,x5,'c')
ylabel('x_c_e_l_l [\mum]')
xlabel('t [s]')
title('Lateral Position Profiles')
legend('Exp. #1','Exp. #2','Exp. #3','Exp. #4','Exp. #5')

hold off
figure
```

```matlab
plot(xi,v1i,'b')
hold on
plot(xi,v2i,'g')
plot(xi,v3i,'r')
plot(xi,v4i,'m')
plot(xi,v5i,'c')
ylabel('\nu_c_x [\mum/s]')
xlabel('x [\mum]')
title('Lateral Velocity Profiles')
legend('Exp. #1','Exp. #2','Exp. #3','Exp. #4','Exp. #5')

if inc_sim == 1

    hold off
    figure
    plot(xi,v_mean,'b')
    hold on
    plot(xi,v_mean+v_std,'r')
    plot(xi,v_mean-v_std,'m')
    plot(xi,v_sim_i,'g')
    ylabel('\nu_c_x [\mum/s]')
    xlabel('x [\mum]')
    title('Lateral Velocity Profile Statistics with Simulation')
    legend('Mean','Mean + Std. Dev.','Mean - Std. Dev.','Sim')

    hold off
    figure
    plot(t_sim,dC_sim,'b')
    ylabel('\DeltaC_M_E_A [aF]')
    xlabel('t [s]')
    title('Simulated dC Signature')

else

    hold off
    figure
    plot(xi,v_mean,'b')
    hold on
    plot(xi,v_mean+v_std,'r')
    plot(xi,v_mean-v_std,'m')
    ylabel('\nu_c_x [\mum/s]')
    xlabel('x [\mum]')
    title('Lateral Velocity Profile Statistics')
    legend('Mean','Mean + Std. Dev.','Mean - Std. Dev.')

end
```

References

[Agil09] *cp.literature.agilent.com/litweb/pdf/genesys200801/elements/ substrate_tables/tablelosstan.htm*, 2009.

[Álv00] A. Álvarez-Barrientos, J. Arroyo, R. Cantón, C. Nombela, and M. Sánchez-Pérez, õApplications of flow cytometry to clinical microbiologyö, *Clin. Microbiol. Rev.*, vol. 13, pp. 167-195, 2000.

[And99] K. Andersson, K.E. Magnusson, M. Majeed, O. Stendahl, and M. Fällman, õ*Yersinia pseudotuberculosis*-induced calcium signaling in neutrophils is blocked by the virulence effector YopHö, *Infect. Immun.*, vol. 67, pp. 2567-2574, 1999.

[Arc00] C. Arcangeli and S. Cannistraro, õIn situ Raman microspectroscopic identification and localization of carotenoids: approach to monitoring of UV-B irradiation stress on Antaric fungusö, *Biopolymers*, vol. 57, pp. 179-186, 2000.

[Arne00] N. Arneborg, L. Jespersen, and M. Jakobsen, õIndividual cells of *Saccharomyces cerevisiae* and *Zygosaccharomyces bailii* exhibit different short-term intracellular pH responses to acetic acidö, *Arch. Microbiol.*, vol. 174, pp. 125-128, 2000.

[Arno82] W.M. Arnold and U. Zimmermann, õRotating-field-induced rotation and measurement of the membrane capacitance of single mesophyll cells of *Avena sativa*ö, *Zeitschrift für Naturforschung*, vol. 37c, pp. 908-915, 1982.

[Asa76] K. Asami, T. Hanai, N. Koizumi, õDielectric properties of yeast cellsö, *J. Membr. Biol.*, vol. 28, pp. 169-180, 1976.

[Asa96] K. Asami and T. Yonezawa, õDielectric behavior of wild-type yeast and vacuole-deficient mutant over a frequency range of 10 kHz to 10 GHzö, *J. Biophys.*, vol. 71, pp. 2192-2200, 1996.

[Ayl99] E.H. Ayliffe, A.B. Frazier, and R.D. Rabbitt, õElectric impedance spectroscopy using microchannels with integrated metal electrodesö, *J. Microelectromech. Sys.*, vol. 8, no. 1, 1999.

[Bak03] K. Baker Megan, K. Mikhitarian, W. Osta, K. Callahan, R. Hoda, F. Brescia, R. Kneuper-Hall, M. Mitas, J. Cole David, and E. Gillanders William, õMolecular detection of breast cancer cells in the peripheral blood of advanced-stage breast cancer patients using multimaker real-time reverse transcription-polymerase chain reaction and a novel porous barrier density gradient centrifugation technologyö, *Clinical Cancer Research*, vol. 9, no. 13, pp. 4865-4871, 2003.

[Bapt99] M. Baptista, P. Rodrigues, F. Depardieu, P. Courvalin, and M. Arthur, õSingle-cell analysis of glycopeptide resistance gene expression in teicoplanin-resistant mutants of a VanB-type *Enterococcus faecalis*ö, *Mol. Microbiol.*, vol. 32, pp. 17-28, 1999.

[Bar99] M.R. Barer and C.R. Harwood, õBacterial viability and culturabilityö, *Adv. Microb. Physiol.*, vol. 41, pp. 93-137, 1999.

[Bech99] C. Bechinger, K.F. Giebel, M. Schell, P. Leiderer, H.B. Deising, and M. Bastmeyer, õOptical measurements of invasive forces exerted by appressoria of a plant pathogenic fungusö, *Science*, vol. 285, pp. 1896-1899, 1999.

[Beck94] F.F. Becker, X-B Wang, Y. Huang, R. Pethig, J.V. Vykoukal and P.R.C. Gascoyne, õThe removal of human leukaemia cells from blood using interdigitated microelectrodesö, *J. Phys. D: Appl. Phys.*, vol. 27, pp. 2659-2662, 1994.

[Beng82] L. Benguigui and I.J. Lin, õMore about the dielectrophoretic forceö, *J. Appl. Phys.*, vol. 53, pp. 1141, 1982.

[Boe01] G. Boeck, "Current status of flow cytometry in cell and molecular biology", *Int. Rev. Cytol.*, vol. 204, pp. 239-298, 2001.

[Bone95] S. Bone and C.A. Small, "Dielectric studies of ion fluctuation and chain bending in native DNA", *Biochim. Biophys. Acta.*, vol. 1260, no. 1, pp. 85-93, 1995.

[Bra08] T. Braschler, N. Demierre, E. Nascimento, T. Silva, A.G. Oliva and P. Renaud, "Continuous separation of cells by balanced dielectrophoretic forces at multiple frequencies", *Lab on a Chip*, vol. 8, pp. 280-286, 2008.

[Bre04] B.F. Brehm-Stecher and E.A. Johnson, "Single-cell microbiology: tools, technologies, and applications", *Microbiol. and Mol. Biol. Rev.*, vol. 68, no. 3, pp. 538-559, 2004.

[Brid00] E.Y. Bridson and G.W. Gould, "Quantal microbiology", *Lett. Appl. Microbiol.*, vol. 30, pp. 95-98, 2000.

[Cai0] C. Cai, B. Liu, and M.V. Mirkin, "Scanning electrochemical microscopy of living cells. 3. *Rhodobacter sphaeroides*", *Anal. Chem.*, vol. 74, pp. 114-119, 2002.

[Campo04] L.S. ampos, D.P. Leone, J.B. Relvas, C. Brakebusch, R. Fässler, U. Suter, and C. Ffrench-Constant, "β1 integrins activate a MAPK signalling pathway in neural stem cells that contributes to their maintenance", *Development*, vol. 131, no. 14, pp. 3433-3444, 2004.

[Campb02] N.A. Campbell and J.B. Reece, Biology (6th Ed.), Benjamin Cummings: San Francisco, 2002.

[Chan97] K.L. Chan, P.R.C. Gascoyne, F.F. Becker, and R. Pethig, "Electrorotation of lipsomes: verification of dielectric multi-shell model for cells", *Biochimica et Biophysica Acta-Lipids and Lipid Metabolism*, vol. 1349, pp. 182-196, 1997.

[Che04] K. Cheung, S. Gawad, and P. Renaud, "Microfluidic impedance spectroscopy flow cytometer: particle size calibration", *Proc. 17th IEEE Microelectromech. Sys. (MEMS)*, pp. 343-346, 2004.

[Cle78] J.K. Clemens, "Capaitive pickup and the buried subcarrier encoding system for the RCA VideoDisc", *RCA Review*, vol. 39, pp. 33-59, 1978.

[Clu00] P. Cluzel, M. Surette, and S. Leibler, "An ultrasensitive bacterial motor revealed by monitoring signaling proteins in single cells", *Science*, vol. 287, pp. 1652-1655, 2000.

[COM08] *www.comsol.com*, 2008.

[Cost03] H.G.L. Coster, "The physics of cell membranes", *J. Biol. Phys.*, vol. 29, pp. 363-399, 2003.

[Cou56] W.H. Coulter, "High speed automatic blood cell counter and cell size analyzer", *Proc. Natl. Electronics Conf.*, vol. 12, pp. 1034, 1956.

[Cri02] M. Cristofanilli, G. De Gasperis, L. Zhang, M.C. Hung, P.R.C. Gascoyne, and G.B. Hortobagyi, "Automated electrorotation to reveal dielectric variations related to HER-2/*neu* overexpression in MCE-7 sublines", *Cli. Cancer. Res.*, vol. 8, no. 2, pp. 615-619, 2002.

[Cri04] M. Cristofanilli, G.T. Budd, M.J. Ellis, A. Stopeck, J. Matera, M.C. Miller, J.M. Reuben, G.V. Doyle, WJ. Allard, L.W.M.M. Terstappen, and D.F. Hayes, "Circulating tumor cells, disease progression, and survival in metastatic breast cancer", *N. Engl. J. Med.*, vol. 351, no. 8, pp. 781-791, 2004.

[Dav96] H.M. Davey and D.B. Kell, "Flow cytometry and cell sorting of heterogeneous microbial populations: the importance of single cell analysis", *Microbiol. Rev.*, vol. 60, pp. 641-696, 1996.

[Dia91] E.P. Diamandis and T.K. Christopoulos, õThe biotin-(strept)avidin system: principles and applications in biotechnologyö, *Clin. Chem.*, vol. 37, no. 5, pp. 625-636, 1991.

[Dub00] G.B.J. Dubelaar and P.L. Gerritzen, õCytoBuoy: a step towards using flow cytometry in operational ocenaographyö, *Sci. Mar.*, vol. 64, pp. 255-265, 2000.

[Eddy58] A.A. Eddy, õThe structure of the yeast cell wall. 2. Degradative studies with enzymesö, *Proc. Roy. Soc. London Series B*, vol. 149, nop. 936, pp. 425-440, 1958.

[Elo02] M.B. Elowitz, A.J. Levine, E.D. Siggia, and P.S. Swain, õStochastic gene expression in a single cellö, *Science*, vol. 297, pp. 1183-1186, 2002.

[Feni98] D. Fenili and B. Pirovano, õThe automation of sediment urinalysis using a new urine flow cytometer (UF-100^{TM})ö, *Clin. Chem. Lab. Med.*, vol. 36, pp. 909-917, 1998.

[Fer07] G.A. Ferrier, A.N. Hladio, D.J. Thomson, G.E. Bridges, M. Hedayatipoor, S. Olson, and M.R. Freeman, õMicrofluidic electromanipulation with capacitive detection for cell diagnositc applicationsö, *Proc. NSTI*, vol. 2, pp. 214-217, 2007.

[Fer08a] G.A. Ferrier, S.F. Romanuik, D.J. Thomson, G.E. Bridges, and M.R. Freeman, õCapacitance signatures for rapid detection of the polarity of the dielectrophoretic force on single yeast cellsö, *Proc. NSTI*, vol. 2, pp. 589-592, 2008.

[Fer08b] G.A. Ferrier, A.N. Hladio, D.J. Thomson, G.E. Bridges, M. Hedayatipoor, S. Olson, and M.R. Freeman, õMicrofluidic electromanipulation with capacitive detection for the mechanical analysis of cellsö, *Biomicrofluidics*, vol. 2, no. 4-044102, pp. 1-13, 2008.

[Fer09a] G.A. Ferrier, S.F. Romanuik, D.J. Thomson, G.E. Bridges, and M.R. Freeman, õA microwave interferometric system for simultaneous actuation and detection of single biological cellsö, *Lab on a Chip*, 2009 (Submitted May 5 2009).

[Fer09b] G.A. Ferrier, S.F. Romanuik, D.J. Thomson, G.E. Bridges, and M.R. Freeman, õRapid classification of biological cells based on dielectrophoretic actuation with simultaneous capacitive detectionö, *Proc. μTAS*, 2009 (Submitted July 1 2009).

[Fla08] L.A. Flanagan, J. Lu, L. Wang, S.A. Marchenko, N.L. Jeon, A.P. Lee, and E.S. Monuki, õUnique dielectric properties distinguish stem cells and their differentiated progencyö, *Stem Cells*, vol. 26, pp. 656-665, 2008.

[Fost89] K.R. Foster and H.P. Schwan, õDielectric-properties of tissues and biological-materials ó a critical-reviewö, *Crit. Rev. Biomed. Eng.*, vol. 17, no. 1, pp. 25-104, 1989.

[Fox03] R. Fox, A. McDonald and P. Pritchard, <u>Introduction to Fluid Mechanics</u>, John Wiley and Sons: Somerset, 2003.

[Fuhr85] G. Fuhr, õÜber die rotation dielektrischer körper in rotierenden feldernö, Ph.D. Dissertation, Humbolt University, Berlin, 1985.

[Gab95] H. Gabriel and W. Kindermann, õFlow-cytometryô principles and applications in exercise immunologyö, *Sports Med.*, vol. 20, pp. 302-320, 1995.

[Gan95] V. Ganeva, B. Galutzov, J. Teissie, õElectric field mediated loading of macromolecules in intact yeast cells is critically controlled at the wall levelö, *Biochim. Biophys. Acta.*, vol. 1240, pp. 229-236, 1995.

[Gar99] G. Garratty and P.A. Arndt, õApplications of flow cytofluorometry to red blood cell immunologyö, *Cytometry*, vol. 38, pp. 259-267, 1999.

[Gasp98]   G.D. Gasperis, X.B. Wang, J. Yang, F.F. Becker, and P.R.C. Gascoyne, "Automated electrorotation: dielectric characterization of living cells by real-time motion estimation", *Meas. Sci. Technol.*, vol. 9, pp. 518-529, 1998.

[Gasc92] P.R.C. Gascoyne, Y. Huang, R. Pethig, J.V. Vykoukal, and F.F. Becker, "Dielectrophoretic separation of mammalian cells studied by computerized image analysis", *Meas. Sci. Technol.*, vol. 3, pp. 439-445, 1992.

[Gasc04] P.R.C. Gascoyne and J.V. Vykoukal, "Dielectrophoresis-based sample handling in general-purpose programmable diagnostic instruments", *Proc. IEEE*, vol. 92, pp. 22-41, 2004.

[Gaw01]   S. Gawad, L. Schildb, and P. Renauda, "Micromachined impedance spectroscopy flow cytometer for cell analysis and particle sizing", *Lab on a Chip*, vol. 1, no. 76, 2001.

[Gift95]   E.A. Gift and J.C. Weaver, "Observation of extremely heterogeneous electroporative molecular uptake by *Saccharomyces cerevisiae* which changes with electric field pulse amplitude", *Biochim. Biophys. Acta.*, vol. 1234, pp. 52-62, 1995.

[Goa97]   A.D. Goater, J.P.H. Burt, and R. Pethig, "A combined electrorotation and travelling wave device: applied to the concentration and viability of *Cryptosporidium*", *J. Phys. D Appl. Phys.*, vol. 33, pp. L65-L70, 1997.

[Goa98]   A.D. Goater and R. Pethig, "Electrorotation and dielectrophoresis", *Parasitology*, vol. 117, pp. S117-S189, 1998.

[Han07] A. Han, L. Yang, and A.B. Frazier, "Quantification of the heterogeneity in breast cancer cell lines using whole-cell impedance spectroscopy", *Clin. Cancer Res.*, vol. 13, no. 1, pp. 139-143, 2007.

[Hayt01] W.H. Hayt and J.A. Buck, <u>Engineering Electromagnetics (6th Ed.)</u>, McGraw Hill, 2001.

[Hard00] C.L. Harding, D.R. Lloyd, C.M. McFarlane, and M. Al-Rubeai, õUsing the mytocyte flow cytometer to monitor cell number, viability, and apoptosis in manmmalian cell cultureö, *Biotechnol. Prog.*, vol. 16, pp. 800-802, 2000.

[Hei02] T. Heida, W.L. Rutten, and E. Marani, õExperimental invesitigation on neural cell survival after dielectriphoretic trappingö, *Arch. Physiol. Biochem.*, vol. 110, pp. 373-382, 2002.

[Höl90] R. Hölzel, õElektromagnetische Felder in der Umgebung lebender Zellenö, PhD Dissertation, Berlin: Berlin-Verlag A Spitz, pp. 14-85, 1990.

[Höl92] R. Hölzel and I. Lamprecht, õDielectric properties of yeast cells as determined by electrorotationö, *Biochim. Biophys. Acta*, vol. 1104, pp. 195-200, 1992.

[Höl97] R. Hölzel, õElectrorotation of single yeast cells at frequencies between 100 Hz and 1.6 GHzö, *J. Biophys.*, vol. 73, pp. 1103-1109, 1997.

[Hua92] Y. Huang, R. Hölzel, R. Pethig and X.B. Wang, õDifferences in the AC electrodynamics of viable and nonviable yeast cells determined through combined dielectrophoresis and electrotation studiesö, *Phys. Med. Biol.*, vol. 37, pp. 1499-1517, 1992.

[Hua97] Y. Huang, X.B. Wang, F.F. Becker, and P.R.C. Gascoyne, õIntroducing dielectrophoresis as a new force field for field-flow fractionationö, *Biophysical Journal*, vol. 73, pp. 1118-1129, 1997.

[Hug03] M.P. Hughes, <u>Nanoelectromechanics in Engineering and Biology</u>, CRC Press, 2003.

[Huh05] D. Huh, W. Gu, Y. Kamotani, J.B. Grotberg, and S. Takayama, "Microfluidics for flow cytometric analysis of cells and particles", *Physiol. Meas.*, vol. 26, pp. R73-R98, 2005.

[Hunt04] T.P. Hunt, H. Lee, and R.M. Westervelt, "Addressable micropost array for the dielectrophoretic manipulation of particles in fluid", *Appl. Phys. Lett.*, vol. 85, no. 26, pp. 6421-6423, 2004.

[Hus88] A. Husebekk, B. Skogen, and G. Husby, "High-density lipoprotein has different binding capacity for different apoproteins. The amyloidogenic apoproteins are easier to displace from high-density lipoprotein", *Scandinavian J. Immunology*, vol. 28, no. 6, pp. 653-658, 1988.

[Jar09] M. Nikolic-Jaric, S.F. Romanuik, G.A. Ferrier, G.E. Bridges, M. Butler, K. Sunley, D.J. Thomson, and M.R. Freeman, "Microwave frequency sensor for detection of biological cells in microfluidic channels", *Biomicrofluidics*, vol. 3, no. 3-034103, pp. 1-15, 2009.

[Jon95] T.B. Jones, <u>Electromechanics of Particles</u>, Cambridge University Press: New York, pp. 39-48, 1995.

[Joux00] F. Joux and P. Lebaron, "Use of fluorescent probes to assess physiological functions of bacteria at single-cell level", *Microbes Infect.*, vol. 2, pp. 1523-1535, 2000.

[Kahn04] J. Kahn Harriette, A. Presta, L.-Y. Yang, J. Blondal, M. Trudeau, L. Lickley, C. Holloway, R. McCready David, D. Maclean, and A. Marks, "Enumeration of circulating tumor cells in the blood of breast cancer patients after filtration enrichment: correlation with disease stage", *Breast Cancer Research and Treatment*, vol. 86, no. 3, pp. 237-247, 2004.

[Karp05] G. Karp, <u>Cell and Molecular Biology: Concepts and Experiments (4th Ed.)</u>, John Wiley and Sons, 2005.

[Kats00] T. Katsuragi and Y. Tani, õScreening for microorganisms with specific characteristics by flow cytometry and single-cell sortingö, *J. Biosci. Bioeng.*, vol. 89, pp. 217-222, 2000.

[Kell98] D.B. Kell, A.S. Kaprelyants, D. Weichart, C.R. Harwood, and M.R. Barer, õViability and activity in readily culturable basteria: a review and discussion of the practical issuesö, *Antonie Leeuwnehoek*, vol. 73, pp. 169-187, 1998.

[Keller99] K.A. Kellerman and J.C. McNally, õMound-cell movement and morphogenesis in *Dictyostelium*ö, *Dev. Biol.*, vol. 208, pp. 416-429, 1999.

[Koch96] A. Koch, õSimilarities and differences of individual bacteria within a cloneö, <u>*E. coli* and *Salmonella:* Cellular and Molecular Biology (2nd Ed.)</u>, pp. 1640-1651, Eds. F.C. Niedhardt, R. Curtiss III, J.L. Ingraham, E.C.C. Lin, K.B. Low, B. Magasanik, W.S. Reznikoff, M. Riley, M. Schaechter, and H.E. Umbarger, ASM Press: Washington, D.C., 1996.

[Koch99] M. Koch, A.G.R. Evans, and A. Brunnschweiler, õDesign and fabrication of a micromachined Coulter counterö, *J. Micromech. Microeng.*, vol. 9, pp. 159-161, 1999.

[Kuo00] S.C. Kuo and J.L. McGrath, õSteps and fluctuations of *Listeria monocytogenes* during actin-based motilityö, *Nature*, vol. 407, pp. 1026-1029, 2000.

[Linc04] B. Lincoln, H.M. Erickson, S. Schinkinger, F. Wottawah, D. Mitchell, S. Ulvick, C. Bilby, and J. Guck, õDeformability-based flow cytometryö, *Cytometry Part A*, vol. 59A, no. 2, pp. 203-209, 2004.

[Liu07] S-L. Liu, A, Karmenyan, M-T. Wei, C-C. Huang, C-H. Lin, and A. Chiou, "Optical forced oscillation for the study of lectin-glycoprotein interaction at the cellular membrane of a Chinese hamster ovary cell", *Optics Express*, vol. 15, no. 5, 2713, 2007.

[Los99] R. Losick and L. Shapiro, "Changing views on the nature of the bacterial cell: from biochemistry to cytology", *J. Bacteriol.*, vol. 181, pp. 4143-4145, 1999.

[Mar94a] G.H. Markx, Y. Huang, X.F. Zhou, and R. Pethig, "Dielectrophoretic characterization and separation of micro-organisms", *Microbiology*, vol. 140, pp. 585-591, 1994.

[Mar94b] G.H. Markx, M. Talary, and R. Pethig, "Seperation of viable and nonviable yeast using dielectrophoresis", *J. Biotechnol.*, vol. 32, pp. 29-37, 1994.

[Mea05] Measurement Computing Corporation, *Universal Library for LabVIEW User's Guide (Document Revision 8)*, Measurement Computing Corporation, 2005.

[Mel91] M.R. Melamed, T. Lindmo, and M.L. Mendelsohn, <u>Flow Cytometry and Sorting</u>, John Wiley and Sons: New York, 1991.

[Mic08] *www.micronit.com*, 2008.

[Misc82] M. Mischel, A. Voss, and H.A. Pohl, "Cellular spin resonance in rotating electric fields", *J. Biol. Phys.*, vol. 10, no. 4, pp. 223-226, 1982.

[Mish98] N. Mishima, T. Kaneta, and T. Imasaka, "The "optical funnel". A technique for measuring a microorganism's power", *Anal. Chem.*, vol. 70, pp. 3513-3515, 1998.

[Moo92]   C.W. Moore, R. del Valle, J. McKoy, A. Pramanik, and R.E. Gordon, õLesions and preferential initial localization of [*S-methyl*-^{3}H]bleomycin A$_2$ on *Saccharomyces cerevisiae* cell walls and membranesö, *Antimicrob. Agents Chemother.*, vol. 36, pp. 2497-2505, 1992.

[Mulh94]   J. Mulholland, D. Preuss, A. Moon, A. Wong, D. Drubin, and D. Botstein, õUltrastructure of the yeast actin cytoskeleton and its association with the plasma membraneö, *J. Cell Biol.*, vol. 125, pp. 381-391, 1994.

[Nor52]   D.H. Northcote and R.W. Horne, õThe chemical composition and structure of the yeast cell wallö, *J. Biochem.*, vol. 51, no. 2, pp. 232-236, 1952.

[Orm00]   M.G. Ormerod, Flow Cytometry, Oxford University Press: New York, 2000.

[Past01]   J.D. Pasteris, J.J. Freeman, S.K. Goffredi, and K.R. Buck, õRaman spectroscopic and laser scanning confocal microscopic analysis of sulfur in living sulfur-precipitating marine bacteriaö, *Chem. Geol.*, vol. 180, pp. 3-18, 2001.

[Per03]   I.R. Perch-Nielsen, D.D. Bang, C.R. Poulsen, J. El-Ali, and A. Wolff, õRemoval of PCR inhibitors using dielectrophoresis as a selective filter in a microsystemö, *Lab on a Chip*, vol. 3, pp. 212-216, 2003.

[Peth79]   R. Pethig, Dielectric and Electronic Properties of Biological Materials, John Wiley and Sons: New York, 1979.

[Peth97]   R. Pethig and G.H. Markx, õApplications of dielectrophoresis in biotechnologyö, *Trends Biotechbol.*, vol. 15, no. 10, pp. 426-432, 1997.

[Peth02]   R. Pethig, V. Bressler, C. Carswell-Crumpton, Y. Chen, L. Foster-Haje, M.E. García-Ojeda, R.S. Lee, G.M. Lock, M.S. Talary, and K.M. Tate, õDielectrophoretic studies of the activation of human T lymphocytes using a newly developed cell profiling systemö, *Electrophoresis*, vol. 23, pp. 2057-2063, 2002.

[Phil09]   R. Phillips, J. Kondev, and J. Theriot, <u>Physical Biology of the Cell</u>, Garland Science: New York, 2009.

[Pie06] A. Pierres, J. Vitte, A.M. Benoliel, and P. Bongrand, õDissecting individual ligand-receptor bonds with a laminar flow chamberö, *Biophys. Rev. Lett.*, vol. 1, no. 3, pp. 231-257, 2006.

[Pohl78] H.A. Pohl, <u>Dielectrophoresis</u>, Cambridge University Press: London, 1978.

[Poly01] *www.polymerprocessing.com/notes/root92a.pdf*, 2001.

[Poly09] *www.polysciences.com/*, 2009.

[Pot01] E.O. Potma, W.P. de Boeij, P.J.M. van Haastert, and D.A. Wiersman, õReal-time visualization of intracellular hydrodynamics in single living cellsö, *Proc. Natl. Acad. Sci. U.S.A.*, vol. 98, pp. 1577-1582, 2001.

[Pow00] C.D. Powell, S.M. Van Zandycke, D.E. Quain, and K.A. Smart, õReplicative ageing and senescence in *Saccharomyces cerevisiae* and the impact on brewing fermentationsö, *Microbiol.*, vol. 146, pp. 1023-1034, 2000.

[Poz05] D.M. Pozar, <u>Microwave Engineering (3rd Ed.)</u>, John Wiley and Sons, 205.

[Pra04] S. Prasad, X. Zhang, M. Yang, Y.C. Ni, V. Parpura, C.S. Ozkan, and M. Ozkan, õSeparation of individual neurons using dielectrophoretic alternative current fieldsö, *J. Neurosci. Methods*, vol. 135, no. 1-2, pp. 79-88, 2004.

[Poz05] D.M. Pozar, <u>Microwave Engineering (3rd Ed.)</u>, John Wiley and Sons, 205.

[Raf07]   M. Raffel, C.E. Willert, S.T. Wereley, and J. Kompenhans, <u>Particle Image Velocimetry: A Practical Guide (2nd Ed.)</u>, Springer, 2005.

[Rai96] V. Raicu, G. Raicu, and G. Turcu, "Dielectric properties of yeast cells as simulated by the two-shell model", *Biochim. Biophys. Acta*, vol. 1274, pp. 143-148, 1996.

[Ras99] D.M. Raskin and P.A.J. de Boer, "Rapid pole-to-pole oscillation of a protein required for direct division to the middle of *Escherichia coli*", *Proc. Natl. Acad. Sci. U.S.A.*, vol. 96, pp. 4971-4976, 1999.

[Rci98] E. Racila, D. Euhus, A.J. Weiss, C. Rao, J. McConnell, L.W.M.M. Terstappen, and J.W. Uhr, "Detection and characterization of carcinoma cells in the blood", *Proc. Natl. Acad. Sci. U.S.A.*, vol. 95, no. 8, pp. 4589-4594, 1998.

[Res02] R. Resnick, D. Halliday, and K.S. Krane, Physics: Volume 1 (5th Ed.), John Wiley and Sons, 2002.

[Roe97] M. Roederer, S. DeRosa, R. Gersein, M. Anderson, M. Bigos, R. Stovel, T. Nozaki, D. Parks, L. Herzenberg, and L. Herzenberg, "8 color, 10-parameter flow cytometry to eludicate complex leukocyte heterogenity", *Cytometry*, vol. 29, no. 4, pp. 328-339, 1997.

[Roc99] D. Rockabrand, T. Austin, R. Kaiser, and P. Blum, "Bacterial growth state distinguished by single-cell protein profiling: does chlorination kill coliforms in municipal effluent?", *Appl. Environ. Microbiol.*, vol. 65, pp. 4181-4188, 1999.

[Rodr07] R. Rodriguez-Trujillo, C.A. Mills, J. Samitier, and G. Gomila, "Low cost micro-Coulter counter with hydrodynamic focusing", *Microfluid Nanofluid*, vol. 3, no. 2, pp. 171-176, 2007.

[Rom08] S.F. Romanuik, G.A. Ferrier, D.J. Thomson, G.E. Bridges, S. Olson, and M.R. Freeman, "All-electronic detection and actuation of single biological cells for lab-on-a-chip applications", *Proc. IEEE Sensors*, vol. 1, pp. 634-637, 2008.

[Rom09] S.F. Romanuik, G.A. Ferrier, M.N. Jaric, D.J. Thomson, G.E. Bridges, and M.R. Freeman, õDielectrophoretic actuation and simultaneous detection of individual bioparticlesö, <u>Advances in Biomedical Sensing, Measurements, Instrumentation, and Systems</u>, Eds. A. Lay-Ekuakille and S.C. Mukhopadhyay, Springer ó Verlag, 2009 (Submitted June 3 2009).

[SACE09] *www.spacebiol.ethz.ch/missions/sacestre*, 2009.

[Sau85a] F.A. Sauer, õInteraction forces between microscopic particles in an external electromagnetic fieldö, <u>Interactions Between Electromagnetic Fields and Cells</u>, pp. 181-202, Eds. A. Chiabrera, C. Nicolini, and H.P. Schwan, Plenum: New York, 1985.

[Sau85b] F.A. Sauer and R.W. Schlögl, õTorques exerted on cylinders and spheres by external electromagnetic fields. A contribution to the theory of field induced rotationö, <u>Interactions Between Electromagnetic Fields and Cells</u>, pp. 203-251, Eds. A. Chiabrera, C. Nicolini, and H.P. Schwan, Plenum: New York, 1985.

[Schm00] K.A. Schmitz, D.L. Holcomb-Wygle, D.J. Oberski, and C.B. Lindemann, õMeasurement of the force produced by an intact bull sperm flagellum in isometric arrest and estimation of the dynein stall forceö, *Biophys. J.*, vol. 79, pp. 468-478, 2000.

[Schu00] K.C. Schuster, E. Urlaub, and J.R. Gapes, õSingle-cell analysis of bacteria by Raman microscopy: spectral information on the chemical composition of cells and on the heterogeneity in a cultureö, *J. Microbiol. Methods*, vol. 42, pp. 29-38, 2000.

[Schwan92] H.P. Schwan, õLinear and nonlinear electrode polarization and biological materialsö, *Ann. Biomed. Eng.*, vol. 20, no. 3, pp. 269-288, 1992.

[Sha95] H.M. Shapiro, <u>Practical Flow Cytometry</u>, John Wiley and Sons: New York, 1995.

[Sha00] H.M Shapiro, õMicrobial analysis at the single-cell level: tasks and techniquesö, *J. Microbiol. Methods*, vol. 42, pp. 3-16, 2000.

[Sims07] C.E. Sims and N.L. Allbritton, õAnalysis of single mammalian cells on-chipö, *Lab on a Chip*, vol. 7, pp. 423-440, 2007.

[Smi00] A.E. Smith, Z. Zhang, C.R. Thomas, K.E. Moxham, and A.P.J. Middelberg, õThe mechanical properties of *Saccharomyces cerevisiae*ö, *Proc. Natl. Acad. Sci. U.S.A.*, vol. 97, pp. 9871-9874, 2000.

[Sohn00] L.L. Sohn, O.A. Saleh, G.R. Facer, A.J. Beavis, R.S. Allan, and D.A. Notterman, õCapacitance sytometry: measuring biological cells one by oneö, *Proc. Natl. Acad. Sci.*, vol. 97, no. 20, pp. 10687-10690, 2000.

[Spurk08] J.H. Spurk and N. Aksel, <u>Fluid Mechanics (2nd Ed.)</u>, Springer-Verlag: Berlin Heidelberg, 2008.

[Stee00] H. Steels, S.A. James, I.N. Roberts, and M. Stratford, õSorbic acid resistance: the inoculum effectö, *Yeast*, vol. 16, pp. 1173-1183, 2000.

[Stein92] D.S. Stein, J.A. Korvick, and S.H. Vermund, õCD4+ lymphocyte cell enumeration for prediction of clinical course of human-immunodeficiency-virus diseaseô A reviewö, *J. Infect. Dis.*, vol. 165, pp. 352-63, 1992.

[Steink73] J.A. Steinkamp, M.J. Fulwyler, J.R. Coulter, R.D. Hiebert, J.L. Horney, and P.F. Mullaney, õNew multiparameter seperator for microscopic particles and biological cellsö, *Rev. Sci. Instrum.*, vol. 44, pp. 1301-1310, 1973.

[Sten02] H. Stender, M. Fiandaca, J.J. Hylgig-Nielsen, and J. Coull, õPNA for rapid microbiologyö, *J. Microbiol. Methods*, vol. 48, pp. 1-17, 2002.

[Step96] M. Stephens, M.S. Talary, R. Pethig, A.K. Burnett, and K.I. Mills, õThe dielectrophoresis enrichment of CD34(+) cells from peripheral blood stem cell harvestsö, *Bone Marrow Transplat*, vol. 18, no.4, pp. 777-782, 1996.

[Str01] A. Strauß, S. Michel, and J. Morschhäuser, õAnalysis of phase-specific gene expression at the single-cell level in the white-opaque switching system of *Candida albicans*ö, *J. Bacteriol.*, vol. 183, no. 12, pp. 3761-3769, 2001.

[Sull99] M.T.E. Suller and D. Lloyd, õFluorescence monitoring of antibiotic induced bacterial damage using flow cytometryö, *Cytometry*, vol. 35, pp. 235-241, 1999.

[Sumn02] E.R. Sumner and S.V. Avery, õPhenotypic heterogeneity: differential stress resistance among individual cells of the yeast *Saccharomyces cerevisiae*ö, *Microbiol.*, vol. 148, pp. 345-351, 2002.

[Taka63] S. Takashima, õDielectric dispersion of DNAö, *J. Mol. Biol.*, vol. 7, no. 5, pp. 455-467, 1963.

[Tal95] M.S. Talary, K.I. Mills, T. Hoy, A.K. Burnett, and R. Pethig, õDielectrophoretic separation and enrichment of CD34+ cell subpopulation from bone marrow and peripheral blood stem cellsö, *Med. Biol. Eng. Comput.*, vol. 33, no. 3, pp. 235-237, 1995.

[Thar08] T. Tharmalingam, K. Sunley, and M. Butler, õHigh yields of monomeric recombinant β-interferon from macroporous microcarrier cultures under hypothermic conditionsö, *Biotechnol. Prog.*, vol. 24, no. 4, pp. 832-838, 2008.

[Track09] *www.cabrillo.edu/~dbrown/tracker/*, 2009.

[Tran01a] T.D. Tran, D.R. Oliver, D.J. Thomson and G.E. Bridges, õZeptofarad (10^{-21} F) resolution capacitance sensor for scanning capacitance microscopyö, *Rev. Sci. Inst.*, vol. 72, pp. 2618-2623, 2001.

[Tran01b] T.D. Tran, ōDevelopment of a zeptofarad (10^{-21} F) resolution capacitance sensor for scanning capacitance microscopyö, MSc Thesis, University of Manitoba, 2001.

[Turn00] N.A. Turner, J. Harris, A.D. Russell, and D. Lloyd, ōMicrobial differentiation and changes in susceptibility to antiomicrobial agentsö, *J. Appl. Microbiol.*, vol. 89, pp. 751-759, 2000.

[Veal00] D.A. Veal, D. Deere, B. Ferrari, J. Piper, and P.V. Attfield, ōFluorescence staining and flow cytometry for monitoring microbial cellsö, *J. Immunol. Methods*, vol. 243, pp. 191-210, 2000.

[Vit61] E. Vitols, R.J. North, and A.W.L. Linnane, ōStudies on the oxidative metabolism of *Saccharomyces cerevisiae*: I. Observations on the fine structure of the yeast cellö, *J. Biophys. Biochem. Cytol.*, vol. 9, no. 3, pp. 689-699, 1961.

[Viv00] J. Vives-Rego, P. Lebaron, and G. Nebe-von-Caron, ōCurrent and future applications of flow cytometry in aquatic microbiologyö, *FEMS Microbiol. Rev.*, vol 24, pp. 429-448, 2000.

[Vol01] J. Voldman, R.A. Braff, M. Toner, M.L. Gray and M.A. Schmidt, ōHolding forces of single-particle dielectrophoretic trapsö, *Biophys. J.*, vol 80, pp. 531-541, 2001.

[Wang93a] X.B. Wang, Y. Huang, R. Hölzel, J.P.H. Burt, and R. Pethig, ōTheoretical and experimental investigations of the interdependence of the dielectric, dielectrophoretic and electrorotational behaviour of colloidal particlesö, *J. Phys. D Appl. Phys.*, vol. 26, pp. 312-322, 1993.

[Wang93b] X.B. Wang, Y. Huang, J.P.H. Burt, G.H. Markx, and R. Pethig, ōSelective dielectrophoretic confinement of bioparticles in potential energy wellsö, *J. Phys. D Appl. Phys.*, vol. 26, pp. 1278-1285, 1993.

[Wat91] J.V. Watson, <u>Introduction to Flow Cytometry</u>, Cambridge University Press: Cambridge, U.K., 1991.

[Wed01] N. Wedemeyer and T. Potter, ôFlow cytometry: an ÷oldø tool for novel applications in medical geneticsö, *Clin. Genet.*, vol. 60, pp. 1-8, 2001.

[Whi03] F.M. White, <u>Fluid Mechanics (5th Ed.)</u>, McGraw-Hill, 2003.

[Wiet99] J. Wietzorrek, N. Plesnila, A. Baethmann, and V. Kachel, ôA new multiparameter flow cytometer: optical and electric cell analysis in combination with video microscopy in flowö, *Cytometry*, vol. 35, pp. 291-301, 1999.

[Wiki09] *en.wikipedia.org/wiki/Loss_tangent*, 2009.

[Wins00] M.K. Winson and H.M. Davey, ôFlow cytometric analysis of microorganismsö, *Methods*, vol. 21, pp. 231-240, 2000.

[Wit07] M.A. Witek, M.L. Hupert, and S.A. Soper, ôChapter 15: Single-cell and single-molecule analyses using microfluidic devicesö, <u>BioMEMS: Technologies and Applications</u>, pp. 391-441, Eds. W. Wang and S.A. Soper, CRC Press, 2007.

[Wood07] D.K. Wood, M.V. Requa, and A.N. Cleland, ôMicrofabricated high-throughput electronic particle detectorö, *Rev. Sci. Inst.*, vol. 78, no. 10-104301, pp. 1-6, 2007.

[Yang95] L. Yang, S. Weerasinghe, P.E. Smith, and B.M. Pettitt, ôDielectric response of triplex DNA in ionic solution from simulationsö, *Biophys. J.*, vol. 69, no. 4, pp. 1519-1527, 1995.

[Yang99] J. Yang, Y. Huang, X. Wang, X.B. Wang, F.F. Becker, and P.R.C. Gascoyne, "Dielectric properties of human leukocyte subpopulations determined by electrorotation as a cell separation criterion", *Biophys. J.*, vol. 76, no. 6, pp. 3307-3314, 1999.

[Yao02] X. Yao, J. Walter, S. Burke, S. Stewart, M.H. Jericho, D. Pink, R. Hunter, and T.J. Beveridge, "Atomic force microscopy and theoretical considerations of surface properties and turgor pressures of bacteria", *Colloids Surf. Ser. B*, vol. 23, pp. 213-230, 2002.

[Yi06] C. Yi, C.W. Li, S. Ji, and M. Yang, "Microfluidic technology for manipulation and analysis of biological cells", *Anal. Chim. Acta*, vol. 560, pp. 1-23, 2006.

[You03] C.F. You, H.Y. QI, and X.C. Xu, "Lift force on rotating spheres at low reynolds numbers and high rotational speeds", *Acta Mechanica Sinica*, vol. 19, no. 4, pp. 300-307, 2003.

[Yu07] C. Yu and L. Shi, "Chapter 9: Bio-MEMS devices in cell manipulation: microflow cytometry and applications", <u>BioMEMS: Technologies and Applications</u>, pp. 237-262, Eds. W. Wang and S.A. Soper, CRC Press, 2007.

[Zill01] D.G. Zill and M.R. Cullen, <u>Differential Equations with Boundary-Value Problems (5th Ed.)</u>, Brookes/Cole: Pacific Grove, CA, USA, 2001.